CHEMICAL SENSING APPLICATIONS OF LUMINESCENT MoS_2 AND WS_2 BASED 2D MATERIALS

A thesis submitted

in partial fulfillment for the Degree of

Doctor of Philosophy

By

NEEMA. P. M

SC15D006

Department of Chemistry

INDIAN INSTITUTE OF SPACE SCIENCE AND TECHNOLOGY

THIRUVANANTHAPURAM

JUNE 2020

CERTIFICATE

This is to certify that the thesis entitled **'Chemical Sensing Applications of Luminescent MoS_2 and WS_2 based 2D Materials'** submitted by **Neema P M** (SC15D006) to the Indian Institute of Space Science and Technology Thiruvananthapuram, in partial fulfillment for the award of the degree of **Doctor of Philosophy** is a *bonafide* record of research work carried out by her under my supervision. The contents of this thesis, in full or in parts, have not been submitted to any other Institution or University for the award of any degree or diploma.

Dr. Jobin Cyriac
Supervisor
Associate Professor
Department of Chemistry

Thiruvananthapuram
June 2020

Countersignature of the HOD with seal

DECLARATION

I declare that this thesis entitled '**Chemical Sensing Applications of Luminescent MoS_2 and WS_2 based 2D Materials'** submitted in partial fulfillment of the degree of Doctor of Philosophy is a record of original work carried out by me under the supervision of Dr. Jobin Cyriac and has not formed the basis for the award of any other degree or diploma, in this or any other Institution or University. In keeping with the ethical practice of reporting scientific information, due acknowledgments have been made wherever the finding of others have been cited.

Neema P M
SC15D006

Thiruvananthapuram-695 547
June 2020

Acknowledgment

I am glad that I have an opportunity to formally thank everyone who shaped me and assisted me, one or the other way for pursuing my dream of doing scientific research in a prestigious institution. I can't but thank all the efforts undertaken by many individuals, for inculcating perseverance and patience right from primary school level, across my academic life that nearly spans twenty-three years. I would like to convey my regards to a lot of people for their immense encouragement and motivation.

First and foremost, I am indebted to my research supervisor Dr. Jobin Cyriac, Associate Professor, Department of Chemistry, for his guidance and support during the tenure of my PhD. I consider myself lucky to work under his guideship. I have been greatly benefitted by his scientific discernments, subject expertise, constructive criticism, endless tolerance and unwavering professionalism. He has been a constant source of motivation and inspiration. My heartfelt gratitude towards him for all the timely help, insightful approach and healthy discussions which pave a way for the completion of this thesis.

My sincere thanks to all the doctoral committee members; Prof. S. Sampath, IISc Bangalore; Dr. Dona Mathew, VSSC Thiruvananthapuram; Dr. Karunakaran Venugopal, CSIR-NIIST Thiruvananthapuram; Dr. Anup S, IIST; Dr. K. Y. Sandhya, IIST for their constructive criticism, valuable feedback and suggestions. I would like to extend my gratitude to Prof. Kuruvilla Joseph, Dean, Student Activities, Prof. Prabhakaran, HOD Chemistry, Prof. Nirmala Rachael James, former HOD Chemistry for their kind patience and warm attitude. I would also like to thank all the faculty members of the Department of Chemistry for their constant support. The healthy academic atmosphere in the department was a catalyst for the professional as well as personal growth.

I am deeply indebted to all staff of the Department of Chemistry, especially Ms. Jayashree L, Ms. Jayashree R, Ms. Bindu Prajeesh, Ms. Bindu P C, Ms. Ramya, Ms. Rahna, Mr. Loveson Albert, Mr. Dilip Kumar K G, Mr. Sreekumaran Nair for their support and help. I wish to express my gratitude to all my seniors; Dr. Roymon Joseph,

Dr. Rakesh, Dr. Sujith Vijayan, Dr. Mukhthar Ali, Dr. Reshma C, Dr. Aswathy R, Dr. Lavanya J, Dr. Devi Renuka and Dr. Meegle S Mathew for offering their time and support whenever I asked for. Words fail me to express my sincerest thanks to my beloved senior, Dr. Manjunath, who has been a legitimate critic, my sanity tester, and my great friend, who showed me how to do the chemistry and how to live. You were and continue to be an inspiration for me. I am incredibly thankful to all my batchmates, Ms. Haritha H, Mr. Yogesh Sanjay Choudhary, Mr. Praveen Wilson, Ms. Gayathri G R, Ms. Anu Kuriakose, Ms. Sonu Tabitha Paulson, Ms. Vijayalakshmi; we started this together, and we had a good time together. I am highly indebted to all my juniors, Mr. Sanu Xavior, Ms. Arya Nair J S, Ms. Saisree S, Ms. Varsha M V, Mrs. Sreekala Arjun, Ms. Chithra Nair and Mr. Govind Sharma for all the good time we spent together. Special thanks to BDS Deeraj, who has always been there when I was in need of help. In no words, I can express my gratitude to my group members Ms. Nisha Balachandran, Ms. Ann Mary Tomy, Ms. Bhasha Sathyan. I remember with pleasure the time I spent with all of you. I sincerely thank Ms. Divyamol R, Ms. Midhula Wilson, Mr. D. Rajasekhar Bhupal, Ms. Mini V, Ms. Karthika Sunil and Ms. Santra Santhosh, with whom I had the privilege to work and discuss.

I must acknowledge the support of many selfless personnel who performed various characterization techniques during my research. Special thanks to Mr. Satheesh, Aerospace Dept., IIST; Mr. Vijayaraghavan, PSGIAS, Coimbatore, Mr. Sarath, AIMS, Cochin, Dr. Saju Pillai CSIR-NIIST Thiruvananthapuram and staff at CUSAT SAIF-STIC for patiently doing the analysis till satisfactory results were obtained. This acknowledgment wouldn't be complete if I didn’t convey my heartfelt thankfulness to all those ambrosial beings (the list is so long), who avail me delicious food all these five years.

I convey my special gratitude to all my friends especially, Dr. Suma Susan Thomas, Ms. Shyni Peter, Ms. Suja Subrahmaniam, Dr. Sudha K S, Mr. Ramachandran, Mr. Mohammed Ramees P, Ms. Neeraja Anand for making my all these years cheerful and colorful. Special thanks to J. K. Rowling, who sprinkle a speck of magic in my life.

Finally, I would like to express my deep sense of gratitude to my family members. For Amma and Achan, who always bestowed me the freedom to choose my ways; my brother, who is always most proud about all my achievements; Edthyamma, with her care and support; Aliyan, with his immaculate affection, Ammu, Appu and Cheruthu who make my each day counts with the magic only kids can summon. I am deeply indebted to my Che, without whose motherly love and parental support, I wouldn't have reached here. I owe them, with my life. Well, this acknowledgment wouldn't be complete without my humble Pranam to my beloved Guru and God almighty. Thank you all.

Neema P M

ABSTRACT

The enduring interest in miniaturizing silicon-based electronics coalesce with the discovery of graphene has driven the focus of the scientific community toward atomically thin two-dimensional (2D) semiconductors. A total of more than forty layered materials have been isolated with unique and intriguing properties. The emergence of photoluminescence (PL) from nearly atomically thin semiconducting layered materials opened a new way for optoelectronic and chemical sensor applications. MoS_2 and WS_2 are two of the typical transition metal dichalcogenides (TMDs) that gain earnest attention in this regard. Although there was a substantial number of applications, where these nanomaterials have scrutinized, there is still room for exploration in terms of understanding the fundamentals, their intriguing physical and chemical nature, and fabrication of these materials in accordance with the current needs.

We have synthesized a range of nanomaterials based on MoS_2 and WS_2 via an environmentally benign hydrothermal route. A comprehensive morphological and photophysical characterizations of these materials have been performed and demonstrated their chemical sensor applications for the detection of biological, environmental and industrially relevant analyte molecules. The studies conducted using various nanomaterials given in this Thesis is briefed below.

Dopamine is a neurotransmitter in our body and the numerous in-depth study of dopamine and its oxidative pathways exhibited its role in diseases such as Parkinson's, Huntington's and Alzheimer's. Though several strategies are available for the detection of dopamine, a handy tool for its detection without being interfered with molecules such as ascorbic acid, uric acid, etc. are highly appealing. The high quenching efficiency of dopamine and its oxidized products towards the PL emission of an alkaline solution of MoS_2 quantum dots dispersed over nanosheets (MoS_2 QDNS), has been explored and a selective sensor for dopamine has been devised. The Förster resonance energy transfer (FRET), along with the inner filter effect (IFE) play a major role in the quenching and a satisfactory dynamic range of 2.5 nm to 10.4 μM with a calculated limit of detection of 0.9 nM.

Though the optical and electronic properties of MoS_2 has been studied in detail, the chemistry of MoS_2 nanomaterials towards different pH is still blurry and an attempt towards understanding the mechanism of difference in PL emission towards different pH of the solution has been carried out meticulously. It has been observed that, by changing the pH of the MoS_2 QDNS solution from highly alkaline to extremely acidic, the PL emission intensity is found to be plummeted, with the change in color of the solution from light yellow to deep yellow. The emergence of new peaks in the

absorption spectra attests to the formation of new compounds in the solution upon the addition of mineral acids such as H_2SO_4, HCl, etc. for altering the pH. The etching of edge S and subsequent formation of smaller molecules such as NaHS are surmised to be the reasons for color change as well as quenching of fluorescence emission. In the presence of the strong oxidizing agent, H_2O_2, the color of the solution is found to be faded away. From XPS and Raman analysis, it has been hypothesized that the oxidation of NaHS to its colorless $NaSO_4$ is the reason behind this observation, and as the energy transfer pathway established between sensor solution and NaHS has been shut away, the PL emission is found to be recovered. Hence we drafted an indirect turn-on sensing of glucose using acidified MoS_2 QDNS (MoS_2 $QDNS_{ac}$), by incorporating it with glucose oxidize (GOx) enzyme. In the presence of ambient oxygen, GOx can oxidize glucose into gluconic acid and H_2O_2, so an indirect quantitative determination of glucose can be achieved. A satisfactory linear range of 2-90 µM was obtained for glucose sensing with a limit of detection of 0.6 µM. A real sample detection of glucose content in the blood sample of a diabetic patient is accomplished with excellent recovery values.

Apart from MoS_2, we have synthesized nanomaterials of another TMDs material; WS_2 materials with luminescence and utilized them as chemical sensors. Förster resonance energy transfer, together with electron transfer, made WS_2 quantum dots a selective turn-off sensor for the detection of trinitrophenol (TNP); a highly explosive nitroaromatic compound. The sensor operates within a dynamic range of 0.5 to 94.5 µM concentration of TNP, which follows the Stern-Volmer equation. The high selectivity of the sensor towards TNP against chemically similar molecules such as dinitrophenol, dinitrotoluene, etc. was achieved because of the existence of FRET as a major quenching mechanism, against commonly observed electron transfer mechanism.

A turn-on sensor for basic amino acids was designed using highly photoluminescent WS_2 nanosheets obtained by the hydrothermal reaction route. The PL emission of nanosheets (λ_{max}= 452 nm upon λ_{ex} 360 nm), were found to be quenched initially upon the addition of $AgNO_3$. The quenching is followed by a color change of the solution from slightly yellow to turn deep yellow with the advent of a distinct absorption peak near to 400 nm. This inferred the formation of Ag NPs, upon the addition of $AgNO_3$ into a solution of WS_2 NS and was confirmed by TEM analysis. The quenching of PL emission is attributed to the FRET mechanism. The negatively charged Ag NPs were selectively aggregated by using three basic amino acids viz, lysine, histidine and arginine, which can shut the FRET pathway and thus the recovery of PL emission of WS_2 nanosheets. The aggregation of Ag NPs occurs in a sensor solution of pH below the isoelectric points of each amino acids help to discriminate

them. The analytical parameters, dynamic range and limit of detection have been evaluated for the sensor system. Various spectroscopic analyses unraveled the mechanism of the quenching and subsequent recovery.

We demonstrated a simple strategy for the synthesis of luminescent MoS_2 and WS_2 nanomaterials and the utilization of the material for the detection of useful molecules. The fundamental understanding of the materials, mechanism of sensor action and demonstration of real sample analysis would help to extend the use of such materials in chemical sensor technologies.

TABLE OF CONTENT

List of Figures

List of Tables

ABBREVIATIONS

AAs	Aminoacids
AFM	Atomic force microscopy
Arg	Arginine
DLS	Dynamic light scattering
DMF	Dimethylformamide
DNP	Dinitrophenol
DNT	Dinitrotoluene
ET	Electron transfer
FET	Field effect transistors
FRET	Förster (fluorescence) resonance energy transfer
FTIR	Fourier transform infrared spectroscopy
GO	Graphene oxide
GOx	Glucose oxidize
H_2O_2	Hydrogen peroxide
H_2SO_4	Sulphuricacid
HCl	Hydrochloric acid
His	Histidine
HRXPS	High resolution X-ray photoelectron spectroscopy
IFE	Inner filter effect
IPA	Isopropylalcohol
Lys	Lysine
MoS_2 QDNS	MoS_2 quantum dots dispersed over nanosheets
NAs	Nitroaromatics
NB	Nitrobenzene
NMP	N-Methyl-2-pyrrolidone
NPs	Nanoparticles
NSs	Nanosheets

PET	Photoinduced electron transfer
PHE	Phenol
PL	Photoluminescence
PVA	Poly-(vinyl alcohol)
QDs	Quantum dots
QY	Quantum yield
SAED	Selected area electron diffraction
SPR	Surface Plasmon Resonance
TCSPC	Time-correlated single-photon counting
TEM	Transmission electron microscopy
TMDs	Transition metal dichalcogenides
TNP	Trinitrophenol
XPS	X-ray photoelectron spectroscopy

NOTATIONS

Φ	Quantum yield
E	FRET efficiency
η	Refractive index
A	Absorbance
I	Intensity
λ	Wavelength
τ	Lifetime
χ^2	CHSQ2
T	Temperature
t	Time
σ	Standard deviation of blank
κ	Slope
F	Fluorescence intensity
C	Concentration

CHAPTER 1

INTRODUCTION

This chapter gives a brief insight into the key properties of 2D layered materials in general, MoS_2 and WS_2 in particular, which made them attractive candidates for applications in various domains such as electronic, optoelectronic, energy harvesting and storage, etc. Different methods of synthesis were discussed with the help of a literature review. A detailed description of the general strategies of fluorescence-based sensors was given in the second section of the chapter.

1.1 Two Dimensional (2D) Layered Materials

The advent of graphene, an atom-thick layered wonder material, coupled with the quest for miniaturization of silicon-based electronics, led the scientific community to channelize their attention towards similar 2D layered materials. While the lack of bandgap hindered the applications of graphene in many occasions, the other 2D layered materials such as transition metal dichalcogenides (TMD), oxides, hydroxides, oxychlorides, etc. with finite bandgap and air stability propel the research in myriad areas such as electronics, catalysts, optoelectronics, photonics, and sensors. These materials are benefitted with unique physicochemical properties, large specific surface area, easy synthesis of large single sheets and flexible nature with good mechanical strength.

1.1.1 Properties of 2D Layered Materials

Transition metal dichalcogenides (TMDs) are one of the best-studied 2D materials. They are having a general formula of MX_2, where M is the transition metal element (such as group IV and V) and X is a chalcogen (S, Se, Te). A monolayer of TMDs consists of hexagonally arranged metal ions, which are sandwiched between two hexagonally ordered planes of chalcogen atoms. In general, the oxidation state of metal ions is +4, whereas that of chalcogen is –2. The thickness of each layer is 6-7 Å,

with strong in-plane covalent bonds and different layers are held together by week van der Waals interactions. Single-layer of MX_2 can exist in two polytypes; octahedral (D3d point group, centered honeycomb motif) and trigonal prismatic (D3h point group, honeycomb motif) in accordance with the position of chalcogen to the metal ion, whereas the stacking of monolayers for the formation of bulk TMDs leads to the generation of different structural polytypes such as 1T (tetragonal symmetry, one layer per repeat unit, octahedral coordination), 2H (hexagonal symmetry, two layers per repeat unit, trigonal prismatic coordination) and 3R (rhombohedral symmetry, three layers per repeat unit, trigonal prismatic coordination). These different stacking arrangements are represented in Figure 1.1.

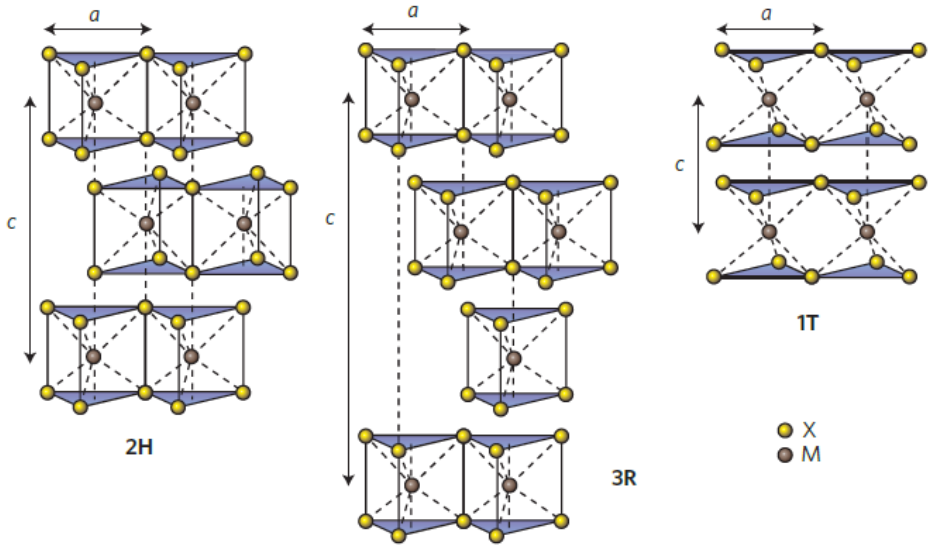

Figure 1.1: Schematics of the structural polytypes of TMDs 2H, 3R and 1T. The yellow balls represent chalcogen atoms (X); the metal atoms (M) are represented as grey. For different materials, the lattice constant a are in the range of 3.1 to 3.7 Å. The *C* represents the stacking index and is an indication of the number of layers in each stacking order, and the interlayer spacing is ~6.5 Å. (Wang et al., 2012)

1.1.1.1 Electronic Properties

All layered TMDs crystallizes either in octahedral or trigonal prismatic form and group VI TMDs prefer to trigonal prismatic coordination (2H). The ligand field splitting of d electrons of metal ions in the presence of chalcogens for this coordination

are d_{xy}, d_{yz}, d_{zx} (t^2_g) and d_z^2, $_x^2-_y^2$ (e_g) for octahedral d_z^2 (a1′), $d_x^2 - _y^2$,d_{xy} (e′), and d_{xz}, d_{yz} (e″) for trigonal prismatic geometry. The two 'd' electrons in the metal ions usually fill in the d_z^2 orbital of trigonal prismatic form, making it a semiconductor. Whereas, the partial filling of t^2_g orbital in the octahedral geometry, results in the metallic 1T form, is generally not stable (Figure 1.2 a and b). The energy dispersion diagram of a typical TMD, MoS_2 is shown in Figure 1.2 c. The two valence band hills are located at the center (Γ) and corners (K′) of the Brillouin zone whereas two conduction band minima (CBM) are at K point and midway between the K−Γ line (Λ point) of the Brillouin zone. The splitting of valence band maxima (VBM) at the K point is attributed to the strong spin-orbit coupling.

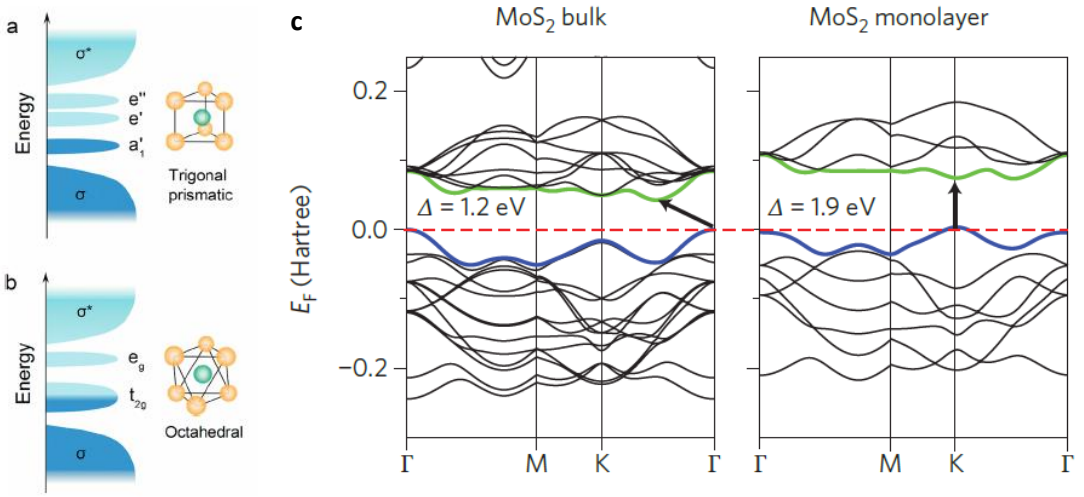

Figure 1.2: (a) and (b) shows the illustration of filling of electrons in octahedral and trigonal prismatic coordination. (c) Electronic band structure of bulk and monolayer MoS_2 (a and b: Zhao et al., 2015; c: Kuc et al., 2011)

Another key point obtained from the energy dispersion diagram is the coincidence of VBM and CBM at the K point of Brillouin zone, which makes monolayer MoS_2 a direct bandgap semiconductor, unlike its bulk counterpart, which is an indirect bandgap semiconductor. These changes in the band structure with layer numbers are attributed to change in hybridization between p_z orbitals on S atoms and d orbitals on Mo atoms which arise due to the quantum confinement effect. This cross over is not limited to MoS_2; other TMDs such as WS_2, $MoSe_2$, and WSe_2, which are

isoelectronic to MoS_2 also show a similar trend. And this cross over from indirect to direct bandgap, upon reducing the number of layers is significant, as it makes these material ideal candidates for the photonics, optoelectronics and in the sensor domains. (Wang et al., 2012; Chhowalla et al., 2013; Jariwala et al., 2014)

1.1.1.2 Optical Properties

1.1.1.2.1 Absorption and Emission Characteristic

The optical properties of TMDs are strongly influenced by their electronic band structures. The change in the number of layers from bulk to mono or a few layers; the shift in indirect to direct bandgap reflected in the photoconductivity, absorption and photoluminescence properties of MoS_2. The optical absorption spectrum of the bulk and monolayered MoS_2 features two major peaks ~620 and ~680 nm, corresponding to two exciton bands, viz. B and A excitons, respectively (Wang et al., 2012; Song et al., 2015a). This is due to the direct gap transitions between the split VBM and the CBM at the K point of the Brillouin zone. Ramasubramaniam (2012) studied band structures and optical properties of different TMDs using the GW approximation in conjunction with the Bethe-Salpeter equation. The study showed that these peak energies correspond to the expected K point gap energies of the layered structures of MoS_2, $MoSe_2$, $MoTe_2$, WS_2, and WSe_2. The splitting of the valence band in monolayer and bulk attributed to two different origins. Monolayer MoS_2 lack of inversion symmetry and splitting of the VBM in a single layer is due to spin-orbit coupling alone. Whereas, the split in the bulk and a few layers, which possess inversion symmetry, is attributed to spin-orbit coupling along with interlayer coupling.

Another important feature that emerged due to cross over from indirect to direct energy gap is photoluminescence (PL) (Mak et al., 2010; Splendiani et al., 2010). Mono and a few-layer MoS_2 show strong fluorescence corresponding to the absorption peaks (as seen in Figure 1.3). The quantum yield (QY) of single-layer MoS_2 is 4×10^{-3}, calculated from direct-gap hot luminescence, which is four orders of magnitude higher than that of the bulk (Wang et al., 2012; Song et al., 2015a). Double layer MoS_2 shows

peaks at 1.59 eV (ca.780 nm) and two peaks near 1.88 eV (ca.660 nm), with QY around 10^{-5} to 10^{-6}. As the number of layers increases, peak at 1.59 eV continuously shifted and reached 1.2 eV for bulk, which corresponds to the indirect bandgap. Still, the QY values are significantly lower than the near-unity values which are expected for a direct-gap semiconductor. The improvement of QY was successfully demonstrated by acid treatment and p-type doping (Kiriya et al., 2018; Mouri et al., 2013). The PL of single-layered MoS_2 can reach near-unity by treatment with bis(trifluoromethane)sulfonimide (TSFI) and sulfuric acid (Kiriya et al., 2018). Different solvents such as 1,2-dichloroethane (DCE), acetonitrile and water having different acidity were employed for the study and found that proton environment can lead to an increase in PL intensity. The mechanism was proposed as a reduction in nonradiative recombination by surface passivation and partial charge transfer processes due to protons present in the solution.

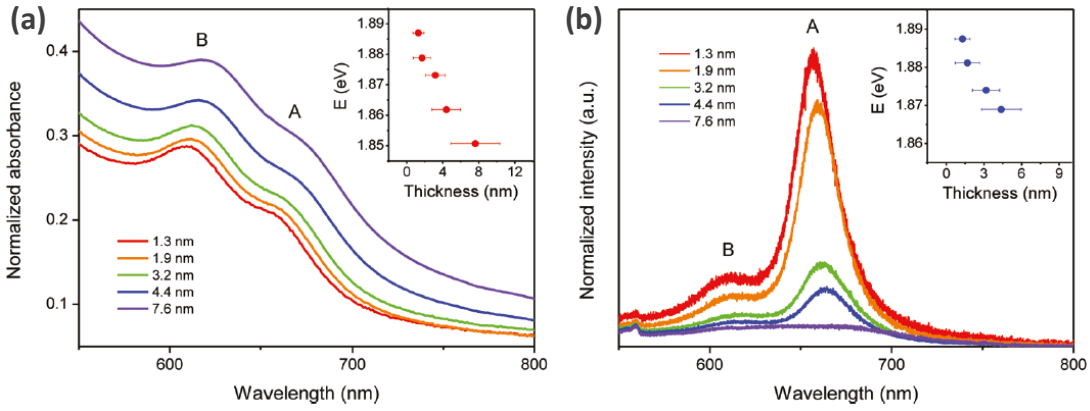

Figure 1. 3: (a) Absorption and (b) photoluminescence spectra of MoS_2 thin films of average thicknesses ranging from 1.3 to 7.6 nm. Insets show energy of the A exciton peak as a function of average film thickness (Eda et al., 2011).

Due to the correlation of absorption and emission profiles with that of band structures, any change in the bandgap will reflect in the absorption or emission features. For example, electrochemical intercalation of alkali metal ions with MoS_2 leads to a phase change from its semiconducting 2H to metallic 1T, which invariably quench the fluorescence emission. The application of strain, which can reduce the direct gap at K point, reduces the intensity and energy of A1 exciton peak (Song et al., 2015a).

1.1.1.2.2 Raman Spectroscopy and Phonon-Phonon Interaction

The phonon structure of 2D layered materials is heavily influenced by the number of layers present, carrier concentration, temperature, strain, etc. Therefore, the different crystalline structure of MoS_2 can be studied using non-destructive Raman spectroscopic analysis. A typical Raman spectrum of bulk MoS_2 consists of four first-order Raman active modes corresponding to E^2_{2g}, E_{1g}, E^1_{2g} and A_{1g}. (Li et al., 2012a). Of these, The E^2_{2g} mode at 32 cm^{-1} results from the vibration of an S–Mo–S layer against adjacent layers. The E_{1g} mode at 286 cm^{-1} is forbidden in the back-scattering experiment on a basal plane. In degenerate E^1_{2g} mode at 383 cm^{-1}, Mo and S atoms are moving in-plane in opposite directions. The A_{1g} mode at 408 cm^{-1} is an out-of-plane mode where the top and bottom S atoms are in out-of-plane motion in opposite directions while Mo is stationary. Different modes of vibrations of MoS_2 can be seen in Figure 1.4. Apart from these modes, other Raman peaks can be observed in bulk MoS_2 that appear due to the second-order process involving the longitudinal acoustic phonons at the M point, widely designated as LA(M).

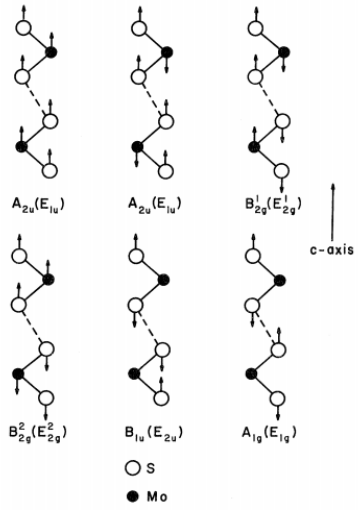

Figure 1.4: Displacement vectors for the six c-axis normal modes of MoS_2 (2H), as viewed along the [1000] direction. Irreducible representations are assigned; those in parentheses are for the analogous basal-plane modes (Wieting and Verble, 1971).

The layer thickness dependence towards peak frequencies, intensities and widths of E^1_{2g} and A_{1g} modes in a few layered MoS_2 flakes were systematically studied

in detail by many groups (Lee et al., 2010a; Li et al., 2012a). According to the study by Li et al. (2012a), the frequencies of E^1_{2g} and A_{1g} peaks can be used as a more accurate benchmark in order to identify the number of layers of MoS_2 flakes ($\leq$ 4 layers). From monolayer to bulk, upon addition of layers, the stiffening of the out of-plane phonon modes (A_{1g}) are observed resulting in its blue shift along with the relaxation of in-plane bonding (E^1_{2g}), causing a red shift. These shifts in positions were attributed to the influence of neighboring layers on the effective restoring forces on atoms (weaker interlayer coupling) and the increase of dielectric screening of long-range Coulomb interactions, respectively (Molina-Sanchez and Wirtz, 2011). Figure 1.5 depicts the thickness dependence on the frequency of E^1_{2g} and A_{1g} modes.

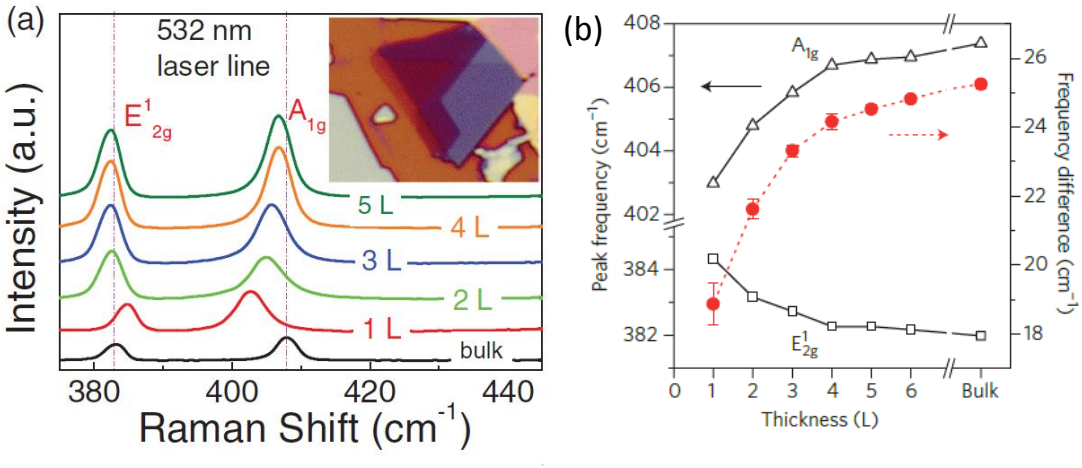

Figure 1.5: (a) Thickness-dependent Raman spectra for MoS_2 (Li et al., 2012a) (b) Peak position shifts for the E^1_{2g} and A_{1g} modes as a function of MoS_2 layer thickness (Lee et al., 2010a).

1.1.2 Synthetic Methods

.

The reliable production of atomically thin layered materials with uniform properties with a high degree of repeatability is a tedious task that is necessary for translating their unique electronic and optical properties into devices. Some of the important strategies for the synthesis of 2D layered materials have been discussed below.

1.1.2.1 Top- down Methods

1.1.2.1.1 Mechanical exfoliation

Atomically thin TMDs can be peeled off from bulk crystals by micromechanical cleavage using adhesive tapes, as in the case of graphene (Novoselov et al., 2005; Alem et al., 2009; Lee et al., 2010b; Mak et al., 2010; Splendiani et al., 2010; Bertolazzi et al., 2011; Radisavljevic et al., 2011a). For example, single-layer MoS_2 was first reported to be cleaved from bulk and these thin films were transferred to silicon oxide layers which can be optically identified by light interference, using 90 nm, 270 nm or 300 nm SiO_2/ Si substrate, as seen in Figure 1.6 (Benameur et al., 2011; Li et al., 2012b). Other layered materials such as BN and oxide nanosheets were exfoliated into single sheets by this method (Alem et al., 2009; Kalantar-Zadeh et al., 2010; Dean et al., 2010; Osada et al., 2012). WS_2 flakes were successfully peeled off from bulk and demonstrated that these materials show very low cytotoxicity and genotoxicity effects and can be used for future biomedical applications (Appel et al., 2016).

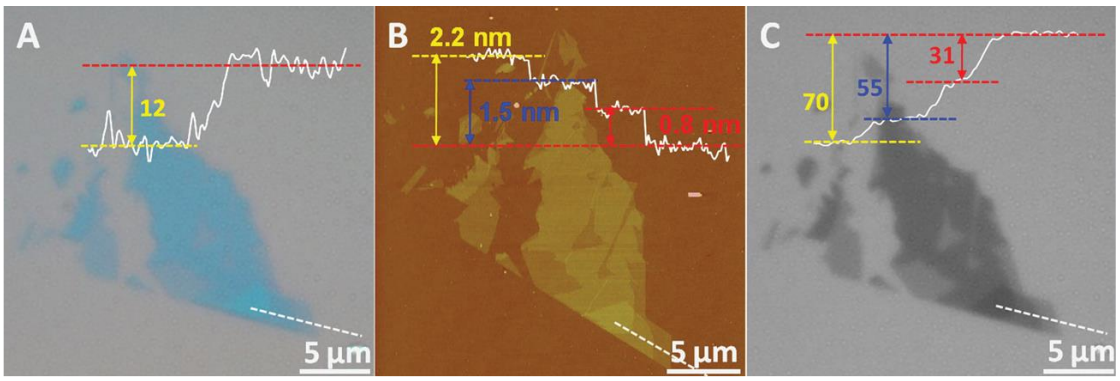

Figure 1. 6: Optical and AFM images of a MoS_2 flake consisting of 1L, 2L, and 3L sheets. (A) Color optical image. Inset: Contrast profile of the dashed line showing the intensity difference between the MoS_2 flake and 300 nm SiO_2 substrate. (B) is the AFM image of the same sample. Inset: Height profile of the dashed line. (C) Grayscale image of the R channel extracted from (A). Inset: Contrast profile of the dashed line showing the intensity difference between the MoS_2 flake and 300 nm SiO_2 substrate (Li et al., 2012b).

One of the pros of mechanical exfoliation is the high purity and cleanliness of the sheets, which are suitable for fundamental characterization and for the fabrication of devices. However, the size of the sheets was only tens of micrometers, which limit

their applications in the fabrication of prototype devices. Another con of this method is their poor thickness-control and was tried to overcome by using a focused laser spot to thin MoS_2 to monolayer thickness by thermal ablation (Castellanos-Gomez et al., 2012). However, the requirement for laser raster scanning makes it difficult for scaling up.

1.1.2.1.2 Liquid exfoliation

Liquid phase exfoliation of bulk TMDs leads to atomically thin 2D materials. Intercalation of 2D layered materials by ionic species and successive exfoliation of materials has been demonstrated by different groups, ever since Dines (1975) and Joensen (1986) used lithium intercalation for MoS_2, WS_2, $MoSe_2$, SnS_2, etc. (Gordon et al., 2002; Kirmayer et al., 2007; Eda et al., 2011; Zeng et al., 2011). In a typical procedure, bulk material can be submerged in a solution containing lithium salts such as n-butyllithium for more than one day so as to allow lithium to intercalate and exfoliate the material using water or ethanol in the second stage. The vigorous reaction of Li intercalated between the layers with the water resulted in the separation of layers with the evolution of H_2 gas (Joensen et al., 1986; Eda et al., 2011). The key aspect of Li intercalation method is the structural and electronic changes accompanying the change in dimension. For example, upon undergoing Li-intercalation, semiconducting nature of bulk MoS_2 changes to metallic in nature, along with the phase change of trigonal prismatic 2H form of bulk to the octahedral 1T phase induced due to the charge transfer from Li to the material (Eda et al., 2011; Eda et al., 2012; Frey et al., 2003; Bissessur et al., 1993; Gordon et al., 2002). Whereas annealing at higher temperatures (95 °C or 300 °C) or simple aging can revert back the phase from 1T form to 2H form (Wypych et al., 1992; Heising and Kanatzidis, 1999; Alexiev et al., 2000; Eda et al., 2011). But the explosive nature of the Li compounds under ambient conditions make this method less favorable. Thus, the replacement of Li compounds with readily available and economically viable materials is of interest.

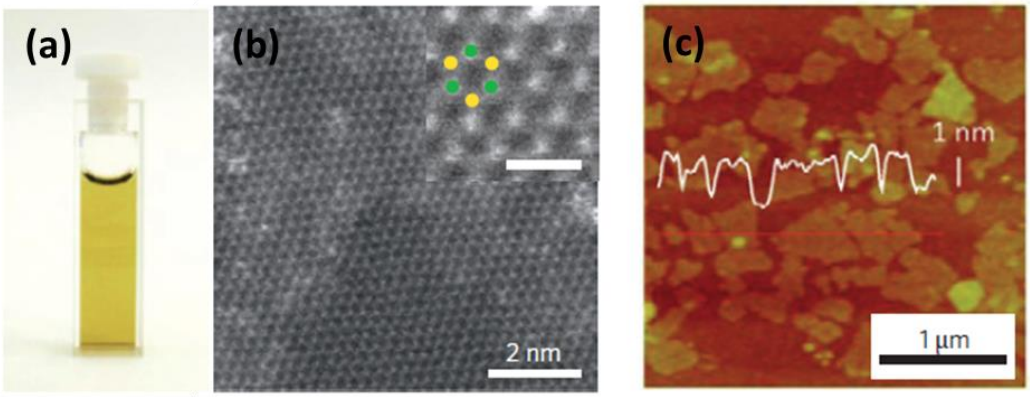

Figure 1.7: (a) A solution of lithium-intercalated and exfoliated MoS_2 in water (b) High-angle annular dark-field scanning transmission electron microscopy (HAADF-STEM) image of this solution. The inset is a magnified view of the HAADF-STEM image, showing a honeycomb arrangement of MoS_2. Green and yellow dots represent Mo and S, respectively. Scale bar is 0.5 nm. (c) Atomic force microscopy (AFM) image of flakes of MoS_2 deposited on SiO_2. The white line is a height profile taken at the position of the red line (Eda et al., 2011).

The direct sonication of bulk materials in the presence of organic solvents such as dimethylformamide (DMF) and N-methyl-2-pyrrolidone (NMP), etc. lead to exfoliation to a few layered materials was demonstrated for MoS_2, WS_2, $MoSe_2$, $NbSe_2$, $TaSe_2$, $NiTe_2$, $MoTe_2$, h-BN and Bi_2Te_3. (Hernandez et al., 2008; Zhi et al., 2009; Coleman et al., 2011), as seen in Figure 1.8. The sonication strategy depends on the nature of the solvent taken, which must overcome the cohesive energy between the neighboring layers of the bulk layered material. The solvent must have comparable surface energy with that of the material to be exfoliated. Surfactants like sodium cholate, which can coat over the surface of sheets to prevent the re-aggregation, are another choice for exfoliating the materials into their single-layered morphology (Afanasiev et al., 1999; Smith et al., 2011).

Though highly versatile, liquid exfoliation techniques, in general, are rigged with inherent limitations. For the Li intercalation method, even though the experiment is carried out at high temperature (for example, 100 °C) the rate of reaction is extremely slow (for example, three days). The intercalation must be carefully controlled so as to obtain complete exfoliation, as there is a chance for the formation of metal nanoparticles and precipitation of Li_2S (Chhowalla et al., 2013).

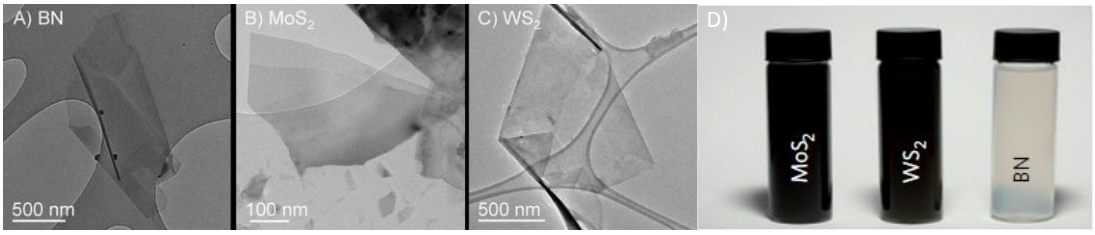

Figure 1.8: (A) to (C) Low-resolution TEM images of flakes of BN, MoS_2, and WS_2, respectively. (D) Photograph of stable suspensions of layered materials MoS_2 (in NMP), WS_2 (in NMP), and BN (in IPA) (Coleman et al., 2011).

The production of large scale homogeneously sized products on a solid substrate using liquid exfoliation technique difficult. Most of the reports demonstrate the formation of sheets of the lateral dimension of a few tens of micrometers, even under optimized conditions (Cunningham et al., 2012; Liu et al., 2014a; O'Neill et al., 2012). Besides, solvent contamination of the final products is possible. The evaporation of the solvent may lead to the formation of discrete flakes, rather than a continuous film. These problems can be satisfactorily be overcome by bottom-up methods (Song et al., 2015a). The chemical exfoliation method is known to produce flakes of quality comparable to mechanically exfoliated ones, by showing a decent photoluminescence emission and comparable charge carrier mobility (Eda et al., 2011; Lee et al., 2011). Additionally, by simple mixing of dispersions of different materials, facile fabrication of composites and hybrid materials are another advantage of liquid exfoliation technique (Coleman et al., 2011; Smith et al., 2011).

1.1.2.2 Bottom-up Methods

1.1.2.2.1 Chemical Vapor Deposition (CVD)

The synthesis of large-area graphene by chemical vapor deposition on copper by Li et al. (2009a) and Bae et al. (2010) have been the breakthroughs. Then the quest was to extend it for the fabrication of other 2D layered materials with a high degree of crystallinity having large surface area. Many reports are available which demonstrate the synthesis of MoS_2 nanoflakes using CVD process, which positively endorse the appealing of this particular method ((Liu et al., 2012; Lee et al., 2012a); Shi et al., 2012; Zhan et al., 2012; Lee et al., 2012b); Wang et al., 2012). A typical CVD process for the

fabrication of 2D layered materials can be classified into three categories: (i) Vaporization of metal and chalcogen precursors and their decomposition, followed by deposition of TMD on a substrate, (ii) Direct sulfurization (or selenization) of the metal film and (iii) Conversion of MO_3 (metal oxide) to MS_2 (metal disulfide) by sulfurization.

The formation of MoS_2 by the adsorption of sulfur on the surface of Mo film had been demonstrated in the 1970s and 1980s (Wilson et al., 1975; Salmeron et al., 1983). The mechanism of formation is described as the nucleation of MoS_2 in conjunction with chemisorbed sulfur species and the film was believed to form by the diffusion of sulfur, which was controlled by pressure and temperature (Wilson et al., 1975).

The epitaxial growth of 2D MoS_2 flakes on graphene was realized by the vapor phase injection of $(NH_4)_2MoS_4$ dissolved in DMF (Shi et al., 2012). Due to prolonged reaction resulted in the formation of rugged films as the film grows and merges together. This problem was successfully overcome by growing MoS_2 film on an insulating substrate by Liu et al. (2012) by a two-step reaction (Figure 1.9). In this method, the deposition of three-layered MoS_2 sheets was realized by dip-coating of ammonium thiomolybdates [$(NH_4)_2MoS_4$] and converting to MoS_2 by annealing at 500 °C followed by sulfurization at 1,000 °C. The formation of the MoS_2 layers is occurring according to the reaction, $(NH_4)_2MoS_4 + H_2 \rightarrow 2NH_3 + 2H_2S + MoS_2$

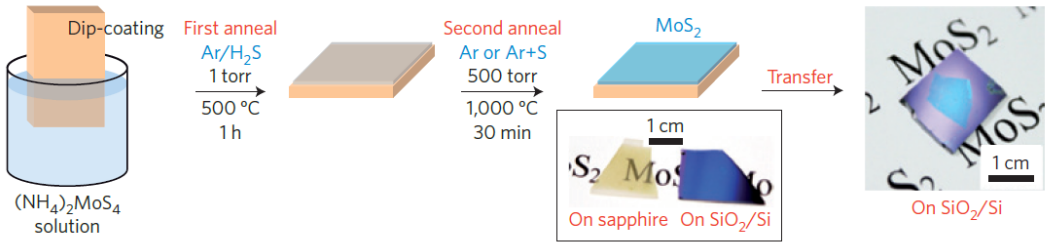

Figure 1. 9: CVD growth of MoS_2 from a dip-coated precursor on the substrate and growth in the presence of Ar gas and S vapour. (Liu et al., 2012)

There are specific unfavorable inherent CVD characteristics to be considered. For example, the random nucleation of the precursors can lead to distorted pattern ability. Scalability is another issue to be dealt with, as there is a competition for lateral growth with vertical growth, upon prolonged reaction. The vapor-phase-grown 2D MoS_2 exhibits various defects such as adlayers or grain boundaries due to the excessive growth in the middle of the flakes or near the crystal edge due to overlap of neighboring layers (van der Zande et al., 2013; Liu et al., 2014b).

1.1.2.2.2 Chemical Methods

Chemical preparation of various materials such as MoS_2, $MoSe_2$, BN has been realized exploiting different synthetic strategies. For example, Rao et al. (2010) prepared boron nitride (BN), with precise control over the number of layers by chemical method. Boric acid/urea mixtures with different molar ratios (1:6, 1:12, 1:24, 1:48, and 1:72) were dissolved in 40 mL of water and heated at 65 °C, until the evaporation of water was complete. The dried mixtures were heated at 900 °C for 5 h in an N_2 atmosphere, yielding white products.

Numerous reports are available on the hydrothermal preparation of MoS_2 nanomaterials from various precursors (Peng et al., 2001a; Gopalakrishnan et al., 2014; Matte et al., 2010; Wang and Ni, 2014; Wang et al., 2014a; Li et al., 2003; Krishnamoorthy et al., 2014; Huang et al., 2013). For example, Wang and Ni (2014) made headway for a facile bottom-up hydrothermal route for the synthesis of photoluminescent MoS_2 QDs by using sodium molybdate and cysteine as precursors (Figure 1.10). Graphene like MoS_2 and WS_2 were prepared by Matte et al. (2010) by three different methods, starting from bulk MoS_2/WS_2 which were intercalated with lithium and exfoliated in water, molybdic acid/tungstic acid reacted with excess of thiourea in an N_2 atmosphere at 773 K and the reaction between MoO_3 and KSCN under hydrothermal conditions at 453 K for 24 h. Generally, the sheets are not defect-free (Matte et al., 2010). The same strategy was made use for the synthesis of selenides as well by the same group, using selenium metal and selenourea (Matte et al., 2011). Synthesis of single-molecular-layer $MoSe_2$ was also realized from Ammonium

molybdate [$(NH_4)_6Mo_7O_{24}\cdot 4H_2O$] and elemental selenium in presence of hydrazine monohydrate by hydrothermal reaction (Peng et al., 2001b).

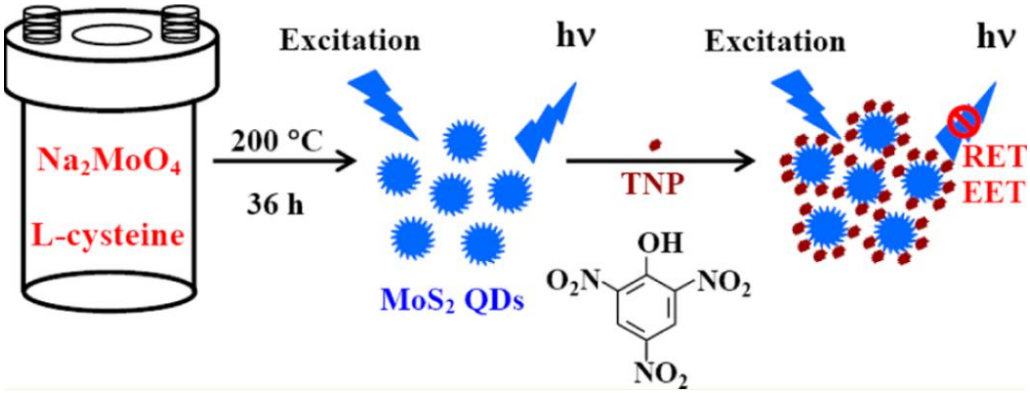

Figure 1.10: A facile bottom-up hydrothermal route for the synthesis of photoluminescent MoS_2 quantum dots (QDs) by using sodium molybdate and cysteine as precursors (Wang and Ni, 2014)

Successful fabrication of different WS_2 nanomaterials such as rod-like, sheet-like and fiber-like nanostructures were rendered via a simple and facile hydrothermal process by adding surfactants cetyltrimethyl ammonium bromide (CTAB) along with polyethylene glycol (PEG) and systematically characterized by the X-ray powder diffraction and scanning electron microscopy (Tang et al., 2011, Cao et al., 2014). The hydrothermal route was exploited for the synthesis of WS_2 nanotubes from WO_3 nanorods by Therese et al. (2005). In this work, hexagonal WO_3 nanorods of diameter 5–50 nm and length 150–250 nm have been synthesized by a hydrothermal route employing citric acid as a structural modifier and hexadecylamine as a templating agent, which is used as a precursor for the synthesis of multiwalled WS_2 nanotubes upon reduction in the presence of H_2S at 840 °C for 30 min. These studies mainly show the importance of concentration of surfactants or precursors, which ultimately define the morphology of the final products.

1.1.3 Applications of 2D Layered TMD Materials

2D materials are unique due to their electron confinement without any interlayer interactions which gives them applicability in electronic devices (Zhang, 2015). Another interesting feature is their atomic thickness providing them

applicability in flexible and transparent electronic/optoelectronic devices. They have high surface areas favouring their surface-active applications (Novoselov and Geim, 2007). The photoluminescence (PL) properties emerging from quantum confinement in few-layered (usually 1-3 layers) MoS_2 make them potential candidate for biological and optoelectronic applications as well (Splendiani et al., 2010). The function of 2D layered materials in these various domains mainly depends on the thickness of the sheets, pristine character of the material, surface structure and defects, strain, etc. (Johari and Shenoy 2012; Xu et al., 2009; Conley et al., 2013). We will be discussing some of the major applications where TMDs are made use as the principal components.

1.1.3.1 Field-Effect Transistors

The 2D layered materials found to be potential candidates for FET applications, which is evident from the available reports (Shin et al., 2020; Zhao, 2019; Lee et al., 2019; Tang et al., 2019; Chen et al., 2009; Sui and Appenzeller, 2009; Nourbakhsh et al., 2016). In a basic FET design adapted for 2D layered materials, a semiconducting channel region is connected to the source and drain electrodes, which is separated by a dielectric layer from a gate electrode (Wang et al., 2012). In a typical example, Radisavljevic et al. (2011b) devised a FET using single-layer MoS_2, exfoliated using scotch tape micromechanical method and transferred to silicon substrates covered with 270-nm-thick SiO_2. Electron- beam lithography was used for fabricating electrical contacts and deposition of gold electrodes of thickness 50 nm was carried out followed by annealing at 200 °C. The as-fabricated FET can be seen in Figure 1.11.

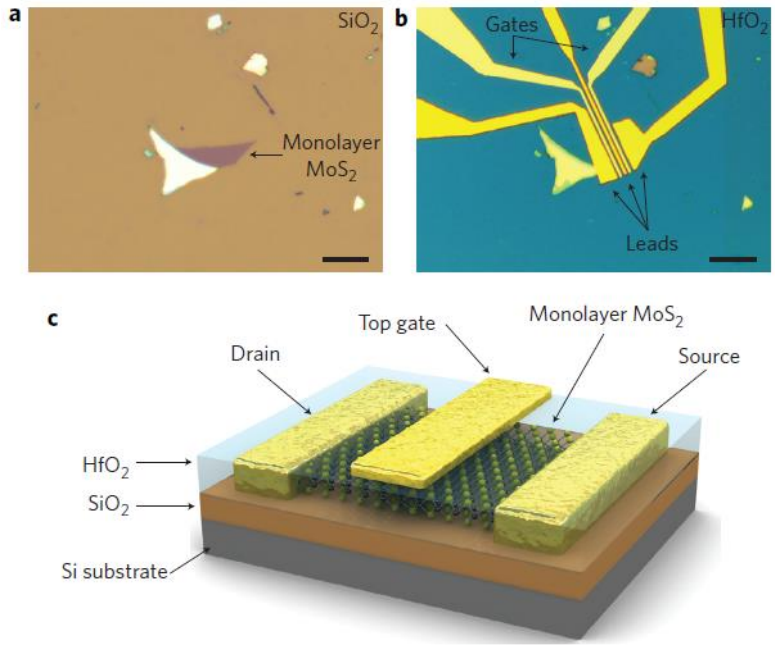

Figure 1.11: Fabrication of MoS_2 transistor. (a) Optical image of a monolayer MoS_2 deposited on top of a Si substrate with a Silica layer of 270 nm thickness. (b) Optical image of a device that consists of two field-effect transistors connected in series. Here, three gold leads serve as source and drain electrodes for the two transistors. The MoS_2 is covered by HfO_2 of thickness 30 nm and acts as a gate dielectric as well as mobility booster. (c) Schematic view of a transistor (Radisavljevic et al., 2011b).

1.1.3.2 Optoelectronics

Optoelectronic devices are electronic devices which can generate, detect, interact with or control light (Wang et al., 2012). Examples of optoelectronic devices are optical switches, lasers, solar cells, LEDs, photodetectors and displays (Kamat, 2008; Wang et al., 2012). The direct band gap in the visible portion of the electromagnetic spectrum, ability to tune the bandgap of TMDs with various intercalants, photoluminescence, and the large exciton binding energies assist monolayer semiconducting 2D layered materials to be a promising candidate for optoelectronic applications (Benavente et al., 2002; Jariwala et al., 2014).

Tsai et al., (2014) demonstrated photovoltaic application of monolayer MoS_2 type-II heterojunction solar cell with p-Si, with a power conversion efficiency of 5.2% (Figure 1.12). Whereas Najafi et al. (2018) able to fabricate a solar cell with an Efficiency of 20%, by amalgamating graphene interface engineering (GIE) with the

hole-extraction and electron-blocking properties of MoS_2 QDs with mesoscopic methylammonium lead iodide ($CH_3NH_3PbI_3$) perovskite. The possibility to combine quantum and chemical effects into GIE, coupled with the graphene and similar layered materials as interfacial layer, is an effective approach for the development of next-generation perovskite solar cells.

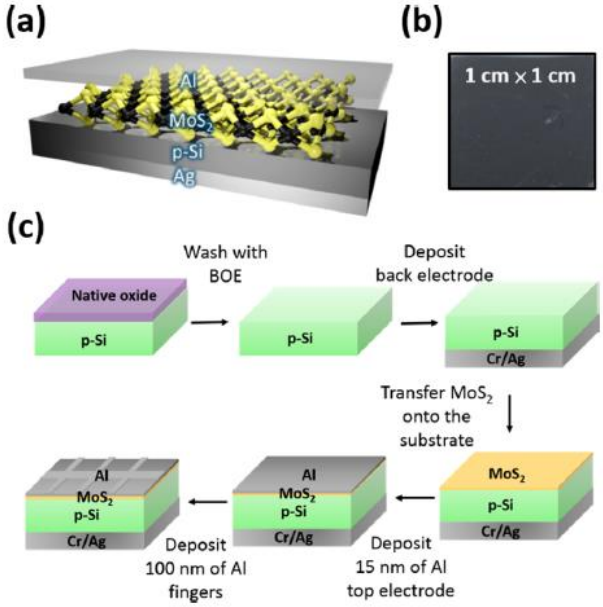

Figure 1.12: (a) Device structure of MoS_2/p-Si heterojunction solar cell. (b) A 1 x 1 cm photographic image of monolayer MoS_2 transferred on p-Si. (c) Fabrication procedure of MoS_2/p-Si heterojunction solar cell (Tsai et al., 2014).

1.1.3.3 Electrochemical Catalysis (Hydrogen Evolution Reaction)

Molecular hydrogen is believed to be the cleanest energy carrier, with its high energy density (143 kJ/g). The hydrogen evolution reaction (HER) is one of the most effective ways to produce this hydrogen energy. HER in the acidic medium can be successfully carried out using noble metals like Pt or its alloys due to their high activity, negligible over potential and chemical inertness (Norskov et al., 2006; Pletcher et al., 1984; Chen et al., 2011a). However, the high cost of these rare earth metals and its alloys limit their applications widely, which on the other hand, open up a way for further exploration of fundamental studies with newer materials. Metals like Fe, Co,

Ni, phosphides such as Ni_2P, CoP, Carbides like Mo_2C, nitrides, graphene doped with suitable elements, carbon nanotubes, fullerenol, pyrite-type cobalt phosphosulphide, etc. are a few of the examples to mention (Faber and Jin, 2014; Zou and Zhang, 2015; Artero et al., 2011; Du and Eisenberg, 2012; Popczun et al., 2013; Popczun et al., 2014; Wan et al., 2014; Chen et al., 2012; Zhuo et al., 2013; Das et al., 2014; Sathe et al., 2014; Duan et al., 2015; Zheng et al., 2014; Caban-Acevedo et al., 2015). There was an upsurge of interest in the recent years towards MoS_2, as a promising catalyst due to its desired qualities such as acid stability, electrochemical stability, thermal resistance, environmentally benign nature, abundance, low cost, etc. for HER activity (Ye et al., 2016; Shi et al., 2017a; Tang and Jiang, 2016; Wang et al., 2017a; Chen et al., 2017a; Li et al., 2019a).

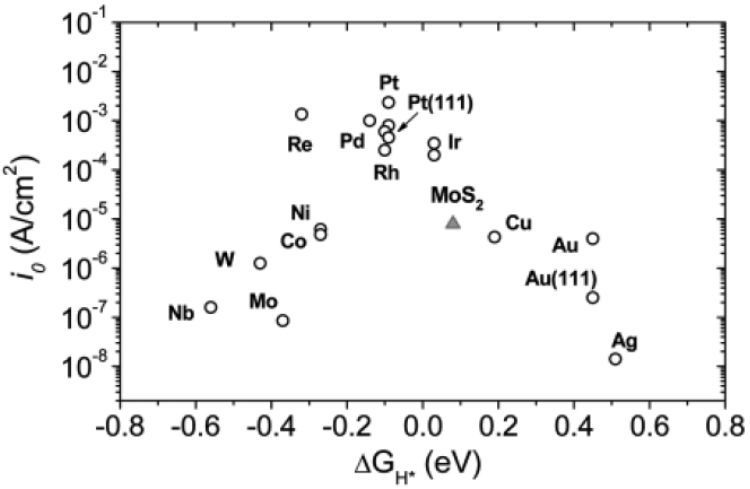

Figure 1.13: "Volcano plot" of experimentally measured exchange current density as a function of the DFT-calculated Gibbs free energy of adsorbed atomic hydrogen for different catalysts (Jaramillo et al., 2007)

When the catalytic activity of a material is plotted against a function of the hydrogen–metal bond strength, a volcano-shaped plot is obtained, as seen in Figure 1.13. These volcano relations reflect the Sabatier principle, which states that the optimal surfaces are the ones that exhibit moderate binding energies of reaction intermediates. The activity reaches a peak value at intermediate bond strengths for several rare noble metals such as Pt, Rh, Re, Ir, etc. Jaramillow et al. (2007) calculated

the free binding energy for MoS_2 using DFT, which is located close to the top of the volcano curve, showing its enhanced potential as that of Pt group metal catalysts.

In a typical HER process in acid media the reduction of protons to hydrogen can takes place via two different mechanisms; Volmer–Heyrovsky or Volmer–Tafel mechanism. The Volmer reaction is adsorption of protons (H_{ad}) from acid solution on the surface of catalyst, which is generally a fast reaction. In Volmer–Heyrovsky mechanism, the adsorbed hydrogen on the surface react with a solvated proton from the water layers forming H_2, whereas in Volmer–Tafel mechanism, two adjacent adsorbed hydrogens react to form an H_2 molecule, as seen below

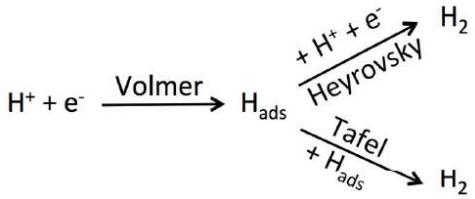

Sound theoretical predictions and experimental validations were carried out to understand the mechanism of HER activity of MoS_2 at its edges and at the basal plane (Hinnemann et al., 2005; Huang et al., 2018). Using computational method, Jaramillo et al. (2007) determined the active site of nanoparticulate MoS_2 for HER by atomically resolving its surface. The study was validated using PVD grown MoS_2 polygons on Au (III) substrate. At different annealing temperatures, (400 and 550 °C), samples with predominant sulfide Mo-edge samples were prepared and studied using scanning tunneling microscopy (STM) (Figure 1.14).

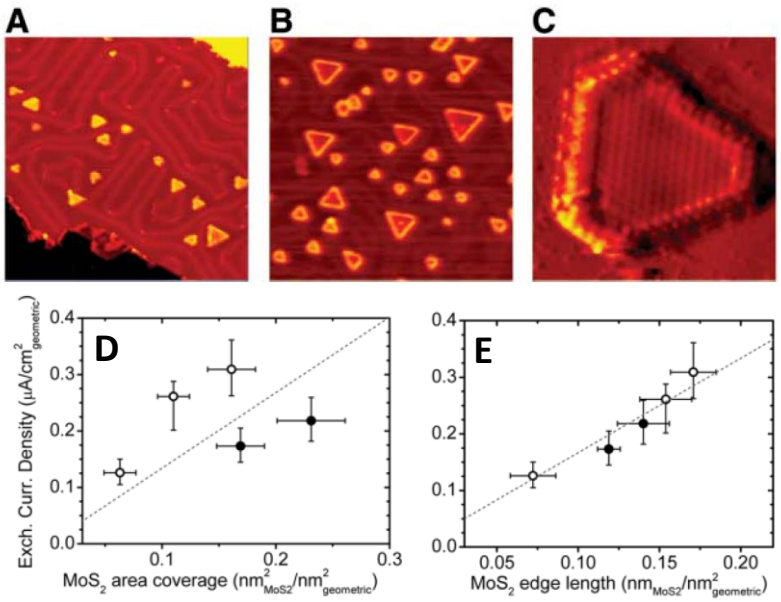

Figure 1.14: STM images of MoS_2 nanoparticles on Au(111) (A) Low coverage annealed to 400°C. (B) High coverage annealed to 550 °C. (C) Atomically resolved MoS_2 particle, from a sample annealed to 550 °C, showing the predominance of the sulfided Mo-edge. Exchange current density versus (D) MoS_2 area coverage and (E) MoS_2 edge length. In both figures, open circles are samples annealed to 400 °C, filled circles are samples annealed to 550 °C. The exchange current density does not correlate with the area coverage of MoS_2, whereas it shows a linear dependence on the MoS_2 edge length (Jaramillo et al., 2007)

1.1.3.4 Energy storage applications

The low theoretical capacity of graphite; the anode material for conventional Li-ion batteries ignites the quest for finding better materials for cathode and anode applications. MoS_2, $MoSe_2$, WS_2, WSe_2 are the layered materials studied well for Li or Na ion batteries, as these ions can be accommodated efficiently within the layers (Shi et al., 2016; Wu et al., 2017; Pumera et al., 2014; Rao et al., 2013; Samadi et al., 2018; Kang et al., 2017; Huang et al., 2019). The structural and electronic changes followed by the intercalation of Li^+ in bulk material leads to undesirable effects, which limit their applications as electrodes. The relatively low average voltage and energy density further lessen their potential as cathode materials. Whereas, flexible exfoliated nanosheets offer room for making use as anode materials by carefully controlling morphology, structure, particle size, etc. For example, Xiao et al. (2010) reported exfoliated MoS_2 nanocomposite as anode material with improved reversible capacity

(Figure 1.15). Due to the structural disorders in the exfoliated MoS_2, a greater number of Li^+ can interact with the expanded MoS_2 structure, resulting in an increase of the initial discharge capacity above 1000 mAh/g. But, the reversible capacity found to gradually decay to a value of 500 mAh/g after 50 cycles. The MoS_2 nanoflakes store lithium reversibly with a capacity of 1175 mAh/g in the voltage range of 0.01–3.0 V vs Li/Li^+ corresponding to 8 mol lithium per mole of MoS_2 (Feng et al., 2009).

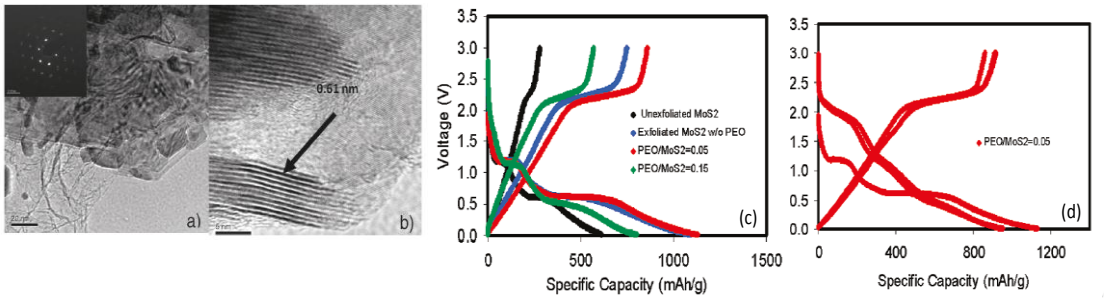

Figure 1.15: TEM images for exfoliated PEO/MoS_2 = 0.05 composite. (a) MoS_2 sheets with expanded spacing after the incorporation of PEO. (b) Restacked MoS_2 without PEO intercalation is also observed in the composite. (c) Comparison of the first charge-discharge curves for unexfoliated MoS_2 and exfoliated MoS_2 with different amounts of PEO. (d) Subsequent charge-discharge curves of PEO/MoS_2 =0.05 composite (Xiao et al., 2010).

The MoS_2 nanosheets prepared by facile aqueous microwave synthetic method were demonstrated as an electrode with environmentally benign and green di(propylene glycol) dimethyl ether (DPGDME) as an electrolyte. The MoS_2-containing cell shown better rate performance and stable cyclability than the cell without MoS_2 (Wang et al., 2019). High-performance Li-S batteries were fabricated using a sponge-like porous 3D network of MoS_2/rGO foam as sulphur cathode. The MoS_2 with mixed 1T and 2H phases were grown on the basal plane of rGO and shows a high reversible capacity of 1100 mAh g^{-1} at 0.2 C, a remarkable cycling stability with a low capacity fading rate of 0.15% after 300 cycles at 1 C, and an excellent rate performance up to 620 mAh g^{-1} at 2 C (You et al., 2019).

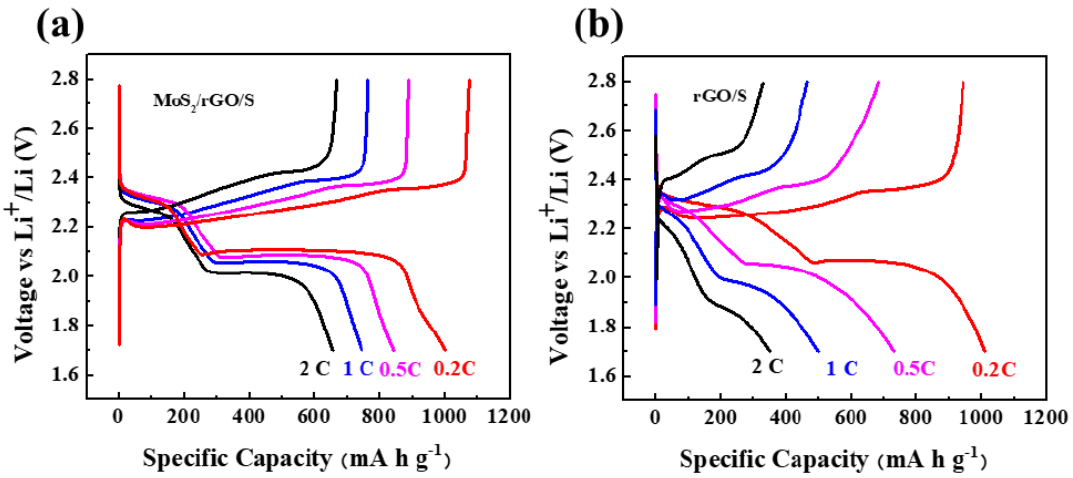

Figure 1.16: Electrochemical performance of Li-S batteries with the rGO/S and MoS_2/rGO/S as the cathodes: (a, b) Galvanostatic charge-discharge profiles of the MoS_2/rGO/S and rGO/S cathodes electrodes at various C rates (You et al., 2019).

1.1.3.5 Chemical Sensors

Intensive research is happening in the field of 2D materials and their chemical sensing applications. The 2D materials-based sensors of the various kind, such as gas sensors, electrochemical sensors, field-effect transistor (FET), biosensors, metal ion sensors, etc. have been demonstrated. Changes in the electronic properties 2D materials stirred by the presence or interaction of target analyte can be monitored by electrical means by incorporating them into transistor devices and measuring the current-voltage behavior, or optically by scrutinizing the changes in the photoluminescence, absorbance or Raman signatures.

The gas sensors are necessary for various applications in the areas of building automation, healthcare, life sciences, consumer and home automation, transportation, industrial and environment security, public safety, etc. (Kim et al., 2017). The easiness of devise fabrication using 2D layered materials, made them a choice for gas sensors. The sensitivity of these sensors mainly owing to the high surface-to-volume ratio of the 2D layered materials, as most of the interaction of probe and analyte can be limited only to the surface, and even a sub-monolayer adsorption of gas molecule can cause significant perturbation in resistance or the device capacitance, due to charge transfer

and doping, intercalation, and shifts in permittivity and lattice vibrations. The successful incorporation of MoS_2 in a FET, for gas sensing applications, was demonstrated by Li et al. (2012c), for the detection of nitrogen monoxide (NO). Single- and multilayer (1–4L) MoS_2 films were deposited onto Si/SiO_2 substrates using the scotch tape-based mechanical exfoliation technique. FETs based on these single- and multilayer MoS_2 sheets exhibit the n-type semiconducting properties and successfully used for sensing NO gas. Figure 1.17 shows a typical current response of a 2L MoS_2 FET device during the exposure to NO with a concentration range from 0.3 to 2 ppm. The detection was carried out due to the high sensitivity of the resistance of two-, three-, and four-layer MoS_2 FETs towards the presence of NO (0.8 ppm) in an N_2 environment. The detection mechanism was probably due to p-doping induced by the adsorbed NO, changing the resistivity of the intrinsically n-doped MoS_2.

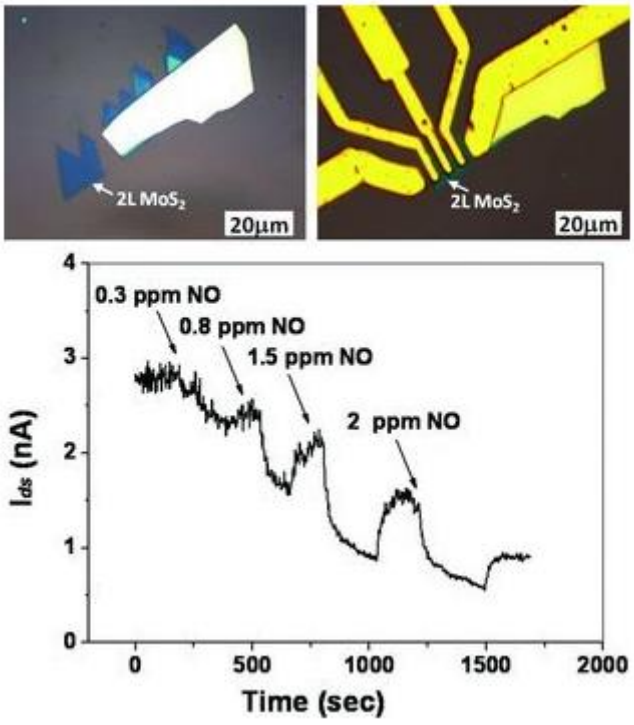

Figure 1.17: Optical microscope image of a bilayer MoS_2 film deposited onto Si/SiO2, and a FET device based on the 2L MoS_2 film. The real-time current response after exposure of the 2L MoS_2 FET to NO with increased concentration shown in the bottom panel (Li et al., 2012c)

Development of state of the art electrochemical approaches based on 2D layered materials such as MoS_2 or WS_2 modified working surfaces is another emerging field in recent years. Electrochemical sensing of DNA was successfully demonstrated by various groups using MoS_2 or modified MoS_2 electrodes (Wang et al., 2014b; Loan et al., 2014; Wang et al., 2015). In one example, free-standing ZnO nanosheets grown on 2D thin-layered MoS_2 was used to immobilize, hybridize and detect DNA with a low detection limit of 6.6×10^{-16} M (Yang et al., 2017), in the presence of methylene blue which possesses different affinities to dsDNA and ssDNA. An ultrasensitive detection of H_2O_2 released from breast cancer 4T1 cells were reported using PtW/MoS_2 hybrid nanocomposite, with an excellent linear relationship in the range of 1 μM to 0.2 mM H_2O_2 and sensitivity of 1.71 μA μM^{-1} cm^{-2} (Zhu et al., 2016). A schematic of the detection of H_2O_2 released from living cells is given in Figure 1.18.

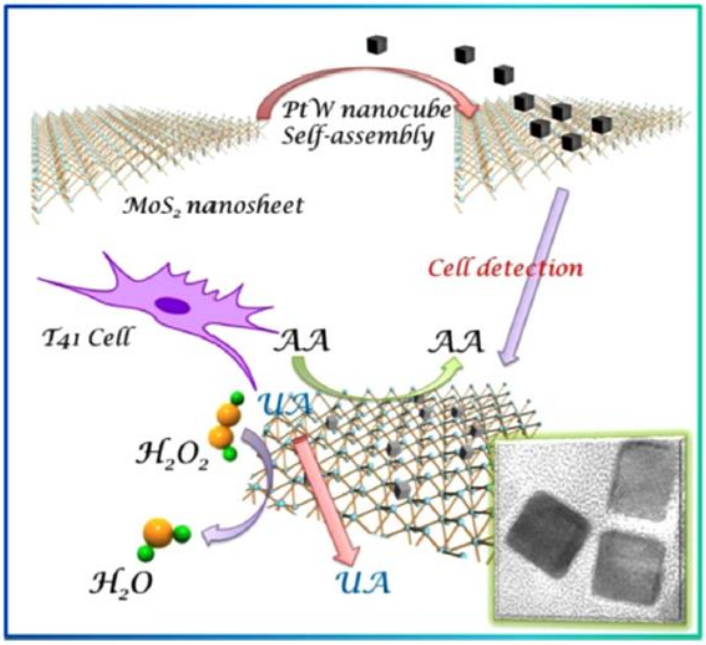

Figure 1.18: Scheme for construction of PtW/MoS_2 nanocomposite acted as a high specific sensing material for detecting H_2O_2 released from living cells (AA: ascorbic acid, UA: uricacid) (Zhu et al., 2016)

Non-enzymatic glucose detection was successfully devised by electrode deposited with MoS_2 mircoflowers (Zhai et al., 2016). Electrochemical analysis reveals that the electrode exhibited synergistic electrocatalytic activity with an excellent

sensitivity of 570.71 μA mM^{-1} and a linear range of from 0 to 30 mM, between the anodic peak current and concentration of glucose concentration. Researchers also tapped the potential of the detection of explosives and pesticides by electrochemical strategy using MoS_2 (Barua et al., 2017; Tan et al., 2019). The remarkable conductivity, superior electron mobility and high electroactive surface area of Ag NPs-decorated nitrogen-fluorine co-doped monolayer MoS_2 nanosheet were exploited for the detection of organophosphorus pesticides, such as monocrotophos and chlorpyrifos, with a low detection limit of 0.2 pM and 3 pM, respectively (Song et al., 2018). Trace level detection and quantitative determination of other analytes of interest such as food contaminants, inorganic ions, pharmaceuticals, gaseous molecules, etc. using electrochemical characteristics of 2D layered materials are demonstrated (Suna et al., 2019; Sinha et al., 2018).

The solution phase fluorescence sensors are another emerging area of sensors. These sensors are found enormous applications in the field of medical and environmental sciences. Fluorescence-based approaches in general, various sensing mechanisms along with a brief literature review of fluorescence-based sensors employing 2D layered materials, are detailed in the following section.

1.2 Fluorescence-Based Sensors

The non-invasive nature, easy-to-handle methodology, high sensitivity with superior selectivity, and inherent versatility drive fluorescent-based sensing at the forefront. In fluorescence-based sensors, the recognition of analytes has been realized either through tagging a target-specific molecule to the fluorophore or monitoring the changes in the physicochemical properties of fluorophore induced by the direct interaction with the analyte molecules/ions. A general approach of fluorescent-based sensors along, with the mechanism, will be discussed briefly in the following sections.

1.2.1 General Approaches to Fluorescence-Based Sensors

Generally, fluorescent-based sensing can be realized via two approaches, either by monitoring the position or variation of the intensity of the excitation or emission

spectra of the fluorophore (intensity-based fluorescence sensors) or by checking the excited state lifetime of the fluorophore (lifetime based sensors). Tracking of anisotropy and phase modulation are other approaches that can be made use. In all the methods, accurate measurement of various parameters of the analyte molecules such as concentration, pH, change in composition, etc. can be performed. The output spectra for fluorescence sensing can be represented as in Figure 1.19.

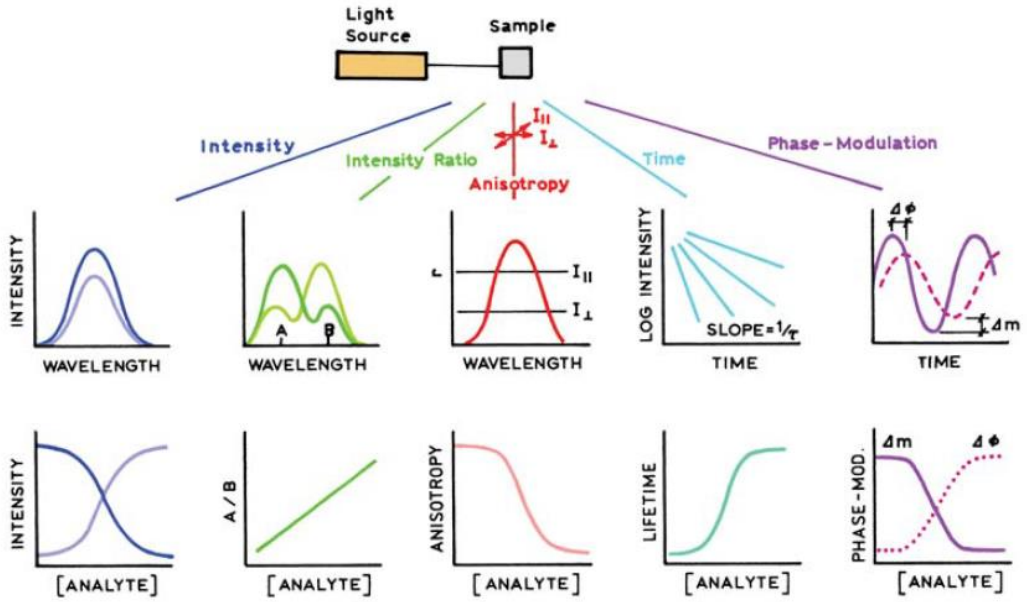

Figure 1.19: Spectral observables for fluorescence sensing. From left to right, sensing is performed using intensities, intensity ratios, anisotropies, time-domain lifetimes, and phase-modulation measurements (Lakowicz, 2013).

1.2.1.1 Intensity Based Fluorescence Sensors

The fluorescent intensity of the fluorophore is continuously monitored upon interaction with the analyte in the intensity-based fluorescence sensors. The intensity can be quenched, enhanced or shifted as a response to the presence of a specific analytes, which in turn can be utilized for the selective detection of the analyte (see Figure 1.20)

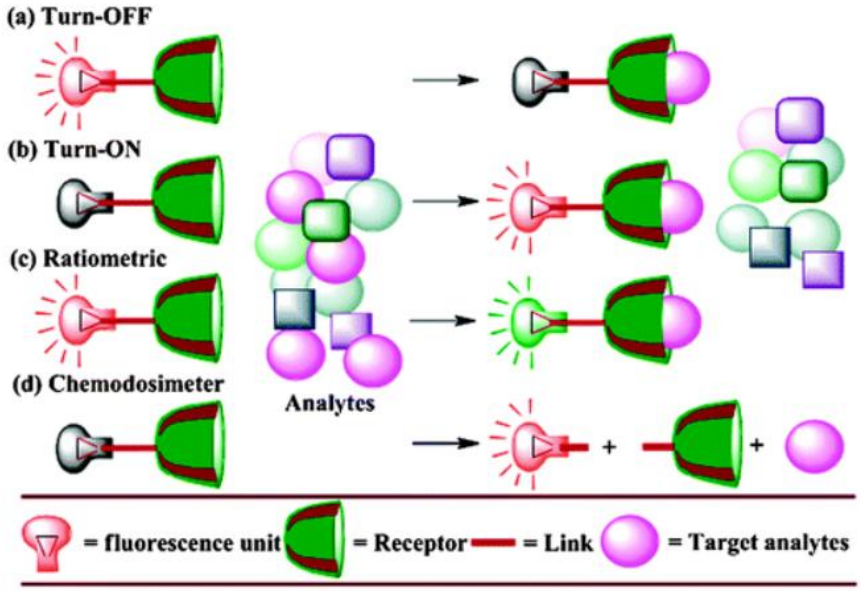

Figure 1.20: Scheme showing different types of intensity-based fluorescence sensors (Sahoo et al., 2014)

The potential application of 2D layered materials based fluorescence sensors has been tapped because of their prime aqueous solubility, high affinity towards various biomolecules and superior fluorescence quenching ability against organic dyes.

The interaction between 2D layered material and various analyte molecules can be of two types: physisorption and chemisorption. In physisorption, the molecules will be attached to the basal planes of the sheets mainly via non-covalent interactions such as van der Waals and electrostatic, which are weak (Meyer et al., 2003). These weak interactions can be advantageous when one looks for a "capture-release" model where fast response and quick recovery of the analyte molecules are desired. A robust covalent interaction will be preferred if immobilization of target molecules such as enzymes are desirable for the assay. Defects play a major role in tuning various properties and modifying chemical reactivities of 2D layered materials. The introduction of Sulphur vacancies, for example, in the case of MoS_2, leads to the formation of highly reactive sites, which will readily form covalent bonds with suitable

ligands such as alkanethiols, and thus can be functionalized accordingly, to improve the specificity of the probe.

1.2.1.1.1 Turn- off Fluorescence Sensors

Graphene, graphene oxides (GO), h- BN, MoS_2, WS_2, etc. are excellent quenchers, therefore used in the detection of various analytes based on the change in the intensity of the emission of the fluorophore; either an organic dye or semiconductor-based QDs. The MoS_2 shows a high affinity towards single-stranded DNA (ssDNA) and interact via van der Waals interaction. Double-stranded DNA (dsDNA), on the other hand, which formed in the presence of target molecule, hardly interacts with the surface due to electrostatic repulsion (Li et al., 2015). Detection of DNA and other biomolecules such as adenosine, thrombin, mediated through turn off of fluorescent emission from the fluorophore by MoS_2 have been realized through following the same strategy (Ge et al., 2004; Xiang et al., 2015; Zhang et al., 2015a, Zhu et al., 2013; Huang et al., 2015a, Huang et al. 2015b)

MoS_2 has been successfully bestowed as a fluorescent probe for the turn off detection of many analytes such as BSA, human serum albumin, microRNA, etc. (Ha et al., 2014; Swaminathan and Balasubramanian, 2018; Swaminathan et al., 2017; Yu et al., 2018). An elaborate study on energy transfer as the turn-off mechanism from MoS_2 QDs to Rhodamine 6G at different excitation wavelengths from 330 to 430 nm through steady-state and time-resolved fluorescence spectroscopy has been conducted. This study is used for the detection of glutathione (GSH) with proper selectivity experiments (Swaminathan and Balasubramanian, 2018 a). The GSH is abundant as cellular biological thiols and is crucial in maintaining the appropriate redox status of the biological systems. MoS_2 QDs have a characteristic broad emission peak at 400 nm, upon exciting at 330 nm, which is being absorbed efficiently by the R6G, which has a characteristic absorption around 450 - 570 nm. R6G shows fluorescence at ~550 nm. Fluorescence intensity in the donor fluorescence region (MoS_2 QDs) was quenched linearly due to the binding of GSH with MoS_2 QDs which makes the pair an efficient sensor for GSH. The LOD of the sensor was 2.7 nM.

When dopamine (DA), a neurotransmitter found in our body, is added to WS_2 QDs solution, it can snap onto the surface of WS_2 QDs and form thin film of polydopamine through the self- polymerization effect, which can be revealed as significant corrugations of WS_2 QDs and the height increment of about 3 nm in microscopic studies (Zhao et al., 2018). The emission of WS_2 QDS was found to be quenched significantly upon the formation of polydopamine through FRET, from WS_2 QDs to poly-dopamine with a change in quantum yield of WS_2 QDs from 21.75% to 13.77% (DA concentration 50 µM; Figure 1.21). The dynamic range of this sensor was reported to function between 0 to 50 µM with a limit of detection of 3.3 µM.

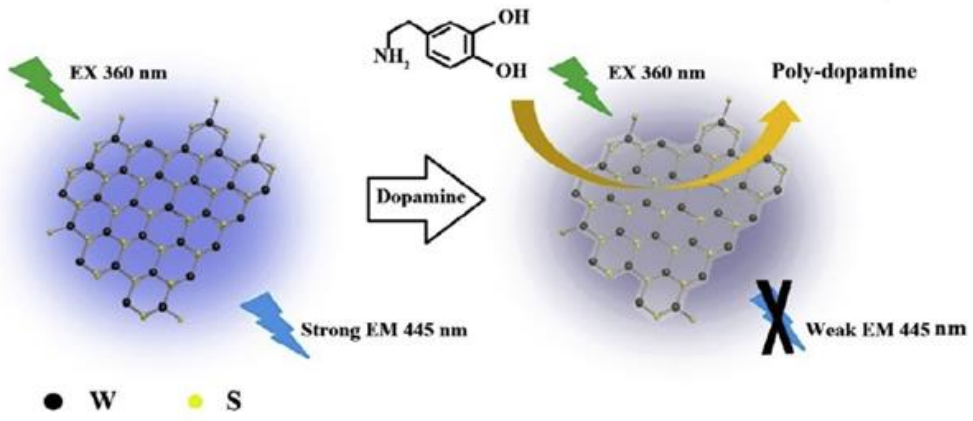

Figure 1.21: Illustration of the detection of dopamine (Zhao et al., 2018).

Zhan et al. (2019) went for ultrasensitive detection of acetylcholinesterase (AChE) activity and its inhibitors, profiting the inherent emission property BN QDs, following mix and detect strategy, bagging a linear range of 0.05 to 6.0 mU/mL with the lower detection limit of 0.0212 mU/mL. AChE can hydrolyze acetylthiocholine (ATCh) to generate thiocholine (TCh), which can reduce chloroauric acid ($HAuCl_4$) into AuNPs, through its thiol group (-SH) and promote the in situ formation of TCh-BNQDs/AuNPs aggregates, resulting in fluorescence quenching of BNQDs. The quenching is facilitated via energy transfer by the formation of TCh-BN QDs/Au NPs aggregates through the interaction of unreacted -SH in TCh-BN QDs with the adjacent Au NPs on TCh-BN QDs through intermolecular cross-linking via Au-S bond.

1.2.1.1.2 Turn-on Fluorescence Sensors

The turn-on sensors are believed to be more selective than turn-off fluorescence sensors as the chances of false-positive is limited. The inherent photobleaching of organic fluorophores prompted to explore other sources of fluorescent probes for sensing applications. Many turn-on sensors are reported using fluorescent 2D layered materials which are endowed with excellent brightness, long fluorescent lifetime and high quantum yield (Zhou et al., 2014; Swaminathan and Balasubramanian, 2018 b; Shi et al., 2017b; Xu et al., 2017a; Xu et al., 2017b; Swaminathan et al., 2017; Wu et al., 2018; Lin et al., 2019). For example, turn-on sensing of BSA was realized using MoS_2 QDs-polyaniline (MoS_2 QD-PANI) pair (Swaminathan and Balasubramanian, 2018 b), with a LOD of 9.86 nM and dynamic range of 10 to 70 nM. The same group has fabricated turn on BSA/HSA sensing, using fluorescent MoS_2 QDs and GO and RGO as initial quenchers (Swaminathan et al., 2017). The quenching of MoS_2 QDs fluorescence in the presence of GO and RGO was attributed to the reduction and electron storage reactions, respectively. The quenched fluorescence of MoS_2 by both GO and RGO recover in a linear fashion in the range of 5–50 nM, upon addition of BSA and HSA which shows the high sensitivity of the sensing nature of MoS_2–GO and MoS_2–RGO couples (Figure 1.22).

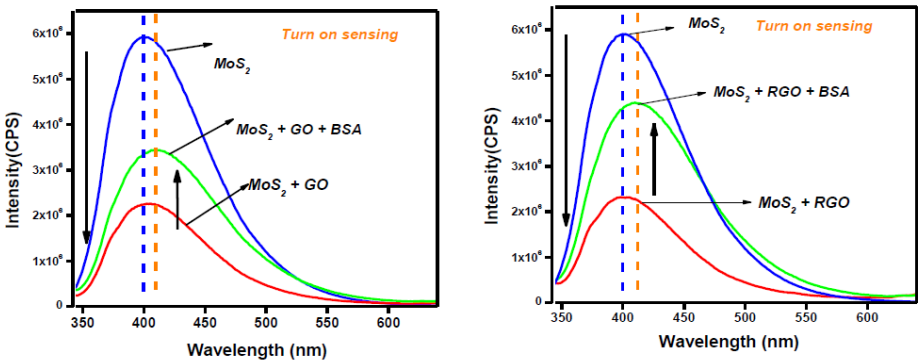

Figure 1.22: Turn-on BSA sensing behavior of MoS_2-GO couple and MoS_2-RGO couple. The arrow line facing upwards indicates the enhancement of fluorescence intensity (Swaminathan et al., 2017).

Detection of ascorbic acid, with a LOD of 39 nmol/L and a linear range of 0.33–5.00 μmol/L were discerned by conjugation of highly fluorescent MoS_2 QDs and MnO_2 nanosheets as the quencher (Xu et al., 2017). The initial quenching of fluorescence of MoS_2 QDs is due to the inner filter effect, which will be recovered in a linear fashion in the presence of ascorbic acid. Detection of metal ions was carried out employing the cysteine functionalized fluorescent MoS_2 QDs (Cys-MoS_2 QDs) (Wu et al., 2018). In the presence of Al^{3+}, the fluorescence of Cys-MoS_2 QDs is found to be enhanced, which attributed to the interaction of the amino group present in the ligand, which could coordinate with Al^{3+}. The coordination can restrict non-radiative decay in QDs and limits the vibration energy loss, and substantially caused the enhancement of fluorescence.

The significance of surface functionality upon determining the specificity of the probe was demonstrated by Lin et al. (2019), using the fluorescent MoS_2 QDs. The surface of MoS_2 QDs was individually modified using suitable capping agents containing thiol functionality to form carboxylic (MoS_2/COOH), amine (MoS_2/NH_2) and thiol functionalized (MoS_2/SH) MoS_2 QDs. These MoS_2 QDs exhibit excellent performance towards the turn-on detection of Co^{2+}, Cd^{2+} and Pb^{2+} ions, with a LOD of 54.5, 99.6 and 0.84 nM, respectively. zThe difference in the interaction of each functional group towards the metal ions is the reason for the selectivity even though the core of the QDs is the same. The mechanism of sensing can be illustrated as shown below (Figure 1.23).

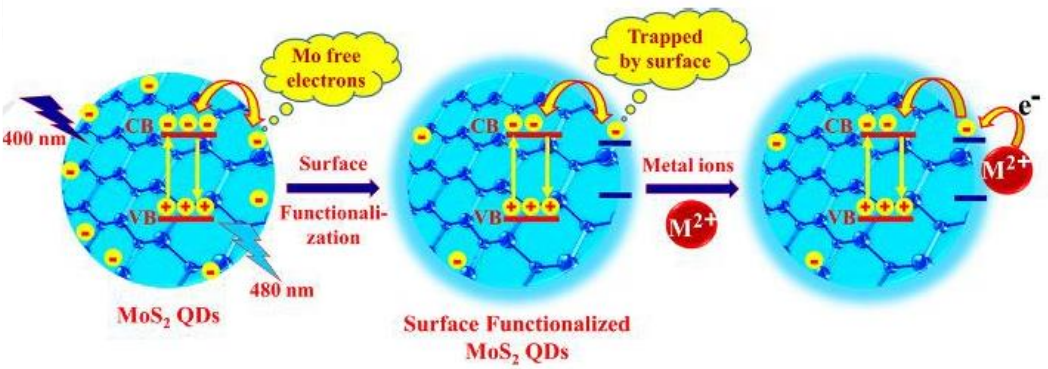

Figure 1.23: Schematic representation for sensing mechanism of metal ions (Lin et al., 2019).

Geldert et al. (2016) demonstrated a facile strategy for the fluorescence detection of a malarial biomarker, *Plasmodium* lactose dehydrogenase (pLDH) protein, adopting "capture-release" sensing method utilizing single-stranded aptamer probe labeled with the fluorescent dye, fluorescein (FAM) and single-layer MoS_2 nanosheet as quencher (Figure 1.24). The strong affinity of nucleic acids together with the robust fluorescence quenching capability of 2D nanomaterials, facilitate energy transfer-based aptasensing platform. The fluorescence of the aptamer will be quenched instantaneously upon its adsorption onto the surface of MoS_2 nanosheets, which will be recovered effectively by the addition of target pLDH protein, as the aptamer will be released from the nanosheets and bind to the target due to the high affinity between the aptamer and the target protein.

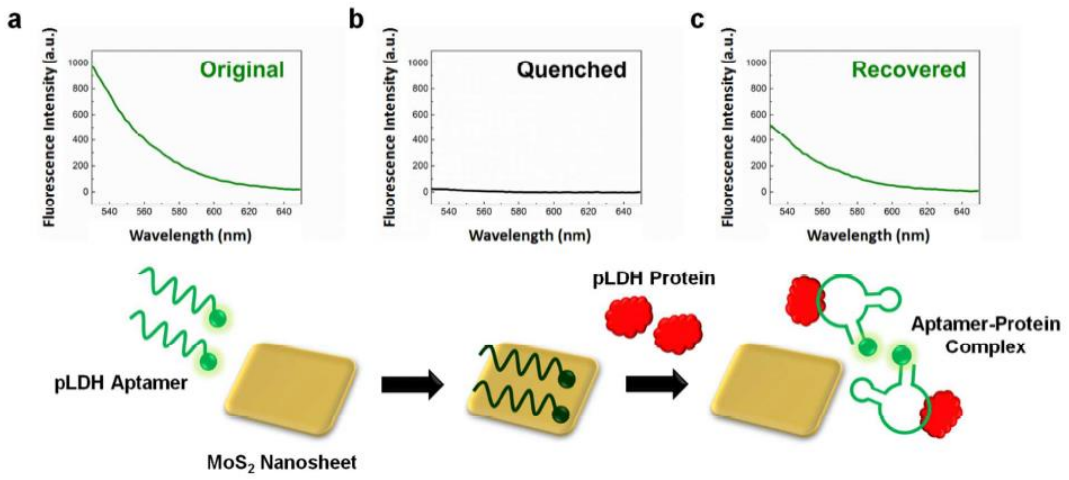

Figure 1.24: Schematic illustration of the aptamer-based "capture-release" sensing assay for the fluorescence detection of a malarial biomarker, pLDH using single-layer MoS_2 nanosheets (Geldert et al., 2016).

The photostability of semiconductor-based QDs as fluorophore was explored by Lu et al., (2017) for labeling the aptamer for the detection of Ochratoxin A (OTA), a typical mycotoxin produced by Aspergillus and Penicillium. The fluorescence of CdTe QDs (585 nm) was initially quenched upon conjugating with an aptamer followed by the adsorption on the surface of MoS_2 and found to be recovered gradually along with the increase of OTA concentration from 1 to 1000 ng/mL. The fluorescent

GQDs with emission at 466 nm have been used for the detection of epithelial cell adhesion molecule (EpCAM), with MoS_2 nanosheet as a quencher (Shi et al., 2017). To prevent the non-specific absorption, the carboxylated aptamer is amalgamated onto GQD which is already conjugated by amine-functionalized PEG by EDC/NHS chemistry. Due to the stronger binding affinity between aptamer and EpCAM protein, upon addition of EpCAM protein, GQD labeled EpCAM aptamer will be detached from MoS_2 nanosheets, leading to the restoration of the fluorescence signal.

The properties such as high-temperature stability, large thermal conductivity and enhanced oxidation resistance together with high reactive edge surface are advantageous for h-BN nanosheets to use as chemical sensors (Zhan et al., 2017). The fluorescence of ROX-labeled single-stranded DNA (ssDNA) was quenched upon adsorbed onto the surface of h-BN nanosheets via π-π stacking. In the presence of a target molecule (DNA), the ROX-labeled ssDNA can hybridize with the target molecule via the intrinsic affinity and the fluorescence is recovered, paving a way for the quantitative determination of DNA as well. The h-BN nanosheets have a weaker affinity towards dsDNA than to ssDNA, due to electrostatic repulsion between duplex DNA and h-BN nanosheets. The same sensor material was used for the quantitative determination of Hg^{2+} as well, with an LOD of 15 nM which is lower than the allowed toxicity level of Hg^{2+} in drinking water (30 nM).

1.2.1.1.3 Ratiometric Fluorescence Sensors

The sensitivity of single wavelength modulation type sensors is usually influenced by factors such as instrumental efficiency, environmental conditions, and the probe concentration. But in ratiometric detection of an analyte, a comparison of fluorescent intensity ratios at two different wavelengths before and after analyte recognition can be performed. It can minimize the measurement errors because of factors such as photo-transformation, sensor concentration and environmental effects (Sahoo et al., 2012). For example, Zhang et al. (2019) synthesized MoS_2 QDs using a bottom-up approach and clubbed with 2, 3-diaminophenazine (DAP) to fabricate a ratiometric sensing system for pH in the range 3.8 to 6, with 0.2 pH unit changes

precisely. The DAP possesses the ability to change its fluorescence intensity with pH due to the protonation of nitrogens in the aromatic ring. Upon changing the pH from 3.0 to 9.0 the fluorescence intensity of MoS_2 QDs is not altered, whereas the fluorescence intensities of DAP at 568 nm increases gradually. The PL emission of MoS_2 QDs quenched considerably due to FRET in the presence of DAP. A ratiometric fluorescence strategy for pH sensing being constructed using this FRET pair by monitoring fluorescence intensity ratio I_{568}/I_{420}; DAP as a pH indicator and MoS_2 QDs as an internal fluorescence reference. They have also demonstrated urea detection as well, with a linear range of 5 to 700 µM, and LOD of 1.8 µM, employing urease as a catalyst, as the hydrolysis of urea can generate ammonium hydroxide, which eventually raises the pH of the solution (Figure 1.25).

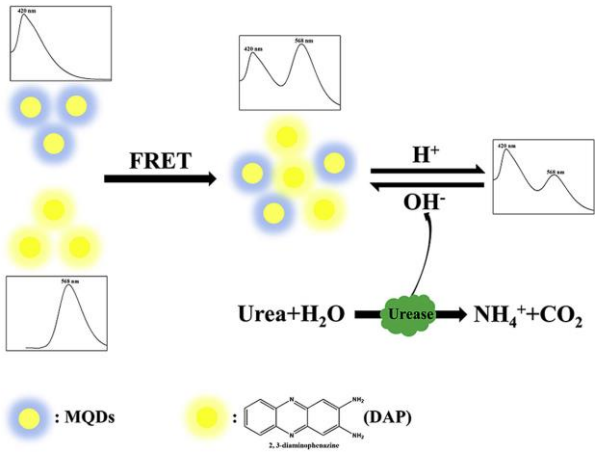

Figure 1.25: Ratiometric fluorescence strategy for pH sensing and the urea detection (Zhang et al., 2019).

1.2.1.1.4 Chemodosimeters

Unlike other strategies of detection, chemodosimeters are based on a specific reaction of the analyte with a fluorescent probe, resulting in the irreversible transduction of a fluorescent signal and thus known to have high selectivity compared to other methods. In order to satisfy the conditions, most of the probes used as chemodosimeters are usually organic compounds such as squaramide hydroxamate (Lim et al., 2009), bis(coumarinyl) Schiff base (Lin et al., 2008), rhodamine-based probe (Lee et al., 2010b2012), catechol ligand linked to a naphthalimide fluorophore

(Jackson et al., 2010) and a few reports are available with inorganic materials such as Mn-doped ZnS QDs for the detection of 2,4,6-Trinitrotoluene (TNT) (Zou et al., 2011), tetraphenylethylene–monoboronic acid for the detection of Hg(II) and methylmercury species (Chatterjee et al., 2017). In the detection of TNT, L-cys-capped Mn-doped ZnS QDs were used for room-temperature phosphorescence to sense and for Rayleigh scattering chemodosimetry to detect TNT in water. Through acid−base pairing interaction between L-cys and TNT, Meisenheimer complexes were formed and induce interdot aggregation of QDs through hydrogen bonding and electrostatic interaction. This complex quenches the fluorescence at 430 nm, and the inter-dot aggregation can significantly influence the light scattering property of the aqueous QDs. This can induce a dominant Rayleigh scattering enhancement at defect-related emission wavelength upon excitation of violet light of Mn-doped ZnS QDs. Mn-doped ZnS QDs also exhibited a high selectivity towards the quenching of the $^4T_1$–$^6A_1$ transition emission and showed a very good linearity in the range of 0.0025−0.45 μM TNT with a detection limit down to 0.8 nM. Scheme of detection can be seen in Figure 1.26

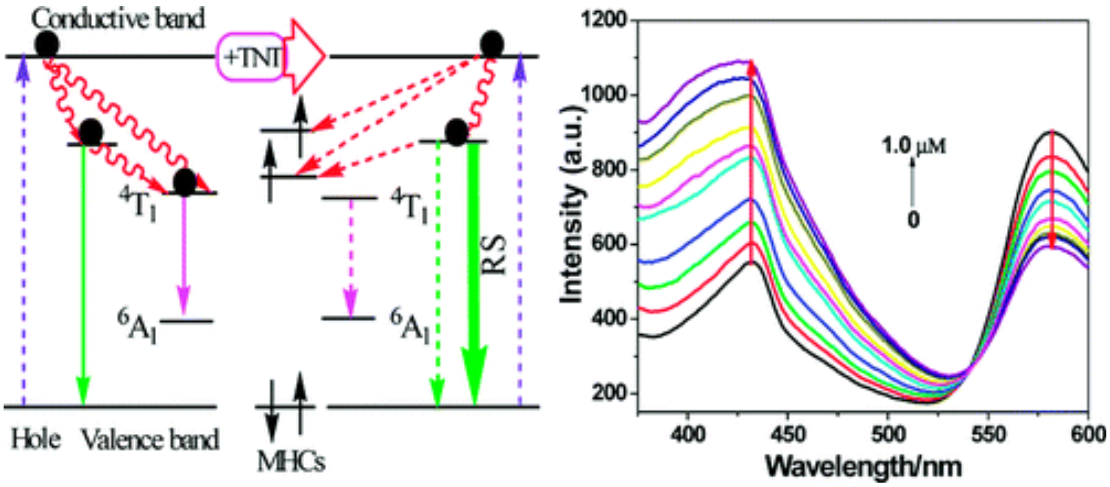

Figure 1.26: Scheme of detection of TNT using L-cys-capped Mn-doped ZnS QDs (Zou et al., 2011)

1.2.1.3 Fluorescence Lifetime Based Sensors

The fluorescence sensors, which work on the modulation of its lifetime, is comparably less in number. This is because lifetime-based sensors are time-consuming

and costly. None the less, the fluorescence lifetime is independent of the concentration of the fluorophore. The lifetime-based sensors are highly advantageous when the local concentration of the fluorophore alters due to washout or photobleaching and hence affecting the intensity based measurements. This is particularly useful in cell imaging using fluorescence microscope, where the local concentration of the probe in each part of the cell is not known. Also, the intensity-based sensors may suffer from the drifts of the optoelectronic system (lamps and detectors), whereas lifetime is independent of these factors (McCranor et al., 2014; Tantama et al., 2011).

1.2.2 Mechanism of Fluorescence Sensing

Any phenomenon that results in a change of fluorescence intensity, wavelength, anisotropy, or the lifetime of the fluorophore upon interaction with target analyte can be used for sensor applications. These changes are mainly governed by electron transfer, energy transfer or the formation of non-fluorescent moieties. The important mechanisms are briefly discussed below.

1.2.2.1 Collisional and Static Quenching

The fluorescence quenching can be attributed to different mechanisms, of which collisional/dynamic and static quenching are general pathways. Both the quenching pathways are significant in terms of fundamental phenomena and applications in chemical, biomedical, environmental safety and industrial domains.

In collisional quenching, the photo-excited fluorophore interacts with the ground state quencher and during this diffusive encounter, the fluorophore is returned to the ground state without any emission. Hence, a collisional quenching relies on the extent of diffusion of fluorophore and quencher in addition to the lifetime of the fluorophore. Another aspect of collisional quenching is that there is no chemical changes occurring during the interaction. In the case of collisional quenching, the decrease in intensity is described by the well-known Stern-Volmer equation:

$$\frac{F_0}{F} = 1 + K_D[Q] \quad \textbf{\textit{or}} \quad 1 + k_q \tau_0[Q]$$

Where F_0 and F are fluorescence intensity before and after the addition of analyte, K_D is the dynamic Stern-Volmer quenching constant, k_q is the bimolecular quenching constant, τ_0 is the unquenched lifetime, and [Q] is the quencher concentration. K indicates the sensitivity of the sensor, higher values of K depicts better sensors (Lakowicz, 2013).

Static quenching relies on the binding of fluorophore and quencher in the ground state, leading to the formation of a non-fluorescent complex. Therefore, it does not rely on diffusion or molecular collisions. Whereas, strong molecular interactions such as electrostatic or π-π interactions, which can form ground state molecular complex is necessitated for the static quenching. For example, highly sensitive detection of TNT was realized using cysteine modified planar MoS_2 QDs (Zhu et al., 2018). TNT is bonded with the amino groups in cysteine, along with strong planar π–π interaction leads to the formation of ground-state complex resulting in the quenching of emission from MoS_2 QDS. In another report, photoluminescent MoO_x QDs used for the turn-off detection of TNT (see Figure 1.27) , through the formation of ground state Meisenheimer complexes (Xiao et al., 2016).

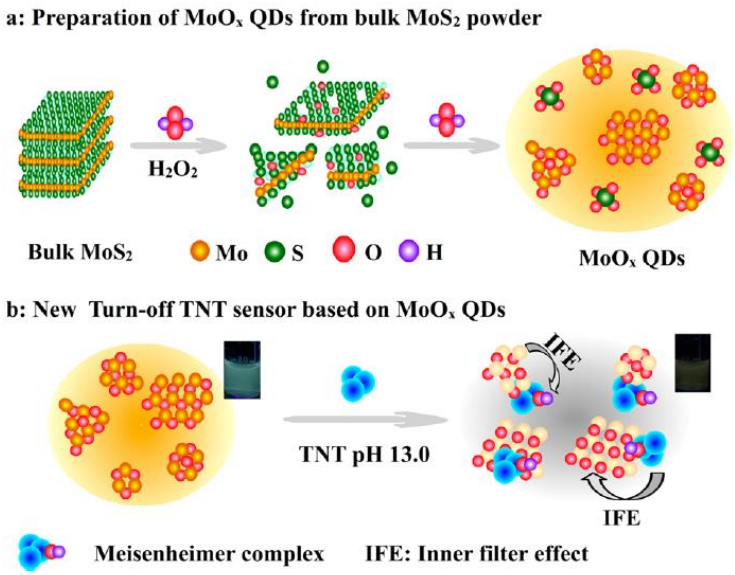

Figure 1.27: Preparation of MoO_x QDs and sensing of TNT using this MoO_x QDs (Zhu et al., 2018)

There are several ways to distinguish static quenching from collisional quenching. One way is to monitor the absorption spectrum of the fluorophore in the presence of the quencher. As the collisional quenching is an excited state process, the absorption spectra of the fluorophore are unlikely to change in the presence of the analyte. In contrast, ground-state complex formation is expected to result in variation in absorption spectral features of the fluorophore. Temperature-dependent steady-state fluorescence spectra are another method to distinguish these two pathways. Since collisional quenching is a diffusion-controlled process, with an increase in temperature, the extent of quenching is expected to increase as the quencher can diffuse quickly at elevated temperatures. The ground state complex between fluorophore and quencher, on the other hand, will be destroyed at elevated temperatures and the emission will increase with a temperature rising. Since collisional quenching is an excited state process, whereas static quenching happens at ground state, time-resolved fluorescence measurements can be made use to distinguish between these two processes. In collisional quenching, the lifetime of the fluorophore is anticipated to decrease due to the emergence of a new non-radiative component and can be governed by the equation,

$$\tau = \frac{1}{\Gamma + knr + kq}$$

where τ is the lifetime, Γ is the emissive rate, k_{nr} is the rate constant for non-radiative process and k_q is the rate constant due to quenching. The static quenching is not accompanied by the alteration of the lifetime of the fluorophore as it only removes some of the fluorophores by forming non-fluorescent ground state complex without affecting its excited state lifetime.

As in the case of collisional quenching, the Stern-Volmer equation can be applied for static quenching as well, which can be expressed as

$$\frac{F0}{F} = 1 + K_{sv}\,[Q]$$

Where K_{sv} is the static Stern-Volmer quenching constant. According to the equation, a plot of F_0/F versus concentration of quencher [Q], will be a straight line

with slope K_{sv} if either of the quenching mechanisms operates. If both quenching mechanisms are involved in the quenching, which is a fair possibility, then the plot of F_0/F versus concentration of quencher will be an upward curve pointing towards the y-axis. In such cases, one can separate dynamic and static quenching contribution by plotting τ_0/τ versus concentration of quencher, where τ_0 and τ are fluorophore's lifetime in the absence and presence of a quencher. This plot will be a straight line, and the slope of the graph gives the contribution from dynamic quenching alone, as static quenching cannot alter the lifetime of the fluorophore (Figure 1.28).

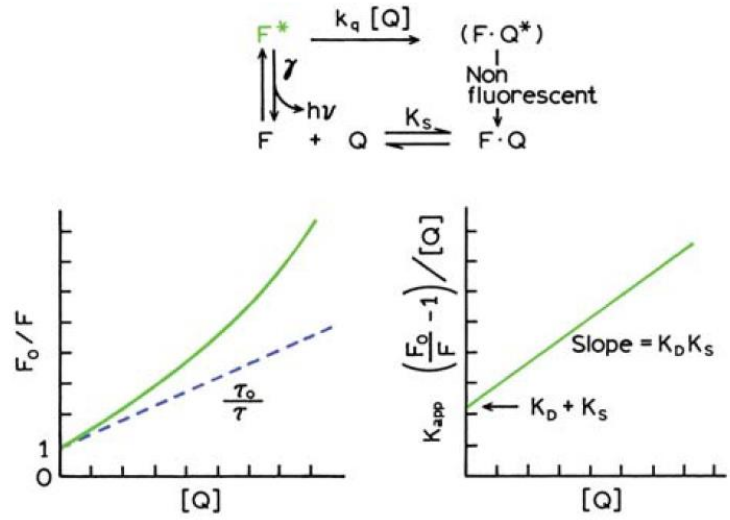

Figure 1.28: Dynamic and static quenching of the same population of fluorophores (Lakowicz, 2013).

1.2.2.2 Energy transfer and Electron Transfer

Two types of energy transfer are possible between fluorophore and quencher: Dexter type energy transfer and Förster resonance energy transfer (FRET), latter being common in practice. Dexter mechanism (Figure 1.29) involves the electron exchange between the excited state donor and ground-state acceptor. The excited electron from the donor moves to the LUMO of the acceptor, then the transfer of an electron back to the ground state of the donor. Both FRET and Dexter mechanisms require the spectral overlap between the donor and acceptor. The later operates at smaller distances (<1.5 nm) and does not need any specific dipole orientation.

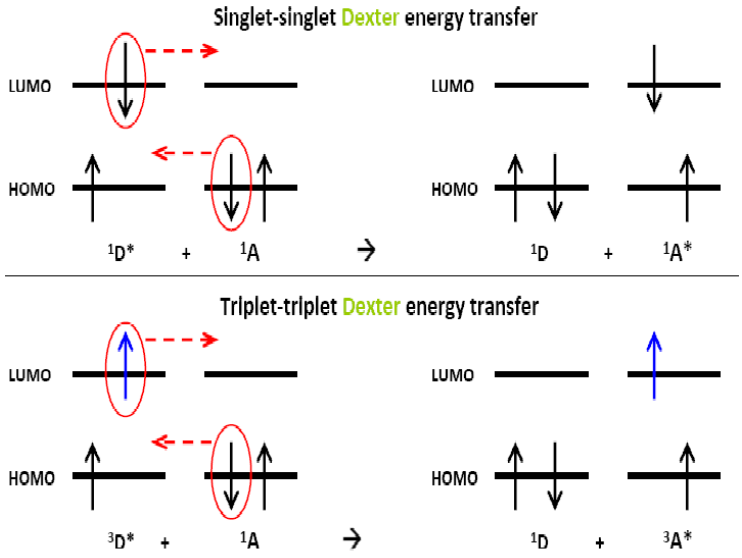

Figure 1.29: Schematic representation of Dexter energy transfer

The presence of the FRET mechanism can be ascertained experimentally. If the acceptor is an emitter, there is a concomitant increase in its emission intensity when the donor is being quenched. This is the direct evidence for the existence of FRET. But care should be taken that the direct excitation of acceptor does not happen at the excitation wavelength of the donor. On the other hand, if the acceptor is a non-emitter, the excited electrons of the acceptor join the ground state hole by non-radiative pathway and hence decrease donor's emission. The time-resolved analysis can be performed to authenticate the existence of FRET. Donor's lifetime will be unambiguously reduced during the FRET because it is an excited state energy transfer process. Schematically FRET can be shown as below (Figure 1.30)

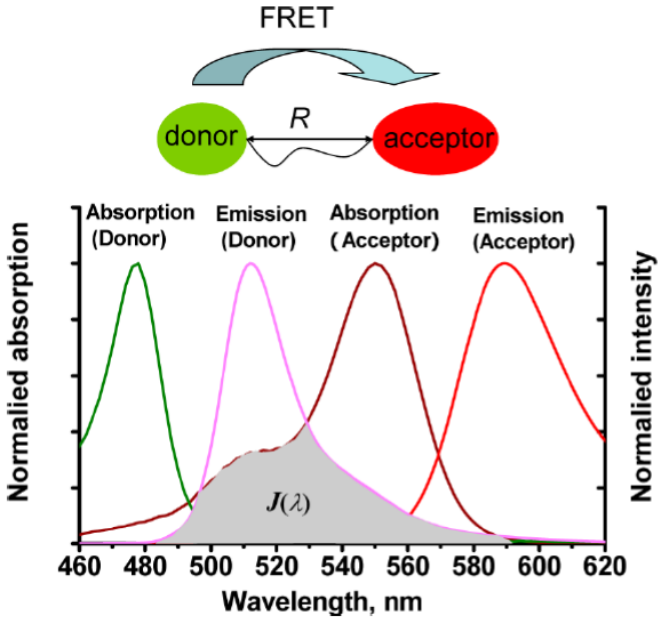

Figure 1.30: Schematic representation of FRET. J (λ) represents spectral overlap (Lakowicz, 2013).

There are essentially three criteria for an efficient FRET process. Primarily, there should be a matching of donor's emission and acceptor's absorption. Secondly, donor and acceptor molecules should be in proximity. This can be accomplished by establishing a dipole-dipole, electrostatic or a covalent interaction between donor and acceptor. Finally, the donor and acceptor must exhibit a proper dipole orientation.

The degree of the spectral overlap between donor's emission and the acceptor's absorption is expressed in terms of spectral overlap (J_{DA}),

$$J_{DA} = \int_0^\infty I_D(\lambda)\varepsilon_A(\lambda)\lambda^4\, d\lambda$$

Where, $I_D(\lambda)$ = Donor normalized fluorescence emission

$\varepsilon_A(\lambda)$ = Acceptor's absorption spectrum in molar absorptivity in units of $M^{-1}cm^{-1}$

λ = wavelength

The critical distance or the Förster distance (R_0) is defined as the distance between the donor and the acceptor at which the FRET efficiency is 50%. The R_0 value can be calculated using the equation

$$R_0^6 = \frac{9000(\ln 10)\kappa^2 Q_D}{128\pi^5 N n^4} \int_0^\infty F_D(\lambda)\,\varepsilon_A(\lambda)\,\lambda^4 d\lambda$$

Where, κ^2 = Orientation factor, 2/3 for randomly oriented dipoles

φ_D = Quantum yield of donor in the absence of the acceptor

n = Refractive index of the medium

N = Avogadro's number

The efficiency of the energy transfer (E%) can be calculated using the equation

$$E = 1 - \frac{F_{DA}}{F_D} \quad \text{-or-} \quad E = 1 - \frac{\varphi_{DA}}{\varphi_D}$$

Where, F_D = Fluorescence intensity of the donor

F_{DA} = Fluorescence intensity of the donor in the presence of acceptor

φ_D = Donor alone quantum yield

φ_{DA} = Donor quantum yield in the presence of acceptor

Quantum yield of the fluorophore (Φc) can be calculated by comparing the quantum yield of a standard, using the equation

$$\varphi_c = \varphi_o \times \frac{I_C}{I_o} \times \frac{A_o}{A_c} \times \frac{\eta_c^2}{\eta_o^2}$$

Where, Φ_o = Photoluminescence quantum yield of the standard

I_o = Integrated emission intensity of the standard

I_c = Integrated emission intensity of the sample

A_o = Absorbance of the standard & A_c = Absorbance of the sample

η_o = The refractive index of the reference solution & η_c = The refractive index of the sample solution

The time-resolved FRET efficiency (E_{TR}) can be calculated using the lifetime of the donor in the absence (τ_D) and the presence of acceptor (τ_{DA}) as:

$$E_{TR} = \frac{\tau_{DA}}{\tau_D}$$

Distance between the donor and the acceptor, r is calculated using the equation

$$r = \frac{R_0[n - En]^{1/6}}{E}$$

Where, n = The number of acceptor to donor ratio

E = FRET efficiency

R_o = Förster distance

r = Distance between the donor and the acceptor

The rate of energy transfer or the resonance energy transfer rate (K_T) is given by

$$k_T = \frac{1}{\tau_D}\left(\frac{R_0}{r_{DA}}\right)^6$$

Where, τ_D is the lifetime of the donor in the absence of the acceptor.

Overall, the quenching mechanism can be schematically represented by a simple Jablonski diagram, as shown below (Figure 1.31)

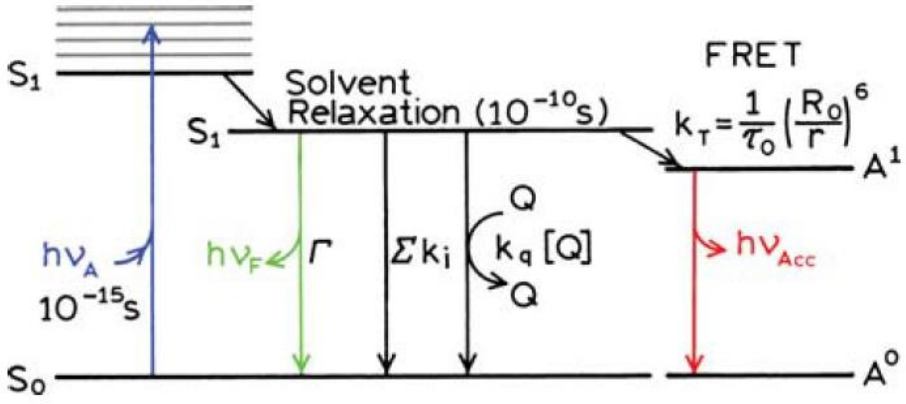

Figure 1.31: Jablonski diagram with collisional quenching and fluorescence resonance energy transfer (FRET). The term Σki is used to represent non-radiative paths to the ground state, aside from quenching and FRET (Lakowicz, 2013).

Modulation of FRET efficiency is the key to most of the FRET-based sensing strategies. This is commonly done in two ways. By altering the distance between donor and acceptor, i.e. by distance-dependent FRET or by changing the spectral overlap between donor and acceptor (Dennis et al., 2012; Moquin et al., 2013). Intensive research is happening in the field of 2D materials for the design and fabrication of

FRET assays either as donors or acceptors. Extend of FRET mainly depends on the nature of the quencher and donor. Graphene being an extended honeycomb network of sp^2 hybridized carbon atoms having a long-range π-conjugation, any system with a positive possibility for non-covalent intermolecular interactions involving π-systems are significant in the sensing events, as even subtle changes in the electronic structure upon interactions, can lead to modifications in their properties. These interactions also promote the physisorption of moieties such as DNAs, proteins, etc. to ensure the maximum closeness of quencher and fluorophores, which is a primary criterion to be satisfied for FRET to occur. In addition to this, the large surface area of graphene enables to load multiple fluorescent donors simultaneously, which is far superior to conventional "one-to-one" FRET pairs. Defects on the sheets are another pivotal parameter considered, as a FRET-based sensor. Graphene is mainly subjected to have point defects, such as the absence of carbon atoms with sp^2 hybridization or the presence of sp^3 hybridized carbon atoms. These electronically perturbed sites are the seats for high chemical reactivity and thus open a way for further functionalization.

Many groups have employed the selective interaction of Ag(I) with cytosine–cytosine (C–C) mismatches to develop highly selective Ag(I) sensors (Ono et al., 2008; Lin, and Tseng, 2009; Xie et al., 2012). Wen et al. (2010) demonstrated a mix-and-detect fluorescent sensor for Ag(I) ions by coupling Ag(I) specific cytosine (C)-rich oligonucleotide (SSO) probe labeled with fluorescein (FAM) with GO, which can specifically adsorb and quench ss fluorogenic DNA probes. Upon addition of Ag^+, the complexation of Ag^+ with the cytosine bases of SSO induce a conformational change from a flexible single-stranded state to a rigid hairpin structure. GO is added then stepwise, to selectively adsorb the unbound SSO and quench its fluorescence, while the Ag^+ ions complexed with SSO remain free and their fluorescence is retained.

Mao et al. (2015) has presented methodology for the detection of Ag^+ ions both in buffered solution and in real water samples such as lake water, tap water, etc., by combining the excellent quenching capability of MoS_2 single layer along with a FITC-labeled Ag^+ specific oligonucleotide, rich in cytosine, that can form a C-Ag^+-C

base pairs, which are more stable. The advantage of this particular combination is that having a smaller van der Waals radius (E1.44Å) compared to the base pair spacing of the DNA duplex (E3.4 Å), the silver ion can be incorporated into the DNA duplex without altering its double-helical structure. Due to the van der Waals force between nucleotide bases and single-layer MoS_2 and the special p-type nature of ultrathin MoS_2 material, the distance from FITC to single-layer MoS_2 was shortened, which will aid to the effective FRET between the two moieties when FITC-labeled DNA probe was in the state of random coil ss-DNA. In the presence of Ag^+ the random coil ss-DNA changes to straight stiff double-stranded DNA (ds-DNA), which in turn force the energy donor FITC far away from the surface of single-layer MoS_2 due to the hydrophilic force of the phosphoric skeleton in ds-DNA and FRET was disappeared, followed by the recovery of PL emission of the dye. A plausible reason for this behavior was given is the terms of adsorption competition among the free FITC-ssDNA.

Another type of quenching mechanism is known as photoinduced electron transfer (PET). In PET, a complex is formed between the electron donor D_P and the electron acceptor A_P, resulting in a $D_P^+A_P^-$ complex upon excitation, as seen in Figure 1.32. This charge transfer complex can return to the ground state without emission of a photon.

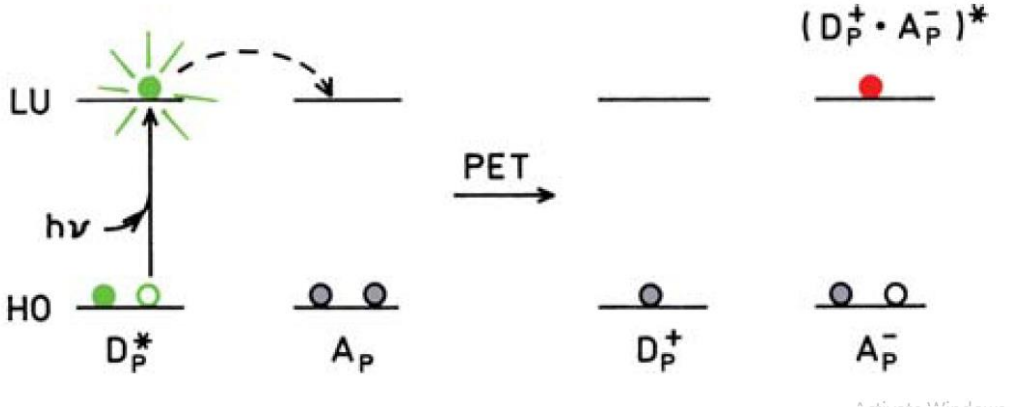

Figure 1.32: Molecular orbital schematic for photoinduced electron transfer (Lakowicz, 2013).

Chen et al. (2017b) reported fluorescence quenching of monolayer MoS_2 QDs by 6-mercaptopurine (6-MP), via acceptor-excited photoinduced electron transfer. 6-

MP molecules are chemically adsorbed and complexed at the sulfur vacancy sites of the M-MoS_2 QDs, which can trigger the quenching through PET. A turn-on sensing of glutathione was formulated, as it can trigger the release of 6-MP from the M-MoS_2 QDs, thereby switching on the fluorescence of the M-MoS_2 QDs.

1.2.2.3 Inner Filter Effect

Fluorescence sensors based on the inner filter effect (IFE) mechanism does not demand any molecular interactions between fluorophore and quencher. IFE happens due to the absorption of excitation or emitted light by the quencher (G. Li et al., 2016). This results in a decrease in emission of fluorophore because of the absorption of part of excited or emitted light, which can be correlated to the concentration of target analyte. Schematically, IFE can be shown as given in Figure 1.33

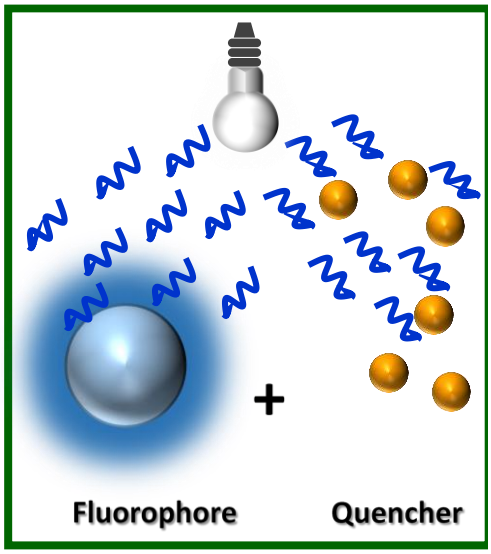

Figure 1.33: Representative scheme of IFE

Many reports are available, where IFE acts as a primary or subsidiary sensing mechanism. A facile and sensitive method for the monitoring of alkaline phosphatase activity (p-Nitrophenylphosphate) in serum and living cells were realized using the luminent MoS_2 QDs based on IFE as a mechanism (Zhong et al. (2018)). Gu et al. (2017a) have constructed a ratiometric fluorescence sensor for the selective and

sensitive detection of Hg^{2+}, using black phosphorus QDs based on IFE of tetraphenylporphyrin tetrasulfonic acid (TPPS) toward the black phosphorous QDs (Figure 1.34).

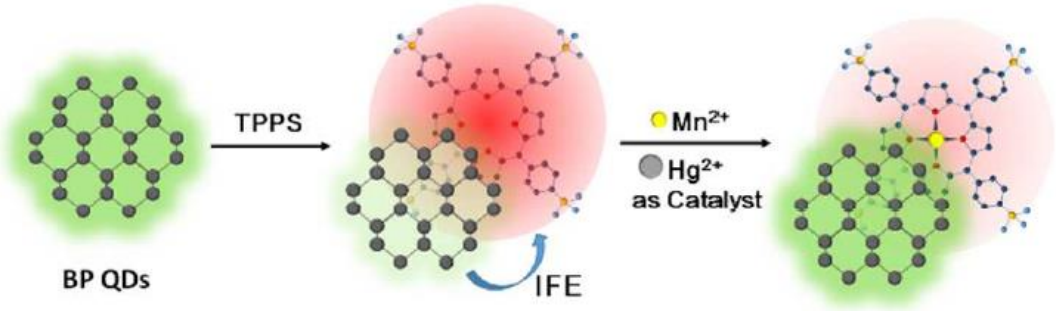

Figure1.34: Schematic illustration of ratiometric fluorescence detection of Hg^{2+} based on the IFE between black phosphorous QDs and TPPS (Gu et al., 2017b)

A fast, sensitive and label-free fluorescence sensing of acetylcholinesterase (AChE) activity was also realized using the black phosphorus QDs (Gu et al., 2017b), based on IFE between the QDs and 2-nitro-5-thiobenzoate anion (TNB). The linear range was from 0.2 to 5-unit L^{-1} with the LOD of 0.04 unit L-1. Another turn-off approach operate IFE was introduced by Shanmugaraj and John (2019) for the detection of bilirubin in human fluids, using MoS_2 QDs as a probe, with the LOD of 2.1 nM. The fluorescence of MoS_2 QDs was drastically quenched by the addition of bilirubin through IFE together with the FRET mechanism between MoS_2 QDs and bilirubin.

1.3 Objective and Scope of the Work

The choice of nanomaterial for fluorescent-based sensing applications is significant, as it can govern different parameters such as selectivity, sensitivity, response time, etc. In recent years, nanomaterials based fluorescence-based sensors using semiconductor QDs, graphene or carbon-based nanomaterials, etc. have been explored. The potential of 2D layered materials as fluorescence sensors is less delved into and there are enough room for understanding the fundamentals of these materials. The unique qualities of 2D layered materials in general and specifically for two typical

examples; MoS_2 and WS_2, are their tunable luminescent properties, excitation dependent emission, photostability, temporal stability, biocompatibility and low toxicity, quenching ability, possibility for fast electron and energy transfer, high surface-area-to-volume ratio for multiplexed sensing, etc. motivated to explore these materials.

The synthesis of stable and highly luminescent 2D layered materials is still cumbersome. One of the easiest method reported, employ the usage of Li containing organic compounds for intercalation and exfoliation, which may lead to the generation of metallic phase, rather than semiconducting nature. The removal of the organic solvent after the exfoliation is strenuous. It may also lead to the generation of thicker layers, as well. The solubility of these materials in water is essential to adapt them to the biological arena. The quantum yield of the as generated single-layer MoS_2, for example, is a low value of ~0.3 %. A simple method for the generation of different types of nanomaterials from the same precursors by altering the reaction condition is also rare. The choice and cost of precursors, the economic viability of the synthetic route followed, are also of paramount importance. Conversely, the response of as-synthesized nanomaterials at different pH conditions was also blurry, which need to be investigated to expand their boundaries of applicability.

Considering the excellent properties of these 6nanomaterials, we attempted to address a few of the challenges, especially in the areas of synthetic procedures, quenching pathways of luminescence and the use in fluorescence-based sensors.

The work presented in this report is useful in terms of the fundamental understanding of MoS_2 and WS_2 based nanomaterials, which will aid in enriching the library of these nanosystems and their potential application in diverse fields. We envisage that facile synthetic strategy proposed would be useful for the synthesis of similar 2D layered materials, which ultimately can extend the technological boundary as well as in further divulging the nature of transition metal dichalcogenides, in general.

1.4 Organization of the Thesis

The thesis describes synthesis, characterization, photophysical behavior and chemical sensing applications of MoS_2 and WS_2 based nanomaterials. The thesis is organized as shown below.

Chapter 1 elaborates the literature review on properties, synthetic methods, and general applications of 2D layered materials, with emphasis on MoS_2 and WS_2 based ones. General approaches of fluorescence-based sensing with different possible mechanisms were detailed with suitable examples.

Chapter 2 highlights the synthesis and characterization of different types of MoS_2 nanomaterials, such as nanosheets (NSs) and a hybrid of quantum dots (QDs) and NSs (MoS_2 QDNS), which will be used in subsequent chapters.

Chapter 3 describes selective turn off detection of dopamine (DA) using a typical MoS_2 hybrid nanomaterial; MoS_2 QDNS. Detailed microscopic and spectroscopic investigations were carried out to propose a mechanism of quenching of fluorescence emission from MoS_2 QDNS by DA.

Chapter 4 outlines the response of luminescence of MoS_2 QDNS towards different pH and a turn-on glucose sensor was also devised using acidified MoS_2 QDNS in conjugation with glucose oxidase.

Chapter 5 deals with the synthesis and characterization of different types of WS_2 based nanomaterials such as quantum dots (QDs), nanosheets (NSs) and a hybrid of QDs and NSs.

Chapter 6 details a turn-off detection strategy of trinitrophenol using WS_2 QDs. An elaborate study has also done formulating plausible mechanisms of sensing.

Chapter 7 demonstrate the reducing action of WS_2 nanosheets, synthesized via hydrothermal method towards $AgNO_3$ solution, resulting in the formation of in-situ Ag nanoparticle onto WS_2 nanosheets and its application as a turn-on sensor for basic amino acids

Chapter 8 summarizes the conclusions drawn from the present thesis and highlights on the future scope of the work.

CHAPTER 2

SYNTHESIS OF MoS_2 BASED NANOMATERIALS

This chapter describes in detail the synthesis of nanomaterials based on MoS_2, using a simple and green reaction route. The synthesis was accomplished by the high-temperature hydrothermal reaction of bulk MoS_2 in aqueous NaOH. Upon changing the molar ratio of MoS_2 to NaOH, different types of nanomaterials such as nanosheets and a hybrid of quantum dots-nanosheets were obtained. Interestingly all of these nanomaterials display high luminescence spanning a large portion of the UV and visible region of the electromagnetic spectrum. These nanomaterials manifest excellent stability, retained its characteristic morphology and photoluminescence (PL) even after a few months of preparation. A detailed photophysical characterization including time-resolved fluorescence were carried out to unfold the inherent nature of these materials including the origin of PL emission from MoS_2 based hybrid nanostructure.

2.1 Introduction

A single layer of MoS_2 crystal consists of a hexagonally packed layer of Mo metal sandwiched between two S layers with a layer thickness around 0.6 nm (Park et al., 2017). Within a layer, the metal and S are bound by covalent linkage, whereas the interlayers are coupled by weak van der Waals forces, which makes it cleave readily along the layer surface by the application of external force (Chhowalla et al., 2013). The few layered sheets shows photoluminescence (PL) due to the crossover from indirect bandgap in bulk to a direct bandgap semiconductor (Mann et al., 2014).

Various methods of synthesis of these materials, such as chemical vapor deposition, thermolysis, hydrothermal, liquid exfoliation techniques, etc. have been discussed in Chapter 1. The requirement of sophisticated instrumentation, use of hazardous reagent materials, pre- and post-synthesis treatment, etc. dampen the receptivity of some of these methods, though. Besides, a single strategy for the synthesis of different types of nanomaterials by varying the reaction conditions is rare.

This chapter focuses on the synthesis and characterization of MoS_2 nanomaterials. MoS_2 nanosheets of varying thickness and a hybrid of MoS_2 nanosheets and nanodots from the same precursors using facile hydrothermal reaction, just by varying the ratio of MoS_2 powder to NaOH; has been realized. By keeping the reaction at 220 °C, for 8 h, at concentration ratios of 1:0, 1:2, 1:5, 1:10 and 1:20, nanomaterials of different morphology and dimensions were obtained. Various photophysical characterization has been carried out to understand the system better, such as UV-Vis absorption and excitation studies, steady-state and lifetime fluorescence, Raman spectra, etc. It has been found that, as the concentration of the NaOH increases, the material is found to be degraded further, probably due to the enhanced oxidative cutting and exfoliation by alkali. We envisage that the present strategy would be a key for the synthesis of similar 2D layered materials and these materials can be made use for various intriguing applications.

2.2 Experiments and Methods

2.2.1 Reagents and Materials

Molybdenum (IV) sulfide, (MoS_2, <2 μm, 99%) powder, quinine sulphate and dialysis bag were purchased from Sigma- Aldrich, USA. NaOH was purchased from Merck India Ltd. Double distilled water was used throughout the experiments. All reagents purchased were of analytical grade and used without further purification.

2.2.2 Instrumentation

UV-visible spectra were recorded using a Carry 100 UV-visible spectrometer. All steady-state fluorescence measurements (excitation and emission) were carried out using FluoroMax-4C Spectrofluorometer (Horiba Instruments, USA). Both excitation and emission slit widths were fixed at 5 nm with an integration time of 0.1 ns. Time-resolved fluorescence measurements were performed using time-correlated single-photon counting (TCSPC). TCSPC measurements were performed at an excitation wavelength of 344 nm and decay profiles were collected at 400 nm. Transmission

electron microscopy (TEM) images were obtained using a JEOL 2100 instrument and the atomic force microscope (AFM) images were taken using the Agilent 5500 scanning probe microscope (non-contact mode). Raman spectra were measured in a Renishaw confocal Raman microscope using a 532 nm laser. The quantum yield of MoS_2 nanomaterials was calculated using quinine sulfate ($\varphi = 0.54$) as standard at 330 nm excitation. Photostability experiments were carried out by irradiating aqueous solution of MoS_2 QDNS under 360 nm UV lamp (48 W power) and fluorescence spectra of photo-irradiated samples were recorded at specified time intervals.

2.2.3 Synthesis of MoS_2 based Nanomaterials

In a typical synthesis procedure, 150 mg of commercially available MoS_2 powder was taken in a Teflon lined autoclave with different amounts of NaOH for making the final concentration ratio of MoS_2 to NaOH of 1:0, 1:2, 1:5, 1:10 and 1:20, and kept for the hydrothermal reaction for 8 h. The products obtained are centrifuged for separating from the precipitate and dialyzed for 12 h, for obtaining purified materials with PL property. The text 'concentration ratio 1:0, 1:2, 1:5, 1:10 and 1:20' in the subsequent part of the chapter represent the MoS_2 nanomaterial synthesized by the hydrothermal reaction of MoS_2:NaOH with those concentration ratios.

2.3 Results and Discussions

2.3.1 Synthesis and Characterization of MoS_2 Nanomaterials

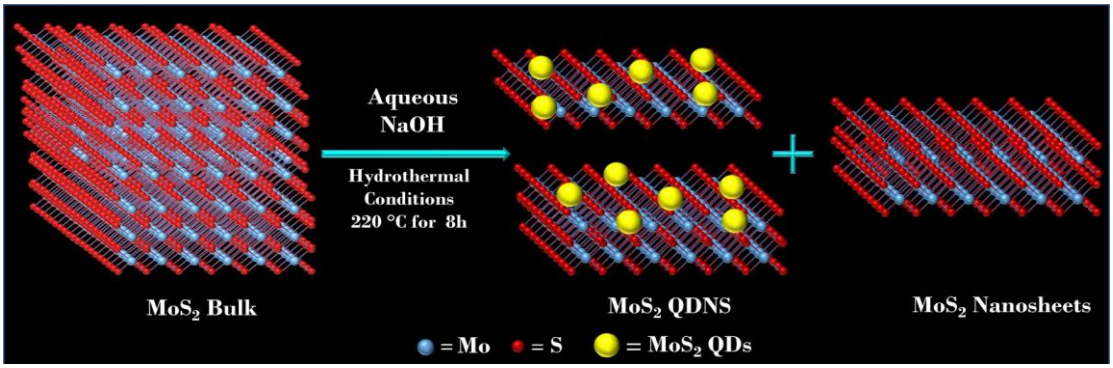

Scheme 2.1: Synthesis of MoS_2 based nanomaterials by hydrothermal route

The Scheme 2.1 demonstrates the formation of two types of nanomaterials based on MoS_2, viz MoS_2 quantum dots dispersed over nanosheets (MoS_2 QDNS) and MoS_2 nanosheets (MoS_2 NS) by varying the ratio of MoS_2 powder to NaOH from 1:0 to 1:20. We surmise that the intercalation of Na^+ ions and the oxidative cutting of MoS_2 sheets under hydrothermal conditions would have led to the formation of MoS_2 QDs and the low dimensional nanosheets. The present synthetic strategy circumvents the use of hazardous organic solvents and organo-lithium intercalating agents. The purified MoS_2 nanomaterials manifested extra-ordinary stability with the retention of its characteristic features even after several months of preparation.

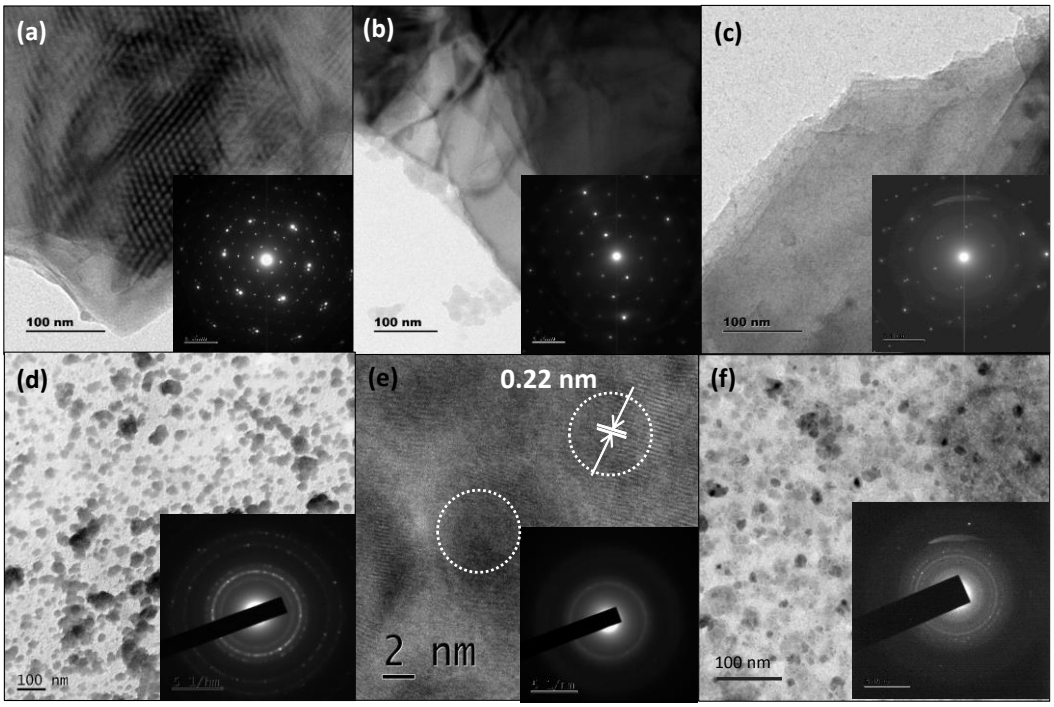

Figure 2.1: TEM images of MoS_2 nanomaterials synthesized using MoS_2:NaOH concentration ratios (a) 1:0, (b) 1:2, (c) 1:5, (d and e) 1:10 and (f) 1:20, respectively. Inset shows the SAED pattern from these TEM images. The image (e) shows the HRTEM image of MoS_2 QDNS showing crystalline nanosheets and amorphous QDs.

The direct evidence for the formation of nanomaterials of different morphologies was coherent from the TEM images, as shown in Figure 2.1. At ratios 1:0, 1:2, and 1:5, nanosheets (MoS_2 NS) of varying thickness have been obtained with high crystallinity, as is evident from SAED patterns. Lattice fringes with spacing ~ 0.22 nm, corresponds to (103) plane of hexagonal crystal system of MoS_2 were present in

the HRTEM images of these materials. The lateral dimensions of the sheets are of the range of a few micrometers to the nanometer. Whereas at 1:10 and 1:20, a new hybrid material of MoS_2 quantum dots dispersed over nanosheets (MoS_2 QDNS), were obtained, with the size of sheets around 100 nm and that of QDs below 10 nm of lateral dimension. For 1:10 sample, it is obvious that the spherically sized dots were having the average size 2.0±0.76 nm, distributed evenly over the exfoliated sheets (size histogram of ~ 200 QDs in the TEM images of all the samples are presented in Figure 2.2). There are two different regions in the HRTEM image of 1:10 sample (Figure 2.1e). A semi-crystalline region which corresponds to MoS_2 QDs and purely crystalline, for MoS_2 nanosheets. The presence of a large number of surface defects in QDs as compared to that of nanosheets might have imparted a weak crystallinity in the QDs.

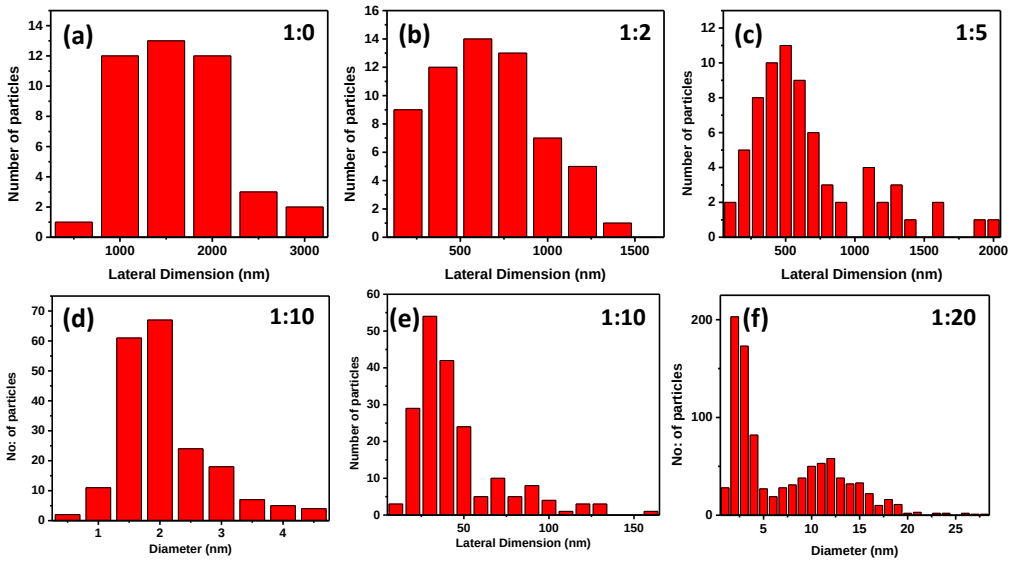

Figure 2.2: Size histogram obtained for MoS_2 nanoparticles. (a-c) and (e) represents the lateral dimension of the sheets whereas (d) and (f) denotes the diameter of QDs on the surface of MoS_2 NS

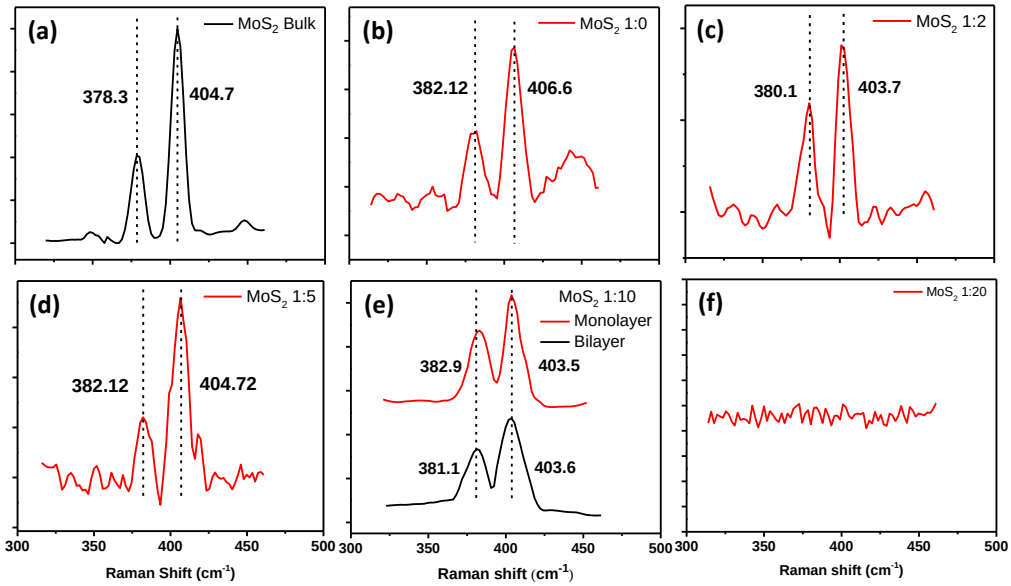

Figure 2.3: Raman spectra of nanomaterials obtained by hydrothermal reaction of MoS_2:NaOH concentration ratios of 1:0, 1:2, 1:5, 1:10 and 1:20 (b) to (f), respectively. The Raman spectrum of MoS_2 powder (a) is given for comparison.

We employed Raman spectral studies for elucidating the number of layers of sheets present in each system by gauging the frequency difference between E^1_{2g} and A_{1g} mode of vibrations (Δk) (Yu et al., 2013). A general trend of decrease in the number of layers was obtained by increasing the concentration of NaOH. This could be attributed to the assistance of NaOH in the delamination and cutting of MoS_2 bulk layers. For sample 1:0, a frequency difference of 24.5 is obtained, which reflects a total of 4 or more monolayers present in the system (Figure 2.3). While, for sample 1:2, a frequency difference of 23.6 is obtained, which corresponds to 3 layers of MoS_2 sheets. Upon further increasing the concentration of NaOH to a ratio of 1:5, Δk value of 22.6 is acquired, an indication of bilayer MoS_2 sheets. By increasing the concentration of NaOH to 1:10, the material is degraded to quantum dots, which are dispersed over nanosheets of mono and bilayer thickness. A frequency difference of 20.6 and 22.5 was obtained by taking the spectra at different regions of the material. On the contrary, for 1:20, no Raman spectral features were obtained as such, which is typical for MoS_2

quantum dots. The smaller size of the particles and the lack of layers could be the reason behind this particular observation.

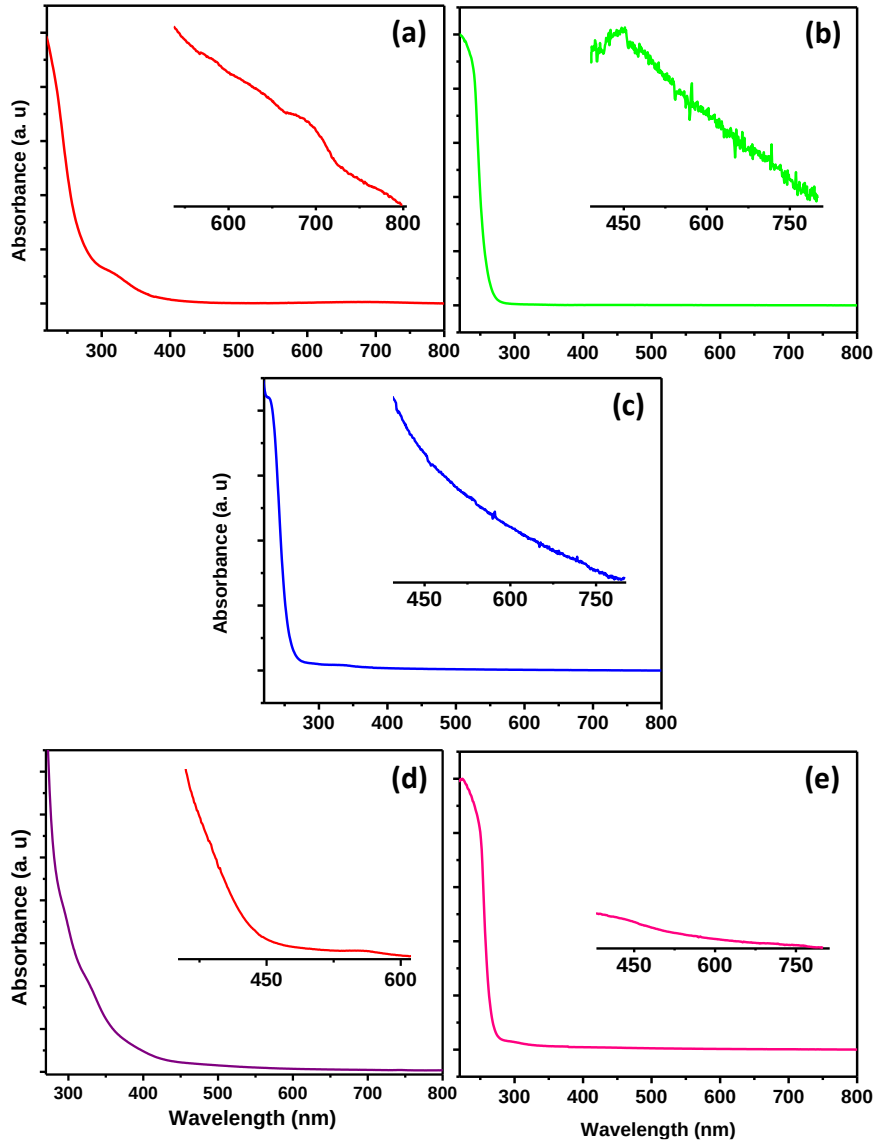

Figure 2.4: Absorption spectra of nanomaterials obtained by hydrothermal reaction of MoS_2:NaOH concentration ratios of 1:0, 1:2, 1:5, 1:10 and 1:20 from (a) to (e), respectively.

The photophysical characterizations such as absorption, excitation, steady-state fluorescence and lifetime fluorescence spectral studies were performed on these materials to understand the optical behavior of the MoS_2 materials. In general, the large MoS_2 nanosheets possess two prominent absorption bands around ~620 and ~680 nm, being attributed to the B and A excitons arising from K point of Brillouin zone,

respectively. These peaks are expected to be strongly blue-shifted when the lateral size falls below 100 nm due to the quantum size effect. As expected, these signature peaks for sheets were present in the UV-Vis absorption spectra of samples 1:0, 1:2, and 1:5 around 680 and 630 nm (Figure 2.4). A continuum of absorption from 600 nm onwards till the UV region, as seen in the other two samples, could be similar excitonic peaks which might have stemmed from the heterogeneity in the lateral dimension of underlying nanosheets. The peaks around 300 nm can attest the presence of quantum dots. For samples containing QDs, two higher energy absorption bands at ~300 and ~330 nm for 1:10 and below 300 for 1:20 must have been aroused from the transition between deep valence band to the conduction band in MoS_2 QDs due to the quantum size effect.

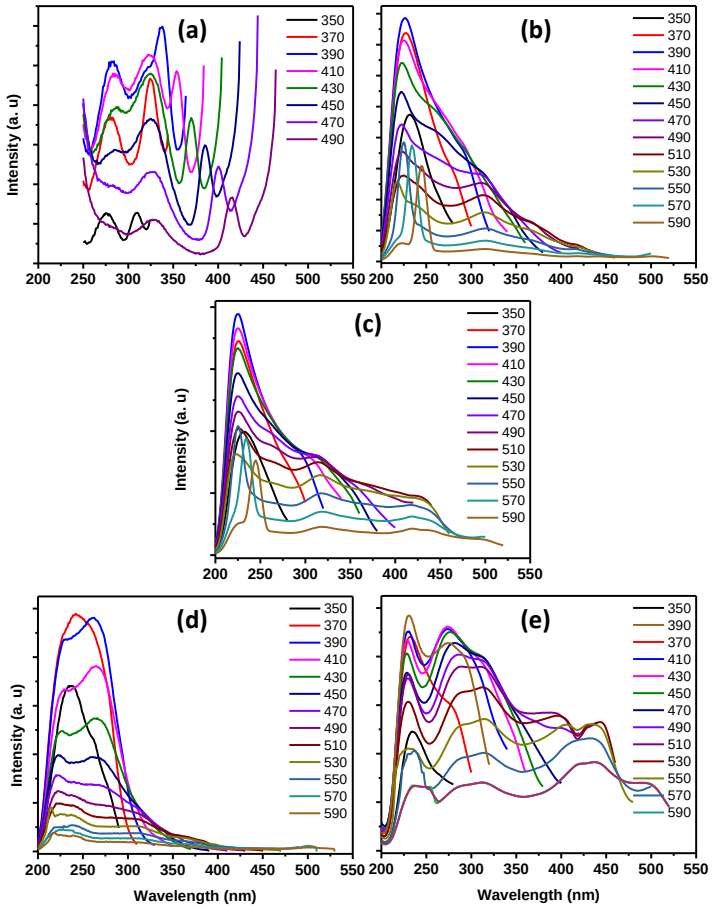

Figure 2.5: Excitation spectra of nanomaterials obtained by hydrothermal reaction of MoS_2:NaOH concentration ratios of (a) 1:0, (b) 1:2, (c) 1:5, (d) 1:10 and (e) 1:20. The emission wavelengths of each spectrum is given as the legend.

The excitation spectra show compound peaks at various emission positions, as seen in Figure 2.5. The complexity in the excitation spectra was duly reflected as excitation dependent emission from these samples. As the lateral size and thickness of the sheets decreases, the emission position is reported to be blue-shifted. All the samples displayed a broad, excitation dependent fluorescence emission response (Figure 2.6) covering a large region of the visible spectrum, owing to polydispersity of the system (Wang and Ni, 2014; Wang et al., 2013a; Ou et al., 2014; Halder et al., 2016). Sample 1:0 shows very weak excitation independent emission around 430 nm at an excitation of 350 nm, and the quantum yield (QY) of the sample is calculated to be 0.01%. Sample 1:2, on the other hand, shows comparatively high emission with a QY of 1.88 %, and maximum emission is found to be at 418 nm, at an excitation of 320 nm. The emission profile from 1:5 is further broadened and almost similar intensity is obtained for excitation from 330 to 370 nm, with emission maxima ranging from 412 to 466 nm, with a QY value of 1.1%. The 1:10 sample shows very broad excitation dependent emission, emerging from the contribution from both the QDs and nanosheets and maximum excitation is found to be at 384 nm at an excitation of 320 nm, with the best QY of 3.7%. On the contrary, the emission profile from sample 1:20, shows entirely different behavior from other samples. It shows high emission at 516 nm, with yellow emission at an excitation of 460 nm. This particular emission could be stemmed from bigger QDs, as seen in the size histogram of this sample (Figure 2.2).

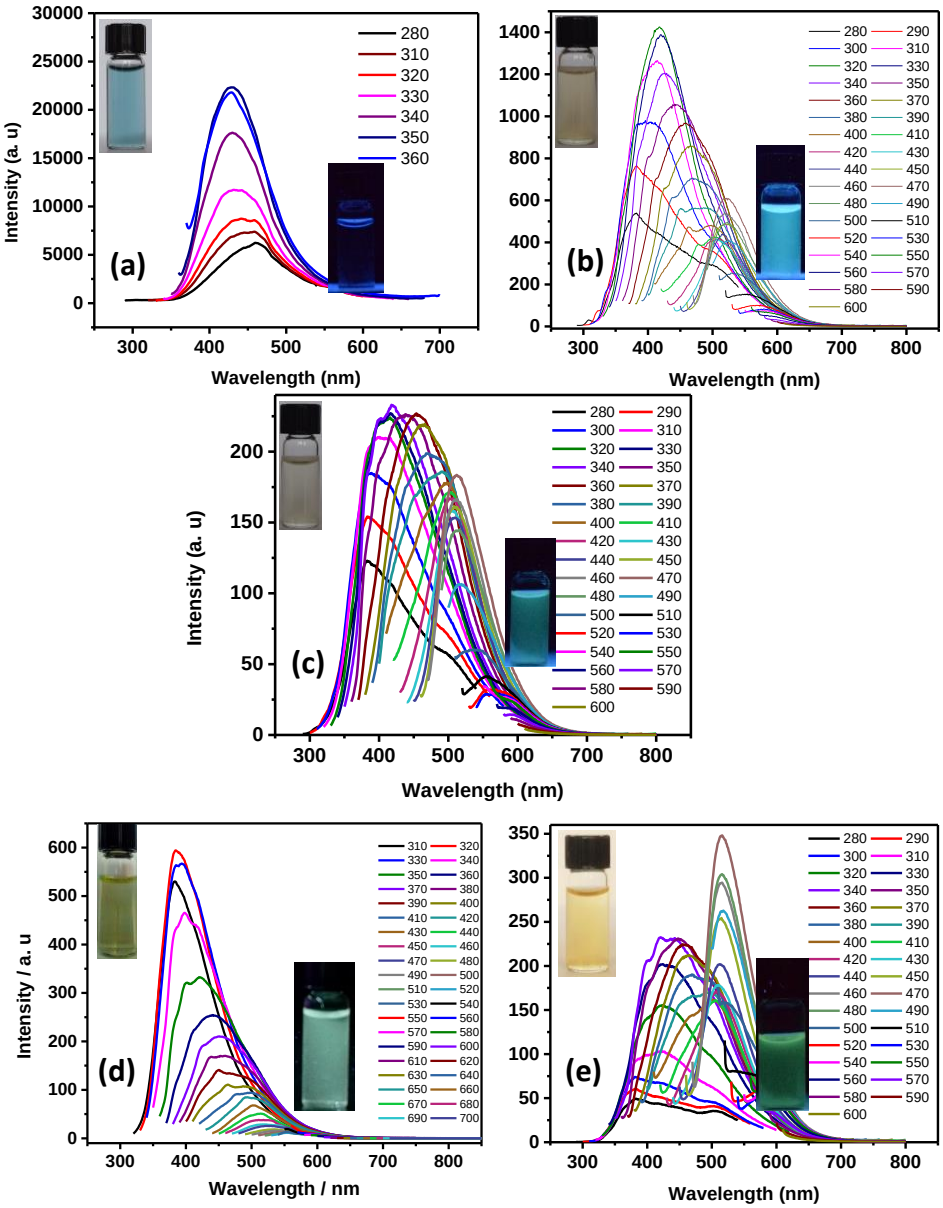

Figure 2.6: Emission spectra of nanomaterials obtained by hydrothermal reaction of MoS_2:NaOH concentration ratios of (a) 1:0, (b) 1:2, (c) 1:5, (d) 1:10 and (e) 1:20.. Insets show the photographs of respective solutions under visible and UV radiation. Excitation wavelengths are given as figure legends.

2.3.2 Origin of Broad and Excitation Dependent PL Emission

A detailed investigation composing the excitation, steady-state and time-resolved fluorescence studies were performed to decipher the excitation dependent emission of the MoS_2 nanomaterials. We chose the MoS_2 nanomaterial 1:10 sample

(MoS_2 QDNS) having the highest quantum yield, for this purpose. As we have already discussed, a continuous absorption due to the direct transition from the valence band to the conduction band of both QDs and low dimensional nanosheets was observed in case of MoS_2 QDNS. The direct recombination of these excited state electrons may be surmised to be responsible for the observed PL emission. We hypothesize that the broad, excitation dependent PL emission spectra of MoS_2 QDNS can be split into three regions. The 'lower wavelength emission' (referred as *region I*) which comes exclusively from small QDs (Qiao et al., 2015; Ren et al., 2015) and the 'moderate wavelength emission' (referred as *region II*) owing to the synergistic contribution of both QDs and the nanosheets (Xu et al., 2015; Haldar et al., 2016). Lastly, the 'higher wavelength emission' (referred as *region III*) arising solely from nanosheets (Nguyen et al., 2015; Liu and Chi, 2015; Mak et al., 2010). Note that, we dismiss the possibility of intersystem crossing due to the involvement of surface states, a phenomenon commonly observed in the case of carbon and semiconductor-based photoluminescence materials (Ganiga and Cyriac 2016).

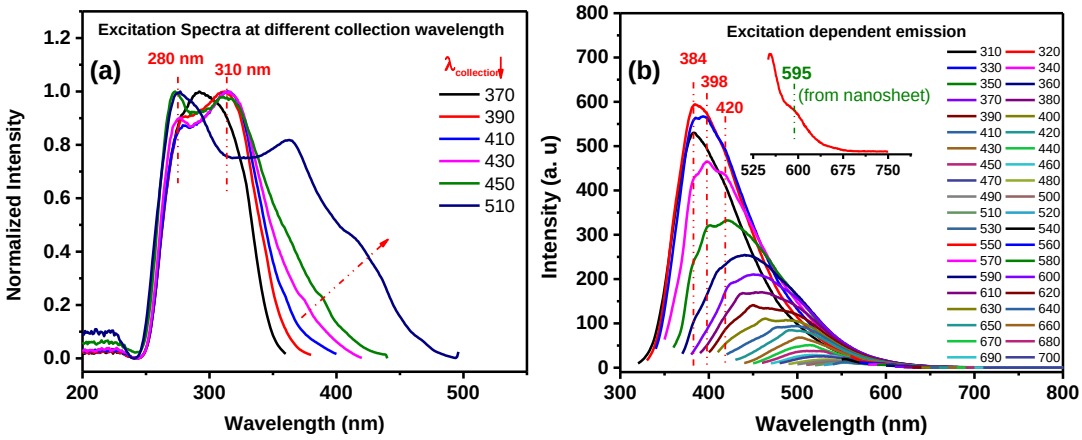

Figure 2.7: (a) Excitation spectra at different collection wavelength (b) PL spectra of MoS_2 QDNS at different excitation wavelengths. *Inset:* Shows a representative PL emission spectrum from the nanosheets excited at 540 nm.

Fluorescence excitation spectra recorded at various collection wavelength is given in Figure 2.7(a). The excitation spectra collected at lower emission wavelength (≤390 nm) is having two prominent bands around 280 and 310 nm, which is correlated

to the high energy absorption observed in the UV-visible absorption spectrum around 300 nm. The direct relaxation of these excitons from the conduction band to the valance band led to the emission at ~385 and ~400 nm, respectively. Since the energy required is high (~4 eV), these emissions must have emerged from the MoS_2 QDs. The assertion was supported by many reports in which the energy gap in the case of MoS_2 QDs was found to be ~4 eV (Qiao et al., 2015; Ren et al., 2015). This emission transition belongs to the region I of the emission spectrum in which the pure contribution from QDs is expected. On the other hand, when the collection wavelength was moved above 390 nm, a collection wavelength-dependent shoulder band was observed (shown with arrow), which could be assigned to the cooperative contribution from QDs and nanosheets. Since the energy required was <4 eV, this might have stemmed from low dimensional sheets (<100 nm) and larger sized QDs. This emission belongs to region II of the emission spectrum of MoS_2 QDNS. Finally, as can be observed in the inset of emission spectra (Figure 2.7 b), when MoS_2 QDNS was excited at lower energy photons, say above 530 nm, only a shoulder band centered at 595 nm was observed. The near red emission was attributed to the large-sized sheets (Ou et al., 2014). This radiative relaxation belong to the region III of the emission spectrum.

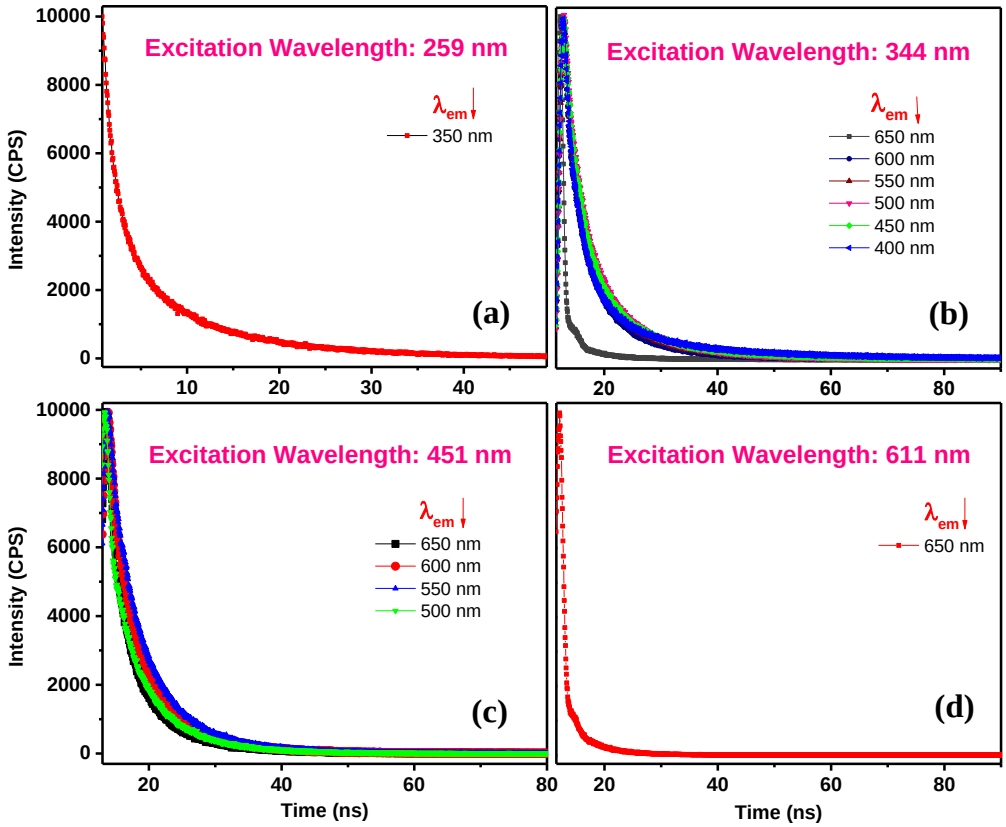

Figure 2.8: Time-resolved fluorescence spectra of MoS_2 QDNS at the different excitation wavelength (a) 259 nm, (b) 344 nm, (c) 451 nm and (d) 611 nm. The corresponding collection wavelengths at each excitation wavelength is given in the inset.

Time-resolved emission spectra at various collection wavelength under different excitation position (259, 344, 451 and 611 nm) has been recorded to further corroborate the hypothesis. Details of lifetime results are given in Table 2.1 and the corresponding decay profiles are shown in Figure 2.8. All decay curves were fitted for the best fit by keeping the numerical fitting parameter, χ^2 near to 1. It is well established that, the large MoS_2 nanosheets exhibit low carrier lifetime <1 ns, as the size of the nanosheets decreases, the lifetime of the photoexcited carrier increases and it reaches a maximum in case of QDs (Doolen et al., 1998; Ha et al., 2014; Ou et al., 2014; Mukherjee et al., 2016). Recently, Mukherjee et al., (2016) showed that small size (~2 nm) MoS_2 QDs were having longer carrier lifetime than big (~7 nm) QDs. This is a piece of direct evidence for the enhancement in temporal stability as the lateral size of the nanosheets shrinks. In the present case, the majority of the decay profiles were fitted

for triexponential function with the longest component (several nanoseconds), a moderate component (2–6 ns) and a fast, instrument response limited component (≤1.2 ns).

Table 2.1: Time-resolved fluorescence results of MoS_2 QDNS at different excitation wavelengths. τ_1, τ_2, τ_3, are the lifetime components. The amplitude values of the respective lifetime are given in bracket.

λ_{Ex} [nm]	$\lambda_{Collection}$ [nm]	τ_1 [ns]	τ_2 [ns]	τ_3 [ns]
259	350	1.7 (32.1%)	7.3 (45.0%)	**19.9 (22.8%)**
344	400	0.7 (25.0%)	4.5 (37.8%)	**19.1 (37.1%)**
	450	0.3 (53.4%)	2.2 (32.5%)	**15.6 (14.0%)**
	500	0.4 (38.5%)	2.0 (35.2%)	**13.6 (26.2%)**
	550	0.9 (38.3%)	5.5 (32.6%)	**12.4 (28.9%)**
	600	0.7 (26.3%)	4.0 (37.6%)	**10.5 (35.6%)**
	650	0.1 (79.8%)	2.4 (9.5%)	**8.8 (10.6%)**
451	500	1.5 (20.3%)	4.6 (55.5%)	**10.5 (24.1%)**
	550	1.2 (77.3%)	–	**9.8 (22.6%)**
	600	1.1 (77.0%)	–	**9.6 (22.9%)**
	650	1.1 (78.4%)	–	**7.6 (21.5%)**
611	650	0.1 (79.0%)	5.0 (20.9%)	–

The slowest- component with the highest lifetime value (around 19.9 nm) was observed for 259 nm excitation with a shortest emission collection (350 nm), where the smaller sized dots are expected to excite preferentially (see Table 2.1). When the excitation wavelength was increased (259 nm → 611 nm), the value of the longest lifetime was found to be decreased (from 19.9 to 7.6 ns). This observation indicates the increased involvement of larger sized QDs/nanosheets over the smaller ones when the excitation wavelength is red-shifted. As the collection wavelength was increased by keeping the excitation position constant, a decrease in the longer lifetime component value was noticed. For example, at 344 nm excitation, when the collection wavelength was increased from 400 nm to 650 nm, the value of longer lifetime was decreased from 19.1 ns to 8.8 ns. This reflects the fact that the contribution from larger sized

QDs/nanosheets will be highest in the higher wavelength region of the steady-state emission spectrum of MoS_2 QDNS. A constant decrease in the value of this lifetime component was not expected, if it involves the same excited state energy levels with different amounts of contribution or because of surface states (in this case, only amplitude values are presumed to alter with an invariable lifetime value). In addition, the contribution from the fastest component was maximum (~80%), when the collection wavelength was kept at 650 nm at all excitation wavelength (344, 451 and 611 nm). This lifetime is anticipated from larger nanosheets, which are expected to participate solely at the extremely high wavelength portion of the steady-state emission spectrum (*region III*) of MoS_2 QDNS. All these results clearly revealed that the observed broad and excitation dependent emission in the case of MoS_2 QDNS emerges from combined contribution from nanosheets and QDs involving quantum size effect, which alters the energy level and hence the concomitant emission. The results were attributed to the presence of multiple emissive states in the material.

2.4 Conclusions

MoS_2 nanosheets of varying layer thickness (bi, tri and more), a hybrid of MoS_2 nanosheets and quantum dots, are synthesized by the hydrothermal reaction from bulk precursors by following the same synthetic procedure, only by varying the concentration ratio of precursors used. The synthesis route is fast and facile, economically viable and does not require any harsh and dangerous chemicals. Detailed photophysical studies, including time-resolved fluorescence analysis of MoS_2 QDNS has been carried out to understand the origin of PL emission. The results were attributed to the presence of multiple emissive states in the material. Finally, we envisage that the present nanomaterials can be prospective candidates for bioimaging, chemical sensing and light-emitting applications. The crystalline sheets obtained can be made use of the electronic applications as well.

CHAPTER 3

SELECTIVE DETECTION OF DOPAMINE USING MoS_2 NANOHYBRID MATERIAL

In this chapter, we demonstrate the fluorescent-based chemical sensing applications of a hybrid nanomaterial composed of MoS_2 quantum dots dispersed over MoS_2 nanosheets (MoS_2 QDNS). Detailed optical and spectroscopic characterization of the sensor material has been conducted. The observation of fluorescent quenching of MoS_2 QDNS in the presence of dopamine, a neurotransmitter found in our body, prompted us to avail of this material as a selective sensor for its detection. A thorough spectroscopic and microscopic characterizations have been carried out in order to unveil the mechanism of quenching. Alongside, we have also demonstrated solid substrate-based sensing and real sample analysis using human blood sample in order to validate the utility of the sensor for practical applications.

3.1 Introduction

With the rapid development of different choices of analytical tools, sensitive and accurate quantification of various analytes of interest has been possible past few years. Dopamine (DA), a catecholamine neurotransmitter found in the mammalian central nervous system is one of the chemical species that caught enormous scientific attention for trace level detection (Lin et al., 2010; An et al., 2017)). The significance of DA detection mainly attributed to its association with several neurodegenerative disorders such as schizophrenia, Parkinson's disease, etc. (Segura- Aguilar et al., 2014; Li et al., 2005). Most of the theories formulated for the origin of these diseases involve aberrant oxidation of catecholamines, and even a picogram production of oxidized catecholamines can cause severe damage to the cells (Tse et al., 1975; Bisaglia et al., 2007). Therefore, unambiguous detection and exact quantification of DA and related species are highly appreciable.

The most common method employed for the determination of DA is electrochemical analysis, owing to the electroactive nature of DA. However, deposition of the polymer formed from the oxidation products of DA on the surface of the electrode can damage the electrode markedly (electrode fouling or poisoning) (Li et al., 2005). Besides, electroanalysis of DA is usually interfered by ascorbic acid and uric acid, as these species have oxidation potentials close to that of DA, resulting in the overlaying of voltammetric responses (Lin et al., 2010). Other approaches for the quantitative determination of DA include high-performance liquid chromatography, mass spectrometry, capillary electrophoresis donor-acceptor etc. (Carrera et al., 2007). Yet, the requirement of sophisticated instruments, time-consuming and complex methodology and the expensive nature of these analytical techniques demands the formulation of an easy, economically viable and fast response technique. Considerable reports are available which take advantage of the simplicity of calorimetric analysis. However, the colorimetric methods generally have low sensitivity. A fluorescence method is highly appealing as it can offer both high sensitivity and simplicity for sensing applications.

Several reports are available on the quantitative determination of DA, devoting the fluorescent emission from nanomaterials. For example, Zhao et al. (2017) designed a turn-off sensor for DA using WS_2 quantum dots through polymerization effect of DA. Another turn-off sensor comprised of citrate protected CdSe nanocrystals were reported by Ma et al. (2005). The turn-off was achieved by trapping of excitons. Highly sensitive determination of DA was realized using silicon nanoparticle prepared from (3-aminopropyl)trimethoxysilane (APTMS) (Zhang et al., 2015b). Förster resonance energy transfer (FRET) from silicon nanoparticle to oxidized DA molecules are responsible for the quenching of fluorescent emission from silicon nanoparticle. Electron transfer of DA to adenosine-capped CdSe/ZnS quantum dots (QDs) were benefitted for the fabrication of yet another turn-off sensor, with a limit of detection of 29 nM (Mu et al., 2014). Motivated by the success of these researches, on the quantitative determination of DA in nanomolar level, we modeled a strategy for the

detection of DA utilizing fluorescent properties of nanoparticles with high selectivity along with satisfactory sensitivity.

Recently 2D layered materials in general and MoS_2 based nanomaterials in particular have been gaining huge attention due to their intriguing properties. As an emerging material, various reports are available on the electrochemical applications of MoS_2-based nanomaterials. The discovery of photoluminescence emission from mono or bilayered MoS_2 sheets by two independent research groups Spendiani (2010) and Mak (2010) paved a strong way for their optical and optoelectronic based applications as well. One of the key aspects of PL emission from these materials is the correlation of dimension with the emission position. A sheet with lateral dimension in the range of micrometers is reported to emit in the red region, whereas reducing the lateral dimensions in the nanometer regime resulted in the emission in the blue region of the spectra. In this chapter, we discuss the fabrication of a nanosensor by taking advantage of the luminescence properties of MoS_2 nanomaterials. A nanohybrid material comprised of MoS_2 quantum dots dispersed over MoS_2 nanosheets (MoS_2 QDNS) was synthesized using a hydrothermal route from MoS_2 powder with the assistance of aq. alkali. The fluorescent emission from MoS_2 QDNS in neutral as well as alkaline pH is found to be quenched in the presence of DA, linearly. Thorough spectroscopic studies were portrayed for supporting the mechanism of quenching suggested. We have also demonstrated a visual detection strategy based on a solid substrate and quantification of DA in the real sample was also carried out using human blood samples.

3.2 Experiments and Methods

3.2.1 Reagents and Materials

MoS_2 powder, dopamine (DA), tyrosine (Tyr), adenine (Ade), were purchased from Sigma-Aldrich, USA. Fructose (Fru), creatinine (Cre), galactose (Gal), thymine (Thy) and uric acid (UA) were purchased from SRL Chemicals Pvt. Ltd, India. Cadmium chloride ($CdCl_2$), tryptophan (Try), tyramine (Tym), were purchased from Alfa Aesar, UK. Lead nitrate ($PbNO_3$) was obtained from Otto Chemicals, India.

Cobalt sulphate ($CoSO_4$), tin chloride ($SnCl_2$), silver nitrate ($AgNO_3$), ferrous sulphate ($FeSO_4$), nickel sulphate ($NiSO_4$), calcium carbonate ($CaCO_3$), aluminum nitrate $Al_2(NO)_3$, copper sulphate ($CuSO_4$), sodium carbonate($NaCO_3$), potassium chloride (KCl), ferric chloride ($FeCl_3$), magnesium sulphate ($MgSO_4$), zinc Sulphate ($ZnSO_4$) sodium hydroxide (NaOH), hydrochloric acid (HCl), glucose (Glu), glutathione (GSH), ascorbic acid (AA), lysin (Lys), and glycin (Gly) were from Merck, India. Double distilled water was used throughout the experiments. All reagents purchased were of analytical grade and used without further purification.

3.2.2 Instrumentation

UV-visible experiments were carried out using a Carry-100 UV-visible spectrophotometer. Fluorescence measurements were performed using FluoroMax-4C spectrofluorometer (Horiba Instruments, USA). The experiments were conducted by fixing excitation and emission slit width at 5 nm with an integration time of 0.1 ns. Time-resolved fluorescence measurements were executed using time-correlated single-photon counting (TCSPC). The excitation wavelength was fixed at 344 nm and decay profile were collected at 415 nm (laser pulse width <1ns). FTIR spectra were recorded in a Spectrum 100T Perkin-Elmer FTIR spectrometer in transmission mode using KBr pellet. Mass spectra was recorded in a Bruker Q-TOF (COMPACT) mass spectrometer. Methanol-water mixture (50:50) was used as the electrospray solvent. Zeta potential measurements were performed using Zetasizer Nano ZS series; Malvern Instruments, Malvern, UK. pH measurements were taken using EUTECH instruments' pH meter.

3.2.3 Synthesis of MoS_2 QDNS

The details of the synthesis were given in Chapter 2. Briefly, 150 mg of MoS_2 bulk powder was mixed with 374.8 mg of NaOH so as to obtain a molar ratio of 1:10 and taken in 10 mL of water in a Teflon-lined autoclave. The hydrothermal reaction was carried out by keeping this reaction mixture for 8 h at 220 °C. The resultant solution containing nanomaterials were centrifuged and filtered using a Millipore filter set-up with a pore size of 0.22 μm. A light-yellow solution having a pH of 13 was

obtained and 2.5 mL of this MoS_2 QDNS solution was utilized as the sensor solution in all experiments.

3.2.4 Selectivity Study using MoS_2 QDNS Sensor solution

The selectivity of the present sensor solution was tested by adding a 100 μL, 1 mM solution of various analytes. Several metal ions such as Na^+, K^+, Mg^{2+}, Al^{3+}, Sn^{2+}, Pb^{2+}, Ca^{2+}, Fe^{2+}, Fe^{3+}, Cu^{2+}, Zn^{2+}, Co^{2+}, Ni^{2+}, Ag^+ and Cd^{2+} and biologically active small molecules such as amino acids and peptides such as glycine, lysine, creatinine, thymine, adenine, glutathione, tyramine, tryptophan and tyrosine and carbohydrates such as glucose, fructose and galactose we aimed for selectivity experiments. Also, common interferents of DA detection such as ascorbic acid (AA) and uric acid (UA) were taken together into the sensor solution and checked the interference study. The excitation wavelength used was 330 nm for all the sensing experiments.

3.2.5 Real sample analysis

For real sample DA detection, blood samples were collected from a healthy volunteer and diluted one thousand-fold before analysis, with the addition of non-coagulating agents. Spiked samples were prepared by adding known concentrations of DA into this diluted blood sample. Aliquots of these solutions were taken in a cuvette containing 2.5 mL of MoS_2 QDNS solution and mixed thoroughly. The PL emission spectra was collected at an excitation wavelength of 330 nm, each time.

For a test strip assay, 10 μL of MoS_2 QDNS was drop-casted on a thin layer chromatography (TLC) plate and kept for drying naturally. DA solution was then added drop-by-drop over these spots on the TLC plate. The response was discerned after an incubation period of 5 min, using a UV light source (365 nm, 8 W). All experiments were performed at room temperature.

3.3 Results and Discussions

3.3.1 Microscopic and Optical Characterization of MoS_2 QDNS

The synthesis of sensor material has been realized by the intercalation of Na^+ ions and the oxidative cutting of MoS_2 bulk sheets under hydrothermal conditions leading to the formation of MoS_2 QDs and the low dimensional nanosheets. The microscopic evaluation uncovers the distinctive morphology of MoS_2 QDNS, as can be seen in Figure 3.1.

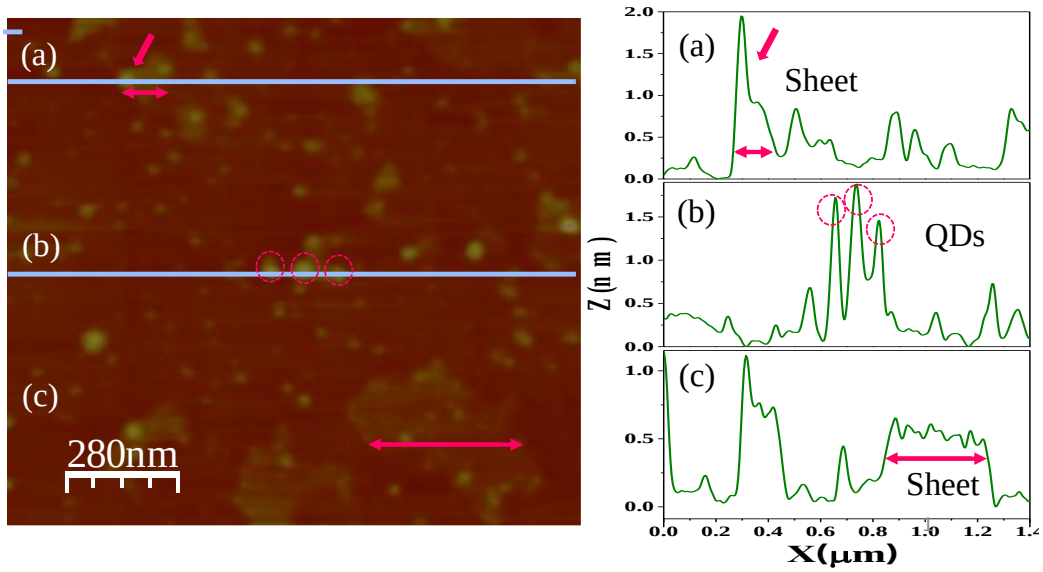

Figure 3.1: AFM image of MoS_2 QDNS with three height profiles drawn at different positions (a, b and c) depicting a sheet thickness ranging from 0.6 to 1.0 nm that corresponds to monolayer with a lateral dimension of spanning from 100 to 400 nm. The sharp peaks with a height of 1-2 nm correspond to the QDs present over the sheets.

The QDs are found to be dispersed uniformly over the nanosheets, with an average of size 2.0 ± 0.76 nm. Whereas, the sizes of the nanosheets are distributed in a random fashion, with most of the sheets fall below 100 nm in lateral size. Possibility for the generation of height profiles of nanomaterials is one of the advantages of AFM micrographs, over TEM analysis. The thickness of a monolayer sheet of MoS_2 is in the range of 0.6 nm. Therefore by measuring the thickness of the sheets of MoS_2 QDNS,

one can directly gauge the number of layers present. The height of the sheets at various locations of AFM images resulted in the generation of a histogram showing thickness distribution with two ranges: 0.5-0.8 nm and 1.2-1.5 nm (Figure 3.2). These height profiles show that there are mono and bilayers of sheets present in the nanohybrid materials. Most of the established strategies for the synthesis of MoS_2 nanomaterials resulted in multi-layered sheets with larger lateral dimensions (>1 μm). Hence, our approach is useful for the synthesis of highly stable low dimensional nanohybrid of MoS_2 with precisely controlled layer thickness.

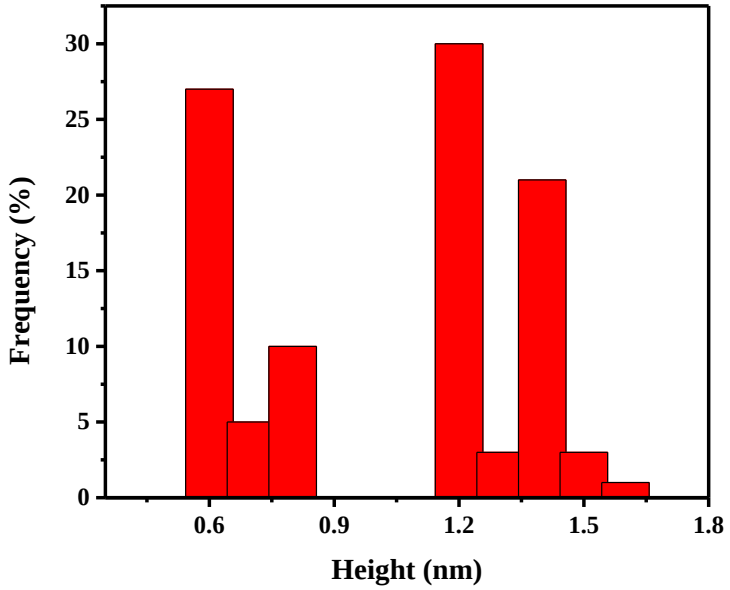

Figure 3.2: The height distribution histogram of sheets obtained by measuring the height of the sheets taken from ~100 locations of various AFM images.

The crystal structure of MoS_2 QDNS was deliberated by X-ray diffraction (XRD), using MoS_2 bulk powder as reference. The diffraction patterns of MoS_2 powder are indexed using ICDD Ref. no. 04-003-3374. The absence of any particular XRD peak indicates the non-availability of interactions for the appearance of that specific peak. All the peaks of MoS_2 QDNS are very weak and subdued as seen in Figure 3.3b, indicating poor crystallinity of the material compared to its bulk counterpart. Besides, the peak at 14.4^o which corresponds to (002) reflection plane of the 2H- MoS_2 directly, indicates the lateral size and number of layers. A rather broad and feeble peak at this

position for MoS_2 QDNS stipulates weaker interlayer interaction. This observation strongly endorses the existence of mono and bilayered nanosheets, as is evident from AFM analysis.

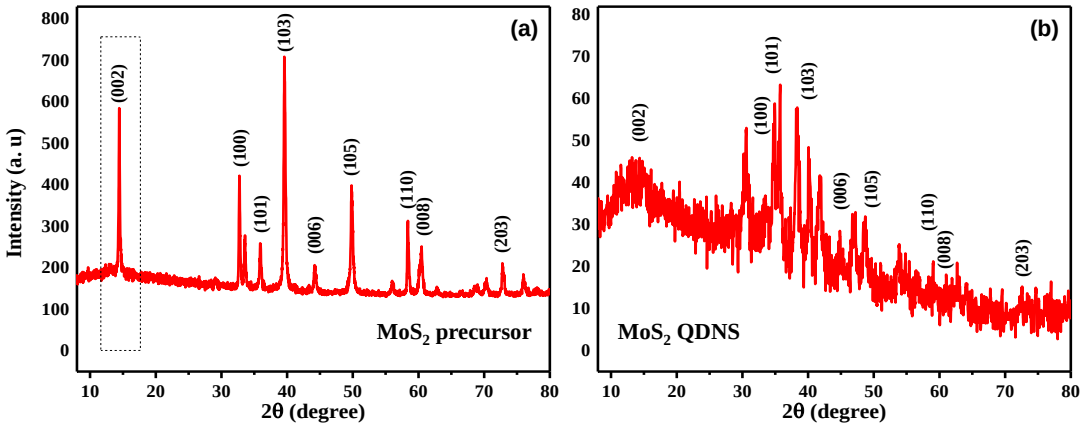

Figure 3.3: XRD patterns of MoS_2 bulk precursor (a) and MoS_2 QDNS (b). Peaks of MoS_2 QDNS, are of less intensity compared to MoS_2 powder. Broad and feeble peak from (002) plane indicate the weak interlayer interaction.

The chemical composition and oxidation states of MoS_2 QDNS have been unearthed by high-resolution X-ray photoelectron spectral analysis (HR-XPS). The HR-XPS of Mo shows two peaks corresponding to Mo^{4+} $3d_{3/2}$ and Mo^{4+} $3d_{5/2}$ at binding energy values 229.1 and 232.2 eV, respectively, along with a small peak at 227. 9 eV for S 2s. This result indicates the dominance of +4 oxidation state for Mo in MoS_2 QDNS (Figure 3.4 b). Whereas multiple peaks were obtained after fitting HR-XPS peaks for S. Peaks for S $2p_{3/2}$ and S $2p_{1/2}$ were observed at 160.4 and 161.6 eV (Figure 3.4 c). The sulphur bonded to Mo having -2 oxidation could be the origin of these peaks. Whereas, two more peaks in the higher binding energy region can be seen at 165.5 and 166.5 eV (Figure 3.4 d). The oxidation of surface sulphur during the hydrothermal reaction can be the reason for the emergence of these two additional peaks. Moreover, the absence of 1T peaks in the survey scan spectra of MoS_2 QDNS indicates that there is no phase transformation during hydrothermal synthesis (Figure 3.4 a). Further, the quantitative analysis of the peak intensity of Mo 3d and S 2p gave rise to an atomic ratio of Mo to S nearly 1:2 indicating the retention of stoichiometry even after undergoing rigorous hydrothermal reaction conditions.

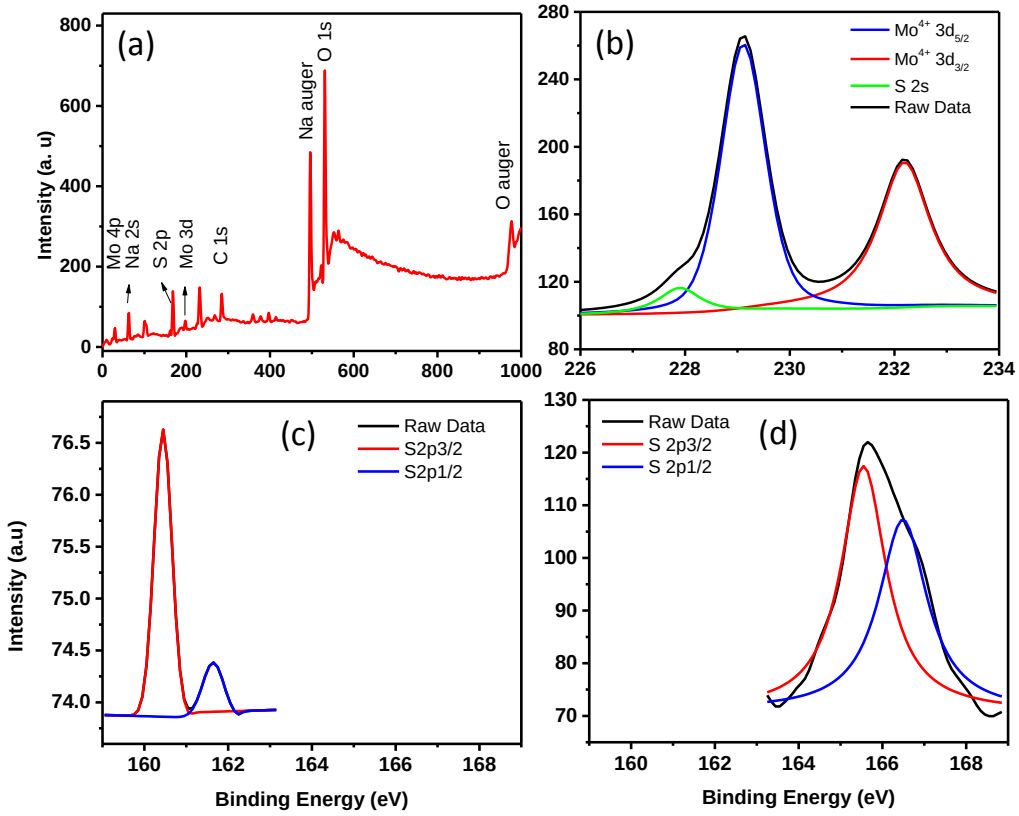

Figure 3.4: a) Survey scan spectra of MoS_2 QDNS. Deconvoluted high-resolution XPS spectra of (b) Mo 3d (c) S 2p corresponding to sulphur bonded to Mo and (d) peaks corresponding to oxidized sulphur.

Lateral dimensions of nanosheets in the present MoS_2 QDNS are smaller than several reported MoS_2 nanosheets of size >1 μM in size (Wu, 2014). Hence, the photophysical behavior of the present hybrid material is expected to be different, as compared to that of the larger nanoflakes (Dong, 2016). The UV-visible absorption spectrum of MoS_2 QDNS (Figure 3.5) exhibits a continuum from 400 till ~600 nm. This could be assigned to the blue-shifted B and A excitonic peaks from underlying low dimensional nanosheets. Other two higher energy absorption bands at ~300 and ~330 nm must have been aroused from the transition between deep valence band to the conduction band in MoS_2 QDs due to the quantum size effect (Wang et al., 2013; Ou et al., 2014). A continuum of absorption is observed in both UV and visible part of the

electromagnetic spectrum as both MoS_2 QDs and underlying nanosheets in MoS_2 QDNS has a broad size distribution. Otherwise, one would expect a distinct sharp absorption feature.

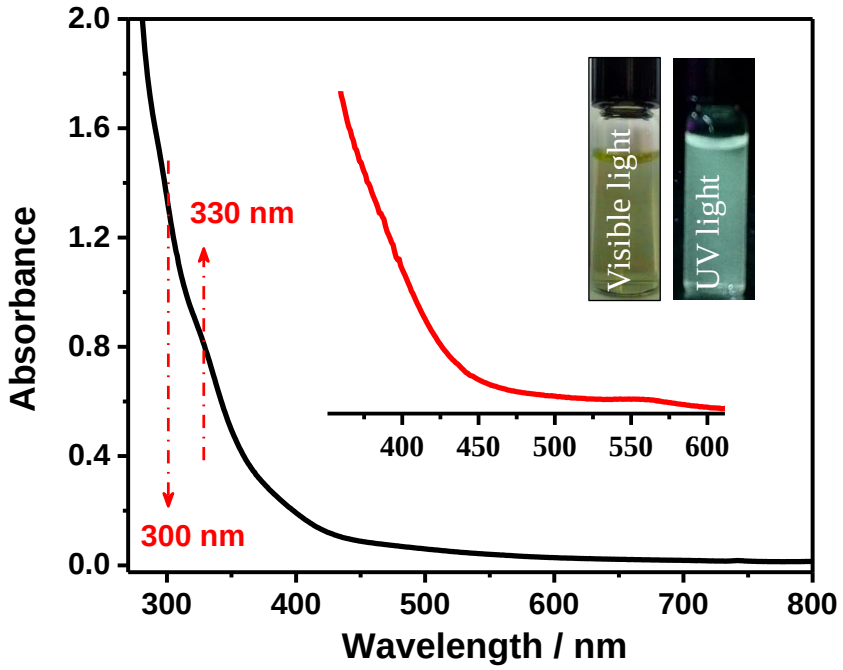

Figure 3.5: UV-Visible absorption spectrum of MoS_2 QDNS. A magnified view of the absorption in the range of 350-600 nm is shown as an inset. Photographs of MoS_2 QDNS solution under visible and UV light are presented as inset.

MoS_2 QDNS displayed a broad, excitation dependent fluorescence emission response (Figure 3.6) covering a large region of the visible spectrum, owing to polydispersity of the system, as reported by Wang (2013), Ou (2014), Haldar (2016), Wang and Ni (2014), etc. The broad and excitation dependent PL was mainly emerged by the synergistic contribution from both MoS_2 QDs and the underlying nanosheets due to quantum size effects. A continuous absorption due to the direct transition from the valence band to the conduction band of both QDs and low dimensional nanosheets was observed in the case of MoS_2 QDNS. The direct recombination of these excited state electrons may be surmised to be responsible for the observed PL emission.

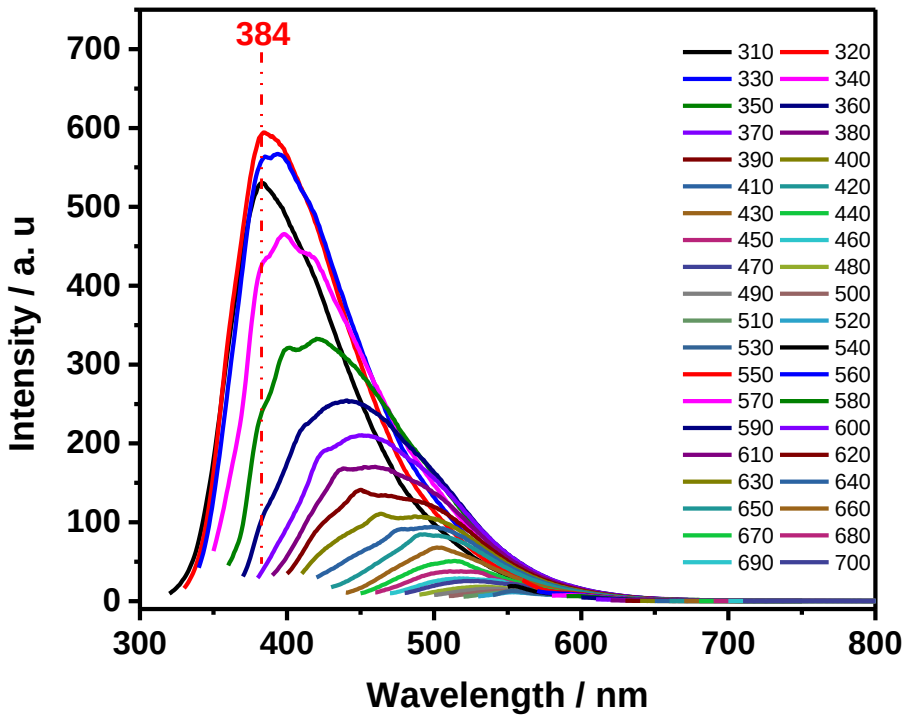

Figure 3.6: PL spectra of MoS_2 QDNS at different excitation wavelengths

Detailed time-resolved emission spectral studies were also carried out and the results obtained were given in Figure 3.7. The decay curve was fitted for the best fit by keeping the numerical fitting parameter, χ^2 near to 1. It is well established that, the large MoS_2 nanosheets exhibit low carrier lifetime <1 ns, and as the size of the nanosheets decreases, the lifetime of the photoexcited carrier increases and it reaches a maximum in case of QDs (Ou et al., 2014; Mukherjee et al., 2016; Doolen et al., 1998, Ha et al., 2014) Recently, Mukherjee et al. (2016) showed that small size (~2 nm) MoS_2 QDs were having longer carrier lifetime than big (~7 nm) QDs. This is a piece of direct evidence for the enhancement in temporal stability as the lateral size of the nanosheets shrinks. In the present case, the decay profile was fitted for triexponential function with the longest component, a moderate component and a fast, instrument response limited component (≤1.2 ns).

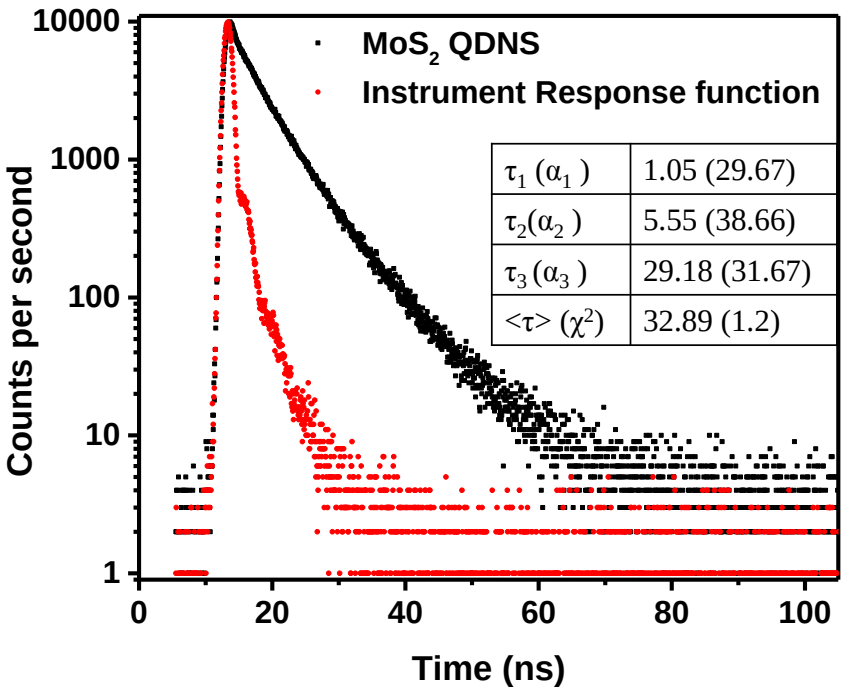

Figure 3.7: Lifetime exponential decay curve of MoS_2 QDNS

Another salient feature of the present MoS_2 QDNS is its extraordinary stability in aqueous media. Even after 7 months of preparation, only 28% of PL intensity of MoS_2 QDNS was lost, depicting the extra-ordinary stability of the hybrid structure (Figure 3.8 a). The morphology of MoS_2 QDNS was found to be intact as revealed in the TEM image (inset of Figure 3.8 a) recorded after 4 months. Fluorophores of having high photostability is demanded in fluorescence imaging and sensing applications. Owing to the poor photostability of modern dyes, the carbon and semiconductor-based fluorescent materials have opted in recent times. Therefore, stable fluorescence chemical sensors are feasible with the present QDNS. The aqueous solution of MoS_2 QDNS was irradiated with UV light (365 nm, Power: 8 W) for different time intervals and the PL intensity was subsequently recorded (Figure 3.8 b). Approximately 76% of PL intensity of MoS_2 QDNS was retained even after 14 h of continuous irradiation, which reflects the high photostability of present nanohybrid, a promising alternative for bio-imaging and sensing applications.

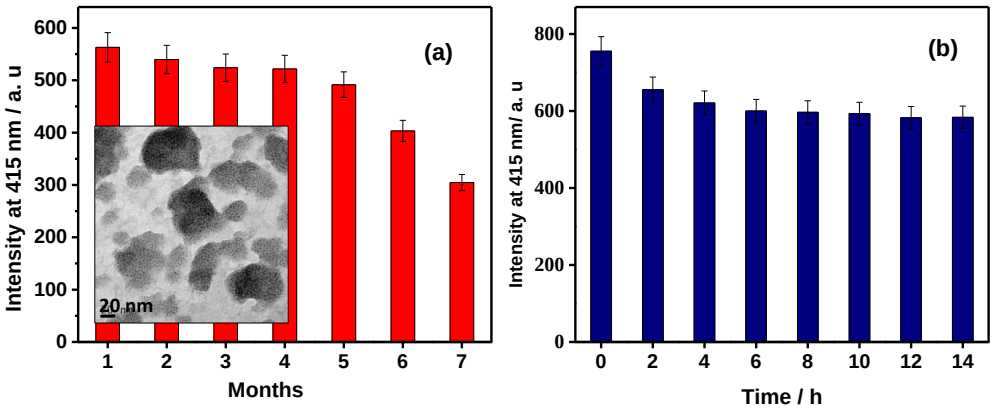

Figure: 3.8: (a) and (b) are the stability of MoS_2 QDNS under ambient conditions and UV light, respectively. Inset of (a) shows the TEM image of MoS_2 QDNS recorded after four months of preparation.

3.3.2 MoS_2 QDNS as a Sensor

The purified MoS_2 QDNS shows excellent fluorescence emission over a long range of excitation wavelengths from 280 nm to 600 nm. Of these, we chose 330 nm excitation, where the emission intensity was maximum, which ensures high sensitivity for the sensor. The pH of the sensor solution was 13. The emission of MoS_2 QDNS was monitored upon addition of different concentrations of the analytes. As Figure 3.9 represents, a monotonous decrease in the PL intensity of MoS_2 QDNS was observed.

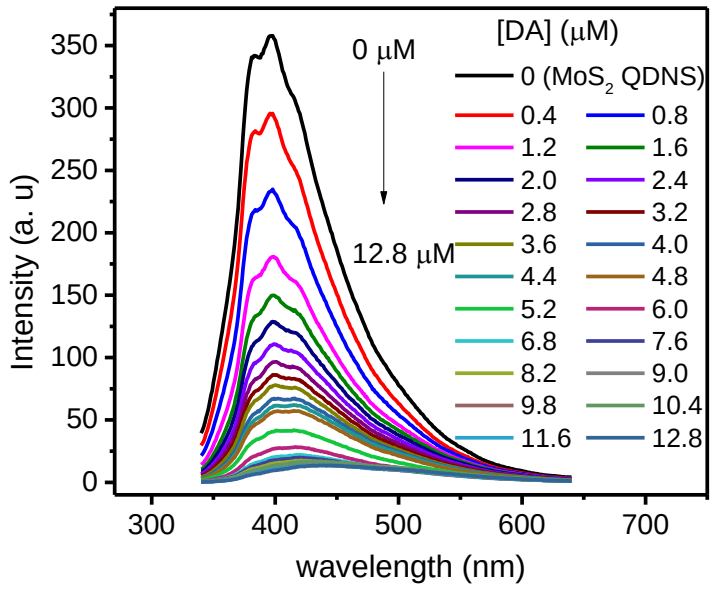

Figure 3.9: Fluorescence response of MoS_2 QDNS with various concentrations of DA.

The response of PL emission of MoS_2 QDNS was found to be linear as can be observed in Figure 3.10 a. It is apparent that the system can respond to the presence of dopamine (DA) at a concentration as low as 2.5 nM (Figure 3. 10 b), with two linear range from 2.5 nM to 5.0 µM and 5 µM to 10.4 µM concentrations. The fluorescence quenching of MoS_2 QDNS follows a typical Stern-Volmer type equation;

$$F_0/F = 1 + K_{sv}[DA]$$

Where F and F_0 are the PL intensity of MoS_2 QDNS in the presence and absence of DA, respectively and K_{sv} is the Stern-Volmer quenching constant. The Ksv values for first linear range (2.5 nm to 5 µM) was 1.149×10^6 M^{-1} (R^2 = 0.9891) and for the linear range from 5 µM to 10.4 µM was 7.724×10^6 M^{-1} (R^2 = 0.9800). The system has reached a saturation limit at 11 µM concentration of DA. Two linear ranges surmised to arise from multiple quenching pathways. The chemistry of these quenching mechanisms and the effect of pH in the PL quenching of MoS_2 QDNS together with selectivity studies are discussed in the forthcoming sections. The limit of detection (LOD) was gauged to be a low value of 0.9 nM (S/N = 3), which is comparable to the LOD value reported so far (Zhang et al., 2015b).

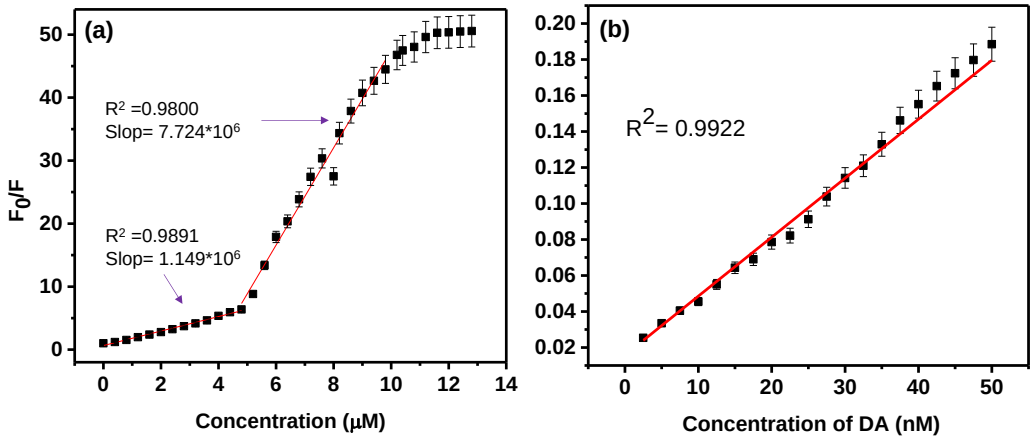

Figure 3.10: a) Dynamic range of the sensor. F_0 and F are the fluorescence intensity before and after the addition of analyte, respectively. Each trial has been repeated three times and deviation from the mean value is represented as error bars. b) Plot obtained for the quenching of PL intensity of MoS_2 QDNS by nanomolar concentrations of DA (2.5-50 nM)

3.3.3 Mechanism of PL Quenching

Several reports are available, where DA was selectively detected using various fluorescence probes with the aid of different mechanisms such as electron transfer, FRET, etc. (Ban et al., 2015; Zhang et al., 2015b). To unveil the mechanism of PL quenching of MoS_2 QDNS by DA, a detailed photophysical characterization has been conducted. Changes in the surface morphology, charge or functionality of the reacting moieties are believed to alter the course of their optical properties. Therefore, absorption spectra can show the possibility of interaction of MoS_2 QDNS with DA in alkaline media. As shown in Figure 3.11 a, the absorption spectra of MoS_2 QDNS at different DA concentration shows a constant increase in the absorption features around 280, 310, 350 and 470 nm. Since it is widely acknowledged that, DA has only one absorption band ~280 nm (Zhang et al., 2015b; Mu et al., 2014; Zhao et al., 2013) (Figure 3.11 b), the appearance of these peaks attest the formation of different moieties, during the interaction.

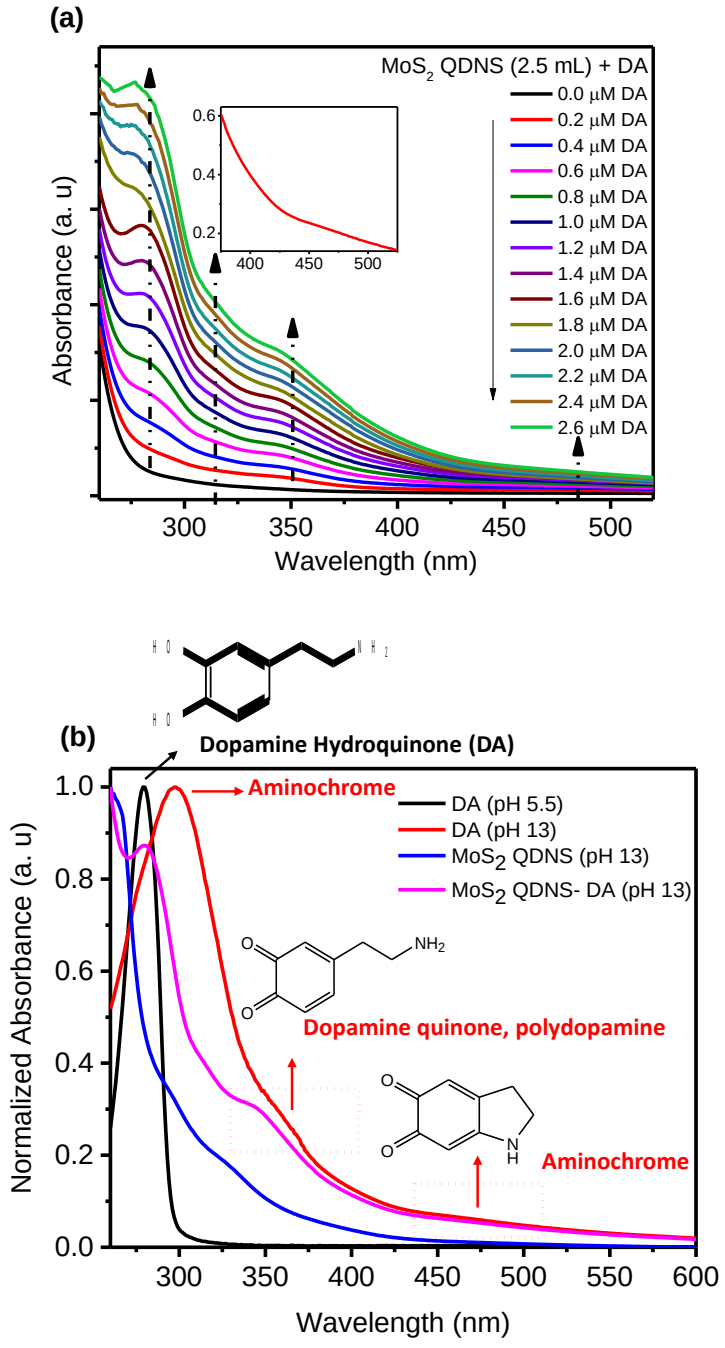

Figure 3.11: (a) UV-visible absorption spectra of MoS_2 QDNS (black) and MoS_2 QDNS at different concentrations of DA (0.2 µM to 2.6 µM). Inset shows the zoomed portion of one spectrum from 380 to 520 nm (b) Absorption spectra of DA and MoS_2 QDNS with and without DA at different pH.

Dopamine chemistry is a far studied area by many researchers, especially in physiological conditions (Segura-Aguilar et al., 2014). DA is widely known to undergo

oxidation at basic pH in the presence of oxygen or in the presence of oxidizing agents (Wei et al., 2010). Since the pH of the present sensor was 13, oxidation of DA is an inevitable possibility. As reported earlier, the oxidation of DA leads to many intermediate oxidation products and ultimately stretch to polydopamine (Figure 3.13). We made use of absorption spectroscopy along with mass spectrometry (MS) to identify the reaction products formed during the interaction of DA with MoS_2 QDNS. Figure 3.11 b depicts the absorption spectra of DA in various experimental conditions. As already stated, DA in hydroquinone form (before oxidation, acidic pH) has only one sharp band at 278 nm, whereas in alkaline media many peaks were surfacing. It is reported that peaks at 310 nm and 470 nm are due to the form known as aminochrome (Bisaglia et al., 2017; An et al., 2017; Dagnino-Subiabre et al., 2000). We have also observed these absorption features and can attribute to the presence of aminochrome in MoS_2 QDNS solution. Another peak around 350 nm can be conferred to another oxidation product, dopamine quinone (Madrakian et al., 2006) which is also found to be increasing with the increase in the concentration of DA.

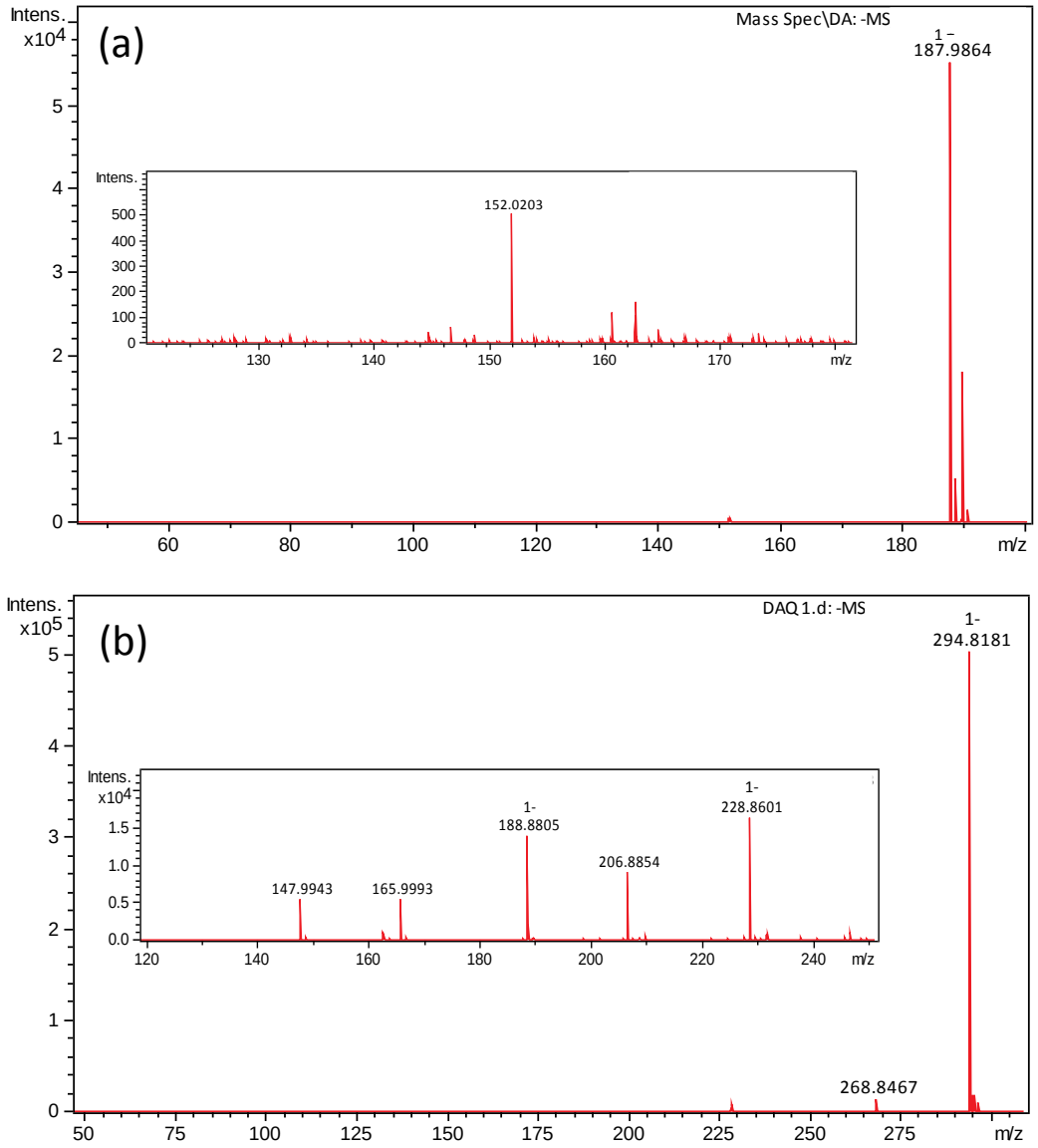

Figure 3.12: Mass spectra of (a) DA in acidic media (pH 5.5) showing $(M-H)^-$ peak for dopamine hydrochloride (m/z 188) and that of dopamine (m/z 152) and (b) dopamine in alkaline media (pH 13) showing peaks for oxidized forms of DA such as aminochrome (m/z 148) and its dimer form (m/z 295). All MS spectra were collected in negative ion mode.

In par with UV-visible studies, electrospray ionization mass spectrum (ESI-MS) further confirm the formation of these molecular species (Figure 3.12 a and b). A micromolar solution of DA was prepared in water. Aliquote of this solution was mixed with 2 mL of 1:1 methanol-water solution and spectra were recorded. The mass spectrum (MS) of DA (prepared from commercial DA at pH ~5.5) contains parent ion

peak at m/z 188, and another peak at m/z 152 corresponds to dopamine hydrochloride $(M+Cl)^-$ and dopamine $(M-H)^-$, respectively. The MS spectra for dopamine in alkaline media mainly contained the peaks corresponds to $(M-H)^-$ species of aminochrome (m/z 148), and the dimer, which formed from 5,6-dihydroxyindole (m/z 295). The peaks corresponding to dopamine hydrochloride and dopamine were absent in this case. The scheme of oxidation pathways of DA and the corresponding molecular weight of ions is given as Figure 3.13 (Xu et al., 2012; Wang et al., 2015; Li et al., 2006; Bisaglia et al., 2007; Ding et al., 2016; Turcheniuk et al., 2013)

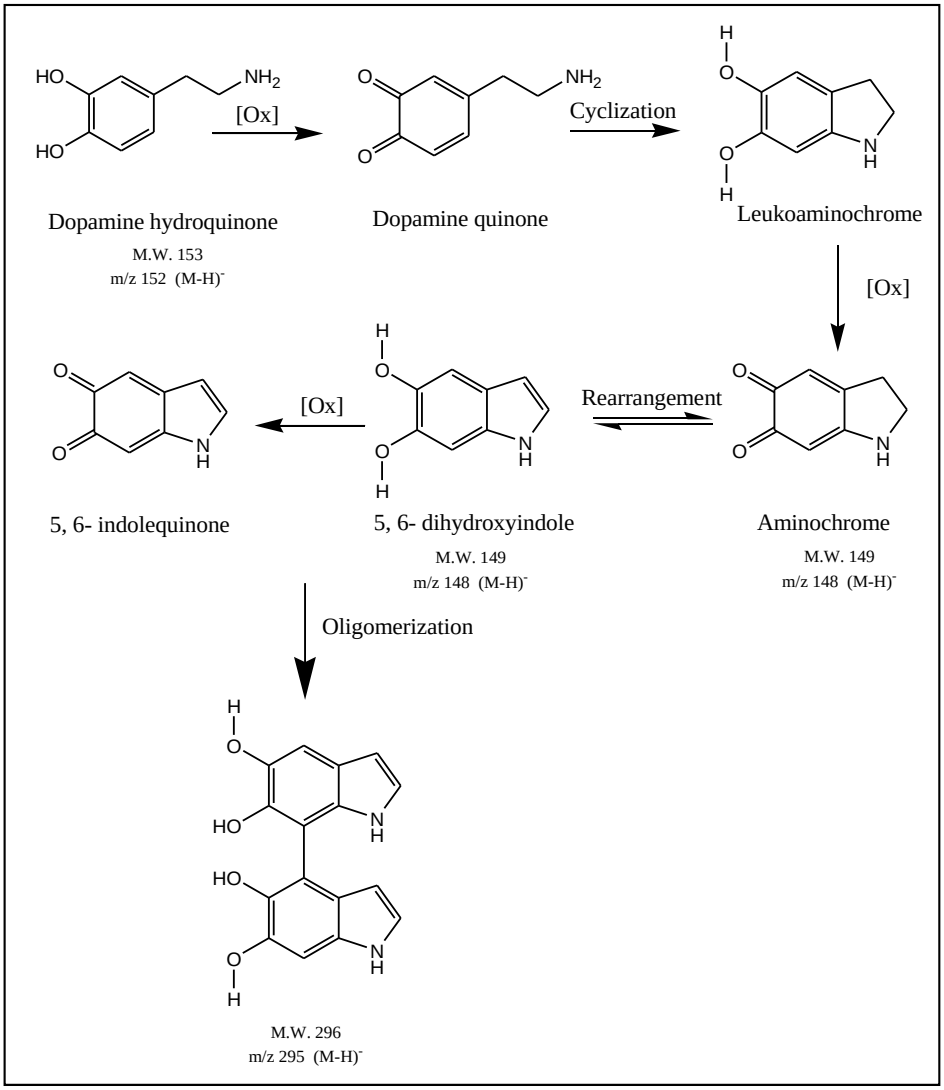

Figure 3.13: Oxidation pathway of dopamine

FTIR studies also offer information about the formation of DA derivatives at higher pH (Figure 3.14). At pH 13, a new absorption feature has emerged at 1630 cm^{-1}, which may correspond to >C=O of aminochrome/quinone form. Apart from this, NH_2 peak at 3245 cm^{-1} which was present in the case of DA at pH 5.5 vanished at higher pH, further support the formation of aminochrome/quinone form (Ankireddy et al., 2015). This is attributed to the absence of a primary amine group in the case of aminochrome species. Another observation was the large shift of 1343 cm^{-1} (pH 5.5) to 1353 cm^{-1} (pH 13). This position is assigned to ring –O-H bending mode and the restricted hydrogen bonding in the case of DA derivative resulted in the blue shift. (Lopez et al., 2011; Chen et al., 2011b).

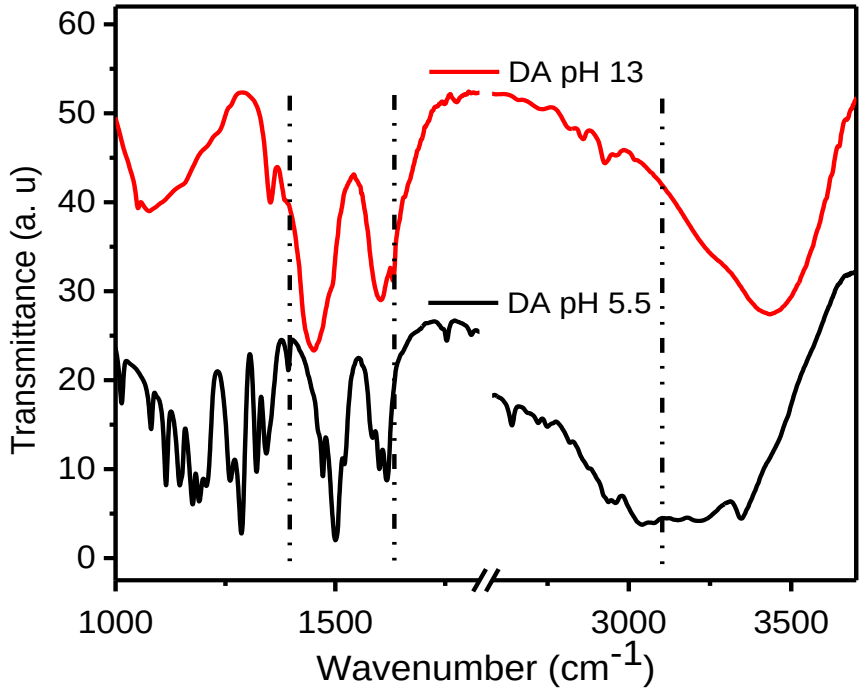

Figure 3.14: Comparative IR spectra of DA at pH 13 and DA as such (pH 5.5).

Corroborating the pieces of evidence given above, the evolution of new absorption features in MoS_2 QDNS-DA solution can be surmised to the increase in the concentration of oxidized forms of DA. Since there was no change in the absorption features of MoS_2 QDNS–DA system (pH 13) compared to the individual absorption

spectra of MoS_2 QDNS and DA, we can rule out the possibility of ground-state complex formation between MoS_2 QDNS and DA. However, the formation of oxidized products of DA, kindled the interest to quantify the percentage of conversion of DA into its oxidized forms. For this purpose, we have recorded the absorption spectra of DA upon incremental addition of DA from 0 to 13 µM to water in two pH conditions; pH 5.5 and 13. The concentration of DA in pH 5.5 is taken as standard, as there is no oxidation and calculated the concentration of aminochrome (AC) and other oxidized products (Ox) at a pH of 13 using molar absorption coefficient of DA and AC (2670 $M^{-1}cm^{-1}$ at 280 nm and 3058 $M^{-1}cm^{-1}$ at 474 nm, respectively) (Baez et al., 1997; Zafar et al. 2006). A graph is plotted taking an actual concentration of DA in the X-axis and % concentration of DA as Y axis (13 µM concentration of DA as taken as 100%) (Figure 3.15). As the concentration of DA increases in alkaline pH, it is notable that, amount of other oxidized products is more compared to the concentration of both DA and AC. Moreover, a close examination of % formation of aminochrome alone is given as Figure 3.15 b. The nature of the increase in the concentration of aminochrome is consistent with the nature of the calibration curve obtained in the sensitivity study. So, we assume a direct connection between the increases in the concentration of AC which reflects in the absorption spectra around 470 nm and quenching mechanism.

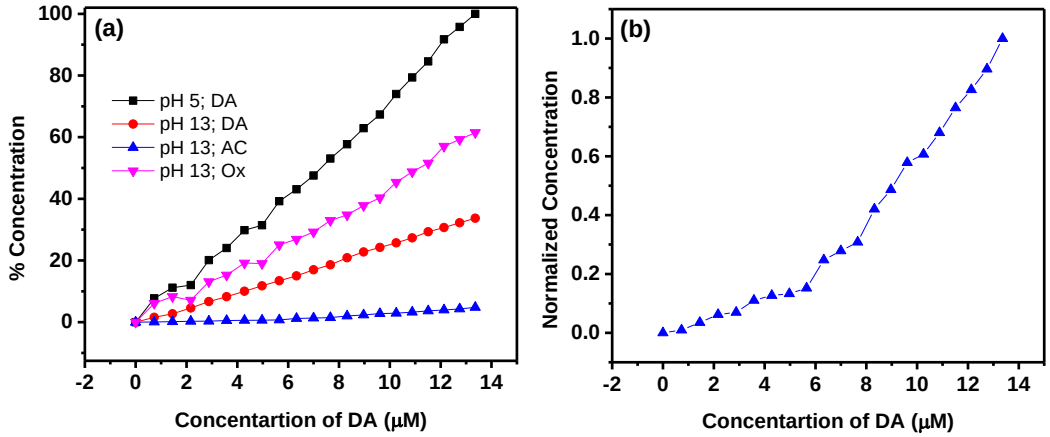

Figure 3.15: (a) Percentage of formation of different oxidation species of DA upon addition of definite amounts of DA (0 to 13 µM). The percentage is calculated using the amount o f hydroquinone form of DA as standard (b) Percentage concentration of aminochrome alone.

The formation of these oxidized products is thus significant in the detection of DA using MoS_2 QDNS sensor. Because the absorption features of DA in MoS_2 QDNS was found to be extended covering the emission region of MoS_2 QDNS (Figure 3.16). The good spectral overlap between the emission spectrum of the donor (MoS_2 QDNS) and acceptor (DA) (pH 13) reflects the possibility of excited-state energy transfer (FRET). Apart from spectral overlap, the proximity/interaction of the fluorophore and quencher (<10 nm) is another condition to be satisfied for the FRET to be active. Since MoS_2 QDNS has been prepared in aqueous NaOH, the surface S could be bonded with –OH, which makes them highly stable in water for a prolonged period. We expect that these surface functionalities also enable it to interact with DA via non-covalent interactions such as hydrogen bonding, electrostatic interaction, etc. This was reflected in the significant reduction of zeta potential values after the addition of DA. The zeta potential values of MoS_2 QDNS was reduced from –22.3 mV to –10.7 mV (at pH 13) by the addition of DA (0.1 mM), indicating the electrostatic interaction between these two species thereby changing the surface potential values.

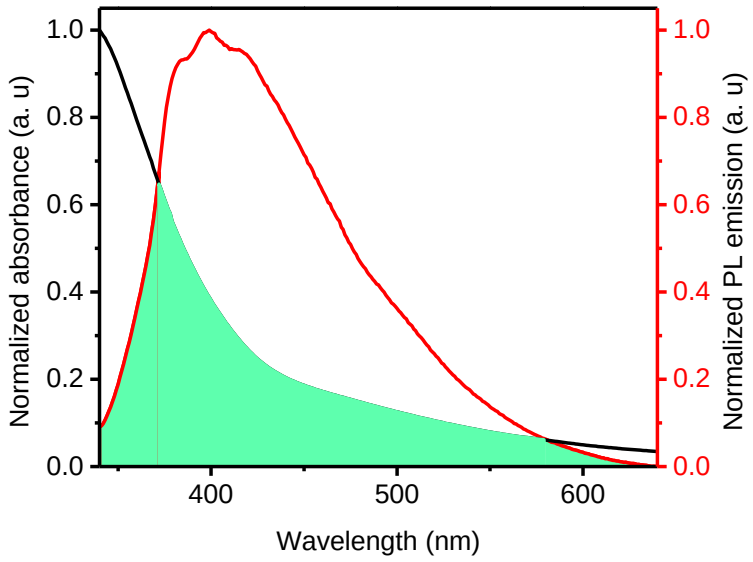

Figure 3.16: Plot showing the spectral overlap between absorption spectra of MoS_2 QDNS-DA (2.5 mL of MoS_2 QDNS + 100 µL of 1 mM DA) and emission spectrum of MoS_2 QDNS (pH 13) (The shaded area indicates the spectral overlap).

The time-resolved fluorescence spectral study provided additional insight into the quenching mechanism, as it can account for any excited-state interactions between the fluorophore and quencher. FRET-based quenching will decrease the lifetime of the fluorophore due to the emergence of non-radiative excited-state energy transfer from the fluorophore to the quencher. The lifetime analysis of MoS_2 QDNS at different concentrations of DA is given in Figure. 3.17, and the results are tabulated in Table 3.1. Both MoS_2 QDNS and MoS_2 QDNS-DA were fitted by a triexponential function with shorter, medium and longer components at ~1 ns, 3-5 ns and 18-29 ns, respectively. It is obvious that the average lifetime of MoS_2 QDNS was decreased in the presence of DA. Moreover, the regular decrease in the average lifetime of MoS_2 QDNS with the concentration of DA was a clear indication of the involvement of the complex quenching mechanism.

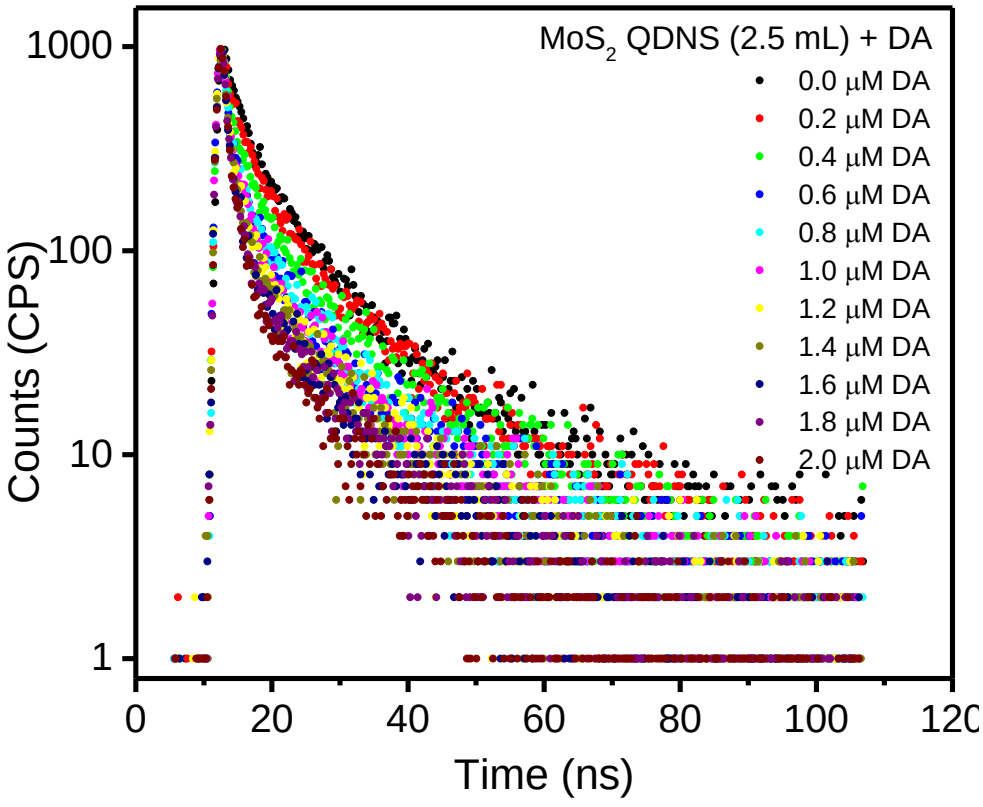

Figure 3.17: Lifetime plots of MoS_2 QDNS (black) and MoS_2 QDNS along with different concentrations of DA (0.2 – 2 μM).

Table 3.1 The lifetime components of MoS_2 QDNS and MoS_2 QDNS-DA, showing concentration-dependent lifetime values. All decay profiles are fitted into tri-exponential functions. The decrease in all the components and average lifetime values of MoS_2 QDNS-DA complex implies the interaction of excited state MoS_2 QDNS with DA. (Excitation was at 344 nm and the emission was collected at 415 nm).

System	τ_1 (ns)	α_1 (%)	τ_2 (ns)	α_2 (%)	τ_3 (ns)	α3 (%)	$<\tau>$ (ns)	χ^2
MoS_2 QDNS	1.05	29.67	5.55	38.66	29.18	31.67	32.89	1.2
0.2 μM of DA	0.83	31.91	5.06	36.40	28.27	31.87	32.62	1.2
0.4 μM of DA	0.60	37.98	4.52	32.44	27.44	29.58	30.20	1.2
0.6 μM of DA	0.56	42.83	4.32	28.85	26.46	28.32	28.78	1.2
0.8 μM of DA	0.54	45.20	4.16	27.35	25.78	27.45	27.94	1.2
1.0 μM of DA	0.51	48.53	3.98	24.74	24.33	26.73	27.17	1.1
1.2 μM of DA	0.50	51.77	3.87	22.99	23.84	25.23	25.91	1.1
1.4 μM of DA	0.50	54.45	3.88	21.31	22.48	24.25	25.13	1.1
1.6 μM of DA	0.48	56.28	3.62	20.09	21.74	23.62	24.64	1.1
1.8 μM of DA	0.45	58.89	3.21	18.47	19.80	22.65	23.98	1.1
2.0 μM of DA	0.45	61.00	3.14	16.85	18.82	22.15	23.73	1.02

We calculated steady-state as well as time-resolved FRET efficiency of MoS_2 QDNS-DA (donor-acceptor) system. Steady-state FRET efficiency was calculated using the quantum yield of MoS_2 QDNS and MoS_2 QDNS-DA solutions and obtained a high value of 83%. The average lifetime of fluorophore in the absence and presence of quencher was used for calculating time-resolved FRET efficiency, which in turn was 56%. Also, the slope of the plot F_0/F v/s concentration of DA ([DA]) has a higher value than that of τ_0/τ v/s [DA] (Figure. 3.18). This indicates the existence of other quenching mechanisms, which may not affect the excited state lifetime of the fluorophore. In the UV-visible spectrum of MoS_2 QDNS-DA, there was a strong absorption at 330 nm, at which the excitation of MoS_2 QDNS was carried out. Hence, the primary inner filter effect (IFE), which arises due to the absorption of quencher at the excitation wavelength of fluorophore could be surmised to the reason behind the difference in the steady-state and time-resolved quenching efficiency. This again ascribes the enhanced value of the slope of F_0/F v/s concentration of DA plot over τ_0/τ v/s concentration of DA. As the excited state lifetime of the fluorophore is not expected

to change by IFE, it is reasonable to surmise the existence of IFE together with the FRET as contributing quenching mechanisms.

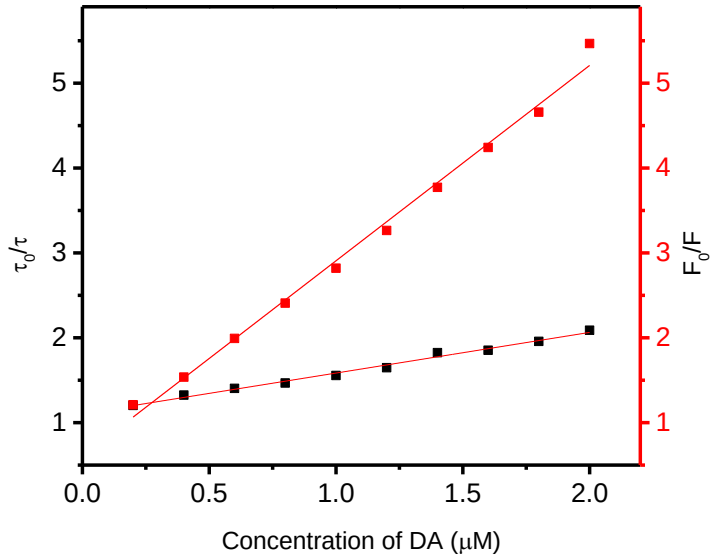

Figure 3.18: Relationships between τ_0/τ and F_0/F vs [DA], show a linear plot with different slops. F_0 and F are the steady-state intensity before and after the addition of DA and τ_0 and τ are the average lifetime of MoS_2 QDNS and MoS_2 QDNS- DA system, respectively.

We have carried out the quenching studies of MoS_2 QDNS-DA at excitation wavelengths of 430 and 550 nm (Figure 3.19 a). Since there is no adequate spectral overlap at 430 excitations, we can exclude the possibility for FRET in this contest and the absorbance of DA was negligible at 430 nm compared to that at 330 nm; hence, the effect of IFE is also minimal, so is the quenching at this excitation (Figure 3.19 b). And at 550 nm excitation, there is neither spectral overlap between fluorophore's emission and quencher's absorption nor absorption of DA at pH 13 at this wavelength, prevents the possibility of FRET as well as IFE. Also, the higher slop in the Stern- Volmer plot as the concentration of DA increases also can be explained based on these mechanisms. As the concentration of DA increases, more oxidation products of DA have been formed, which in turn increases the intensity of the corresponding absorption peaks. Matching with this intensity increase, the effect of IFE also would escalate, which reflects the sudden increase in the quenching.

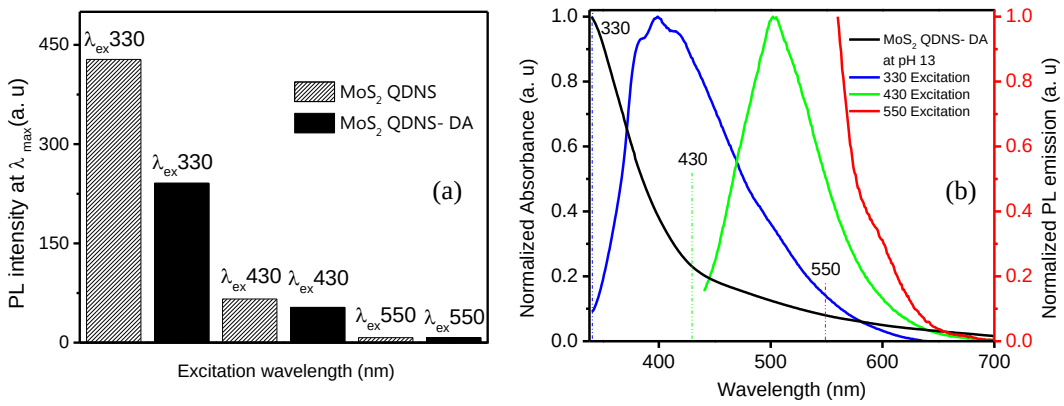

Figure 3.19: (a) Comparison of PL intensity of MoS_2 QDNS and MoS_2 QDNS-DA complex at the different excitation wavelengths. (b) Spectral overlap of absorption spectra of MoS_2 QDNS-DA solution (black) to that of PL spectra of MoS_2 QDNS excited at different wavelengths (330, 430 and 550 nm).

3.3.4 Selectivity of the Sensor

The selectivity of the sensor towards a specific analyte is of paramount importance. The selectivity of MoS_2 QDNS was investigated by measuring the $(F_0 - F)/F_0$ values of MoS_2 QDNS for various analytes. Since we aimed to detect DA in biological fluids, we carefully chose those analytes which are present in biological fluids such as a few metal ions, amino acids, carbohydrates peptides, etc. The efficacy of MoS_2 QDNS as a selective sensor for DA, upon addition of 100 µL of 1 mM solution of DA and various other analytes, is evident as in Figure 3. 20.

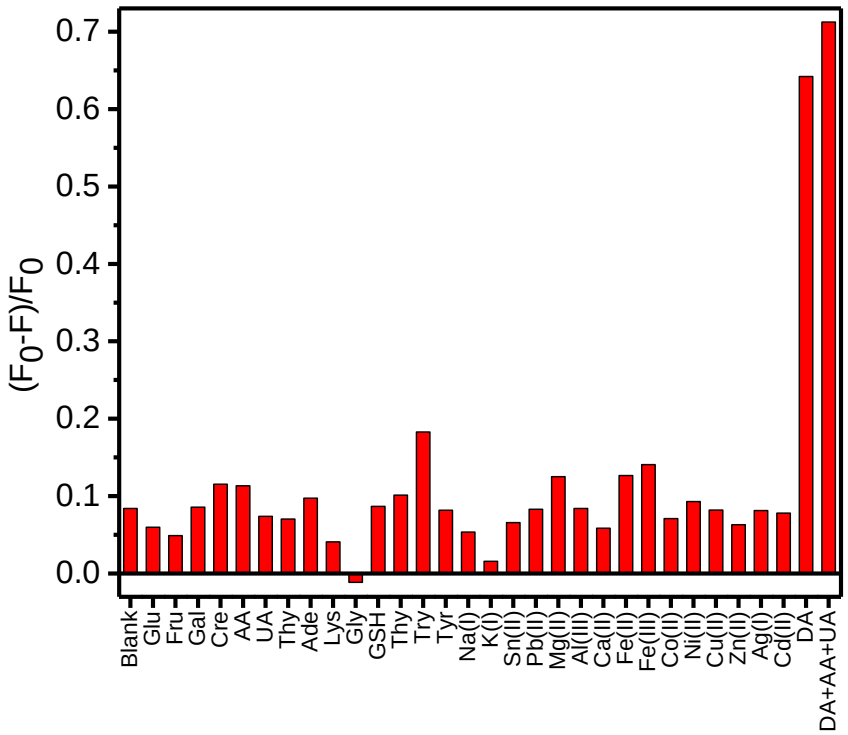

Figure 3. 20: Selectivity profile of MoS_2 QDNS towards DA. The studies were conducted using different metal ions and biologically relevant molecules (Concentration used: 100 µL of 1 mM solution).

One of the salient features of MoS_2 QDNS as a sensor is that it is highly selective over two of the major interfering molecules in the detection of DA; ascorbic acid (AA) and uric acid (UA). This makes the sensor system particularly promising compared to many reported sensors. The reason for this exceptional selectivity towards DA over these interfering molecules lies upon the fact that the absorption spectrum of AA and UA does not overlap with the PL spectra of MoS_2 QDNS, which shut away from the possibility of FRET. And the absence of a discernable peak at 330 nm, avert the possibility of IFE-based quenching as well (Figure 3. 21). Hence, the present sensor can be used for the detection of DA in biological samples without demanding separation of interfering molecules.

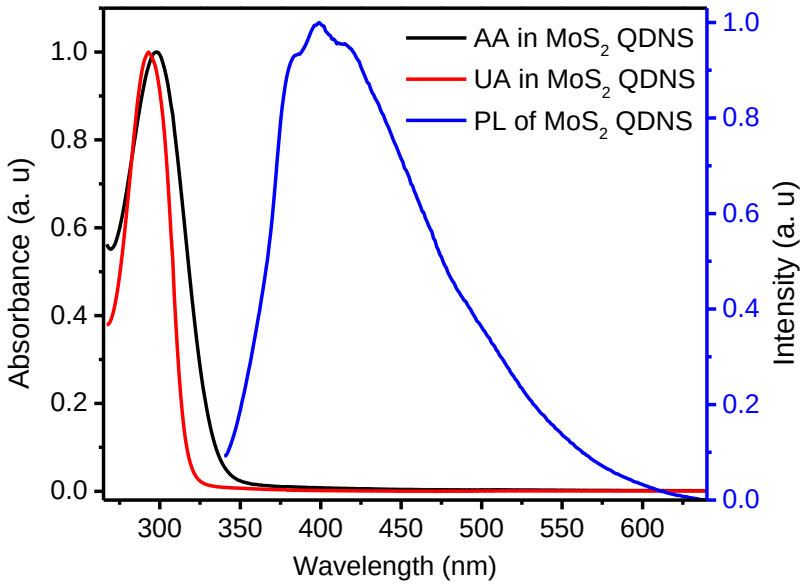

Figure 3. 21: Absorption spectra of AA and UA in MoS_2 QDNS along with the PL spectra of MoS_2 QDNS at pH 13.

3.3.5 Effect of pH on sensor Action

Since MoS_2 QDNS was prepared in the presence of NaOH in a 1:10 ratio, the pH of the solution is highly alkaline, nearly 13. And a detailed study on the response of PL emission of MoS_2 QDNS at different pH reveals that PL intensity was maximum at basic pH (Mani et al., 2017). As the characteristics of the solution changes with the pH, monitoring the performance of the sensor at different pH values are highly necessary. A detailed study was performed to uncover the quenching ability of DA at different pH conditions. We selected three different pH for undertaking the study; pH 7, 9 and 13. At acidic pH, since oxidation of DA is not possible, absorption spectra contain only one specific feature at 280 nm, corresponding to its hydroquinone form where neither FRET nor IFE is possible. Hence, MoS_2 QDNS failed to respond at acidic pH. So, we restricted our study in neutral and basic pH. At a pH of 13, both the magnitude of the PL intensity of MoS_2 QDNS and the quenching upon interaction with DA were found to be maximum. As the pH decreases to 9, we noticed that along with the PL intensity of the original solution, the extent of quenching by DA was also found to plummet. We surmise that the origin of this particular behavior can be attributed to

the reduced scale of the formation of oxidized forms of DA at reduced pH compared to that of hydroquinone form. By further reducing the pH to neutral, though DA quinone started to form, since the amount of this form was very low, the impact of the inner filter effect, as well as FRET, was subsided accordingly. The observations are summarized in Figure 3.22 a and b

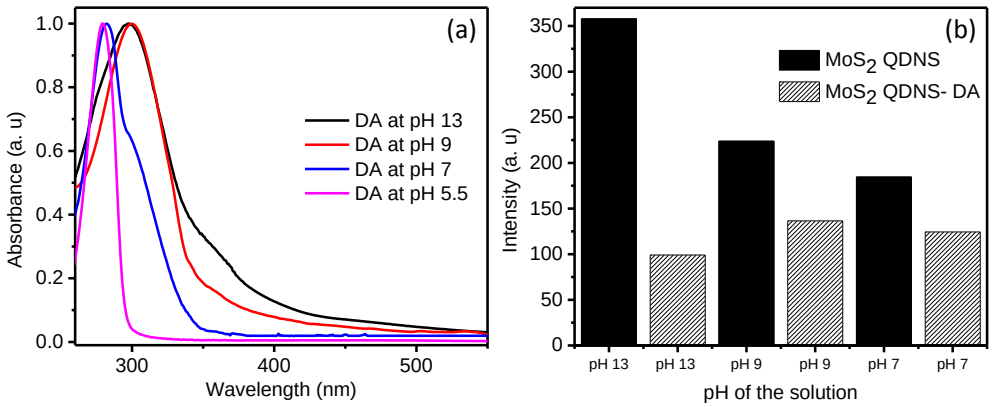

Figure 3. 22: (a) UV- Vis absorption spectra of DA at different pH (pH 13,9,7 and 5.5), showing a shift in peak position, as DA changes from hydroquinone form (acidic pH) to different oxidized form (neutral and basic pH). (b) The response of PL emission of MoS_2 QDNS at pH 13, 9, and 7 towards DA.

3.3.6 Real Sample Analysis

Evaluation of the utility of MoS_2 QDNS as a sensor for DA in real samples analysis was performed using human blood samples. The blood sample was collected from a healthy volunteer, and the solution was diluted 1000 fold after the addition of citrate anticoagulant. The sample was spiked with known concentrations of DA and introduced into 2.5 mL of MoS_2 QDNS solution. The PL intensity of the solution was recorded before and after the addition of the blood samples. A calibration graph is generated and the amount of DA recovered was calculated. Each experiment was repeated three times and the average values with the corresponding percentage recovery are summarized in Table 3. 2. The quenching of fluorescent emission by non-spiked blood samples was considered as the background response from the real sample (3.4% of quenching by the addition of 10 µL of the blood sample; data not shown). This quenching can be induced by DA or any other unstudied biological quenchers

present in the blood. The present detection strategy was found to be superior, as it can detect the amount of spiked DA concentration with relatively good accuracy.

Table 3.2: Detection of DA in the human blood sample.

Sample	Spiked (μM)	Measured (μM)	Recovery (%)
Human blood	0.00	--	--
	0.49	0.56	87.52 – 107.91
	0.99	0.98	91.27 – 106.51
	1.49	1.47	99.68 – 103.98

Qualitative recognition of DA in a handy substrate was conducted to inspect the feasibility of the present sensor system as a solid-state sensor platform. We chose the TLC plate as our solid substrate in which several MoS_2 QDNS dried spots were prepared. Different concentrations of DA were drop-casted to these dried spots containing our sensor material and illuminated with UV light (365 nm). Figure 3. 23 clearly demonstrates the utility of the TLC test strip in the qualitative detection DA. The fluorescence intensity of the spots was found to be decreased in accordance with the increasing concentrations of DA. Hence, easy detection of DA can be realized using MoS_2 QDNS based sensor scaffold, without the need for any sophisticated instruments.

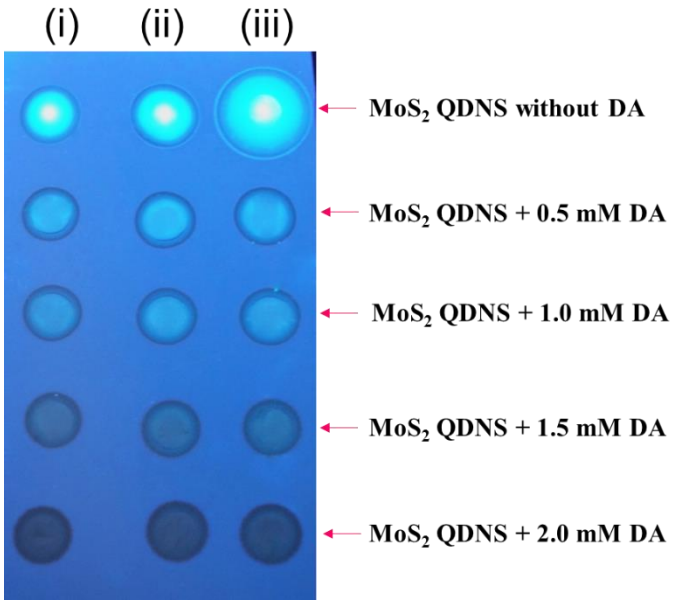

Figure 3.23: Photographs of TLC plate-based sensor platform. The first row represents MoS_2 QDNS drop-casted on TLC under UV light, other rows represent MoS_2 QDNS treated with 10 µL of various concentrations of DA. (i), (ii) and (iii) represent three different experiments.

3.3.7 Comparison with Other Studies

Various methodologies such as electrochemical, calorimetry and fluorescence-based, amperometry, etc. have been tested and succeed for the detection of DA in aqueous solution, human serum, blood and urine, etc. Yet, one of the important aspects to be considered is the choice of the method adopted for the synthesis of the probe to be used. Generally, a method which follows simple steps, without the use of any hazardous organic solvents or precursor materials or time-consuming routes are favored. Also, the economic viability of the materials is also a concern. For example, even though the sensitivity of enzyme immobilized sensors is fairly high, the high cost of these materials makes them less preferable (Lisdat et al., 1997; Njagi et al., 2010). Thence, fabrication of a simple sensor with desirable qualities still holds scientific significance. The present sensor stands out from the other methods in various ways. For example, the use of easy synthetic strategy from low-cost precursors, straightforward fluorescence detection procedure, the rapid response of PL emission of MoS_2 QDNS towards DA, satisfactory LOD with wide linear range etc. Also, the present sensor system has proven its potential for the selective and sensitive detection of DA in aqueous as well as blood samples. As an addition, the proposed sensor is found to be competent for detection using a strip-substrate based as well, along with its proficiency for the precise quantitative determination of DA in real samples. Table 3.3 compares the response characteristics of the sensor with published reports. Our method has comparable sensitivity to other methods.

Table 3.3: Comparison of the analytical performance of MoS_2 QDNS as DA sensor with other sensors

Method	Sensor System	LOD, Dynamic range	Reference
Colorimetry	40-aminobenzo-18-crown-6 (ABCE) and 4-mercaptophenyl boronic acid (MPBA) modified Au nanoparticles.	46 nM	(Palanisami, 2015)

Electrochemistry	Thin layer of poly(tetrafluoroethylene) (PTFE) with nanoparticle arrays and an aluminum film	0.5 µM 10 µM–1mM (S/N=3)	(Jie, 2015)
Electrochemistry	GS-Au_{25} modified sol–gel electrode	0.30 µM	(Kwak, 2012)
Electrochemistry	Glassy carbon electrodes were modified by laccase.	10 nM	(Lisdat, 1997)
Electrochemistry	carbon fiber microelectrode modified with tyrosinase immobilized in chitosan and ceria-based metal oxides	1 nM	(Njagi, 2010)
Fluorimetry	Mono-6-amino-β-cyclodextrin (NH2-β-CD) functionalised gold nanoclusters (β-CD-Au NC)	2 nM 5–1000 nM (S/N=3)	(Ban, 2015)
Fluorimetry	Water-soluble silicon nanoparticles (Si NPs)	0.3 nM 0.005 to 10.0 µM	(Zhang, 2015)
Fluorimetry	Hierarchical CdS Spherical Aggregates	10 nM	(Sun, 2012)
Fluorimetry	Polydopamine	40 nM	(Yildirim, 2014)
Fluorimetry	MoS_2 QDNS	0.9 nM 2.5 nM- 6 µM	Present study

3. 4 Conclusion

In summary, we have presented a novel sensor for the detection of DA, utilizing the photoluminescent attributes of a unique MoS_2 nanohybrid material, MoS_2 QDNS, for the first time. The sensor was prepared via a hassle-free hydrothermal route, from readily available low-cost precursors, without using any hazardous organic solvents or organic lithium reagents. MoS_2 QDNS at a pH of 13, was successfully employed for the detection of DA, owing to the quenching of PL emission from the former, with good selectivity with satisfactory sensitivity. The selectivity of the present sensor was attributed to the FRET from MoS_2 QDNS to oxidize products of DA, a specific quenching mechanism functioning at basic pH, along with IFE as supporting quenching mechanism. The detection limit of the sensor was calculated to be a low value of 0.9 nM, with two linear ranges spanning from 2.5 nM to 5.0 µM and from 5.0

μM to 10.4 μM. The sensor was demonstrated to be useful for the detection of DA in real samples as well, endowed with high accuracy. A visual detection possibility was also demonstrated, by the introduction of DA to dried spots of MoS_2 QDNS sensor prepared on a TLC plate.

CHAPTER 4

EFFECT OF pH ON THE LUMINESCENCE OF MoS_2 QDNS AND A TURN- ON GLUCOSE SENSOR

The response of photoluminescence (PL) of MoS_2 QDNS was checked against different pH and it has been observed that the emission is prominent only in alkaline solution, whereas in acidic pH, the PL intensity is found to be dropped significantly. The reason for this quenching is attributed to different mechanisms, such as creating sulphur vacancies. The compounds formed by this sulfur lead to fluorescence quenching via FRET and IFE. Whereas in the presence of strong oxidizing agent H_2O_2, the quenched fluorescence is found to be recovered. Thus, we drafted an indirect turn-on sensing of glucose using acidified MoS_2 QDNS (MoS_2 $QDNS_{ac}$), by incorporating it with enzyme glucose oxidize (GOx).

4.1 Introduction

Reactive oxygen species (ROS) are a class of compounds found in most of the animal cells, which are generated by the stepwise reduction of oxygen in biological systems. The functions and effects of these compounds vary with the concentration and environment at which they are produced (Shu et al., 2007; Chang et al., 2013; Wu et al., 2011). At higher concentrations, they are known to impair major cell functions by damaging DNA, proteins, lipids and by modifying membrane fatty acids (Francesca et al.; Sanford et al., 2010). This ultimately leads to conditions such as neurodegeneration, aging, and diseases such as cancer, Alzheimer's, Parkinson's, cardiovascular & cognitive dysfunctions, inflammatory conditions, autoimmune diseases, etc. (Zhang et al., 2014; Shu et al., 2007; Chang et al., 2013; Wu et al., 2011; Francesca et al.; Sanford et al., 2010). On the contrary, extensive studies on the effect of ROS reveals their role as secondary messengers for several growth factors, cytokines and reductive-oxidative-based signal transduction cascades. Hence these species are essential for normal cell functions (Wu et al., 2011; Zhang et al., 2014; Sanford et al., 2010). Superoxide anion

radical ($O_2^{\bullet-}$), hydroxyl radical ($OH^{\bullet-}$), singlet oxygen ($^1O_2$), and hydrogen peroxide (H_2O_2) are major ROS produced and regulated in aerobic organisms. Of these, H_2O_2 has been gaining recognition due to its stability, unlike other ROS and penetrability through cellular membranes that cause oxidative stress and other harmful biological modifications. Also, studies unveiling the role of H_2O_2 in the antineoplastic action of certain anticancer drugs (Doroshow, 1986; Chen et al., 2005) makes it a key factor in the studies aimed for the better understanding of function and concentration dependence of ROS in cellular physiology (Zhang et al., 2014). Therefore, quantification of the accurate amount of H_2O_2 is of utmost importance, as it is significant regarding clinical and pharmaceutical analysis and broadly, for understanding its chemical pathways.

Various strategies such as colorimetry, electron spin resonance, chemiluminescence, electrochemical sensing, fluorescence-based sensing, etc. were employed for the detection of H_2O_2 in aqueous and in biological media using enzymatic or non-enzymatic substrates (Wu et al., 2011; Zhang et al., 2014; Sanford et al., 2010; Chang et al., 2013; Roberts et al., 2017; Wang et al., 2017b; Abo et al., 2011; Wen et al., 2011; Yuan et al., 2015; Maeda et al., 2004; Vasileva et al., 2011; Luo et al., 2009). Of these, non-enzymatic systems have more advantages over an enzymatic counterpart, as the latter requires complicated immobilization procedures. Besides, high cost and environmental instability of the enzymes are other concerns (Zhang et al., 2014). Several groups have successfully fashioned photoluminescence (PL) turn-on probes for the detection of H_2O_2 (Abo et al., 2011; Yuan et al., 2015; Germain and Knapp, 2008; Xu et al., 2013). For example, Germail and Knapp, (2008) developed a turn-on fluorescence sensing approach for the detection of H_2O_2 as well as triacetone triperoxide (TATP) using Zn(Salen) Fluorophore. In another study, 5-benzoyl carbonyl fluorescein derivatives were used as a fluorescent probe, for a PL turn-on sensor. The PL was low due to intramolecular photo-induced electron transfer (PET) and in the presence of H_2O_2 it was converted into 5-carboxyfluorescein; a highly fluorescent organic molecule (Abo et al., 2011). Another label-free turn- on detection was

demonstrated utilizing the MnO_2-modified upconversion nanosystem with a limit of detection (LOD) of 0.9 μM (Yuan et al., 2015). A vapor phase detection of H_2O_2 was performed using a specially designed organic fluorophore, taking advantage of the specific reaction between aryl boronate group and H_2O_2 (Xu et al., 2013)

Several research groups have successfully extended the H_2O_2 detection strategy for the indirect sensing of glucose in aqueous solutions (Yuan et al., 2015; Wang et al., 2017b). Glucose detection is significant as it can advocate the diagnosis of diabetes, and its applications on wastewater treatment, food analysis, etc. (Yang et al., 2012; Gan et al., 2016; Song et al., 2010). The motive behind these double detection schemes lies upon the fact that glucose can be easily be oxidized by the enzyme glucose oxidase (GOx) in the presence of dissolved oxygen to gluconic acid and H_2O_2 (Yuan et al., 2015; Wang et al., 2017b). The mechanism of this conversion is well established and can be deployed for the determination of glucose concentration by quantifying H_2O_2 produced during the reaction (Song et al., 2010; Gill et al., 2008; Wang et al., 2013b).

The MoS_2 based 2D nanomaterials are widely acknowledged and their optical attributes are exploited extensively for applications in various domains. Nonetheless, the change in its properties to pH is still an under-explored area and as such, it is significant in understanding the system better. Many reports are available, where the chemical sensing potential of these materials is being tapped (Pumera and Loo, 2014). For example, a turn-off sensor for H_2O_2 was developed by Gan et al. (2016), using MoS_2 quantum dots (QDs). Interaction with H_2O_2 induces partial oxidation in MoS_2 QDs, which sequentially quench the PL of the QDs. Another turn-off sensor was fashioned using MoS_2 QDs prepared from sodium molybdate and glutathione (Wang et al., 2017b). Aggregation followed by oxidation of MoS_2 QDs by H_2O_2 was manifested as fluorescence quenching. The turn-on fluorescent sensors are more demanding as the approach generally demonstrates very high selectivity towards the target molecules. Therefore, a turn-on sensor for H_2O_2 detection by MoS_2 will be highly appealing.

In this chapter, we discuss a facile fluorescence strategy for the detection of H_2O_2 and indirect detection of glucose with high selectivity and sensitivity. MoS_2 nanohybrid material composed of MoS_2 QDs dispersed over MoS_2 nanosheets (MoS_2 QDNS) was prepared by a facile hydrothermal synthetic route in the presence of NaOH. The pH of the MoS_2 QDNS was 13 and showed a sound emission. The PL was quenched significantly by changing the pH to slightly acidic (pH 6.5). A plausible quenching mechanism is discussed with experimental support. This hybrid material at pH 6.5 is used as the fluorescent probe and referred to as MoS_2 $QDNS_{ac}$. The PL of MoS_2 $QDNS_{ac}$ recovered in the presence of H_2O_2. The increase in the PL was linear over a dynamic range of 2 to 80 µM with a LOD of 2 µM. In the presence of GOx, the MoS_2 $QDNS_{ac}$ was found to be highly specific towards the detection of glucose over other saccharides. In this case, the LOD was 0.6 µM with a dynamic range of 2- 90 µM. A detailed mechanism of interaction of H_2O_2 with MoS_2 $QDNS_{ac}$ is proposed (Scheme 1). The utilization of the sensor for real sample analysis was demonstrated using human blood and green tea samples.

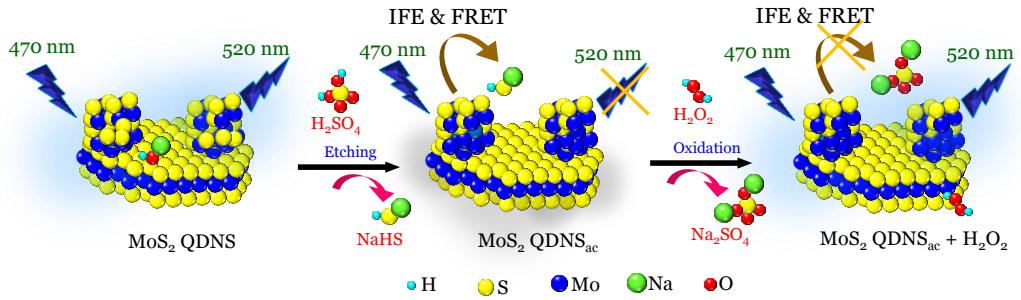

Scheme 4.1: Detection of H_2O_2 using MoS_2 $QDNS_{ac}$

4.2 Experiments and Methods

4.2.1 Reagents and Materials

MoS_2 powder, dopamine (DA), adenine (Ade), tyrosine (Tyr) were purchased from Sigma-Aldrich, USA. Fructose (Fru), galactose (Gal), creatinine (Cre), thymine (Thy), uric acid (UA), adenosine (Ads), folic acid (FA), cholesterol (Cho), caffeine

(Caf), L-dopa, L-cysteine (L-Cys), L- hydroxytryptophan (h-Try) were purchased from SRL Pvt. Ltd, India. Tryptophan (Try), tyramine (Tym), cadmium chloride ($CdCl_2$) were purchased from Alfa Aesar, UK. Lead nitrate was obtained from Otto Chemicals, India. H_2O_2, Glucose (Glu), glutathione (GSH), cysteamine (Cysm), cobalt sulphate ($CoSO_4$), ascorbic acid (AA), tin chloride ($SnCl_2$), lysine (Lys), glycine (Gly), sodium carbonate ($NaCO_3$), potassium chloride (KCl), silver nitrate ($AgNO_3$), ferrous sulphate ($FeSO_4$), ferric chloride ($FeCl_3$), nickel sulphate ($NiSO_4$), copper sulphate ($CuSO_4$), magnesium sulphate ($MgSO_4$), calcium carbonate ($CaCO_3$), aluminum nitrate $Al_2(NO)_3$, zinc sulphate ($ZnSO_4$), sodium hydroxide (NaOH) and hydrochloric acid (HCl) were purchased from Merck, India. Double distilled water was used for all the experiments. All reagents were of analytical grade and used without further purification.

4.2.2 Instrumentation

UV-visible absorption spectroscopy was done using a Carry-100 UV-visible spectrophotometer. Fluorescence measurements were carried out using a FluoroMax-4C spectrofluorometer (Horiba Instruments, USA) by fixing excitation and emission slit width at 5 nm with an integration time of 0.1 ns. Time-resolved fluorescence measurements were executed using the time-correlated single-photon counting (TCSPC) spcetroscopy. For TCSPC measurements, the excitation wavelength was fixed at 454 nm and decay profiles were collected at 530 nm (laser pulse width <1 ns). The lifetime profiles were fitted using DAS software by maintaining χ^2 value ~1 (best fit). Transmission electron microscopy (TEM) images were obtained using a JEOL 2100 instrument and FTIR spectra were acquired by a Spectrum 100 Perkin-Elmer FTIR spectrometer by KBr pellet method. X-ray photoelectron spectroscopy (XPS) spectra were collected using an Omicron ESCA probe spectrometer with Mg-Kα line and pH measurements were conducted using EUTECH instruments' pH meter.

4.2.3 Sample Preparation for XPS analysis

The S content was determined using XPS analysis. Two sets of equal amounts of MoS_2 QDNS (pH 13) solution was taken for the XPS analysis. The pH of one set of the solution was changed to 6.5 by the addition of H_2SO_4 or HCl. This solution was dialyzed for 24 h, then solidified and used for the analysis. For control experiments, a 100 µM H_2O_2 solution was added to MoS_2 QDNS (pH 13) solution, dialyzed for 24 h and used for analysis after solidification.

4.2.4 Selectivity Study

The selectivity of the present sensor solution towards H_2O_2 was tested using 100 µL of a 1 mM solution of various analytes. We used several metal ions (K^+, Sn^{2+}, Pb^{2+}, Mg^{2+}, Hg^{2+}, Ca^{2+}, Fe^{2+}, Fe^{3+}, Co^{2+}, Ni^{2+}, Cu^{2+}, Zn^{2+}, Ag^+, Cd^{2+} and Cr^{3+}) and biologically active small molecules (Cre, DA, Ade, AA, FA, Ads, Cho and Tyr) carbohydrates (Glu, Fra and Gal) and oxidizing agents such as $KMnO_4$ and $K_2Cr_2O_7$ for the selectivity experiments. The selectivity of MoS_2 $QDNS_{ac}$-GOx towards glucose was tested using various carbohydrates such as sucrose, mannose, ribose, xylose, galactose, fructose and biologically active molecules such as AA, DA, L-Tyr, Cre, Cho, Ade, Caf, Ade, FA, GSH, Cysm, L-dopa, L-Cys, h- Try and metal ions such as Zn^{2+}, K^+, Fe^{2+}, Fe^{3+} and $KMnO_4$.

4.2.5 Real Sample Analysis

Green tea samples were prepared by soaking commercially available dried green tea leaves in water. Different concentrations of H_2O_2 were added to this extract. 10 µL of this solution was added to 2.5 mL of sensor solution and the emission spectra were recorded instantaneously at 470 nm excitation wavelength. Blood samples were collected from a healthy person, added anti-coagulants and diluted 1000-fold before analysis. Spiked samples were prepared by adding different concentrations of glucose into the diluted blood sample. Subsequently, aliquots of these solutions (10 µL each)

were added to 2.5 mL of MoS_2 $QDNS_{ac}$-GOx mixture and mixed thoroughly, and the PL emission was taken at an excitation wavelength of 470 nm.

4.3 Results and Discussions

4.3.1 MoS_2 $QDNS_{ac}$ as a Sensor for H_2O_2

For the ease of the discussion, the utility of MoS_2 $QDNS_{ac}$ as a sensor, will be discussed, followed by the explanation of pH-responsive emission of MoS_2 QDNS. MoS_2 QDNS solution was prepared from MoS_2 powder by hydrothermal reaction in the presence of aqueous NaOH. The pH of the purified MoS_2 QDNS solution was 13. It was noticed that, as the pH decreases to an acidic range, the fluorescence of the MoS_2 QDNS solution quenches with a spectral shift. Further, it was realized that the quenched luminescence could selectively turn-on by H_2O_2. This observation made us utilize MoS_2 QDNS at acidic pH as a turn-on sensor towards the detection of H_2O_2. Since the PL response of the sensor solution varies with pH, the optimization of pH was a necessary step to obtain maximum sensitivity. At each pH, the same concentration of H_2O_2 was added to equal volumes of sensor solution. It has been found that the maximum enhancement of PL intensity was observed at pH 6.5 (Figure 4.1). Hence, we selected this solution as our sensor solution and termed as MoS_2 $QDNS_{ac}$.

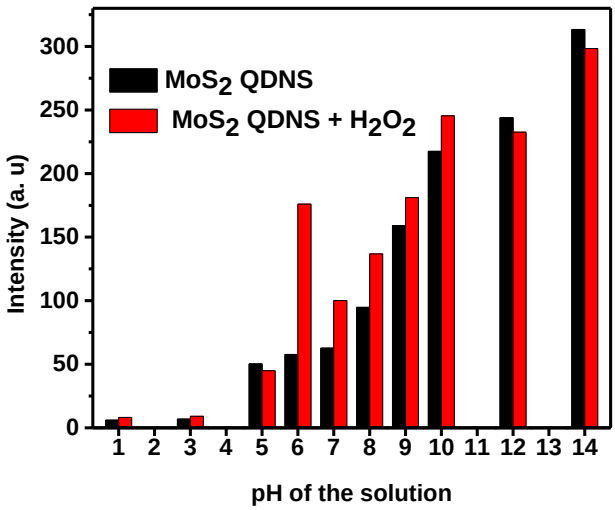

Figure 4.1: The response of MoS_2 QDNS towards H_2O_2 at different pH.

The response of MoS_2 $QDNS_{ac}$ towards various concentration of H_2O_2 is given in Figure 4.2. The excitation wavelength was fixed at 470 nm. A linear increase in PL intensity was observed for H_2O_2 in the concentration range of 2 µM to 94 µM with a LOD of 2 µM, which is commensurate with the already reported results (Zhang et al., 2014; Wen et al., 2011). It should be noted that above 110 µM concentration of H_2O_2, the PL response was saturated and decreases afterward.

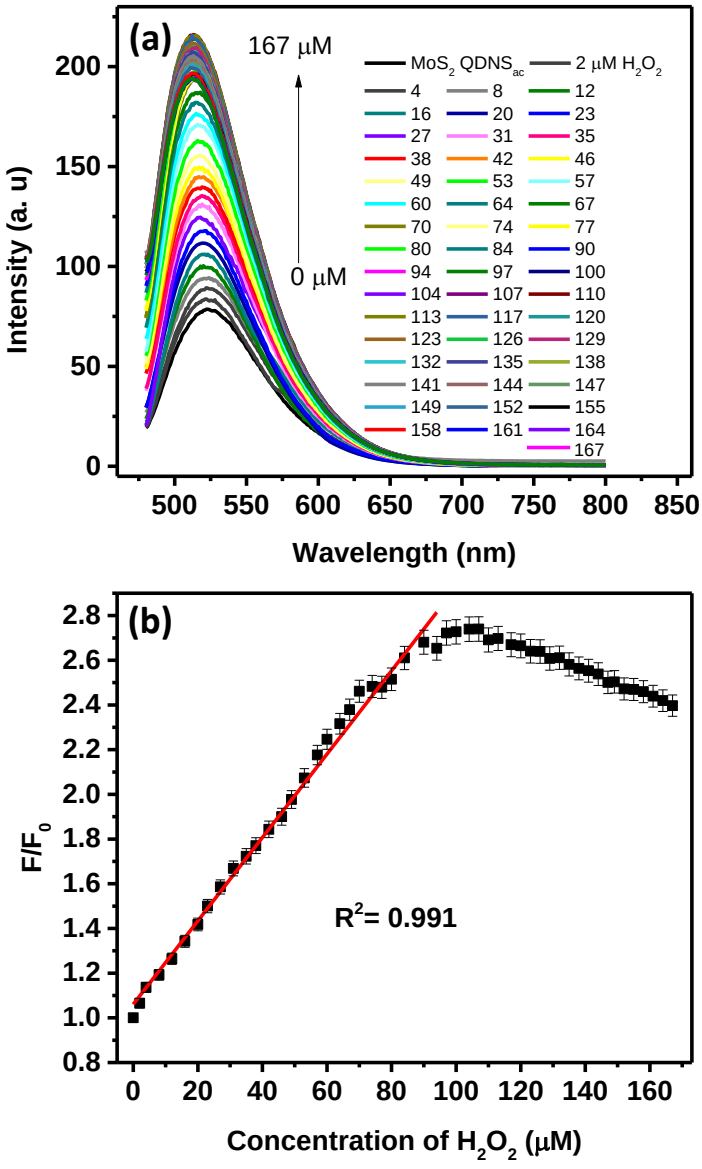

Figure 4.2: (a) PL spectra of MoS_2 $QDNS_{ac}$ at different concentrations of H_2O_2 (from 0 to 167 µM). The excitation wavelength was 470 nm. (b) Fluorescence response of the sensor system

showing a dynamic range of 2–94 μM. Mean deviation of 3 experiments are shown as error bars.

4.3.2 Selectivity Study

Selectivity is a major concern of any sensor platform. To evaluate the selectivity of MoS_2 $QDNS_{ac}$ towards H_2O_2, we measured the PL response of MoS_2 $QDNS_{ac}$ in the presence of biologically relevant metal ions and molecules, oxidizing agents, etc. (Figure 4.3). It has been observed that the turn-on was effective only in the case of H_2O_2 (~10 times higher) compared to other analytes, which attest to the selectivity of the MoS_2 $QDNS_{ac}$ towards H_2O_2. A plausible reason for the selectivity towards H_2O_2 over other oxidizing agents such as $KMnO_4$ and $K_2Cr_2O_7$ is given in the following section.

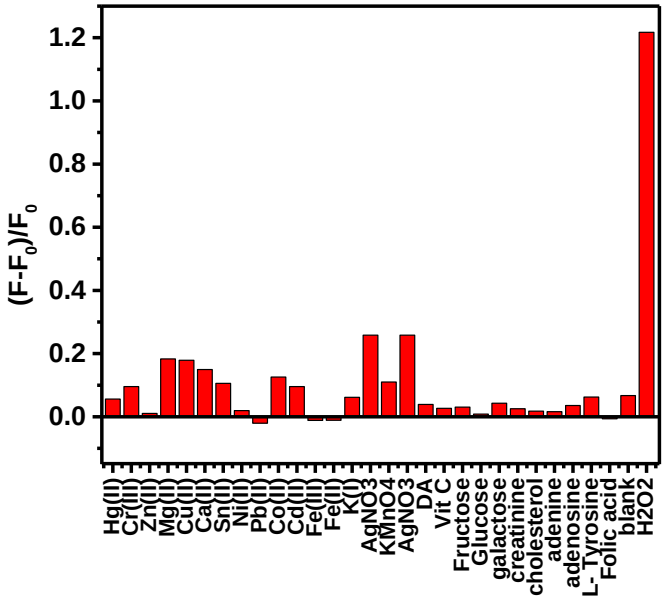

Figure 4.3: The PL response of MoS_2 $QDNS_{ac}$ towards various analytes (100 μM of each analyte has been made use).

4.3.3 Towards the Mechanism of Sensor

It is of great interest to know that, why does the PL intensity vary with pH and in the presence of H_2O_2. Detailed photophysical studies have been executed to fathom the mechanism of these observations. The MoS_2 QDNS shows its best emission at pH

13 and is gradually deteriorating with decreasing the pH. The pH was altered by adding conc. H_2SO_4 or HCl to the sensor solution. The PL quenching by lowering the pH of the medium could be reasoned to the removal of S containing functional groups that act as surface passivators and block the non-radiative recombination of excitons (Zhang et al., 2016). The S content in MoS_2 QDNS and MoS_2 $QDNS_{ac}$ was examined using XPS analysis of purified samples. It has been found that the Mo:S ratio at pH 6.5 was significantly lower than that of pH 13, which positively endorse this speculation.

Table 4.1: Elemental ratio obtained by XPS analysis.

Parameter	**Mo 3d pH 13**	**S 2p pH 13**	**Mo 3d pH 6.5**	**S 2p pH 6.5**	**Mo 3d (after the addition of excess H_2O_2)**	**S 2p (after the addition of excess H_2O_2)**
Peak position (eV)	229.0	165.0	232.0	168.0	232.2	168.2
FWHM (eV)	5.408	5.039	4.738	3.870	6.033	5.268
Atomic/ Mass conc. (%)	0.51	1.03	15.85	26.67	21.07	17.01
Mo:S Ratio	**1: 2.01**		**1: 1.68**		**1: 0.807**	

The formation of the defect state was investigated by fluorescence lifetime analysis also. Lifetime values of the MoS_2 QDNS at pH 13 were a triexponential fit with lower (3.5 ns), medium (7.8 ns) and longer (29.8 ns) components. The longer component has emerged from QDs present in the system, lower component arises from underlying sheets and the medium component is coming from the synergic contribution from the larger QDs or smaller sheets. The origin of these lifetime components has been studied thoroughly (Mani et al., 2017). On the other hand, at pH 6.5, the longer lifetime, which is a radiative component, is completely disappeared and a new ultrafast

lifetime has been emerged (Figure 4.4). This supports the observation of the removal of S containing functional groups and subsequent defect states formation, which leaks the excitons by non-radiative routes.

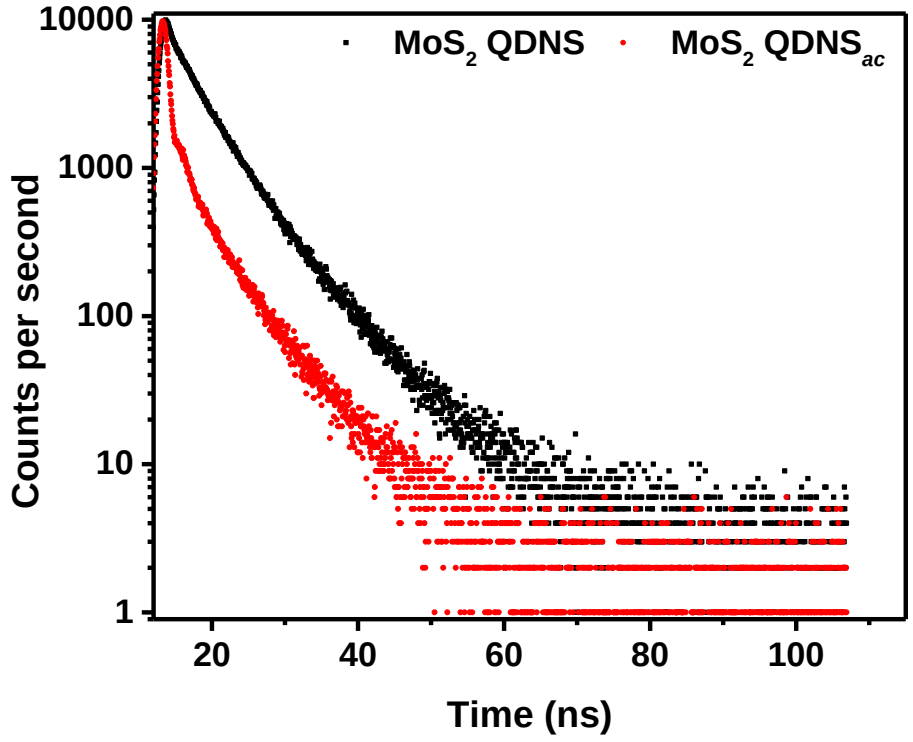

System	τ_1 (ns)	α_1	τ_2 (ns)	α_2	τ_3 (ns)	α_3	χ^2
MoS_2 QDNS pH 13	3.54	50.78	7.84	36.10	29.82	13.12	1.14
MoS_2 QDNS pH 6.5	2.37	10.68	6.98	16.24	0.008	73.08	0.906

Figure 4.4: Lifetime plot of MoS_2 QDNS and MoS_2 $QDNS_{ac}$

As an additional observation, the pale-yellow color of the MoS_2 QDNS solution at pH 13 has been turned to a dark yellow at pH 6.5 (inset to Figure 4.5). This color change is attributed to the fact that dangling S may be etched away upon the addition of H_2SO_4 and in turn, they form yellow-colored inorganic salts such as sodium hydrosulphide (NaHS), polysulphides, etc. (Kamyshny et al., 2006; Hoffmann, 1977).

We anticipate that the source of Na^+ could be the unreacted NaOH left behind in the solution/ or the intercalated Na^+ ions. Upon prolonged dialysis, the color of the solution was disappeared. We surmise that the removal of the above-mentioned small molecules could be the reason for the disappearance of the color. To rule out the involvement of H_2SO_4/SO_4^{2-} for the formation of the sodium salts, we repeated the pH-dependent studies using conc. HCl, instead of H_2SO_4. Similar results, in terms of S content and color changes, were obtained, which support that S was etched away from MoS_2 QDNS. Besides, the difference in the color of MoS_2 QDNS with pH change was duly reflected in the absorption spectral features (Figure 4.5). At pH 13, a distinct absorption feature near to 300 nm was present along with a very feeble continuous absorption till 500 nm, corresponds to the absorption from MoS_2 QDs and sheets, respectively (Mani et al., 2017). Whereas, new features at 288, 391 and 465 nm were emerged at pH 6.5 (note the color change from pale-yellow to dark yellow as mentioned above). This is direct evidence for the formation of new chromophores after the addition of acid. The significance of this newly formed chemical species is that they may contribute via self-absorption/reabsorption (inner filter effect -IFE) or Förster resonance energy transfer (FRET) in the luminescence quenching pathway, alongside the formation of previously discussed surface defects. As the newly formed S compounds (Na salts) are having absorption at 470 nm where the MoS_2 QDNS is excited, this unambiguously contributes towards the PL quenching of MoS_2 QDNS via IFE.

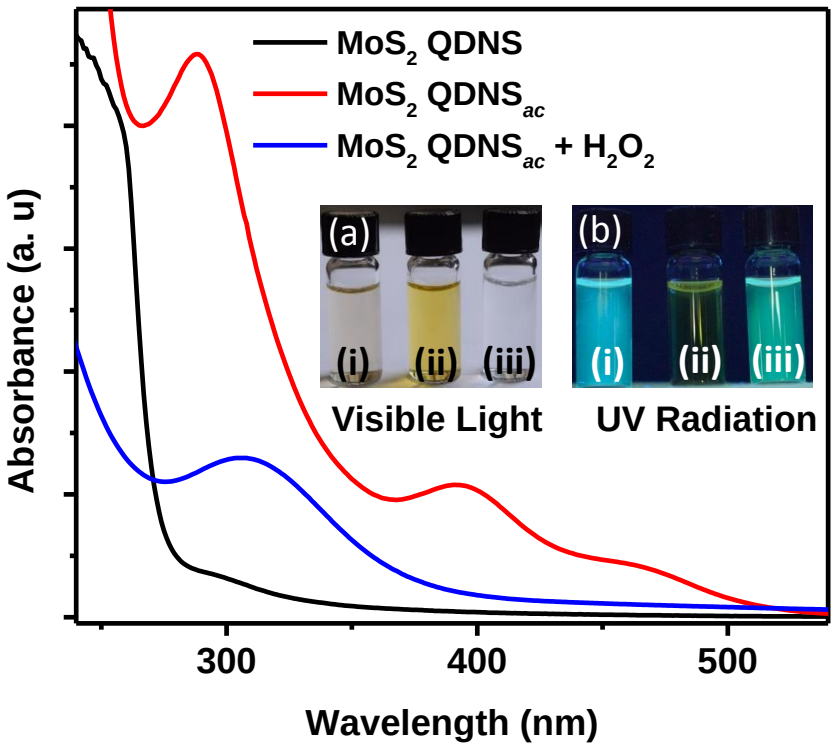

Figure 4.5: UV-visible spectra of MoS_2 QDNS, MoS_2 $QDNS_{ac}$, MoS_2 $QDNS_{ac}$+H_2O_2. Inset shows the photograph of (i) MoS_2 QDNS (pH 13) solution, (ii) MoS_2 $QDNS_{ac}$ (pH 6.5) and (iii) MoS_2 $QDNS_{ac}$+H_2O_2 solutions, respectively, under (a) visible and (b) UV light.

The involvement of FRET is also valid since the new absorption band has partial spectral overlap with the emission band of MoS_2 QDNS (Figure 4.6). This spectral overlap satisfies the condition for the resonance energy transfer from donor to acceptor. Hence, a combined contribution from the formation of defect states, IFE and FRET surmised to be the factors responsible for the luminescence quenching of MoS_2 QDNS upon lowering the pH.

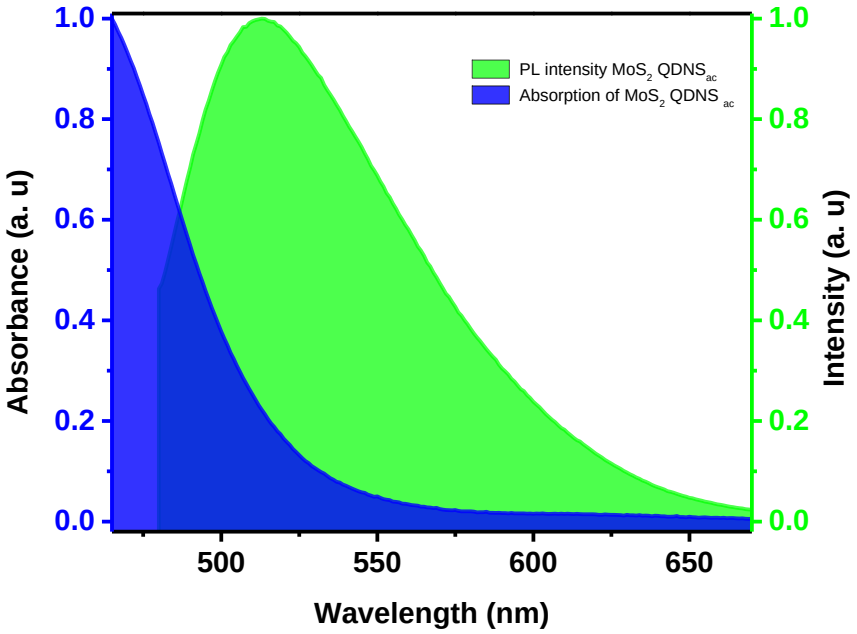

Figure 4.6: Spectral overlap of absorption spectra of MoS_2 QDNS with the PL spectra of MoS_2 QDNS at pH 6.5.

We observed that the addition of H_2O_2 could recover the quenched PL of MoS_2 QDNS$_{ac}$. We speculate that being a strong oxidizing agent, H_2O_2 can oxidize the yellow salts formed in the reaction mixture, hence remove the salts responsible for IFE and FRET. Various spectroscopic analysis has been carried out to support this claim, including UV-visible absorption studies, time-resolved fluorescence spectroscopy and XPS analysis. Pronounced changes in UV-visible absorption spectra were observed, such as the decrease in absorption of MoS_2 QDNS$_{ac}$ at 400 and 460 nm, along with the advent of a peak at ~310 nm. These alterations are reflected as a color change of the solution from dark yellow to light yellow, accompanying the recovery of PL intensity (See inset of Figure 4.5). A plausible argument for the color change is that H_2O_2 oxidized the yellow salts present in the solution to its colorless sulphate forms (Kamyshny et al., 2006; Hoffmann et al., 1977), which has no absorption at ~ 460 nm. As the absorption at 460 nm was disappeared, the IFE and FRET quenching pathways were shunned, resulting in the recovery of PL emission.

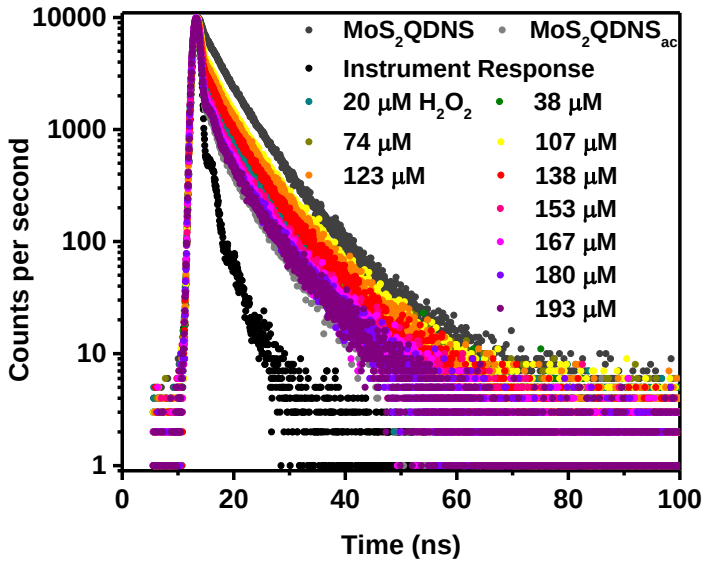

Figure 4.7: Lifetime plot of MoS_2 QDNS and MoS_2 $QDNS_{ac}$ at different concentrations of H_2O_2.

Table 4.2: Lifetime results of MoS_2 $QDNS_{ac}$ with various concentrations of H_2O_2. A gradual decrease (red) and increase (blue) of the amplitude of fast component (α_3) have been highlighted.

	τ_1	α_1	τ_2	α_2	τ_3	α_3	$\langle\tau\rangle$	κ^2
MoS_2 QDNS (pH 13)	3.54	50.78	7.84	36.10	29.82	**13.12**	17.003	1.14
MoS_2 $QDNS_{ac}$	2.37	10.68	6.98	16.24	0.008	**73.08**	6.112	0.91
20 μM of H_2O_2	2.94	20.10	7.27	23.28	0.009	**56.62**	6.135	0.97
38 μM of H_2O_2	2.95	24.90	7.31	28.59	0.008	**46.51**	6.167	1.02
74 μM of H_2O_2	3.04	31.12	7.42	32.67	0.013	**36.21**	6.181	1.02
107 μM of H_2O_2	3.06	33.59	7.44	34.94	0.016	**31.47**	6.190	1.01
123 μM of H_2O_2	3.06	31.54	7.42	33.05	0.014	**35.54**	6.179	1.04
138 μM of H_2O_2	2.93	25.34	7.28	29.75	0.012	**44.91**	6.158	0.97
153 μM of H_2O_2	2.87	14.89	7.19	18.05	0.0096	**67.06**	6.097	0.99
167 μM of H_2O_2	3.01	14.67	7.36	15.29	0.001	**70.04**	6.131	1.01
180 μM of H_2O_2	2.92	12.66	7.40	14.02	0.009	**73.32**	6.194	0.92
193 μM of H_2O_2	2.98	12.28	7.27	14.33	0.01	**73.39**	6.120	0.96

Detailed time-resolved fluorescence spectral analysis of MoS_2 $QDNS_{ac}$ has been executed at different concentrations of H_2O_2 as it can provide a better insight to the excited state phenomenon happening between two reactive species, say donor and

acceptor (Figure 4.7 and Table 4.2). A linear increase in the lifetime was observed until a quencher concentration of 110 µM. In steady-state measurements as well, a linear increase in the emision was observed until the same concentration. Another notable point is the trend of contribution from the non-radiative component (τ_3). A regular decrease of contribution from this component is an indication of enhancement of PL intensity. On the contrary, a sudden hike in its contribution above 110 µM is a clear sign of the introduction of new non-radiative pathways to the system. Even though there was a steady increase in the PL emission of the sensor until a concentration of 110 µM H_2O_2, beyond this concentration, the PL emission was found to be decreased slightly.

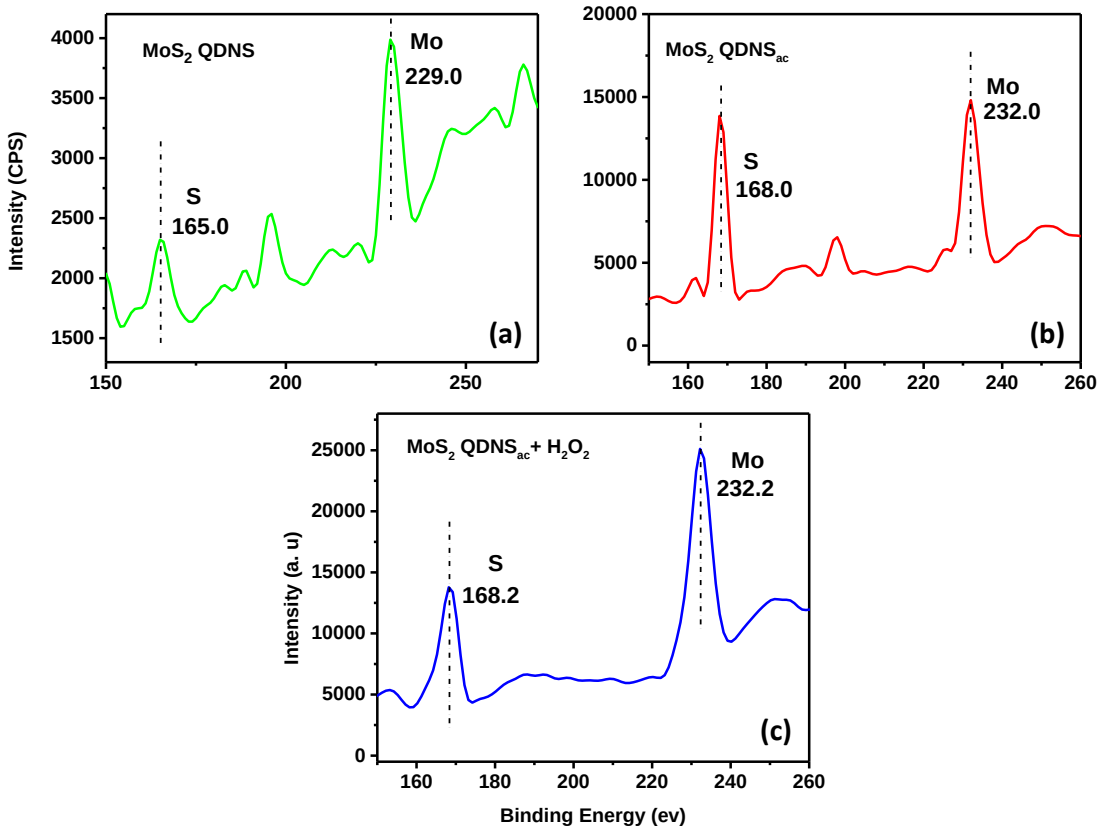

Figure 4.8: XPS survey scan spectra of MoS_2 QDNS, MoS_2 $QDNS_{ac}$ and MoS_2 $QDNS_{ac}$+ excess H_2O_2 showing peaks corresponding to S and Mo. The peak position for both Mo and S has shifted to a higher binding energy region. It could be due to the oxidation of both the species.

This peculiar behavior of turn-off can be attributed to the fact that the sensor material degrades in the presence of excess H_2O_2, which was supported by lifetime measurements, XPS and TEM analysis. As the concentration of H_2O_2 increases >110 µM, it is surmised that H_2O_2 started oxidizing MoS_2 QDNS$_{ac}$, which decreases the PL emission. XPS results are validating this assumption. The XPS peak of Mo and S of MoS_2 QDNS (165.0 eV for S and 229.0 eV for Mo) have been shifted to high binding energy values for MoS_2 QDNS$_{ac}$ (168.0 eV for S and 232.0 eV for Mo) and MoS_2 QDNS$_{ac}$ + excess H_2O_2 (168.2 eV for S and 232.2 eV for Mo) (Figure 4.8). Oxidation of the sensor in the presence of acid and further decomposition by excess H_2O_2 could be the reason behind this behavior. Besides, deconvoluted high-resolution XPS of Mo 3d shows the peaks corresponding to +6 oxidation states of Mo (Figure 4.9). The Mo:S ratio was also altered from 1:2.01 to 1:1.68 to 1:0.81 for MoS_2 QDNS, MoS_2 QDNS$_{ac}$, MoS_2 QDNS$_{ac}$+ excess H_2O_2 (150 µM), respectively due to the deterioration of sensor material (Table 4.1).

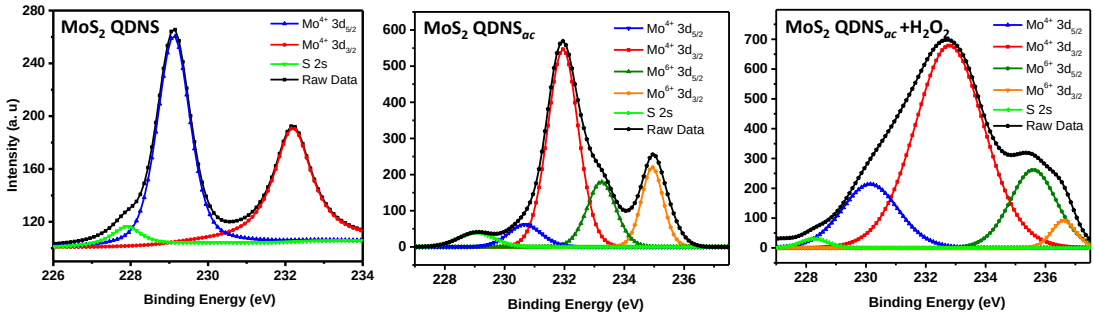

Figure 4.9: Deconvoluted XPS peak of Mo in MoS_2 QDNS, MoS_2 QDNS$_{ac}$, MoS_2 QDNS$_{ac}$+ excess H_2O_2

Additionally, the formation of Mo-O bond was evident in FTIR spectra (Figure 4.10). The FTIR spectra of MoS_2 QDNS$_{ac}$+excess H_2O_2 shows a peak at 992 cm^{-1} corresponds to Mo=O antisymmetric stretching, peaks at 823 cm^{-1} and 619 cm^{-1} are due to Mo-O-Mo symmetric stretching and bending vibrations, respectively (Chen et al., 2011c; Kee, 2015; Ivanova and Kolev, 2011). These support the formation of oxidation products of MoS_2 QDNS$_{ac}$ by the reaction of excess H_2O_2.

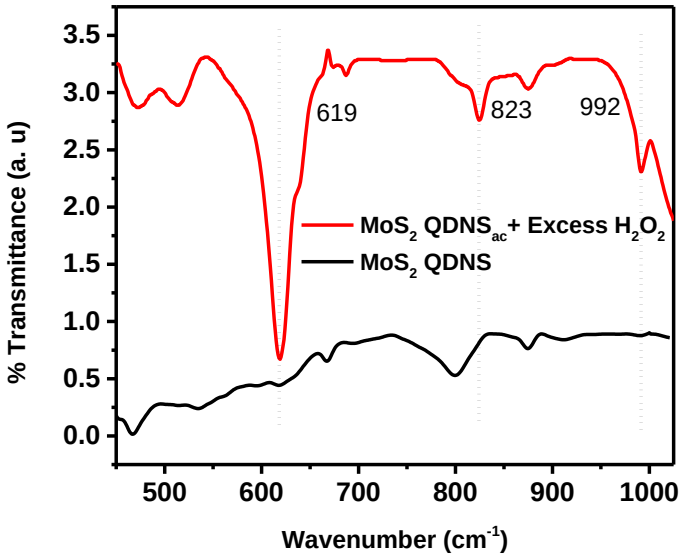

Figure 4.10: FTIR spectrum of MoS_2 $QDNS_{ac}$+ excess H_2O_2 showing the bands corresponding to Mo–O bonds.

The etching of MoS_2 $QDNS_{ac}$ by H_2O_2 was visible in TEM images as well. The absence of distinguishable QDs and the formation of inscribed markings on the surface of the material in TEM image substantiate the hypothesis of degradation of sensor materials followed by oxidation (Figure 4.11).

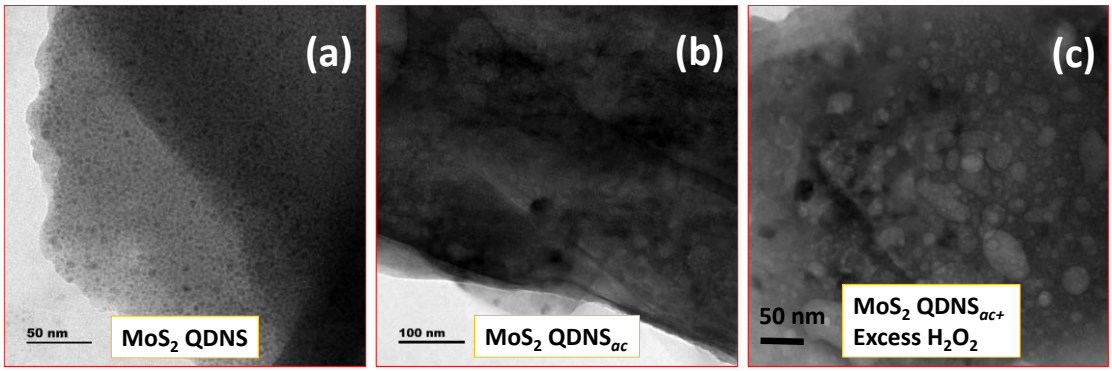

Figure 4.11: TEM images of (a) MoS_2 QDNS, (b) MoS_2 $QDNS_{ac}$ (c) MoS_2 $QDNS_{ac}$+ excess H_2O_2

The mystery of the yellow-colored compounds formed upon the addition of mineral acids was tried to comprehend using Raman as well as XPS analysis (Figure 4.12 and 13). Raman spectra of MoS_2 $QDNS_{ac}$ and MoS_2 $QDNS_{ac}$+ H_2O_2 has been recorded using a 531 nm laser power source and compared with the spectra obtained

for MoS_2 QDNS. Peaks corresponding to S-H stretching in the spectra of MoS_2 $QDNS_{ac}$ (around 2600 cm^{-1}) is quite an evidence for the formation of NaSH, a yellow-colored salt in the solution. Whereas the absence of this peak in MoS_2 $QDNS_{ac}$+ H_2O_2 reveals the possibility of its oxidation to its sulphates, which is appeared in the 1100 cm^{-1} region.

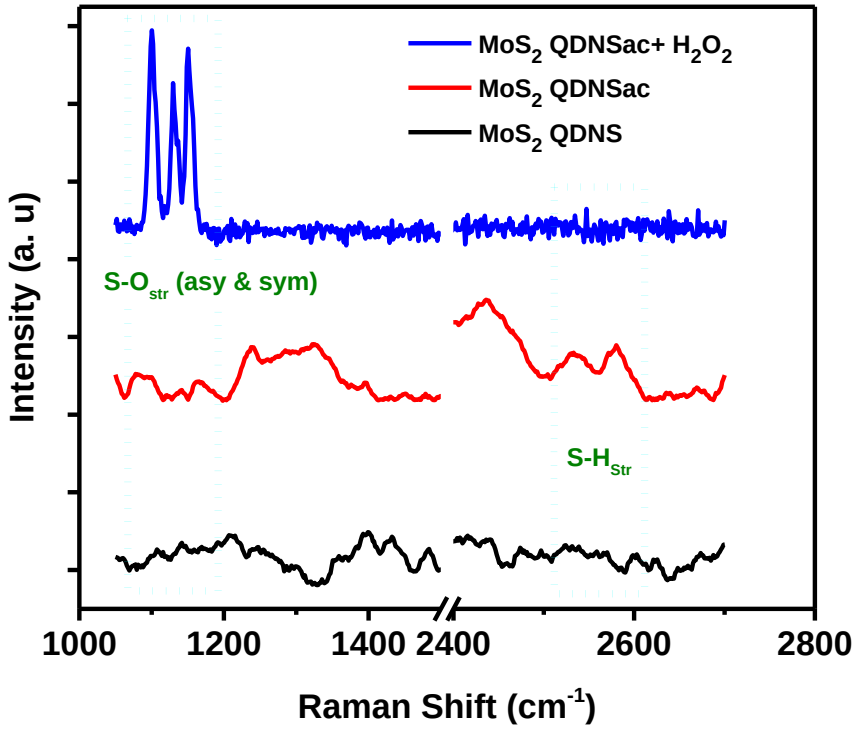

Figure 4.12: Raman spectra of MoS_2 QDNS, MoS_2 $QDNS_{ac}$ and MoS_2 $QDNS_{ac}$+ H_2O_2.

The results obtained from Raman spectral analysis were further corroborated by HRXPS analysis of sulphur. For the easiness of comprehending, we split the multi-fitting spectra into two regions (low and high binding energy regions). For MoS_2 QDNS, at pH 13, the sulphur peaks can be fitted into four, each corresponding to $S2p^{3/2}$ and $S2p^{1/2}$ of sulphur bonded to Mo (lower binding energy) and sulphur bonded to oxygen (higher binding energy region). The vigorous environment of the hydrothermal condition might have instigated some of the surface sulphur to undergo oxidation, which results in the appearance of peaks in higher binding energy region. These particular oxidized peaks are present in MoS_2 $QDNS_{ac}$

as well, along with the emergence of new sulphur peaks in the lower binding energy region. This could be due to the formation of salts, as discussed above. The disappearance of these lower energy extra peaks in the case of MoS_2 QDNS$_{ac}$+H_2O_2 exposes the possibility of complete oxidation of these molecules, which crop up in the higher binding region, as multiple peaks. Thus, we theorize that the etched sulphur from the surface of MoS_2 QDNS after the addition of mineral acids was forming NaHS which oxidized to its sulphate upon addition of H_2O_2 resulted in the subsequent quenching of fluorescence emission.

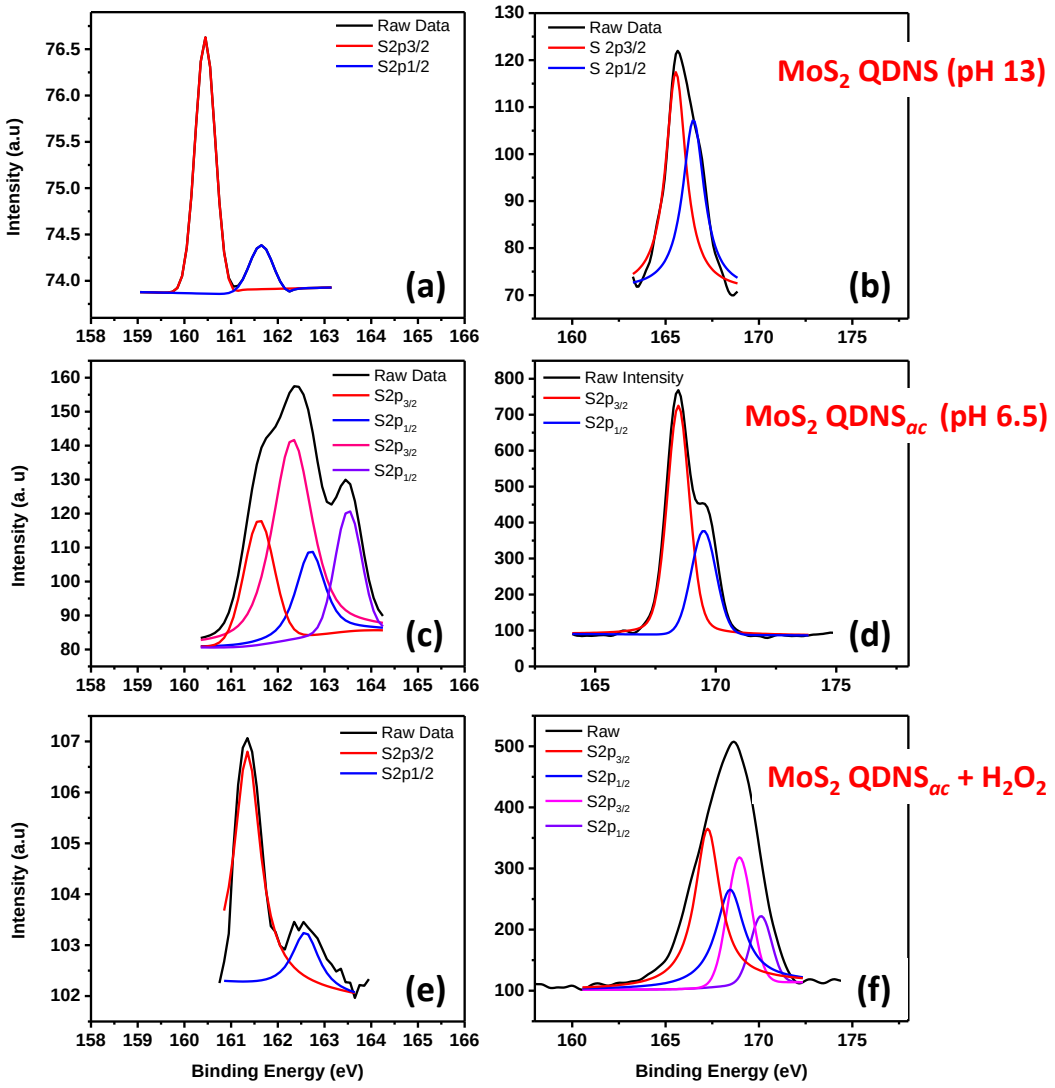

Figure 4.13: HRXPS S2p spectra of MoS_2 QDNS, MoS_2 QDNS$_{ac}$, MoS_2 QDNS$_{ac}$+ H_2O_2

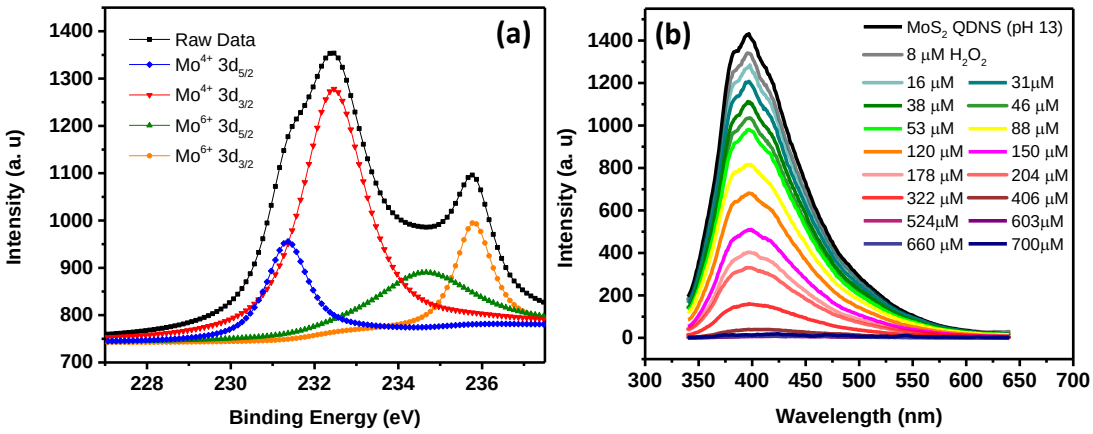

Figure 4.14: a) HRXPs spectra of Mo 3d of MoS_2 QDNS (pH 13) after the addition of H_2O_2 b) Response of PL emission of MoS_2 QDNS towards different concentrations of H_2O_2.

We have carried out control experiments to support our arguments related to the mechanism. The response of MoS_2 QDNS (pH 13) towards H_2O_2 showed that the sensor material underwent oxidation, which was manifested as PL quenching. The XPS results of MoS_2 QDNS + H_2O_2 showed the presence of Mo^{6+} oxidation state, which endorses the oxidation of the metal (Figure 4.14 a and b). Upon prolonged dialysis of the yellow-colored MoS_2 QDNS$_{ac}$, it was turned to light yellow. We are surmising this to the removal of small molecules (Na salts, as discussed previously) responsible for the yellow color. The PL emission from this dialyzed colorless solution was retained as expected due to the removal of IFE and FRET mediated quenching. It was noted that this solution was not responding to the H_2O_2 as a sensor in the linear concentration range (range given in Figure 4.2). These factors provide the proof that the emergence of PL emission upon addition of H_2O_2 is due to the oxidation of the above-mentioned small molecules (Figure 4.15).

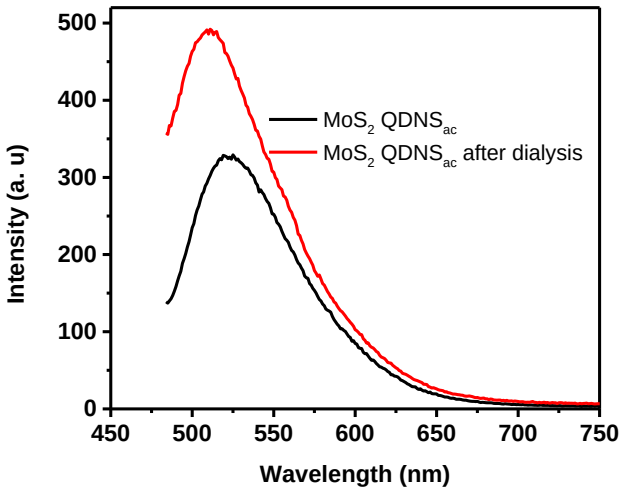

Figure 4.15: The PL emission spectra of MoS_2 $QDNS_{ac}$ (yellow-colored solution) and after dialysis (colorless solution)

The selectivity of H_2O_2 over other oxidizing agents such as $KMnO_4$ and $K_2Cr_2O_7$ can be explained based on their absorption behavior (Figure 4.16). Absorption of $KMnO_4$ has a substantial overlap with the PL emission of the sensor solution, which in turn can reduce the PL by energy transfer. A negligible enhancement effect of $K_2Cr_2O_7$ can be attributed to its feeble absorption at ~470 nm, the wavelength, used for exciting the sensor solution, which in turn leads to IFE and thus resulting only a weak enhancement.

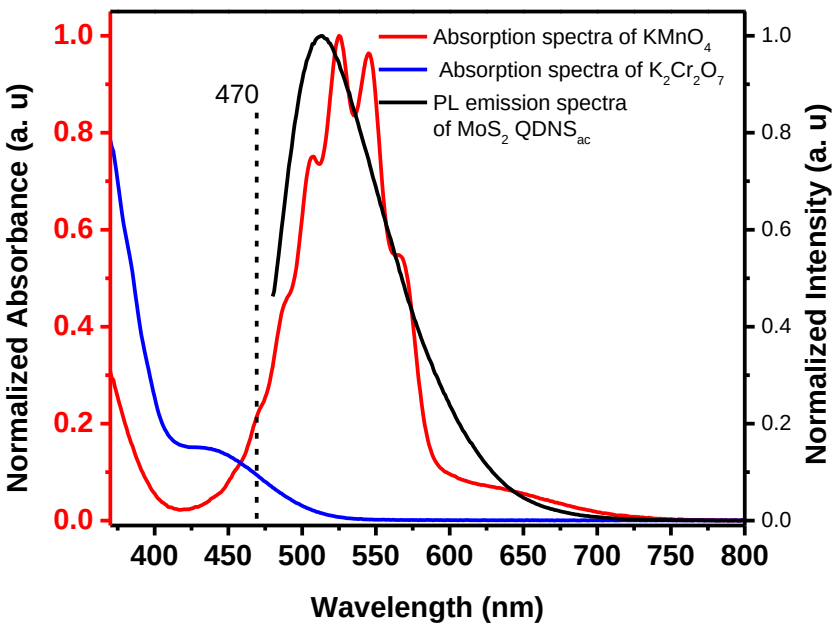

Figure 4. 16: Absorption spectra of $KMnO_4$ and $K_2Cr_2O_7$ along with the PL emission spectra of MoS_2 $QDNS_{ac}$.

4.3.4 MoS_2 $QDNS_{ac}$ as a Glucose Sensor

It is well known that the enzyme, glucose oxidase (GOx) selectively oxidizes glucose to gluconic acid and H_2O_2 (Pickup et al., 2005). Therefore, MoS_2 $QDNS_{ac}$ solution in the presence of GOx could be a potential candidate for the indirect detection of glucose. Before using it as a glucose sensor, we have ruled out the possibility of the PL recovery by glucose or GOx. It was found that there was negligible change in the luminescence properties of MoS_2 $QDNS_{ac}$ solution after the addition of either glucose or GOx.

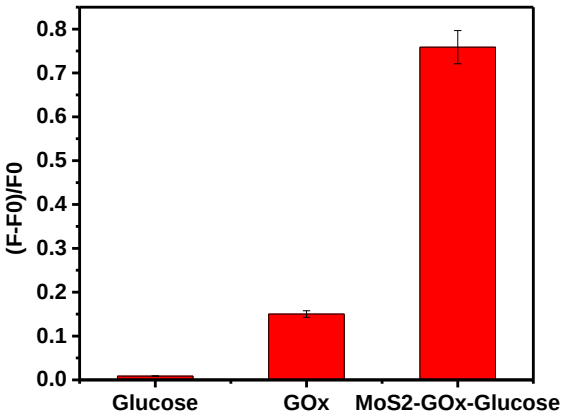

Figure 4.17: Comparison of PL enhancement of MoS_2 $QDNS_{ac}$ by glucose, GOx and glucose-GOx mixture. (50 µL of 1 mM of each solution has been used).

The quantity of GOx in the sensor was optimized initially by the titration of different concentrations of MoS_2 $QDNS_{ac}$-GOx with glucose to obtain maximum enhancement, and an optimum concentration of 0.2 mg/mL was used in the glucose detection experiments. The MoS_2 $QDNS_{ac}$-GOx (0.2 mg/mL of GOx in 2.5 mL of MoS_2 $QDNS_{ac}$) solution was our sensor system for glucose. This sensor responds linearly to the concentrations of glucose. It has been observed that the present glucose sensor enhances the PL intensity of MoS_2 $QDNS_{ac}$, nearly the same extent as that of H_2O_2 alone can do (Figure 4.18 a).

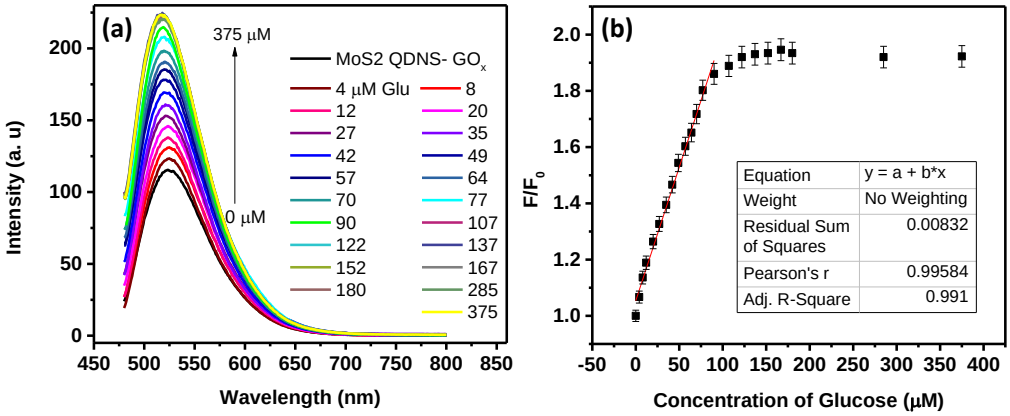

Figure 4.18: Enhancement of PL emission of MoS_2 $QDNS_{ac}$-GOx by glucose (0 to 286 µM concentrations of glucose have been used and glucose is abbreviated as Glu). (b) Calibration curve of the fluorescence of MoS_2 $QDNS_{ac}$ at λ_{max} (523 nm) Vs [Glucose] showing the linear relationship between F/F_0 Vs [Glucose].

The plot of F/F_0 to the concentration of glucose shows the Michaelis-Menton type curve (Figure 4.18 b), which is typical for enzyme-catalyzed reactions (Li et al., 2009b). There is good linearity between relative PL intensity and concentration of glucose until 90 µM, which shows the sensitivity of the sensor solution towards the detection of glucose. The dynamic range of the sensor was 4-90 µM. The selectivity of the sensor was also crucial as it determines the feasibility of the system as a potential sensor towards specific target analytes. To prove the specificity of the sensor (MoS_2 $QDNS_{ac}$–GOx) towards glucose, we have tested the response of the sensor towards other saccharides, amino acids, common metal ions, biologically active molecules, etc. and the response is summarized in Figure 4.19. It has been observed that the sensor responds selectively to glucose.

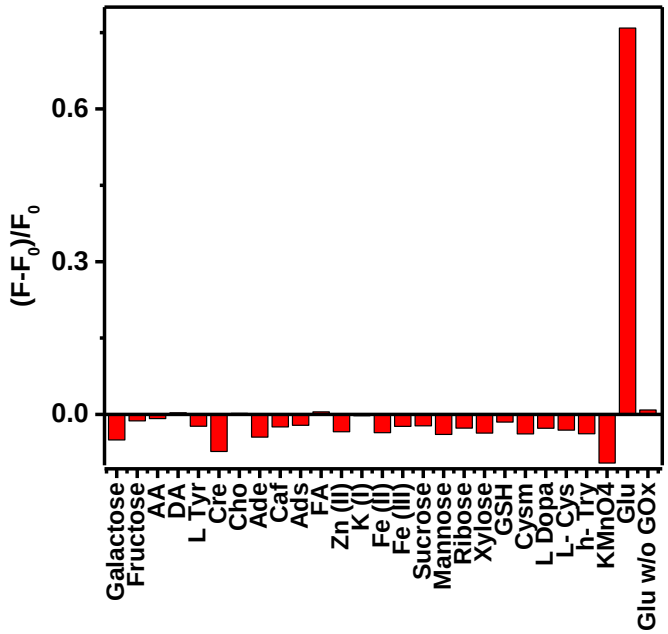

Figure 4.19: Fluorescence response of MoS_2 $QDNS_{ac}$–GOx towards various molecules, metal ions, etc. (50 µL of 1 mM of each solution has been used).

4.3.5 Real Sample Analysis

To verify the feasibility of the present sensor for the detection of H_2O_2 or glucose in real samples, we have analyzed green tea samples for H_2O_2 and blood samples for glucose detection by the standard addition method. PL spectra of the green

tea samples spiked with different concentrations of H_2O_2 were recorded and tabulated (Table 4.3). The recovery of H_2O_2 was in the range of 92-102%. To demonstrate the practicability of the detection of glucose content in blood samples, to a solution of MoS_2 $QDNS_{ac}$- GOx, aliquots of blood samples spiked with glucose were added. Recovery of the range of 96-109% was observed. All experiments were repeated three times and a mean value is reported.

Table 4.3: The concentration of H_2O_2 and glucose in green tea and blood samples, respectively.

Sample	Spiked (μM)	Measured (mean)	% Recovery
Green tea (spiked with H_2O_2)	38	36.4	95.7- 97.5
	50	49.2	92.1–100.3
	75	75.5	96.2–102.3
Human blood (spiked with glucose)	20	20.2	96.5–109.0
	40	40.2	97.3–102.3
	60	59.8	98.5–101.5

To demonstrate the capability of our sensor, we quantified the blood glucose of a diabetic patient and compared it with the clinical results (Table 4.4). The comparable values proclaim the effectiveness of the present method for accurate determination of glucose present in human blood without any tedious sample preparation step.

Table 4.4: Comparison of clinical test Vs. measurements taken using our sensor solution. In the clinical test, a standard colorimetric method GOD-POD method has been used. In this method, Glucose oxidase (GOD) catalyses the oxidation of glucose to gluconate. The formed hydrogen peroxide (H_2O_2) is detected by a chromogenic oxygen acceptor, phenol, 4-Aminophenazone (4-AP) in the presence of peroxidase (POD).

Test	Glucose Concentration (mM)	% Recovery	Glucose Concentration (mg/dL)	% Recovery
Clinical Result	8.30	-	150	-
Using Sensor Solution	8.15	98.19	146.7	97.8
	8.95	107.83	161.1	107.4
	8.25	99.39	148.5	99.0
	8.87	106.86	159.66	106.44
	8.38	100.96	150.84	100.56
Mean Value	8.52	102.65	153.36	102.24

4.4 Conclusion

In summary, we have developed a turn-on sensor for H_2O_2, using acidified MoS_2 hybrid nanoparticle (MoS_2 $QDNS_{ac}$). MoS_2 QDNS was prepared from the hydrothermal synthesis of bulk MoS_2 with NaOH, and the pH of the solution was changed to 6.5 by the addition of H_2SO_4. The PL intensity of MoS_2 $QDNS_{ac}$ was selectively enhanced by H_2O_2, which made it useful as an H_2O_2 sensor. The LOD of the sensor is 2 µM, with a linearity of 2- 94 µM. Upon integrating GOx with MoS_2 $QDNS_{ac}$, the same system could make use for the detection of glucose as well, as decomposition of glucose by GOx generate H_2O_2, which in turn will enhance the PL intensity of MoS_2 $QDNS_{ac}$. The feasibility of the sensor for the detection of real samples was tested in green tea and human blood, and the results were very satisfactory. We envisage that the present study can be extended for the detection of any biologically active samples which can generate H_2O_2 upon reaction with a suitable enzyme.

CHAPTER 5

SYNTHESIS OF WS_2 NANOMATERIALS

This chapter describes the synthesis and characterization of nanomaterials based on WS_2, using the hydrothermal reaction route, the same strategy used for the synthesis of MoS_2 based nanomaterials. The synthesis was accomplished by the hydrothermal reaction of WS_2 powder in aqueous NaOH. By varying the molar concentration ratio of WS_2 to NaOH, different types of nanomaterials such as quantum dots, nanosheets and a hybrid of quantum dots-nanosheets were obtained. Interestingly, all of these nanomaterials display luminescence emission spanning major portions of the UV and visible spectrum. Size-dependent photophysical properties of various WS_2 nanomaterials were investigated using UV- visible absorption spectroscopy as well as fluorescent emission spectroscopy. The morphological and structural aspects were unraveled by TEM, AFM, Raman spectroscopy and time-resolved fluorescence spectroscopy.

5.1 Introduction

Bulk 2H- WS_2 is a layered material with a monolayer thickness of ~0.9 nm that consists of a sandwiched atomic layer of W between two S layers forming a trigonal prismatic structure. Each W is connected to six S by strong covalent bond within a layer, whereas weak van der Waals force of attraction is playing a role in holding different layers intact. Thinning of vertical dimensions (thickness) of these multilayers into mono or bilayers of nanometer size regime is associated with a sudden leapt from indirect semiconductor to direct semiconductor character, which basically alters the electronic and optical properties of these materials (Chhowalla et al., 2013). Due to enhanced charge confinement, further reduction of size in the lateral dimension will lead to the formation of QDs having a direct energy gap of ~4 eV, which in a way manifest as visible light emission (Nguyen et al., 2016; Sharma et al., 2017).

Various methods, exploited for the synthesis of these photoluminescent (PL) WS_2 nanomaterials including mechanical and liquid exfoliation, chemical vapor deposition, hydrothermal synthesis, etc. (Xu et al., 2015; Gutiérrez et al., 2012; Yuan et al., 2014; Feng et al., 2017; Kim et al., 2017). Among these, hydrothermal based methods are preferred due to their easiness, green strategy and environmental viability. But due to extreme conditions inside the autoclave, generally, hydrothermal reactions end up with the formation of QDs and not of nanosheets. Nevertheless, the broader possibilities of these layered nanomaterials, the development of a simple yet cost-effective way for the size-controlled synthesis by tuning the synthetic reaction conditions such as concentrations of precursor materials, temperature or time, is still challenging and thus provide a wider berth for exploration.

This chapter focuses on the facile synthesis and characterization of different types of WS_2 based nanomaterials from WS_2 powder. We varied the ratio of WS_2 powder to NaOH such a way that tuning of the morphology and type of nanoparticles formed during the hydrothermal synthesis can be possible. Highly fluorescent nanoparticles such as pure quantum dots (QDs), and nanosheets (NSs) of the size ranging from 2 nm to 1 µm were obtained along with the hybrid materials which contain both QDs and NSs. The WS_2:NaOH molar ratio was varied from 1:0, 1:0.25, 1:0.50, 1:0.75 to 1:1. Detailed morphological and spectroscopic characterization has been carried to understand the chemical and physical nature of the nanomaterials. Further calculations show that the quantum yield (QY) of each solution is different and obtained the highest value of 4.9% for 1:0.25 molar ratio of WS_2 to NaOH. One of the interesting properties of the present WS_2 nanomaterials is their excitation dependent PL emission. We envisage that the present strategy would be a key for the synthesis of similar 2D layered materials and these materials can be made use for various intriguing applications.

5.2 Experiments and Methods

5.2.1 Reagents and Materials

Tungsten disulphide (WS_2 powder of particle size 2 μm, 99% assay) and sodium hydroxide were purchased from Merck India Ltd. Quinine sulphate and dialysis bag were purchased from Sigma- Aldrich, USA. Doubly distilled water was used throughout the experiments. All reagents purchased were of analytical grade and used without further purification.

5.2.2 Instrumentation

UV-visible spectra were recorded using a Carry 100 UV-visible spectrometer. All steady-state fluorescence measurements (excitation and emission) were done using FluoroMax-4C Spectrofluorometer (Horiba Instruments, USA). The excitation and emission slit widths were fixed at 5 nm with an integration time of 0.1 ns. Time-resolved fluorescence measurements were performed using the time-correlated single-photon counting (TCSPC). TCSPC measurements were performed at the excitation wavelength of 344 nm and decay profiles were collected at 410 nm for WS_2 QDs. Transmission electron microscopy (TEM) images were obtained using a JEOL 2100 instrument and the atomic force microscope (AFM) images were taken using the Agilent 5500 scanning probe microscope (non-contact mode). Raman spectra were measured in a Renishaw confocal Raman microscope using a 532 nm laser. Quantum yield was calculated using quinine sulfate ($\varphi = 0.54$) as standard at 330 nm excitation. Photostability experiments were carried out by irradiating aqueous solution of WS_2 QDs under 360 nm UV lamp (48 W power) and fluorescence spectra of photo-irradiated samples were recorded at specified time intervals.

5.2.3 Synthesis of WS_2 based Nanomaterials

Different WS_2 nanomaterials were prepared by hydrothermal reaction of commercially available WS_2 powder and NaOH in aqueous medium by taking different molar ratios. Briefly, WS_2 powder (100 mg) was mixed with NaOH (0, 4.03, 8.06, 12.09, 16.13 mg respectively for 1:0, 1:0.25, 1:0.50, 1:0.75 and 1:1 ratios) in 10 mL of water. The resultant solution was taken in a Teflon-lined autoclave and kept for 24 h at a temperature of 220 ºC. The solution obtained after the reaction was centrifuged at

3000 rpm for 10 min, the supernatant was collected filtered and dialyzed for 24 h using a dialysis bag (MWCO 500). This purified, light-yellow solutions were used for all further studies.

5.3 Results and Discussions

5.3.1 Synthesis and Characterization of WS_2 Nanomaterials

The success of the synthesis of MoS_2 nanomaterials viz MoS_2 QDNS and MoS_2 NSs by the hydrothermal reaction of MoS_2 powder and NaOH motivated us to check the generalization of this strategy for the synthesis of WS_2 based nanomaterials. Since our primary aim is to fabricate WS_2 nanomaterials for fluorescent-based sensing applications, various synthetic parameters were monitored for the optimization of reaction conditions such as temperature, time, and concentration of WS_2 to NaOH to obtain nanomaterials with high PL emission. By changing the concentration ratio of WS_2 to NaOH in a small scale (1: 0, 1: 0.25, 1: 0.50, 1: 0.75, and 1: 1 molar ratio of WS_2 to NaOH), we have obtained different types of nanomaterials such as quantum dots (QDs), nanosheets (NSs) and heterostructures consist of QDs-NSs, by keeping the reaction at 220 $^{\circ}$C for 24 h. Solutions with WS_2 to NaOH ratio of 1:0, 1:0.25 and 1: 0.50 preferably form QDs, whereas the ratio of 1:1 solution gives nanosheets. The WS_2 to NaOH ratio of 1:0.75, on the other hand, gives a hybrid mixture of QDs and NSs. These results essentially denote that, the lower the concentration of NaOH, the higher the chance for the formation of QDs. We tried to comprehend the difference in the behavior of MoS_2 and WS_2 powder towards hydrothermal reaction in the presence of alkali based on their surface energy and wettability. The wettability of MoS_2 towards water is low compared to WS_2. Upon the addition of alkali, the surface energy of water will decrease. Therefore, a higher amount of alkali (say 1:20 concentration ratio) will be favorable for MoS_2 to be miscible with water in a better proportion which can further facilitate exfoliation and oxidative cutting of MoS_2 sheets into smaller particles. Whereas for WS_2, with comparable surface energy with water, can go for extensive exfoliation even without the presence of alkali (note that, we obtained QDs for WS_2 to

NaOH ratio 1:0). Further, the OH^- ions furnished by NaOH might be aiding for the retention of sheets, by increasing its concentration (WS_2 to NaOH ratio 1:1) by satisfying the dangling bonds formed during the hydrothermal reaction and thus giving them extra stability.

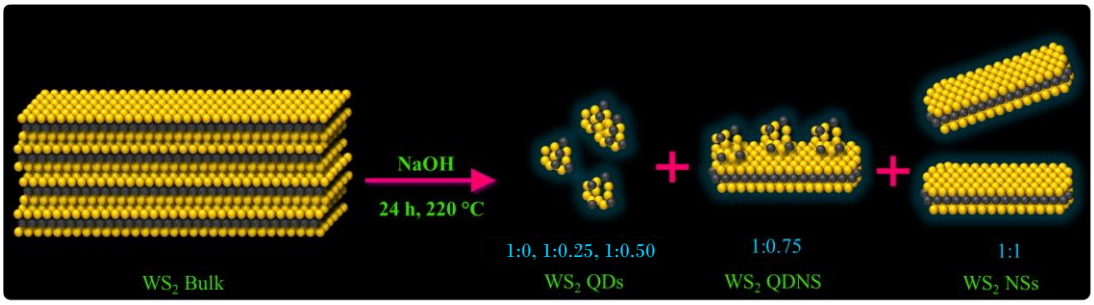

Figure 5.1: Synthesis of WS_2 based nanomaterials by hydrothermal route

The synthesis of WS_2 nanomaterials from WS_2 powder and alkali via hydrothermal reaction is shown in Figure 5.1. The color of the QDs solutions is slightly yellow, whereas the nanosheets solutions are colorless. Detailed morphological and spectroscopic characterization such as TEM, AFM, XRD, UV-vis absorption spectroscopy, steady-state and time-resolved fluorescence spectroscopy, Raman spectroscopy have been employed for better understanding the synthesized materials.

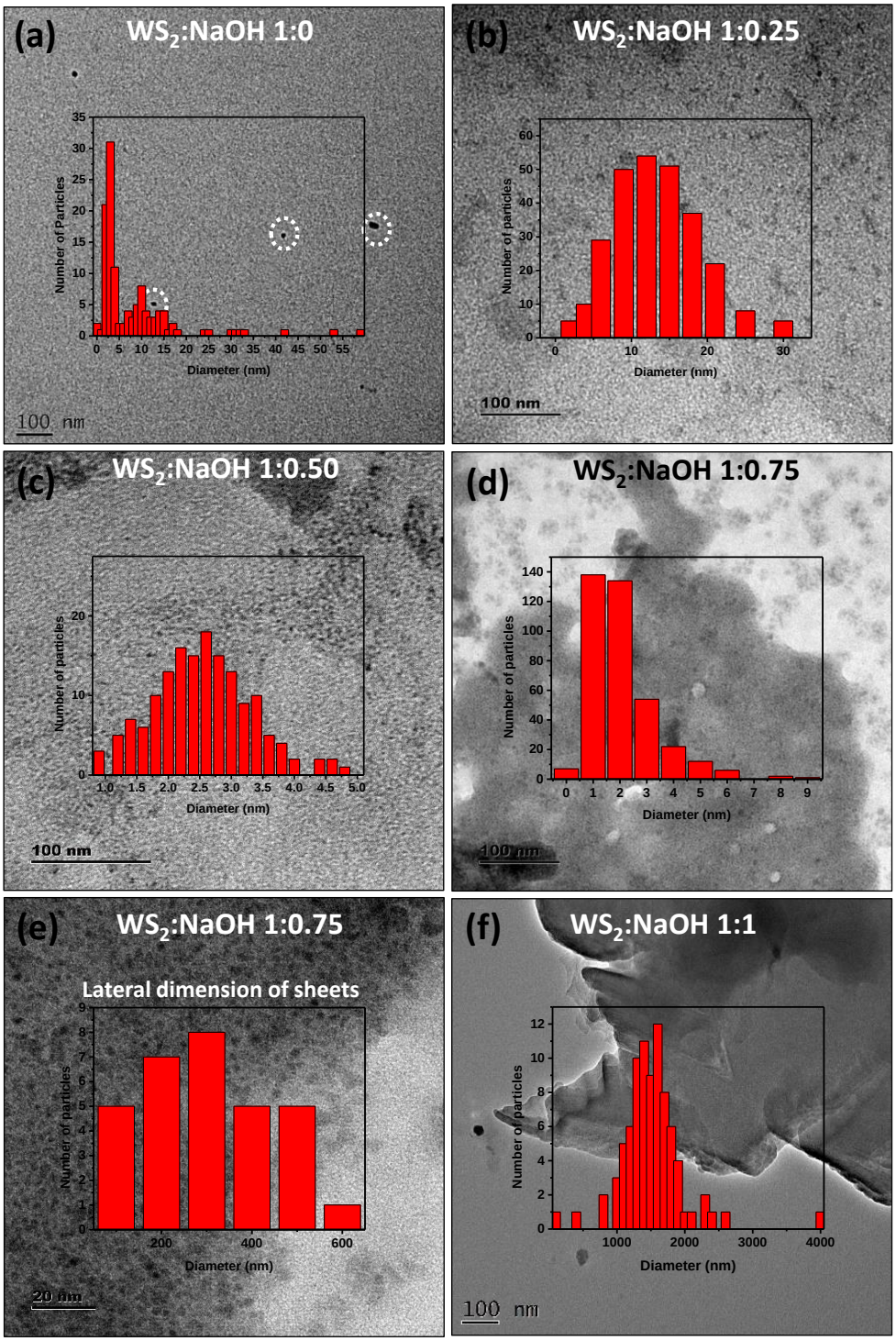

Figure 5.2: TEM images of WS_2 nanoparticles synthesized by varying the molar ratios of WS_2 to NaOH: (a) 1:0, (b) 1:0.25, (c) 1:0.50, (d) and (e) 1:0.75, (f) 1:1. Inset shows the size histogram obtained for QDs (a to d) and NS (e and f) of respective samples.

The morphological and nanostructural characteristics of the WS_2 materials were analysed using TEM analysis. The TEM micrographs (Figure 5.2) show the formation of the nanomaterials with various sizes and shapes. For 1:0 sample, where there is no NaOH, the size distribution of QDs is heterogeneous and the average value is ~21 nm is observed. As the concentration of NaOH increases, the average size of QDs decreases to ~12 nm for WS_2 to NaOH ratio of 1:0.25, ~2 nm for 1:0.5, and 1:0.75. For the concentration of NaOH 1: 0.75 and 1:1, the formation of nanosheets are observed. The size of the sheets for WS_2 to NaOH ratio of 1:0.75 is around 350 nm, and that of 1:1 is in the range of micrometers.

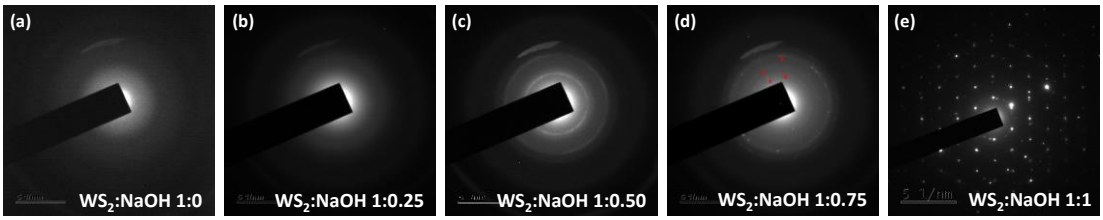

Figure 5.3: SAED patterns of WS_2 nanoparticles synthesized by varying the molar ratios of WS_2 to NaOH: (a) 1:0, (b) 1:0.25, (c) 1:0.50, (d) 1:0.75, and (e) 1:1.

The SAED pattern obtained from these materials depicts their amorphous or crystalline nature (Figure 5.3). The aureole present in the SAED pattern of QDs is a clear indication of their amorphous nature, which might have stemmed from the enhanced surface defects or dangling bonds found in QD surfaces. On the other hand, sheets are present in the samples 1:0.75 and 1:1 retained their crystallinity even after undergoing vigorous hydrothermal reaction conditions. The spots in SAED suggest the polycrystalline nature of these materials which demonstrate the exfoliation of bulk WS_2.

The Raman studies provide structural information of the WS_2 nanomaterials. Raman spectrum of WS_2 powder consists of first-order and second-order peaks, of which four modes are important; viz. E_{1g}, E^2_{2g} A_{1g} and E^1_{2g} modes (Cong et al., 2014; Loh et al., 2015). The first two modes are generally absent in the spectra due to forbidden selection rule in the back-scattering geometry and the limited rejection against Rayleigh scattering (Zeng et al., 2013). The WS_2 powder shows two main peaks

at 415 and 348 cm^{-1}, see Figure 5.4(a), which corresponds to the first order in-plane E^1_{2g} and out of plane A_{1g} phonon modes of 2H-WS_2, respectively. The key aspect of these modes is that the frequency difference between these two can showcase the number of layers present (Zeng et al., 2013; Yuan et al., 2015). For the samples prepared from WS_2 to NaOH ratio of 1:0.75 and 1:1; the two modes are present with a frequency difference of 69.8 and 66 cm^{-1}, which corresponds to the tri-layer and monolayer, respectively. On the other hand, for the WS_2:NaOH ratios of 1:0, 1:0.25 and 1:0.50, these two peaks are absent and this particular observation is typical for QDs. This absence is due to the decrease in the interaction force caused by van der Waals among interlayers (Yuan and Huang, 2015; Yan et al., 2016b; Xu et al., 2015).

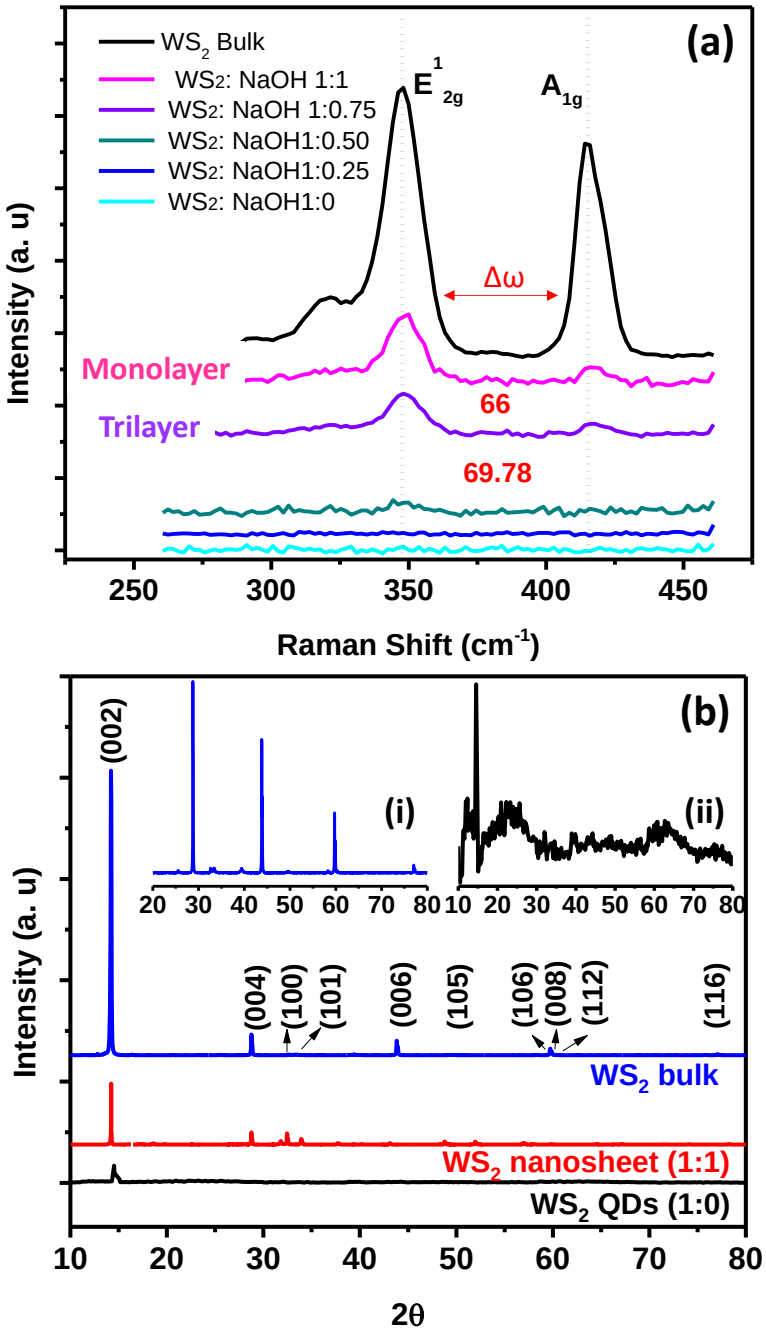

Figure 5.4: (a) Raman spectra of WS_2 nanoparticles synthesized with the various molar ratios of WS_2 to NaOH. (b) XRD patterns of WS_2 powder, WS_2 nanosheet, WS_2 QDs. Inset: (i) shows the enlarged XRD spectrum of WS_2 powder and (ii) WS_2 QDs.

The crystalline phase of the WS_2 nanomaterials was examined as there is a possibility for phase change in hydrothermal conditions. As shown in Figure 5.4(b), XRD patterns of the pure sheet (WS_2:NaOH ratio of 1:1) and a typical QDs

(WS_2:NaOH ratio of 1:0) were recorded, along with the precursor powder. The WS_2 powder displays various diffraction peaks corresponding to the different planes of highly crystalline hexagonal 2H form, with maximum intensity from (002) plane along with peaks corresponding to (004), (100), (101), (006), (105), (106), (008), (112) and (116) planes. Interestingly, for nanosheets, though less in intensity, most of the peaks are present such as (002), (004), (100), (101), (106) and (008) which reflects its crystalline nature along with the retention of 2H phase. But for the QDs sample, the patterns suggest a mixture of crystalline and amorphous nature. The peak corresponding to (002) plane is of less intense along with broadening of the peak due to the scaling down of thickness into a few nanometers upon exfoliation.

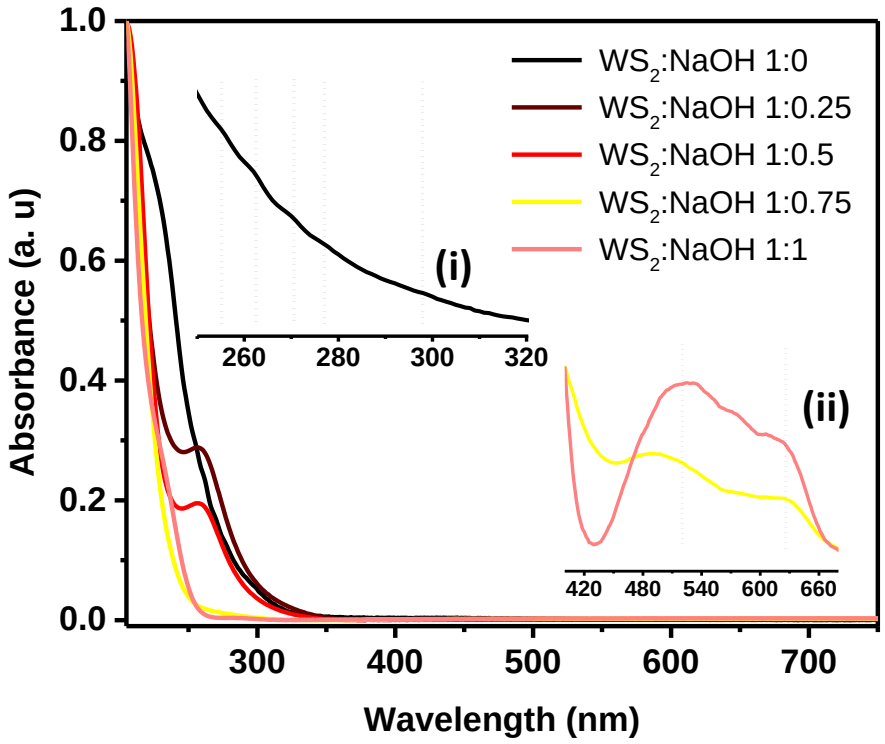

Figure 5.5: Normalized UV-visible absorption spectra of WS_2 nanomaterials obtained at different molar ratios of WS_2 to NaOH: (1:0, 1:0.25, 1:0.50, 1:0.75, and 1:1) 1:0 to 1:1. Inset shows the zoomed spectra of (i) 1:0 sample from 220 to 350 nm and (ii) 1:0.75 and 1:1 sample from 400- 700 nm.

Based on these characterizations, it is clear that nanoparticles of varying morphology and structural attributes have been produced during the hydrothermal

reaction, merely upon changing the molar ratio of the precursors; WS_2 powder and NaOH, by keeping the optimsed synthetic parameters such as temperature and time. Umpteen reports are available regarding the change in optical behaviors of nanoparticles by varying the size from a few hundred to tens of nanometers. Therefore, thorough photophysical studies were performed to explore the optical properties of these materials. Genarally, in the case of WS_2 powder, four major absorption peaks are available at positions 630, 528, 456 and 417 nm, which corresponds to A, B, C and D excitonic peaks, respectively (Bayat et al., 2017). The excitonic absorption arising from direct gap transitions at the K point of the Brillouin zone is responsible for the emergence of A and B peaks whereas the electronic transitions from the deep valence band to the conduction band are manifested as C and D peaks (Mishra et al., 2015). As the size of the sheets shrinks vertically or laterally, due to enhanced quantum confinement effects, and edge effects, these excitonic positions will be blue shifted. Reports are available, where for QDs absorption features will be available only in the UV region (Lin et al., 2013). Therefore we are anticipating optical features for different nanoparticles following the same fashion. As seen in Figure 5.5, the 1:0 (the WS_2:NaOH ratio) samples which contain QDs of various sizes show multiple absorptions features starting from 300 nm onwards/to lower wavelength, with shoulder peaks at 297, 277, 269, 260 and 255 nm. The reason behind these multiple shoulder peaks could be due to the presence of wide size distribution of QDs formed during the synthesis, ranging from the as small value of 0.8 nm to 50 nm. Whereas other nanomaterials show a narrow range of size distribution, which makes NaOH a crucial precursor in the synthesis of WS_2 nanomaterials. When the WS_2:NaOH ratio was 1:0.25 and 1:0.50, it shows a distinct absorption feature around 270 nm, which implies the homogeneity of the QDs present. For WS_2:NaOH ratio, 1:0.75, having the smallest QDs, gives a sudden hike in absorption in high energy region (~260 nm) along with the presence of peaks around 625 and 500 nm which correspond to A and B excitons emerging from the sheets lying below the QDs. For 1:1 (WS_2:NaOH ratio) sample also gives two absorption peaks, at 626 and 525 nm which are considered as the signature peaks for sheets.

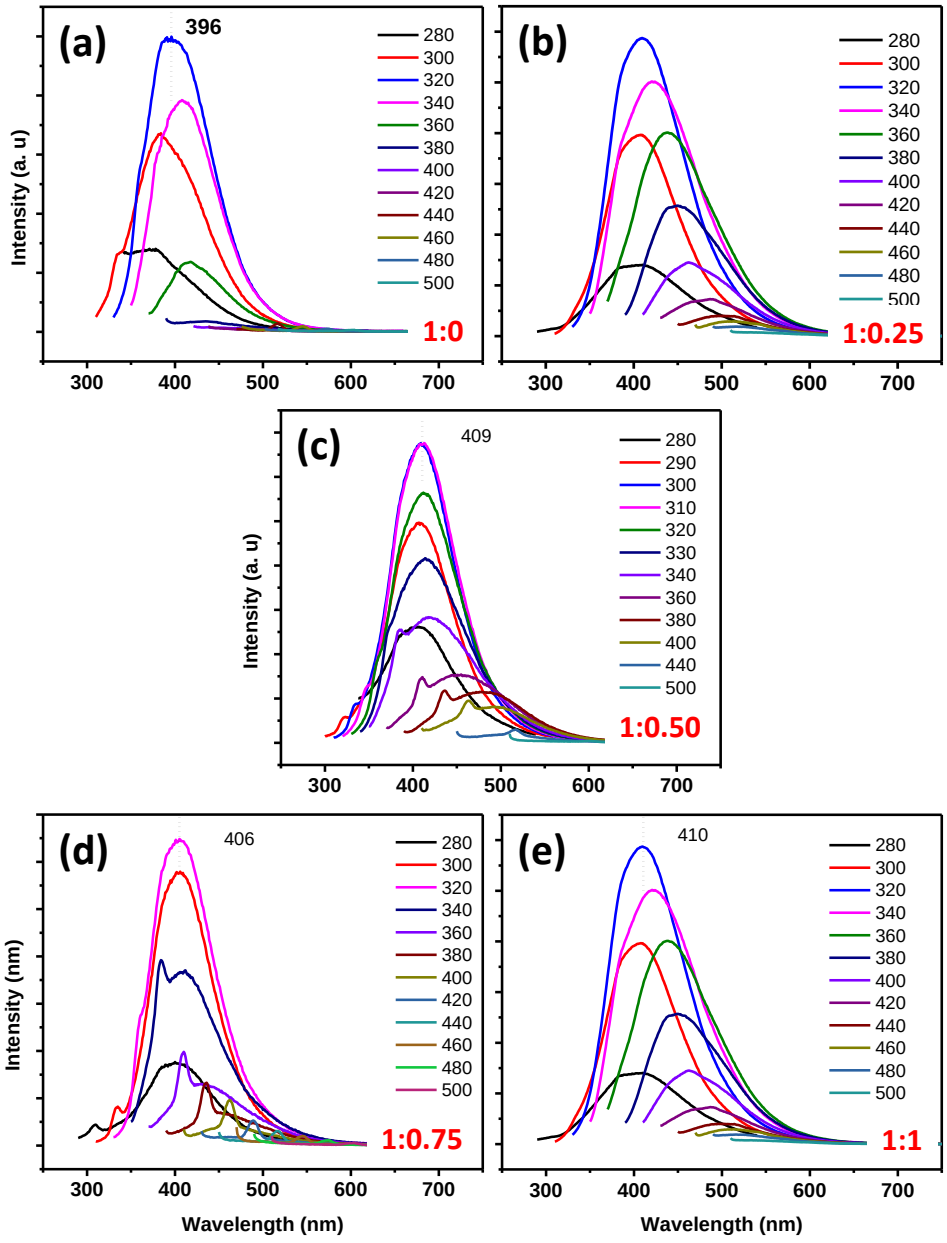

Figure 5.6: Excitation dependent emission of WS_2 nanomaterials at different molar ratios of WS_2 to NaOH: (a) 1:0, (b) 1:0.25, (c) 1:0.50, (d) 1:0.75, and (e) 1:1 samples

Table 5.1: Quantum yield of five WS_2 nanomaterials at different molar ratios of WS_2 to NaOH (1:0 to 1:1)

Sample (WS_2:NaOH)	Quantum Yield (ϕ)
1:0	1.14%
1:0.25	4.92%
1:0.50	2.53%
1:0.75	1.89%
1:1.0	2.15%

Another vital feature manifested as a result of the quantum confinement effect is the emergence of PL from these materials. All the five samples show good PL emission (see Figure 5.6) with quantum yield ranging from 1.14 to 4.92% calculated using quinine sulphate as the standard (Table 5.1). One of the major characteristics of all the five samples are, their excitation depended emission, with emission maxima ~396 nm (for WS_2:NaOH ratio of 1:0, 320 λ_{ex}), 431 nm (for WS_2:NaOH ratio of 1:0.25, 350 λ_{ex}), 409 nm (for WS_2:NaOH ratio of 1:0.50, 310 λ_{ex}), 406 nm (for WS_2:NaOH ratio of 1:0.75, 310 λ_{ex}) and 452 nm (for WS_2:NaOH ratio of 1:1, 360 λ_{ex}). Even though WS_2:NaOH ratio of 1:1 contains sheets, the PL emission spectra give maximum intensity around blue region upon exciting at 360 nm, instead of the red region as reported elsewhere (Hazarika and Mohanta, 2018; Li et al., 2019b). A reason behind this extraordinary behavior is still blurry and needs more systematic analysis. The photocarrier lifetime of excitons, generated upon excitation of nanoparticles WS_2:NaOH ratio of 1:0 to 1:1 using a 344 nm pulsed diode laser source, have been investigated using time-correlated single-photon counting spectroscopy (TCSPS). Earlier studies show that WS_2 monolayer sheets are having a very short lifetime of 800 ps (Yuan et al., 2015). As the lateral and longitudinal dimension of the bulk sheets decreases, the photo-excited carrier lifetime found to be increased due to enhanced stability of the excitons in the case of MoS_2 based nanoparticles and we are anticipating the same in the case of WS_2 as well (Mukherjee et al., 2016; Mani et al.,2017). Table 5.2 gave a clear reflection of this phenomenon. All decay curves were fitted bi-exponential except for WS_2:NaOH ratio of 1:0.75, which has three-lifetime component,

by keeping the numerical fitting parameter, χ^2 near to 1. The WS_2 to NaOH ratio of 1:0 sample, having the largest QDs present have the fastest lifetime components of 1.69 and 7.48 ns. As the size of QDs decreases, there is a regular increase in these components (4.42 and 14.70 ns for WS_2:NaOH ratio of 1:0.25, 5.31 and 14.60 for WS_2:NaOH ratio of 1:0.50, 6.76 and 15.01 ns for WS_2:NaOH ratio of 1:0.75). The third lifetime component in the case of 1:0.75 might have emerged from the sheets of lateral dimension in the nano regime, again having a small value of 2.69 ns. On the other hand, for 1:1, which contains only sheets from nano to micro size, there is a sudden decrease in the lifetime values which is comparable with 1:0 (WS_2 to NaOH ratio) sample. From this, we conclude that the lifetimes of photo-excited carriers from these nanoparticles were strongly depends on their morphology and dimension.

Table 5.2: Table showing lifetime analysis of WS_2 different nanoparticles with WS_2: NaOH ratio, 1:0 to 1:1

System	τ_1 (ns)	α_1	τ_2 (ns)	α_2	τ_3 (ns)	α_3	χ^2
1:0	1.69	57.45	7.48	42.55			1.03
1:0.25	4.42	33.54	14.70	66.46			1.05
1:0.50	5.31	58.51	14.60	41.49			1.17
1:0.75	6.76	65.37	15.01	19.15	2.69	15.47	1.16
1:1	1.94	14.19	11.8	85.81			1.24

5.3.2 Stability of WS_2 based Nanoparticles

Fluorophores of having high photostability are demanding in fluorescence imaging and sensing applications. Owing to the high photo-degradability of modern dyes, the carbon and semiconductor-based fluorescent materials have opted in recent times. We have checked the temporal as well as photostability of WS_2 QDs, the sample that possesses the highest QY. As is visible from Figure 5.7, WS_2 QDs, possess good temporal stability as 57% of the original intensity is maintained after six months of preparation under room temperature conditions. Therefore, stable fluorescence chemical sensors are feasible with the present QDs. For photostability studies, an aqueous solution of WS_2 QDs was irradiated with UV light (365 nm, Power: 8 W) for different time intervals and the PL intensity was subsequently recorded. In the case of

WS_2 QDs phenomenal stability under UV radiation, 90% of the initial intensity was maintained even after continuous irradiation of UV for a duration of 8 h, which reflects the high photostability of present nanomaterial, a promising alternative for bio-imaging and sensing applications.

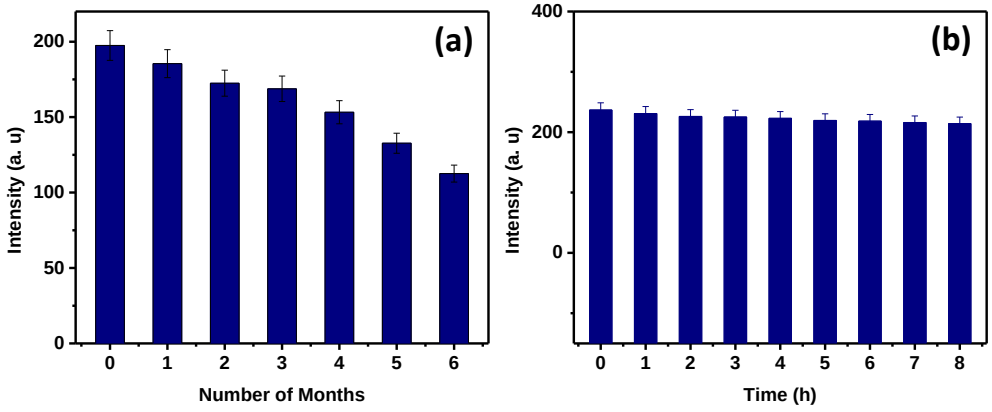

Figure 5.7: (a) Temporal as well as (b) photostability of WS_2 QDs with a WS_2 to NaOH molar ratio of 1:0.25.

5.4 Conclusion

WS_2 nanosheets of varying layer thickness (bi and tri), a hybrid of WS_2 nanosheets-quantum dots and WS_2 QDs were synthesized by the simple hydrothermal reaction by varying the concentration ratio of precursors. The synthesis route is fast and facile, economically viable and does not require hazardous chemicals. The WS_2 nanomaterial formed by the hydrothermal reaction of WS_2 to NaOH ratio of 1:0.25 shows the best QY value compared to other samples. A detailed microscopic and photophysical characterizations have been carried out to unearth the unique properties of the present nanomaterials. Excellent temporal as well as photostability, makes the current nanomaterials prospective candidates for bio-imaging, chemical sensing and light-emitting applications. We envisage that the scope and reach of the WS_2 nanomaterials can be exorbitant and can be readily applicable in the areas of energy storage, electrochemical, chemi-resistive, fluorescent-based sensing, adsorbents for the removal of toxic materials, hydrogen evolution catalysis, etc.

CHAPTER 6

SELECTIVE DETECTION OF TRINITROPHENOL USING HIGHLY LUMINESCENT WS_2 QUANTUM DOTS

This chapter deals with the selective sensing of trinitrophenol (TNP) aka picric acid in a solution using the luminescent WS_2 quantum dots (WS_2 QDs). The high fluorescent emission of WS_2 QDs was found to be quenched in the presence of trace amounts of TNP, due to energy transfer as well as electron transfer. These multiple mechanisms of quenching are reasoned for the high selectivity towards TNP compared to structurally and chemically similar interferants such as dinitrophenol (DNP), dinitrotoluene (DNT), etc.

6.1 Introduction

Trinitrophenol (TNP), *aka* picric acid is an explosive belong to nitroaromatics (NAs) family. Even though it received less attention by the scientific community compared to trinitrotoluene (TNT), another NA explosive, the superior explosive caliber and heavy toxicity of TNP earn its wide recognition recently (Ma et al., 2012; Dong et al., 2013; Lin et al., 2015; Jing and Li, 2018; Jiang et al., 2018; Chen et al., 2019). TNP is widely used in the dye industry, rocket fuels, fireworks, pharmaceuticals, chemical laboratories, forensic research, etc. and easily find their way to soil and water bodies (Rong et al., 2014). TNP is proven to be harmful to aquatic as well as terrestrial lifeforms, and it can cause various health issues such as skin irritation, damage to respiratory systems, abnormal liver functioning, anemia etc. in human beings (Wang and Ni, 2014). It is also recognized as a human carcinogen and the poor biodegradability of these molecules ensures its quantitative trace- level detection urgent and appealing. Liquid- liquid-based microextraction technique, immunosensor based on the surface plasmon resonance, optical methods such as fluorescence,

Raman, colorimetry etc. are general methods adopted for the selective and sensitive detection of TNP (Sylvia et al., 2000; Naddo et al., 2007; Peng et al., 2011; Ye et al., 2015). The major challenge of many of these detection strategies towards specific detection of TNP over other NAs owes to the electron-deficient nature of TNP as well as other NAs. Therefore, any method, which can foster selective detection of TNP without the need of any chemical separation is highly appealing.

A selective turn off sensing of TNP was realized using highly photoluminescent (PL) MoS_2 quantum dots with a detection limit of 95 nM. PL resonance energy transfer, electronic energy transfer, together with electrostatic interaction of TNP with MoS_2 QDs warrant the selectivity towards TNP compared with TNT or other NAs (Wang and Ni, 2014). Whereas the fast quenching of PL emission of nitrogen-doped graphene quantum dots due to electron transfer as well as the formation of non-fluorescent spirocyclic Meisen- Heimer complex was accomplished by Lin et al. (2014). The limit of detection of the sensor solution was 0.30 µM with linearity ranging from 1 to 60 µM. A label-free sensing approach was designed by Rong et al. (2014) employing fluorescent graphitic carbon nitride nanosheets. Remarkable selectivity and sensitivity were obtained thanks to the inner filter effect and molecular interaction operating as quenching mechanism, with a limit of detection of 8.2 nM with a linear range of 0- 10 µM.

It has been observed that the fluorescence intensity of highly luminescent WS_2 quantum dots, synthesized using the hydrothermal method from WS_2 powder and NaOH in 1:0.25 molar ratio, were quenched in a linear fashion in the presence of TNP. The acute quenching of PL emission of WS_2 QDs by TNP is attributed to multiple mechanisms such as Förster resonance energy transfer, electron transfer and inner filter effect which fortify the selectivity towards TNP compared to structurally similar molecules. Whereas at higher concentrations, the rate of quenching was amplified due to the advent of aggregation of QDs. The limit of detection of the present sensor is found to be a low value of 0.27 µM, with two linear ranges from 0.5 to 63 µM and 63 to 94.5 µM. We have also portrayed the selectivity towards TNP over other NAs such

as dinitrophenol (DNP), orthonitrophenol (ONP), dinitrotoluene (DNT), phenol (PHE) and nitrobenzene (NB) and the selectivity of the sensor of in terms of selectivity factor (SF). We have also illustrated a visual detection of TNP using a PVA film impregnated with WS_2 QDs.

6.2 Experimental Section

6.2.1 Reagents and Materials

Tungsten disulphide, sodium hydroxide and sodium nitrate were purchased from Merck India Ltd. TNP was purchased from Sigma Aldrich, India. DNP was from Otto Chemicals. Dinitrophenol (DNT), *o*-nitrophenol (ONP), *o*-nitrotoluene (ONT), nitrobenzene (NB), benzaldehyde (BAL), benzoic acid (BA), aniline (ANI), phenol (PHE), benzene (BEN) and toluene (TOL) were procured from SRL Chemicals, India. Double distilled water was used throughout the experiments. All purchased reagents were of analytical grade and used without further purification.

6.2.2 Instrumentation

UV-visible spectra were recorded using a Carry 100 UV-visible spectrometer. All steady-state fluorescence measurements (excitation and emission) were carried out using FluoroMax-4C Spectrofluorometer (Horiba Instruments, USA). Both excitation and emission slit widths were fixed at 5 nm with an integration time of 0.1 ns. Time-resolved fluorescence measurements were performed using time-correlated single-photon counting (TCSPC). TCSPC measurements were performed at an excitation wavelength of 344 nm and decay profiles were collected at 410 nm. Transmission electron microscopy (TEM) images were obtained using a JEOL 2100 instrument and the atomic force microscope (AFM) images were taken using an Agilent 5500 scanning probe microscope (non-contact mode). Raman spectra were measured in a Renishaw confocal Raman microscope using 532 nm laser. X-ray photoelectron spectroscopy and (XPS) studies of WS_2 powder, sensor solution and WS_2-TNP mixture were performed using an Omicron ESCA probe spectrometer with polychromatic Mg Kα radiation.

6.2.3 Synthesis of WS_2 QDs

The synthesis of WS_2 nanomaterial were discussed in the previous chapter (Chapter 5). We used WS_2: NaOH ratio as 1:0.25 in this work. Briefly, WS_2 powder (100 mg) was mixed with NaOH (4.03 mg) in 10 mL of water. The resultant solution was taken in a Teflon-lined autoclave and kept for 24 h at a temperature of 220 °C. The solution after the reaction was centrifuged at 3000 rpm for 10 min, the supernatant was collected filtered and dialyzed for 24 h using a dialysis bag (molecular weight cut off 500, MWCO500). This purified, light-yellow solutions were used for all further studies.

6.2.4 Sensor Applications of WS_2 QDs

The PL quantum yield of the QDs solution was quantified using quinine sulphate as the reference. 2 mL of WS_2 QDs solution was utilized as the sensor solution in all experiments. To this solution, 10 μL of 10^{-4} M TNP solution was added stepwise and fluorescence measurements were conducted. Response time of the sensor is calculated to be 5 minutes.

The selectivity of the present sensor solution was tested using 100 μL of a 1 mM solution of various analytes. We used several metal ions (Na^+, K^+, Sn^{2+}, Pb^{2+}, Mg^{2+}, Al^{3+}, Ca^{2+}, Fe^{2+}, Fe^{3+}, Co^{2+}, Ni^{2+}, Cu^{2+}, Zn^{2+}, Ag^+ and Cd^{2+}), common organic solvents such as benzaldehyde (BAL), benzoic acid (BA), aniline (ANI), phenol (PHE), benzene (BEN) and toluene (TOL), *o*-toluidine (O-TOL), aniline (ANI), also compounds such as 2,4-dinitrophenyl hydrazine (DNPH) and 2-hydroxy-5-nitro-benzaldehyde (HNB) were also used for selectivity studies. The excitation wavelength used was 320 nm for all the sensing experiments.

6.2.5 Fabrication of QDs impregnated PVA film (Sensor film)

A sensor film was fabricated using polyvinyl alcohol (PVA) as a matrix. For this, 5 mg of WS_2 QDs was dissolved in 15 mL of water containing 1.2 g of PVA at 85 °C and continuously stirred for 1 hr. The resultant solution was then cast on a clean

glass plate and annealed at 60 °C. After cooling to room temperature, the sheet is peeled off from the glass plate and used as the sensor film.

6.3 Results and Discussions

6.3.1 Characterization of WS_2 QDs

WS_2 QDs prepared at a molar ratio of 1:0.25 of WS_2 to NaOH shows a quantum yield (4.9 %) which is best among the various molar ratio. We made use of this sample for fluorescent-based sensing applications. Detailed microscopic and photophysical characterization of WS_2 QDs were performed before use it as a sensor. The TEM and AFM micrographs of WS_2 QDs show its nanostructure and the homogeneous size distribution. As evident from the TEM image (Figure 6.1), the QDs were found to be distributed in homogenous fashion with an average size of 12 nm (calculated from 250 QDs present in the TEM). The aureole pattern in the SAED shown in the inset reveals its amorphous nature.

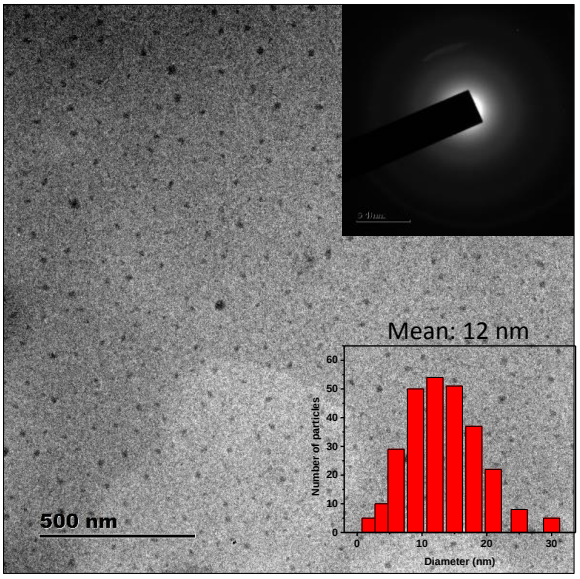

Figure 6.1: TEM image of WS_2 QDs prepared from WS_2 powder and NaOH at a molar ratio of 1:0.25

AFM micrographs provide the information regarding the thickness and lateral dimensions of the QDs. The height profile from the AFM image shows that the dimensions of QDs are in the range below 20 nm and the height is about 2-3 nm.

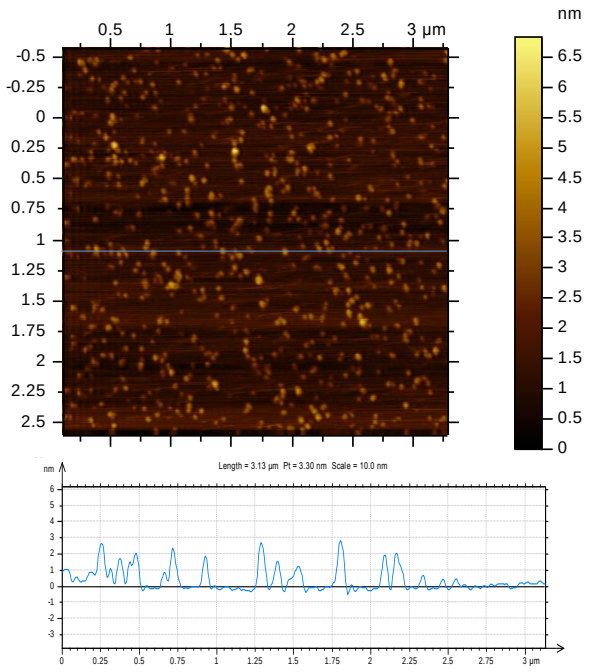

Figure 6.2: AFM image of WS_2 QDs and the height profile of the line drawn across the AFM image.

The chemical composition of the QDs and oxidation states of the elements are unraveled by X-ray photoelectron spectroscopy (XPS) studies. Peaks corresponding to W and S along with peaks for C and O were present in the survey scan spectrum of WS_2 QDs. The carbon peak could be originated from the surface adsorption of CO_2 as reported earlier (Yan et al., 2016; Zhang et al., 2018a), whereas surface oxidation also contributed to the emergence of oxygen peak. The HRXPS peaks of W and S were fitted using XPSPEAK software after the subtraction of Shirley background with the Gaussian− Lorentzian sum function (20% Gaussian and 80% Lorentzian),. The W $4f^{7/2}$ and 4 $f^{5/2}$ peaks for W^{4+} were observed at 34.4 and 36.2 eV, respectively along with a peak at 37.5 eV, which corresponds to W $5p^{3/2}$. The high-resolution XPS spectra of S 2p shows four peaks at 163.0 eV, 164.3 eV, 167.9 and 169.1 eV corresponding to $2p^{3/2}$ - $2p^{1/2}$ doublet of S^{2-} oxidation state and the oxidized form of S, respectively. The lack

of peaks corresponding to +6 oxidation state of W acknowledges that oxidation happens only for S of the QDs.

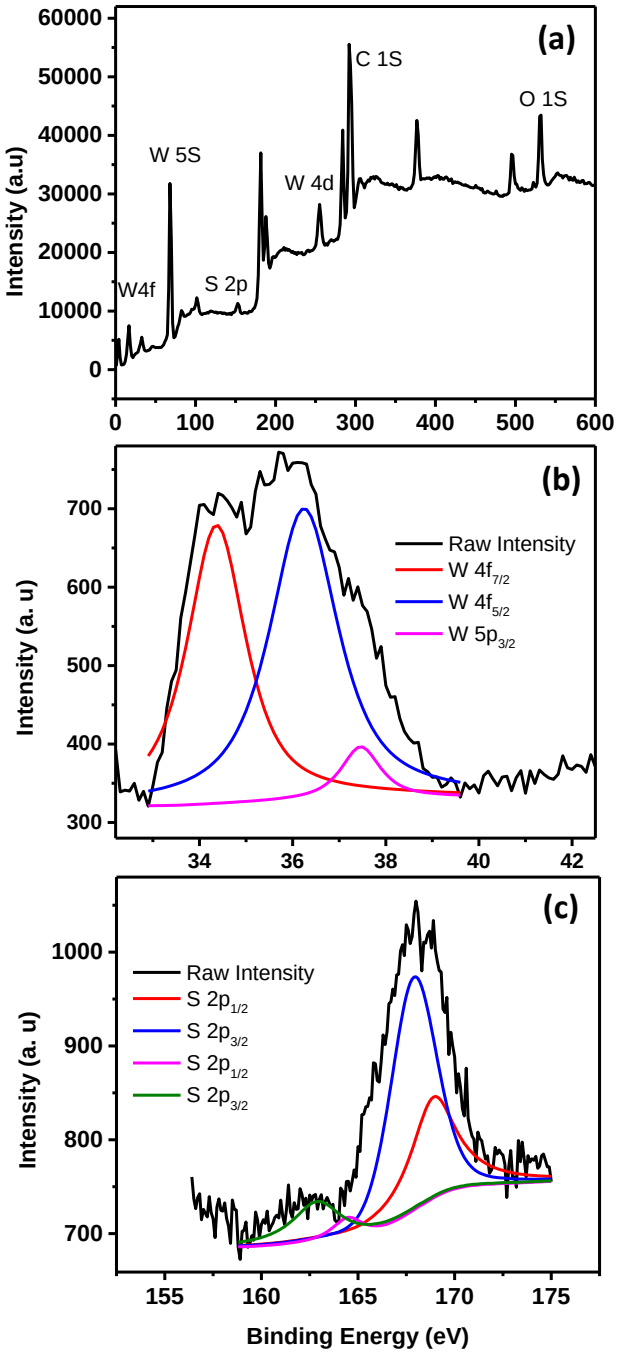

Figure 6.3: Survey scan XPS spectrum of WS_2 QDs. High-resolution XPS spectra of (c) W 4f and (d) S 2p region of WS_2 QDs.

The photophysical characterization of WS_2 QDs clarifies the reason behind the unique optical nature of these nanomaterials. The absorption spectrum of QDs displayed peaks at UV region which correspond to the excitonic feature (Mishra et al., 2015; Lin et al., 2013; Bayat et al., 2017). The bandgap of the QDs is larger (> 4 eV) compared to that of WS_2 monolayer (1.98 eV). The small size of the QDs which can dramatically strengthen the spin−valley coupling (Lin et al., 2013, Zhang et al., 2018b), leads to stronger quantum confinement effect, which in turn widens the bandgap.

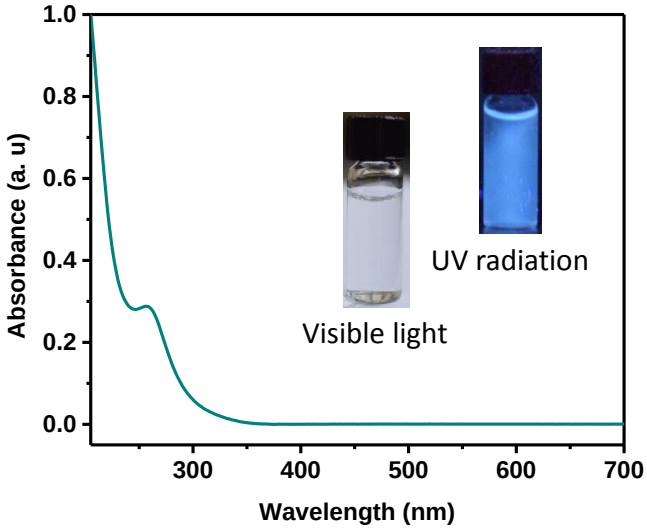

Figure 6.4: UV-visible absorption spectra of WS_2 QDs. Inset shows the photograph of WS_2 QDs solution under visible and UV radiation.

The emergence of photoluminescence emission from WS_2 2D layered material upon scaling down the dimension in the nanometer regime is another consequence of quantum confinement effect. It has been observed that the emission is highly excitation dependent, which is typical for MoS_2 and WS_2 based QDs (Lu et al., 2019; Yin et al., 2019, Caigas et al., 2018). The polydispersity of the QDs (size ranging from 6 nm to 21 nm), could be a plausible reason behind this particular behavior. The best emission was at a wavelength of 410 nm, upon exciting at 320 nm, as shown in Figure 6.5. This high emission from WS_2 QDs is desirable for employing them as fluorescent-based chemical sensors.

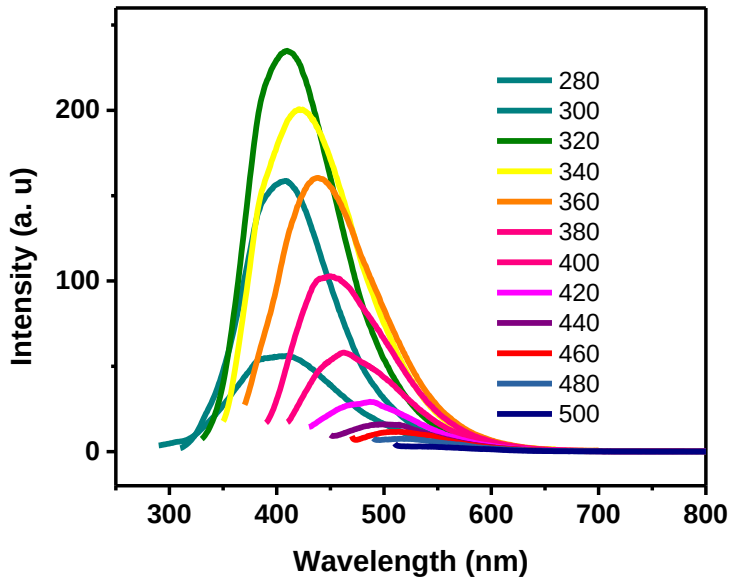

Figure 6.5: Excitation dependent emission spectra of WS_2 QDs showing a maximum emission ~410 nm upon 320 nm excitation.

The photocarrier lifetime of excitons generated in WS_2 QDs, upon excitation using a 344 nm pulsed diode laser source was scrutinized using time-correlated single-photon counting spectroscopy (TCSPS). WS_2 monolayers are proven to be having a very short lifetime of 800 ps (Yuan and Huang, 2015). Upon decreasing the dimension of the bulk sheets, the lifetime of the photoexcited carrier is found to be increased due to the enhanced stability of the excitons. The decay curve was fitted with bi-exponential by keeping the numerical fitting parameter χ^2 near to 1 and carrier lifetimes of 4.4 and 14.7 ns was obtained, as seen in Figure 6.6 a. Prominent temporal stability is another salient feature of these QDs. Even after months of preparation, the PL emission from these samples was found to be analogous with the initial intensity. Also, the absence of photobleaching is another aspect that made them a suitable candidate for bio-imaging applications as well (Figure 6.6 b and c).

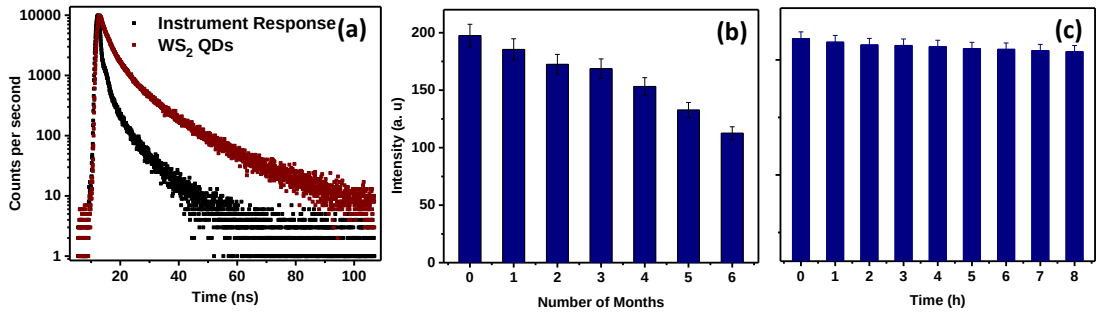

Figure 6.6: (a) Lifetime Spectra of WS_2 QDs. (b) Temporal as well as (c) photostability of the WS_2 QDs

6.3.2 WS_2 QDs as TNP Sensor

Owing to their unique electronic and optical properties, WS_2 based nanomaterials are endowed with various applications in their credit. These multifarious responses largely depends on their morphology and dimension. By exploiting the PL emission property of these materials, in this Chapter, we have demonstrated its application as nitro explosive sensor. The PL spectra of WS_2 QDs, exhibit a strong emission ca. 410 nm, by exciting at 320 nm. This PL emission is observed to be quenched gradually in the presence of incremental concentrations of TNP solution (Figure 6.7 a). The time dependency of the response of PL emission towards TNP has been carried out and observe that, the emission intensity or maxima do not change with a waiting period (Figure 6.7 b). However, we have waited 5 min after mixing the analyte to the sensor solution to perform fluorescence measurements. Methodical quenching titration were implemented by adding aliquots of TNP into a 2 mL solution of WS_2 QDs stepwise approach (10 µL each of 10^{-4} M TNP). The distinguishable response of WS_2 QDs, even with trace amount of TNP attest its potential as a sensor. To eliminate inner filter effect, fluorescence intensities obtained upon addition of each aliquotoes of TNP were corrected based on the following formula:

$$F_{corr}\,(\lambda ex) = F_{obs}\,(\lambda ex)\,/W$$

Where, W is correction factor, which can be obtained from the equation

$$W= (1-10^{-A_{FL}})/A_{FL}$$

F_{corr} (λex) is the corrected fluorescence in the absence of inner- filter effects, F_{obs} (λex) is the measured fluorescence intensity, and A_{FL} is the absorbances of the fluorescent component, respectively.

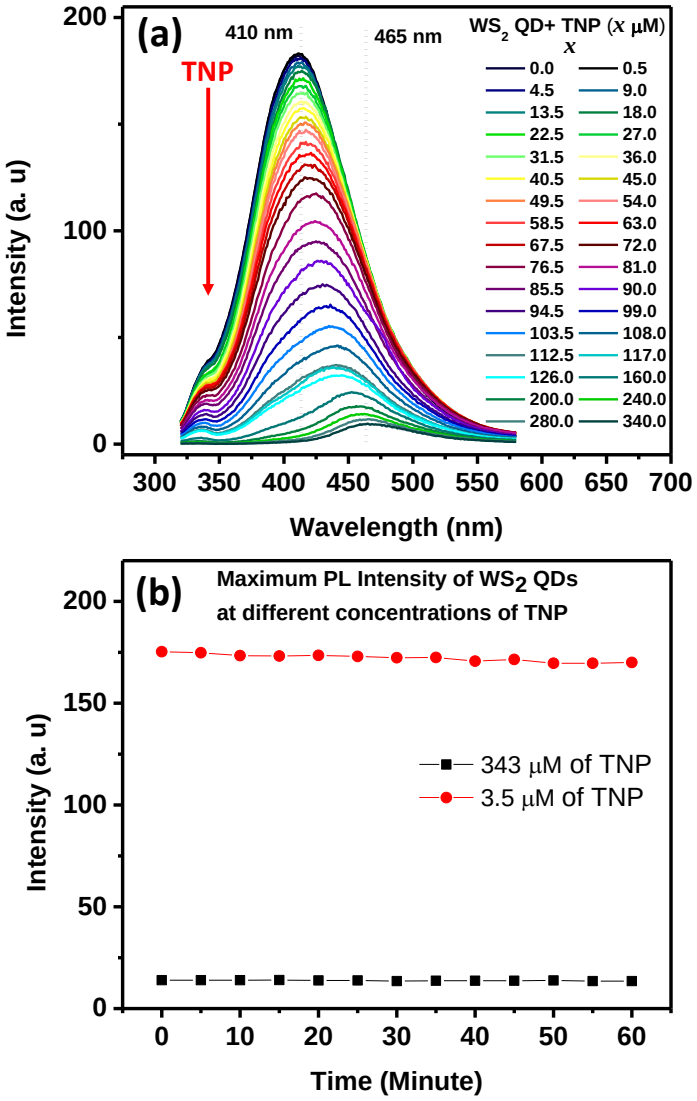

Figure 6.7: (a) The PL response of WS_2 QDs towards various concentrations of TNP (b) Calculation of response time of the sensor.

The quenching was following a linear fashion, as evident in Figure 6.8. A linear relationship was obtained between the concentrations of TNP with (F_0-F)/F;

where F and F_0 are the PL emission intensity with and without the presence of TNP, respectively, with a dynamic range of 0.5 to 94.5 µM. It complies with a low limit of detection (LOD) value of 0.27 µM (calculated using the formula 3σ/b; where σ is the standard deviation of the blank and b is the slope of the regression curve). It was observed that the dynamic range consists of two linear ranges; 0.5 to 63 µM and 63 to 94.5 µM, which endorse multiple mechanisms involved in the quenching process. The response of WS_2 QDs above 100 µM is not linear, owing to contribution from aggregation along with other quenching mechanisms, and we haven't included that concentration ranges in our studies.

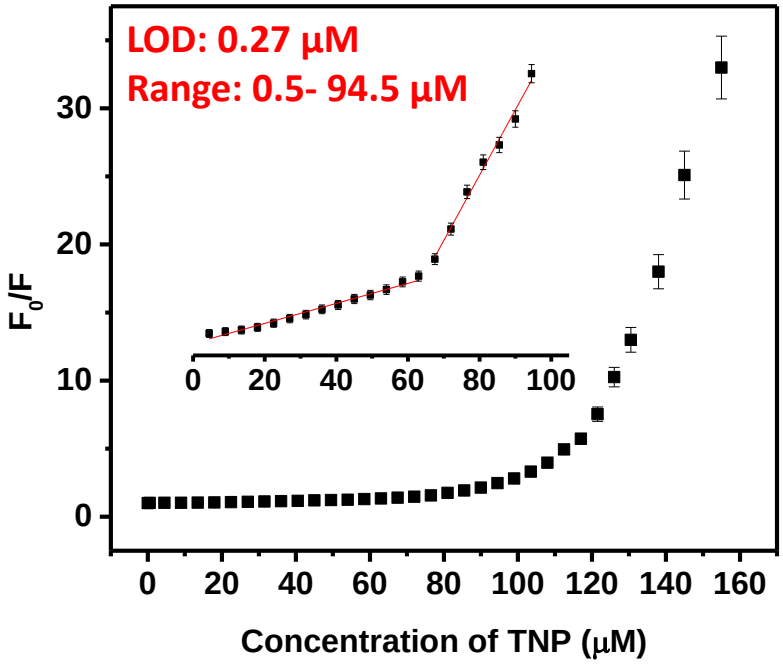

Figure 6.8: Relationship between concentration of TNP (in µM) and ratio of change in fluorescent intensity of WS_2 QDs in the presence of TNP with respect to blank.

The TEM micrographs of WS_2 QDs in the presence of different concentrations of TNP (100 µM and 250 µM), shed further light into the changes in the morphology of the sensor material. As evident from Figure 6.9, at a concentration of 100 µM there is no change in the morphology of the sensor, which implies that aggregation is not a reason for the quenching within the dynamic range. Whereas, at a concentration of 250 µM, there is a marked aggregation of QDs, which could positively enhance the strength

of the quenching of PL emission by TNP. DLS measurements also validated this effect, as given in Table 6.1. This result is further corroborated with the observation of a redshift in the position of emission maximum upon addition of TNP from 410 nm to 465 nm.

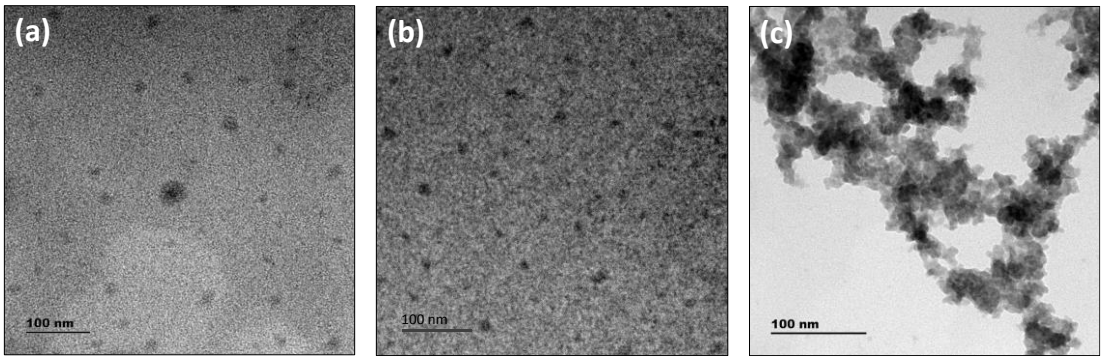

Figure 6.9: TEM images of (a) WS_2 QDs alone in presence of (a) 100 µM and (b) 250 µM concentrations of TNP

Table 6.1: Table showing the size distribution and zeta potential of sensor material with and without the presence of analyte. The reduction in zeta potential indicate the destabilizing action of TNP which in turn lead to the aggregation sensor materials.

	Size (nm)	**Zeta**
WS_2	37.84	-21.1
WS_2+ TNP	92.60, 436.5	-10.5
TNP	-	-0.911

6.3.3 Mechanism of Sensing

NAs can activate quenching of PL emission of any fluorophore, through various well-established pathways. All these nitro explosives can trigger PL quenching by electron transfer mechanism because of their high electron-deficient nature (Naddo et al., 2007; Liu et al., 2013; Sun et al., 2014). The inner filter effect is another pathway through which PL quenching can be achieved (Rong et al., 2014; Ganiga et al., 2018). The acidic nature of these nitroaromatics paves a clear way for the formation of non-fluorescing Meisen Heimer complexes with the fluorescent sensing materials (Aparna et al., 2018). Hence to understand the PL quenching of WS_2 QDs by TNP and the

selectivity towards this analyte, comprehensive spectroscopic investigations are beneficial.

UV-visible spectroscopy reveals electronic level interaction between any two moieties, as it can illustrate the changes in their chemical structure, functionalities or charges. Careful monitoring of changes in the absorption features of sensor solution is performed upon the incremental addition of TNP. As can be seen in Figure 6.10a, no apparent changes are visible in the absorption features of either sensor solution or TNP in the alkaline media. This observation circumvents the possibility of non-fluorescing ground-state Meisenheimer complex formation. Although, the steady increase in the spectral absorption feature around 400 nm is relevant in the present case, as this portion of the absorption spectra can effectively overlap with the emission spectra of WS_2 QDs sensor solution, one of the pre-requisites for the manifestation of the quenching mechanism- Förster resonance energy transfer (FRET). The closeness of sensor material and target molecules are another criterion to be satisfied for FRET to materialize. A remarkable change in the zeta potential value from -21.1 mV to -10.5 mV attests electrostatic interaction and thus ensures the closeness between TNP and the QDs (Table 6.1).

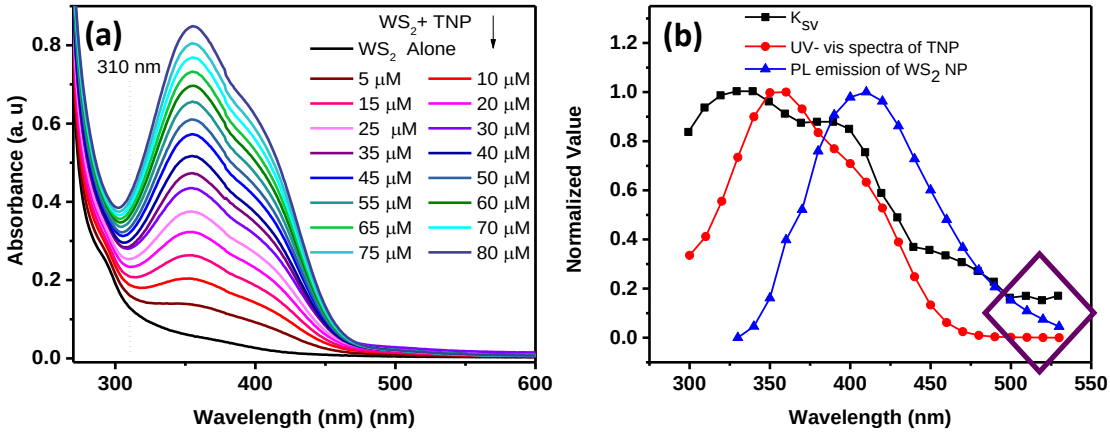

Figure 6.10: (a) Absorption spectra of WS_2 QDs at different concentrations of TNP. (b) Plot showing the spectral overlap of absorption spectra of WS_2-TNP solution with the PL emission spectra of WS_2 QDs along with a plot showing the excitation wavelength dependence of Ksv values.

An additional proof for the energy transfer mechanism was obtained from the comparative study of the absorption spectrum of WS_2 QD- TNP solution, PL emission spectrum of WS_2 QDs and a plot of K_{sv} at various wavelengths (Figure 6.10b). The K_{sv} values at different wavelengths show that quenching is excitation wavelength dependent. Also, the nature of K_{sv} vs. wavelength plot is in correlation with the variation of absorbance of WS_2 QDs- TNP solution at those wavelengths. Thus, we surmise that FRET is the primary quenching mechanism. If the quenching mechanism were electron transfer (ET), such a change in K_{sv} value with respect to excitation wavelength would not be expected. However, we cannot rule out the possibility of electron transfer. A close observation of K_{sv} plot reveals that sizeable K_{sv} values are present, even after 450 nm wavelength, where there is no spectral overlap between absorption spectra of TNP solution and the PL emission spectra of WS_2 QDs. Therefore, along with FRET, ET also contributes to the PL quenching of WS_2 QDs. This hypothesis was further confirmed by time-resolved fluorescence spectral analysis of WS_2 QDs at different concentrations of TNP. As seen in Figure 6.11 and Table 6.2, there is a small yet regular decrease in both the lifetime components, upon increasing the concentration of TNP, which attest the involvement of multiple quenching mechanism. Also, the high absorbance value of WS_2 QDs solution in the presence of TNP at 320 nm wavelength opened up a way for IFE as well, which in turn further quench the PL emission from WS_2 QDs. To differentiate the contribution of excited-state phenomena like electron transfer and FRET from the non-specific quenching mechanism of IFE, we have calculated FRET efficiency using steady-state and time-resolved fluorescence spectral studies. Steady-state FRET efficiency was calculated using the fluorescence intensity of WS_2 QDs and WS_2 QDs-TNP solutions and obtained a value of 56.3 %. This quenching was attributed to all the quenching mechanisms involved. FRET efficiency was also calculated using the average lifetime of WS_2 QDs in the absence and presence of TNP, which comes around 28.5 %. Since IFE cannot influence excited-state phenomena, the difference in FRET efficiencies can be the contribution from IFE (27.8 %).

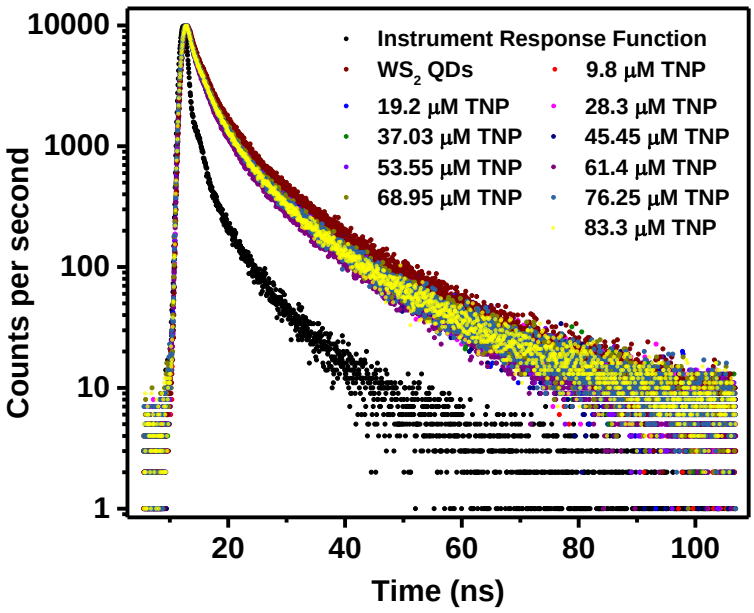

Figure 6.11: Lifetime analysis of WS_2 QDs at different concentrations of TNP.

Table 6.2: Table showing the corresponding lifetime components along with average lifetime values. The small decrease in the lifetime components and average life with respect to concentration of TNP marks the complexity of the quenching mechanism involved.

	τ_1 (ns)	a_1	τ_2 (ns)	a_2	$\langle\tau\rangle$ (ns)	χ^2
WS_2	4.42	33.54	14.70	66.46	13.34	1.05
9.8 mM TNP	4.35	33.86	14.56	66.14	13.20	1.11
19.2 mM TNP	3.66	39.93	13.64	60.07	12.12	1.21
28.3 mM TNP	3.59	43.25	13.45	56.75	11.78	1.19
37.0 mM TNP	3.57	43.52	13.26	56.48	11.59	1.04
45.5 mM TNP	3.49	43.52	13.11	56.48	11.47	1.31
53.5 mM TNP	3.47	42.89	12.82	57.11	11.24	1.17
61.4 mM TNP	3.34	43.21	12.75	56.79	11.18	1.18
68.9 mM TNP	3.16	43.43	11.93	56.57	10.44	1.16
76.3 mM TNP	3.12	43.01	11.78	56.99	10.33	1.13
83.3 mM TNP	2.91	47.43	11.12	52.57	9.55	1.19

To unravel the superior selectivity of WS_2 QDs towards TNP, we have chosen five structurally similar compounds (trinitrophenol (TNP), dinitrophenol (DNP), *o*-nitrophenol (ONP), dinitrotoluene (DNT), nitrobenzene (NB) and phenol (PHE)) and quenching experiments were performed by titrating incremental concentrations of these compounds with WS_2 QD solution. Stern-Volmer plots were generated for all the six compounds by plotting $(F_0\text{-}F)/F$ vs. concentrations of each compound, where F_0 and F is the PL emission intensity of WS_2 in the absence and presence of analyte molecules, respectively (Figure 6.12). The significance of Stern-Volmer constant K_{sv} is that it can furnish an overall idea regarding the competence of the analyte molecules to quench the PL emission of the fluorophore. A greater K_{sv} value indicates the higher slop value, which in turn notifies its increased capability to quench the fluorescence. Hence a comparison of Ksv value of each six analytes has been done to distinguish the quenching efficiency of these analytes towards the sensor solution. Interestingly, the Ksv value of TNP is much higher compared to other analytes, which in turn qualitatively shows the selectivity of WS_2 QDs towards TNP.

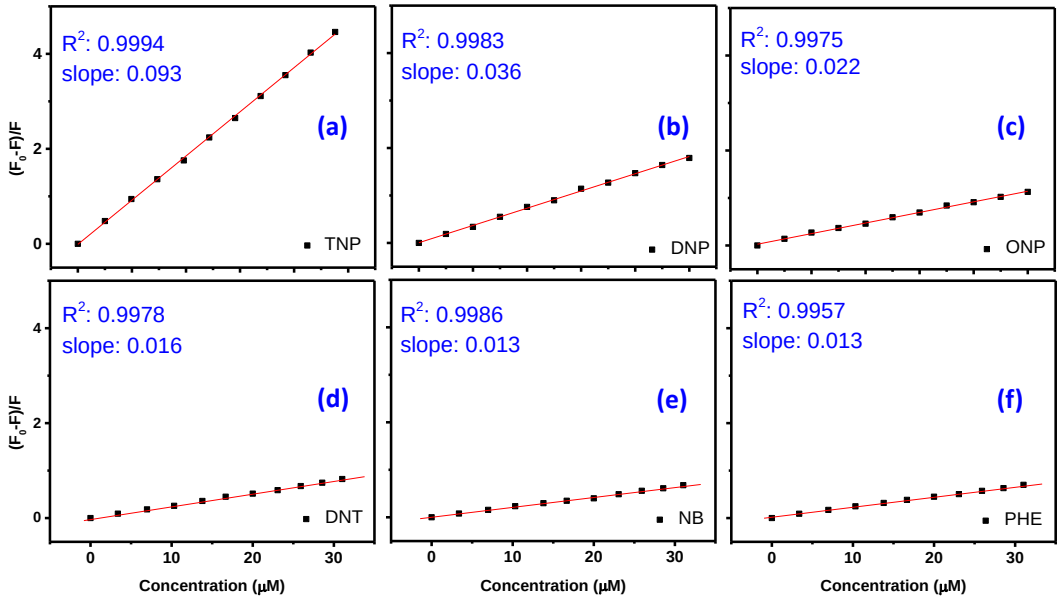

Figure 6.12: K_{sv} plots of TNP (a), DNP (b), ONP (c), DNT (d), NB (e) and PHE (f)

The selectivity factor (SF) calculated by considering the Ksv values of different analytes in comparison with TNP; is given in Table 6.3. It has been observed

that the SF values for DNP, ONP, DNT, NB and PHE are 0.39, 0.25, 0.17, 0.15 and 0.1397, respectively. These selectivity factors connote the efficiency of WS_2 QDs as a sensor for TNP.

Table 6.3: The comparison of K_{sv} values for different analyte molecules, showing the highest Ksv for TNP.

System	K_{sv}	R^2 Value	SF ($K_{sv\ of\ analyte}/K_{sv\ of\ TNP}$)
TNP	0.093	0.999	1.00
DNP	0.036	0.998	0.39
ONP	0.023	0.997	0.25
DNT	0.016	0.997	0.17
PHE	0.014	0.998	0.15
NB	0.013	0.995	0.14

The reason behind the high SF of WS_2 QDs towards TNP is ascribed by the spectral overlap of the absorption spectra of all NAs (concentration 10^{-4} M) with the PL emission spectra of WS_2 QDs (Figure 6.13). Even though DNP shows similar spectral features as that of TNP, the lower absorbance reduces the extent of overlap and thus the efficiency of FRET. All other NAs, on the other hand, either have very low absorption feature in the emission range of WS_2 QDs, or no spectral overlap at all, which circumvent the room for FRET or IFE to operate. The reduced acidic nature of DNP and ONP might as well contributed to the reduced quenching efficiency compared to TNP (Rong, 2014). Besides, the time-resolved fluorescence spectral analysis of WS_2 QDs in the presence of these NAs are tabulated in Table 6.4. The results convey that, for the same concentrations of analytes, the plummet in the lifetime value of WS_2 QDs is more for TNP, which positively ascertain the higher efficiency of energy and electron transfer between WS_2 QDs and TNP.

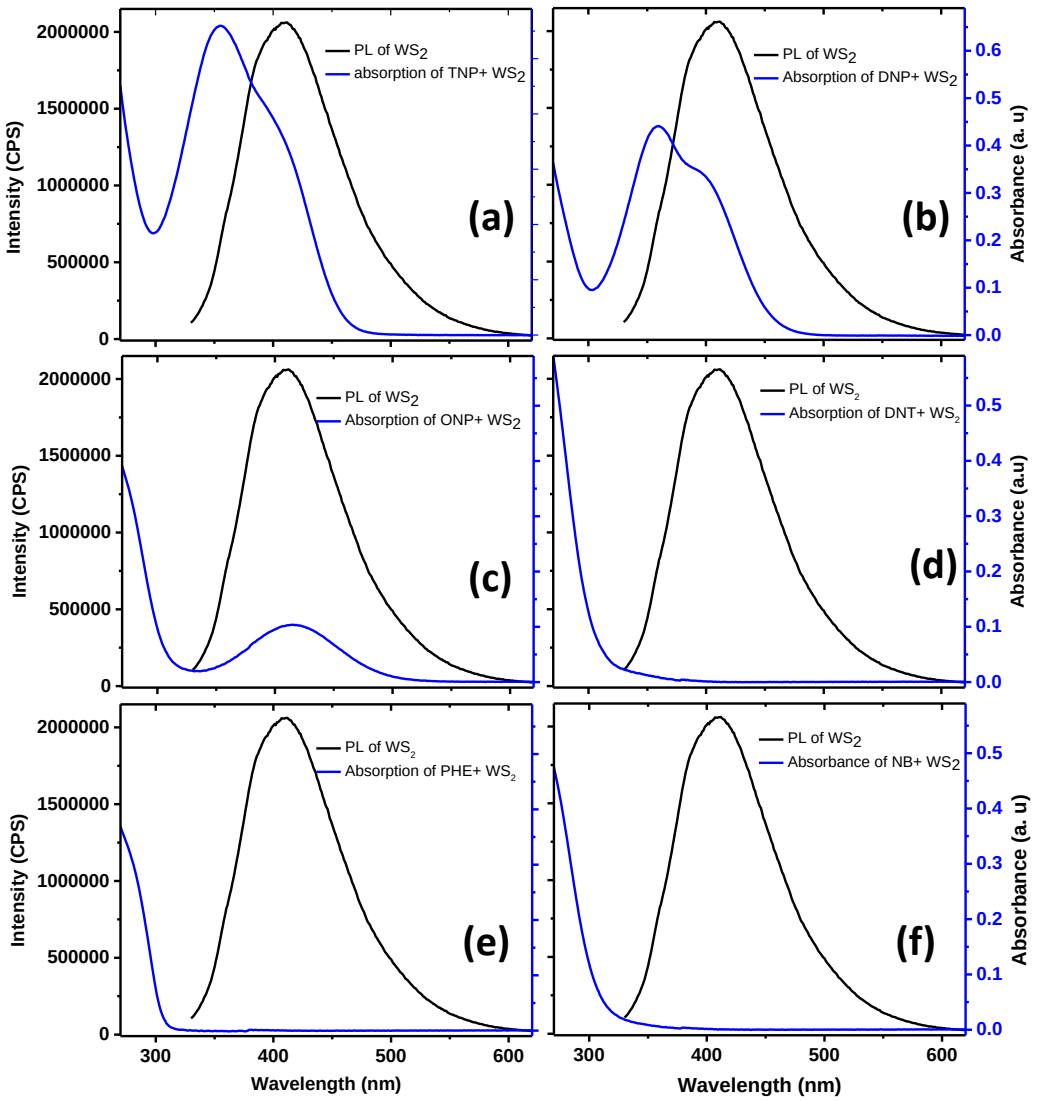

Figure 6. 13: Spectral overlap of PL emission spectra of WS_2 with the absorption spectra of WS_2 along with TNP (a), DNP (b), ONP (c), DNT (d), NB (e) and PHE (f)

Table 6.4: Lifetime analysis of WS_2 QDs with different analytes showing a decrease in the lifetime component

	τ_1 (ns)	α_1	τ_2 (ns)	α_2	$<\tau>$ (ns)	χ^2
WS_2	4.42	33.54	14.70	66.46	13.3	1.11
TNP	3.49	43.52	13.11	56.48	9.5	1.31
WS_2	4.27	31.59	14.46	68.41	13.2	1.02
DNP	4.16	41.81	14.25	58.19	12.5	1.07

WS_2	4.32	31.97	14.43	68.03	13.1	1.01
ONP	4.11	39.62	14.39	60.38	12.7	1.05
WS_2	4.38	32.96	14.71	67.04	13.3	1.03
DNT	4.13	37.07	14.3	62.93	12.8	1.09
WS_2	4.39	32.83	14.63	67.17	13.3	1.06
PHE	4.12	43.97	14.63	56.03	12.7	1.08
WS_2	4.32	31.56	14.48	68.44	13.2	1.14
NB	4.20	33.21	14.21	66.79	12.9	1.08

The detection of TNP can interfere with the presence of other species also. Therefore, selectivity study was elaborated using various metal ions, biologically active molecules, etc. in order to check the response of PL emission of WS_2 QDs towards these moieties. The results indicated that the influence of these moieties on the quenching of PL emission of the sensor solution is negligible compared to NAs, thus these hassle-free detection of TNP can be carried out, even in the presence of these ions/compounds. The result is summarized in Figure 6. 14.

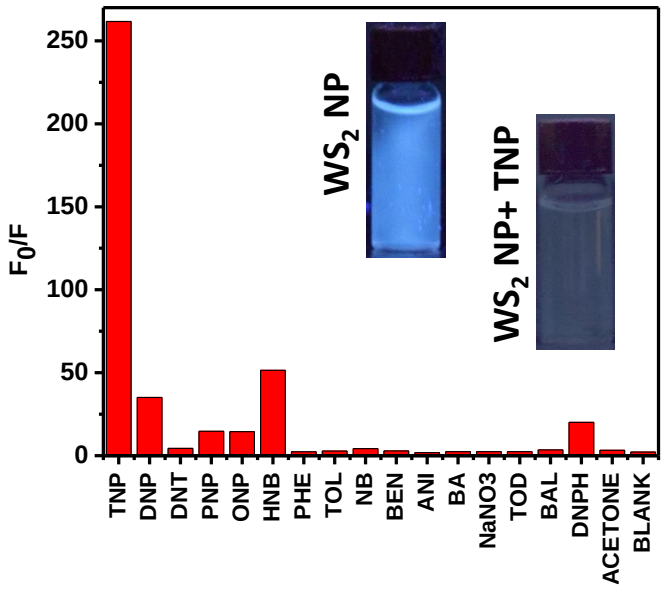

Figure 6.14: Selectivity study; only TNP could quench the PL emission of WS_2, with remarkable efficiency.

6.3.4 Solid State Detection

A solid substrate-based detection of TNP was demonstrated in order to check the utility of the present sensor for the practical application scenario. The sensor material was incorporated in a PVA matrix film. The PL intensity of the sensor incorporated PVA film were measured using 320 nm excitation. The film was kept in desiccator for one day which contain 100 mg of TNP taken in an open Petri dish and the PL emission spectra was again recorded. The PL emission of the test strip was found to be decreased, significantly. Thus, we are anticipating that, the new sensor material is effective in detection of TNP in solid-state as well. Besides, by keeping this sensor impregnated PVA film in a UV cabinet, before and after exposure to TNP, a qualitative visual detection is also possible, as seen in Figure 6.15

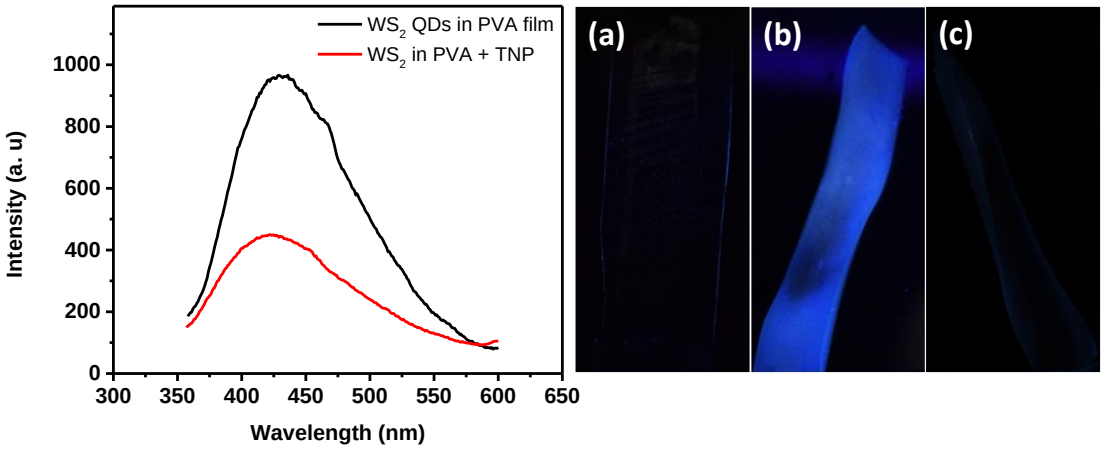

Figure 6.15: The PL emission spectra of WS_2 quantum dots incorporated in PVA film (black) and WS_2 quantum dots incorporated in PVA film after keeping the film in a desiccator containing 100 mg of TNP for one day (red spectra). Photographs of (a) bare PVA film (b) WS_2 quantum dots incorporated in PVA film (c) WS_2 quantum dots incorporated in PVA film after keeping the film in a desiccator containing 100 mg of TNP for one day.

6.3.5 Comparison with other Methods

The quenching of fluorescence emission of WS_2 QDs were initiated by three prominent mechanism, in the present case, which endorse the high selectivity with marked sensitivity. A comparison of the performance of present TNP sensor with

various strategies are presented in Table 6.5. It is apparent that the WS_2 sensor is having a comparable performance with the existing reports.

Table 6.5: A Comparison of the analytical performance of various TNP sensing methods.

Method	Sensor System	LOD	Reference
Colorimetry	N-acylhydrazone L	0- 50.0 μm 4.30×10^{-7} M	(Peng, 2011)
Electrochemistry	Anti-TNT DNA aptamer sandwiched structure	10^{-14}–10^{-3} M Sensitivity: 10^{-14} M	(Ho, 2012)
Electrochemistry	Copper electrodes using flow injection system	20–300 μmol L^{-1} 6.0 μmol L^{-1}	(Joao, 2013)
Electrochemistry	Nitrogen-doped graphene quantum dots (N-GQDs)	1 to 400 ppb 0.2 ppb	(Cai, 2015)
Fluorimetry	Nitrogen-doped graphene quantum dots (N-GQDs)	1 to 60 μM 0.30 μM	(Lin, 2015)
Fluorimetry	Chemically oxidized and liquid exfoliated graphitic carbon nitride (g-C3N4) nanosheets	0-10 μm 8.2 nM	(Rong, 2015)
Fluorimetry	photoluminescent carbon nanodots prepared using yam	22 nM	(Dengab and Wu, 2014)
Fluorimetry	WS_2 QDs	0.27 μM 2.5-100μM	Present study

6.4 Conclusion

We have developed a fast and straightforward strategy for the rapid detection of TNP utilizing the luminescent WS_2 QDs, owing to the selective quenching of its PL emission in the presence of even trace amounts of TNP. The favorable quenching by TNP over other nitroaromatics were expressed using the selectivity factor. The

quenching is confirmed to arise from the three different mechanisms; energy transfer, electron transfer and aggregation of QDs in the presence of TNP over a concentration of 0.5 to 340 µM. The LOD of the sensor is found to be a low value of 0.27 µM with a dynamic range of 0.5µM to 94.5 µM. The major quenching within this linear range is found to be due to energy and electron transfer. We have also performed a solid-state detection of TNP using a film fabricated using WS_2 QDs incorporated within polyvinyl alcohol.

CHAPTER 7

IN SITU FORMATION OF Ag NANOPARTICLE ONTO WS_2 NANOSHEETS AND ITS RESPONSE AS TURN-ON SENSOR FOR BASIC AMINO ACIDS

The Förster resonance energy transfer (FRET) pair-based detection were gaining considerable attention due to the promising sensitivity and selectivity. A turn-on sensor for the detection of basic amino acids utilizing the fluorescence emission properties of WS_2 nanosheets (WS_2 NSs) having a size of a few hundred nanometers has been developed. The sensor functions based on a FRET dyad. The addition of $AgNO_3$ into the WS_2 NSs solution leads to the in-situ formation of silver nanoparticles (Ag NPs) without additional reducing agent. The negative surface charge, presence of sulphur vacancies, together with the possibility for multiplexed adsorption platform of WS_2 nanosheets accredit the formation Ag NPs on its surface. In the WS_2 NSs-Ag NPs system (0D-2D composite), the fluorescence emission of the nanosheets became subdued, due to FRET. This 0D-2D composite is proven to be an excellent turn-on sensor for basic amino acids. Histidine, lysine, and arginine can induce the aggregation of the Ag NPs, which shut the FRET pathway, along with the regeneration of fluorescence of WS_2 NSs. The aggregation of Ag NPs occurs at a pH below the isoelectric points of each amino acids help to discriminate them. The analytical parameters, dynamic range and limit of detection have been evaluated for the sensor system.

7.1 Introduction

In layered materials, the van der Waals interactions are not limited to interplanar interactions. Generally, any passivated, dangling bond-free surface interacts with another moiety via van der Waals forces. Consequently, any layered 2D material can be integrated with an array of materials of different dimensionality to form mixed-

dimensional structures. The 0D-2D materials are such heterostructures produced by the integration of 2D materials with 0D materials, primarily through noncovalent interactions. The 2D components may be graphene or transition metal dichalcogenides (TMDCs) and the 0D part may be small organic molecules or quantum dots.

In contrast to conventional, epitaxially grown heterostructures, the interface in a mixed-dimensional structure is relatively complex and less constrained due to the absence of the need for lattice matching. The usual discontinuity in the band structure and resulting potential energy barriers, the density of states (DOS), also undergoes an abrupt transition, which has several observable implications, such as additional resistance at the junction that results from the change in the number of conductance channels. The 0D-2D materials have wide applications and show better performance than individual components in the area such as photocatalysis, electronic devices and optical applications. This chapter discusses the synthesis and fluorescence sensor application of the WS_2 nanosheets-Ag nanoparticles composite material. We utilized the composite for the screening of basic amino acids.

Amino acids (AAs), being the building units of proteins, are associated with various physiological processes and a key component of the life process (Zhou and Yoon, 2012; Sharma and Dietz, 2006). For example, one of the basic amino acids lysine (Lys) is associated with the weight gain in animals, polyamine synthesis and the Krebs–Henseleit cycle (Yoshida et al., 2001). Histidine (His); another basic AAs, on the other hand closely related to the growth and repair of tissues, the control of transmission of metal elements in biological bases, etc. (Xiong et al., 2008). Arginine (Arg), third and most basic AAs is known for its association with cell division, immune function, the healing of wounds, the release of hormones, etc.(Liu et al., 2017). The AAs detection, in general, is thus significant in terms of valuable information it can render in the fields of nutritional analysis, diagnosis of diseases such as Alzheimer's, Pancreatitis, etc. Among AAs, the detection of thiol-containing AAs were rather easy owing to their unique nucleophilicity (Lu et al., 2015). Whereas discrimination of non-thiol containing AAs is still challenging. Electrochemical and chromatographic approaches

are widely used strategies for the detection and characterization of AAs (Naqvi et al., 2020; Liu et al., 2020; Suprun et al., 2020; Hasanzadeh et al., 2016; Silva et al., 2017; Kolanu et al., 2017). Yet, the demand for sophisticated instruments, operational inconveniences, economic viabilities, choice of various parameters such as response time, detection limit, etc. pave the way for the quest for more desirable and convenient methods. Optical chemosensors are marked with their high sensitivity with notable selectivity along with the possibility of visual discrimination (Zhou and Yoon, 2012). Hence a potential fluorimetric or colorimetric probe for recognizing specific AAs susceptible to high-throughput assays holds a breakthrough in the current scenario.

The chemistry of noble metal nanoparticles with fascinating surface plasmon resonance (SPR) was another field that attends enormous interest. Continuous monitoring of the changes in the SPR as a function of the chemical and physical environment of the nanoparticles has been performed for sensor applications (Lee and El-Sayed, 2006). The ease of surveilling the light signal made them a potential candidate for calorimetric sensing. Myriad reports are available that exploit the changes in the SPR peak of noble metal nanoparticles, upon interaction with AAs. For example, p-sulfonatocalix[4]arene thiol modified Au nanoparticles have been made use as calorimetric sensor for Lys, His and Arg in water, on the principle of broadening and shifting of SPR bands to red region upon interaction, with the linear detection limits of 1 mM, 2 mM and 4 mM, respectively (Patel and Menon, 2009). Chiral detection of L-His was reported based on L-Arginine- sulfonated-substituted zinc tetraphenylporphyrin modified silver nanoparticle clusters (L-Arg–ZnTPPS–Ag NPs) (Sun et al., 2012). Fluorescence-based detection of AAs was also reported by many groups with improved sensitivity. Lu et al., (2015) utilized the fluorescence emission of water-soluble fluorescein-bis-acrylate carrying pyridinium moiety having high sensitivity towards biothiols which can discriminate simultaneously basic amino acids and thiol-containing amino acids from other amino acids. A simple fluorescent turn-on sensor employing two complementary cucurbit[n]uril based microarray has been demonstrated for the sensitive detection of basic AAs in water (Minami et al., 2014). A close observation of literature reveals that the detection strategy depends on either

agglomeration of nanoparticles followed by a change in the SPR band, or the change in fluorescence emission of the probe. A combined approach having the ease of agglomeration of nanoparticles along with the sensitivity of fluorescence turn-on methodology would be attractive in chemical sensor applications.

In this chapter we discuss the formation of silver nanoparticles (Ag NPs) from $AgNO_3$ by the reducing action of fluorescent WS_2 nanosheets (WS_2 NSs). The luminescent WS_2 NSs were synthesized using a facile hydrothermal method. The fluorescence of WS_2 NS was quenched upon the formation of Ag NPs due to resonance energy transfer. The obvious spectral overlap of WS_2 NSs emission with that of surface plasmon resonance (SPR) absorption of Ag NPs explains the non-radiative energy transfer. The quenched fluorescence was selectively recovered in the presence of three basic amino acids; Lys, His and Arg at a pH above the isoelectric point of each the amino acids. The fluorescence recovery was attributed to aggregation of Ag NPs and thereby the lack of spectral overlap between WS_2 NSs and Ag NPs. The sensor has an appreciable dynamic range and limit of detection (LOD) for all the three AAs analytes at different pH. The formation of Ag NPs, the comprehensive mechanism of quenching and the recovery of fluorescence of WS_2 NSs were proposed with the experimental support.

7.2 Experiments and Methods

7.2.1 Reagents and Materials

Tungsten disulphide (WS_2) and sodium hydroxide (NaOH) were purchased from Merck India Ltd. L-Arginine, L-Aspartic acid, Creatinine, Glycine, L-Glutamic acid, L(+)-Glutamine, L-Isoleucine, L-Methionine, L-Proline, L-Phenylalanine, L-Serine, L-Tryptophan, L-Valine were purchased from Spectrochem Pvt Ltd, India. DL-Homocysteine and L-Cysteine were obtained from Sigma Aldrich, USA, Cysteamine hydrochloride was purchased from Otto Chemical Reagents, India. L-Histidine (98%) was procured from Avra Synthesis Pvt Ltd, India. L-Aspargine monohydrate, L-(+) Lysine and Alanine were purchased from TCI Chemicals, India.

7.2.2 Instrumentation

UV-visible experiments were carried out using a Carry-100 UV-visible spectrophotometer. Fluorescence measurements were performed using FluoroMax-4C spectrofluorometer (Horiba Instruments, USA). The experiments were conducted by fixing excitation and emission slit width at 5 nm with an integration time of 0.1 ns. Time resolved fluorescence measurements were executed using time-correlated single-photon counting (TCSPC). The excitation wavelength was fixed at 344 nm and decay profile were collected at 452 nm (laser pulse width <1ns). Transmission electron microscopy (TEM) images were obtained using a JEOL 2100 instrument and Zeta potential measurements were performed using Zetasizer Nano ZS series; Malvern Instruments, Malvern, UK. X-ray photoelectron spectroscopy (XPS) spectra were collected using an Omicron ESCA probe spectrometer with Mg-Kα line and pH measurements were taken using EUTECH instruments' pH meter.

7.2.3 Synthesis of WS_2 nanosheet (WS_2 NS)

WS_2 nanosheets were prepared by hydrothermal reaction of commercially available WS_2 powder and NaOH in aqueous medium by taking a molar ratio of 1:1. Briefly, WS_2 powder (100 mg) was mixed with NaOH (16.0 mg) in 10 mL of water. The resultant solution was taken in a Teflon-lined autoclave and kept for 24 h at a temperature of 220 °C. The solution after the reaction was centrifuged at 3000 rpm for 30 min, the supernatant was collected filtered and dialyzed for 24 h using a dialysis bag (molecular weight cut off 500). This purified, light-yellow solutions were used for all the studies.

7.2.4 Synthesis of WS_2 NS -Ag NPs nanocomposite

To a 2.5 mL of purified WS_2 nanosheet solution, aliquots of $AgNO_3$ solution (1, 2 or 3 mL of 0.02 M) are added drop by drop by stirring. The color of the solution turned yellow in situ due to the formation of Ag NPs on the surface of WS_2 nanosheet.

7.2.5 Sensor Application of WS_2 NS -Ag NPs nanocomposite

2 mL of WS_2 nanosheet -Ag NP nanocomposite solution was utilized as the sensor solution in all the experiments. To this solution, 10 μL of 10^{-3} M Lys, His and Arg solution was added stepwise and fluorescence measurements were conducted without a waiting period.

The selectivity of the present sensor solution was tested using 100 μL of a 1 mM solution of various analytes. We used amino acids such as Alanine, L-Arginine, L-Aspartic acid, L-Aspargine monohydrate, Creatinine, L-Cysteine, DL-Homocysteine, Glycine, L-Glutamic acid, L(+)-Glutamine, L-Histidine, Leucine, L-Isoleucine, L-(+) Lysine, L-Methionine, L-Proline, L-Phenylalanine, L-serine, L-tryptophan, L-Valine, several metal ions (Na^+, K^+, Mg^{2+}, Fe^{2+}, Fe^{3+}, Zn^{2+} and Cd^{2+}) common biologically relevant molecules such as glutathione (GSH), Dopamine, Adenine, thiourea for selectivity studies. The excitation wavelength was 360 nm for all the sensing experiments.

7.3 Results and Discussions

7.3.1 Synthesis and Characterization of WS_2 nanosheets

We used a simple approach for the preparation of 2D layered materials in nanosize regime employing hydrothermal reaction. The vigorous reaction of WS_2 powder with 1:1 molar ratio of NaOH at 220 °C yielded exfoliated WS_2 nanosheets. The optimized reaction time was 24 h and the NSs show high photoluminescence (PL). Detailed microscopic and photophysical characterizations have been carried to understand the structural and optical attributes of the material. The transmission electron microscopy (TEM) images (see Figure 7.1a) demonstrate the formation of nanosheets of lateral dimensions in the range of a few hundreds of nanometers. It is notable that the crystallinity of the sheets is maintained even after vigorous hydrothermal reaction as evident in the selected area electron diffraction (SAED) pattern. The AFM micrographs further confirm the formation of nanosheets (Figure

7.1c). The thickness measurement from height profiles drawn at different regions of AFM micrographs affirms the layer thickness of 2.8 nm, indicating the presence of 2-3 layers of sheets.

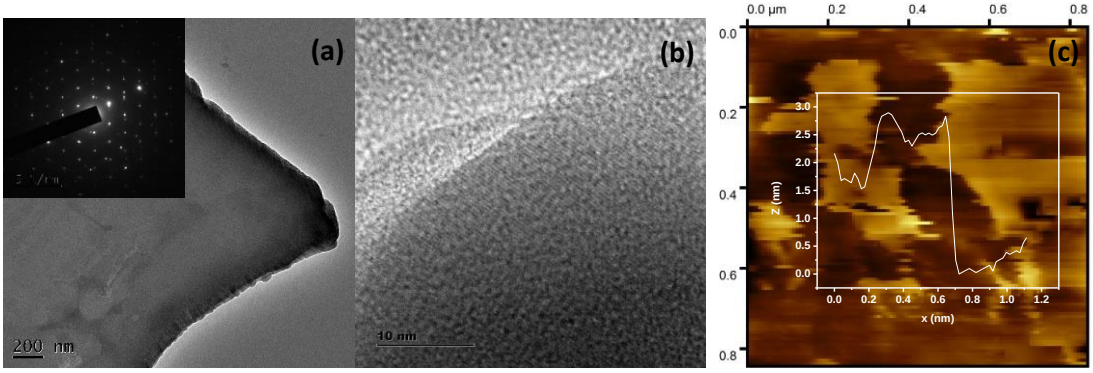

Figure 7.1: (a) TEM micrographs of WS_2 nanosheets. The inset of (a) shows the SAED pattern illustrating the crystalline nature of WS_2 nanosheets. (b) is a magnified TEM image of the WS_2 sheets. (c) AFM micrograph of WS_2 nanosheet showing a thickness of ~2.8 nm.

Raman spectroscopy is a useful tool to perceive the number of layers in the exfoliated TMDs. Generally, there are four major Raman-active modes in bulk WS_2, namely A_{1g}, E_{1g}, E^1_{2g}, and E^2_{2g} modes. Due to the forbidden selection rule in the back-scattering geometry and the limited rejection against Rayleigh scattering, it is difficult to see E_{1g} and E^2_{2g} modes by commercial instruments. However, the in-plane vibrational E^1_{2g} mode and the out-of-plane vibrational A_{1g} modes are more significant as it can advocate the number of layers present in the sheets. A thorough study regarding the frequency trends of the A_{1g} and E^1_{2g} modes with varying layer thicknesses was performed by Molina-Śanchez and Wirtz (2011). As the number of layers increases from monolayer to bulk, A_{1g} modes tend to be blue-shifted, whereas E^1_{2g} shows red-shift. Weak interlayer interaction and strong dielectric screening of the long-range Coulomb interactions are the reason for this behavior. Therefore, a direct correlation can be established between the frequency difference ($\Delta\omega$) of the E^1_{2g} mode and A_{1g} mode and the sample thickness (Zeng et al., 2013). In the present case, for WS_2 nanosheets, the value of $\Delta\omega$ is below 65, which corresponds to monolayer thickness, which invariably denotes the exfoliation of bulk material into nanosheets (Figure 7.2a).

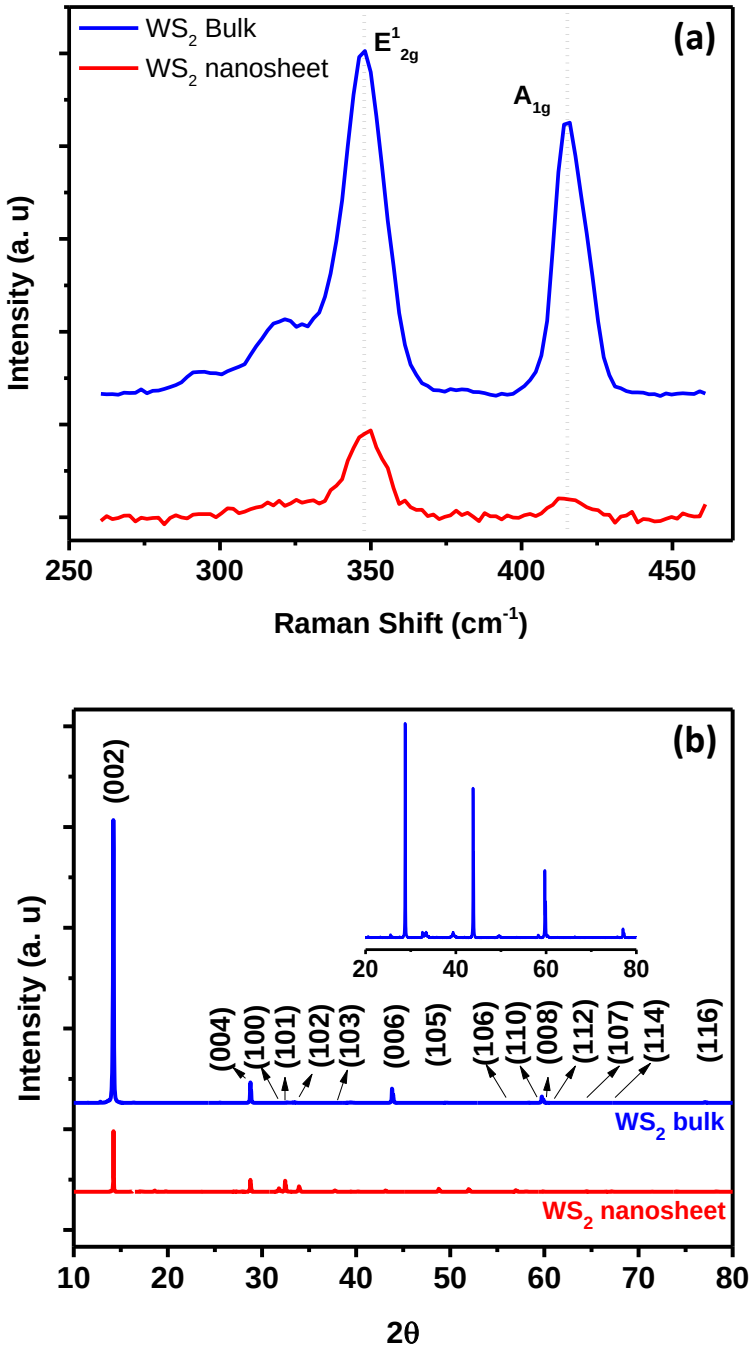

Figure 7.2: (a) Raman spectra of WS_2 powder (blue) and WS_2 nanosheets (red) (b) XRD pattern of WS_2 nanosheets (red trace), with commercial WS_2 powder as reference (blue trace). Inset shows the diffraction peaks of WS_2 powder in 20-80°.

The crystalline structure and phase of WS_2 NSs were investigated by X-ray diffraction (XRD), using WS_2 powder as reference (Figure 7.2b). The diffraction peaks

were indexed using JCPDS CARD NO 08-0237, corresponding to the pure hexagonal (P63/mmc space group) WS_2 phase. The (002) peak attest the neat stacking of layers in the powder sample, along with the peaks corresponding to (004), (100), (101), (102), (103), (006), (105), (106), (110), (008), (112), (107), (114) and (116) planes (Cheng et al., 2016; Zhang et al., 2015). It can be observed that all the diffraction peaks of WS_2 NSs can be indexed to the hexagonal 2H phase of bulk WS_2, demonstrating a well resolved crystalline structure of WS_2 NSs exfoliated in the hydrothermal condition. The absence of any additional peak indicates neither any discernible impurity of the nanosheets nor any phase change to the 1T phase during the synthesis. Besides, the weak signal from (002) plane, compared to WS_2 powder, denotes a few-layer structure of WS_2 NSs (Han et al., 2015).

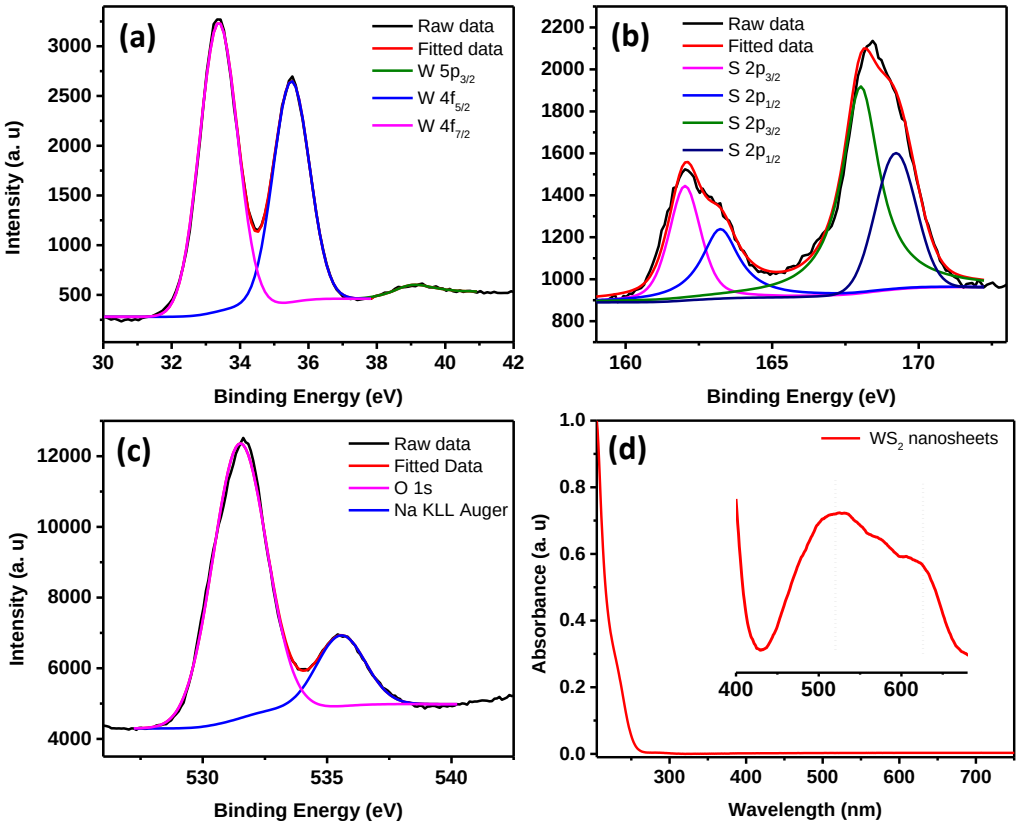

Figure 7.3: (a) to (c) High-resolution XPS spectra of W, S, and O region of WS_2 NS, respectively. (d) The UV-visible absorption spectrum of WS_2 nanosheets. The inset of (d) provides the zoomed view showing the signature peaks of sheets corresponding to A and B excitons.

The chemical state and elemental composition of WS_2 NSs were examined by X-ray photoelectron spectroscopy (XPS) analysis. The high-resolution core-level XPS peaks corresponding to W^{4+} $4f_{7/2}$ and W^{4+} $4f_{5/2}$ were observed at binding energy values 33.3 and 35.5 eV, respectively (Figure 7.3) along with a small peak at 39.3 eV for W $5p_{3/2}$. These peaks indicate the dominance of (IV) oxidation state for W in WS_2 NSs (Han et al., 2015; Zhang et al., 2018; Mao et al., 2013). The absence of peaks corresponding to the 1T phase (in the range of 31.6−32.2 eV) support that, there is no phase transformation during the hydrothermal synthesis, corroborating the observation in the XRD spectrum (Leong et al., 2017). The peaks at 162.0 and 163.2 eV, corresponding to the S $2p_{3/2}$ and $2p_{1/2}$ orbital of divalent S, bonded to W^{4+}. The peaks corresponding to the oxidized form of S are present at binding energy values of 168.0 and 169.2 eV corresponding to S $2p_{3/2}$ and $2p_{1/2}$ respectively. We surmise that, during the hydrothermal reaction, the edge S may be oxidized, leading to the formation of S and O containing functionalities, manifested as substantial aqueous solubility and phenomenal temporal stability. A single peak in high-resolution XPS of oxygen at 531.6 eV indicates this S-O bond. The absence of multiple peaks for oxygen high resolution XPS spectrum and (VI) oxidation state for W depicts that W was not oxidized during the synthesis.

The investigation of the optical signatures of WS_2 NSs has been performed through absorption and emission studies. In general, WS_2 powder possesses four major absorption bands around 630, 528, 456 and 417 nm, which are attributed to A, B, C and D excitons, respectively (Bayat and Saievar-Iranizad, 2017). The transitions from the spin-splitting valence band to the conduction band at the K point of the Brillouin zone are responsible for the emergence of peaks A and B, whereas the optical transitions from the deep valence band to the conduction band are manifested as C and D peaks (Mishra et al., 2015). As the size of the sheets decreases, due to enhanced quantum confinement effects, and edge effects, these excitonic positions can be blue shifted (Lin et al., 2013). Reports are available where a continuum of absorption in the excitonic position affirms the phase change of semiconducting 2H form to metallic 1T

form. The signature peaks of A and B excitons present in the UV-visible absorption spectrum of WS_2 NSs at 625 and 520 nm, respectively, attest the retention of semiconducting nature of the bulk powder after the vigorous hydrothermal reaction in the presence of alkali (Figure 7.3d). The quantum confinement effects that emerged due to the reduction in lateral dimensions of the sheets to the nano regime are manifested as high PL (see the fluorescence spectra given in Figure 7.4a). A typical excitation depended emission was observed for WS_2 NSs, with the best emission centered on 452 nm at an excitation wavelength of 360 nm. The heterogeneous size distribution of the sheets ranging from a few hundred nanometers to micrometers can be one of the reasons behind this behavior. The quantum yield (QY) of the sample was calculated using quinine sulphate as standard has a value of 2.2%, which is comparable with the reported QY values of WS_2 nanosheets (Zhao et al., 2013; Zhu et al., 2015). This remarkable PL from nanosheets opens the opportunity to exploit these materials in the field of fluorescence-based chemical sensors. Time-resolved fluorescence spectroscopic analysis of WS_2 NSs was performed, to unveil the information regarding the excited state phenomenon occurring within the fluorophore material. The WS_2 NSs are reported to have a very short lifetime of 800 ps (Yuan and Huang, 2015). With the shrinking of the thickness (the lateral and longitudinal dimensions) of the bulk sheets, the photo-excited carrier lifetime is found to be increased due to the enhanced stability of the excitons. In the present case, the decay curves for WS_2 NSs were collected and obtained a bi-exponential fitting with a carrier lifetime of 2.75 and 9.07 ns by keeping the numerical fitting parameter χ^2 near to 1 (Figure 7.4b).

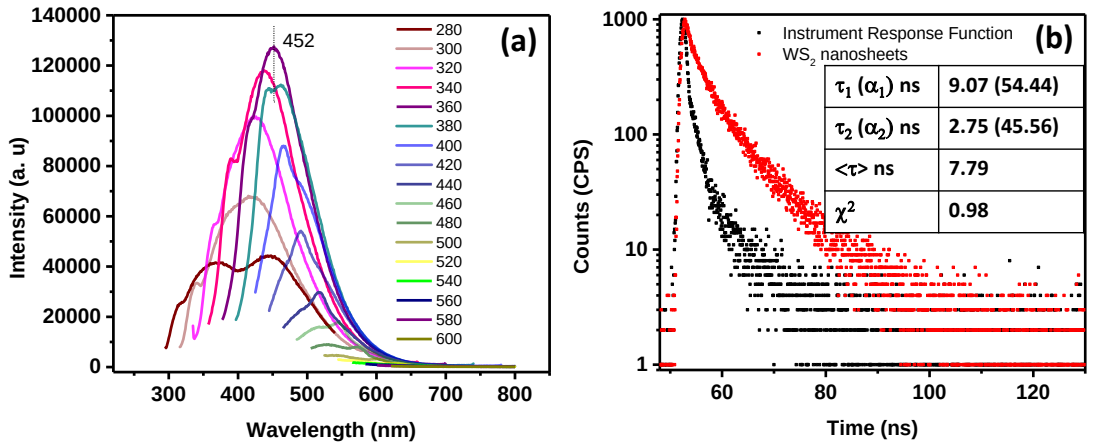

Figure 7.4: (a) Excitation dependent emission spectra of WS_2 nanosheets (b) Lifetime spectra of WS_2 nanosheets fitted with a bi-exponential function.

7.3.2 Fabrication of WS_2 nanosheets-Ag nanoparticles composite

One of the remarkable properties of the present WS_2 NSs is their stable PL and is found to be unaltered for several months in laboratory conditions. However, it was observed that the PL of the nanosheets were quenched instantaneously by the addition of a dilute solution of $AgNO_3$. Upon incremental addition of $AgNO_3$ solution (100 µL each of 0.02 M), to a solution of 2.5 mL of WS_2 nanosheets, the PL emission is found to plummet accordingly with a change in color. The colour of the solution changed from pale yellow to deep yellow (Figure 7.5a). The color change, as well as the change in PL, was rapid. This change in color was reflected in UV-Vis spectrum also. It has been observed that along with the addition of $AgNO_3$, a new absorption peak below 400 nm were emerged (Figure 7.5b). The new peak at ~400 nm prompt us to surmise that the in-situ reduction of $AgNO_3$ might have taken place at the surface of WS_2 NSs, leading to the formation of silver nanoparticles (Ag NPs).

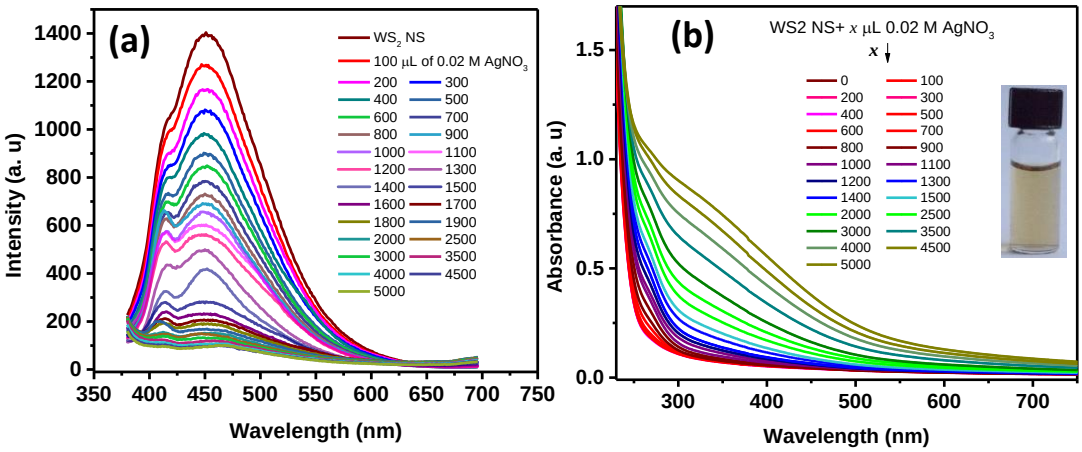

Figure 7.5 (a): The PL emission of WS_2 nanosheets after the addition of various concentrations of the $AgNO_3$ solution. (b) Absorption spectra of WS_2 nanosheets after the addition of various concentrations of $AgNO_3$ solutions. The inset of (b) shows the photograph of the WS_2 NSs solution and WS_2-AgNP nanocomposite under visible light.

TEM analysis ratifies the formation of a typical 0D-2D nanocomposite composed of Ag NPs on the surface of WS_2 NSs (Figure 7.6). Optimization of the concentration of WS_2 to $AgNO_3$ was carried out to obtain the homogenous size distribution of Ag NPs. From TEM, it was evident that for a volume ratio of 2.5 mL of WS_2 solution to 3 mL of 0.02 M $AgNO_3$ resulted in the best uniform size distribution of Ag NPs and this nanocomposite material is used for further studies.

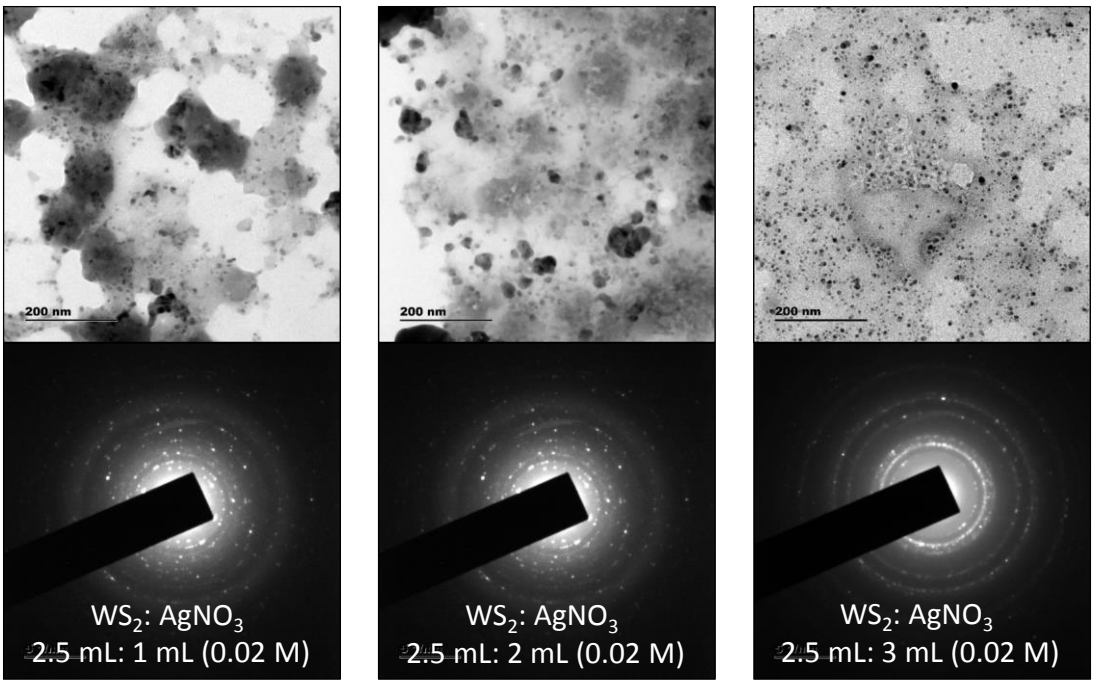

Figure 7.6: TEM images of WS_2 NSs solution after the addition of different volumes of $AgNO_3$ solution.

X-ray diffraction study was carried out to analyze the crystalline nature Ag NPs. The XRD pattern of WS_2 NSs-Ag NPs nanocomposite shows remarkable peaks at 2θ values 39.0°, 43.9° and 64.3°, apart from the peaks corresponding to WS_2 nanosheets (Figure 7.7). These peaks were indexed to (111), (200), and (220) crystal planes of the in-situ formed Ag NPs, having face-centered cubic (FCC) type nanoparticle crystals [JCPDS (CAS no. 7440-22-4)], and suggesting the existence of Ag(0) state.

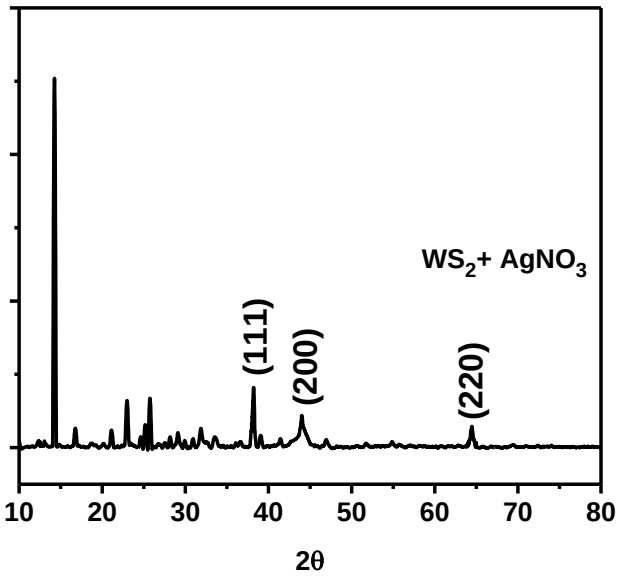

Figure 7.7: XRD patterns of WS_2 NSs-Ag NPs nanocomposite, showing peaks corresponding to the Ag NPs.

XPS analysis supports the results obtained from TEM and XRD analysis. The high-resolution XPS peaks corresponding to Ag 3d shows chemically reduced Ag(0) at 367.5 and 373.5 eV, which can be assigned to $3d_{5/2}$ and $3d_{3/2}$, respectively (Figure 7.8 a). The peak splitting with doublet separation of 6 eV, ascribed to the presence of silver in zero oxidation state (Ag(0)) (Agnihotri et al., 2015; Ambroziak et al., 2019). The ratio of the peak area of Ag $3d_{5/2}$ to Ag $3d_{3/2}$ was 3:2. A small, second spin-orbit pair at lower binding energy values (Ag $3d_{5/2}$ at 366.5 eV and Ag $3d_{3/2}$ 372.4 eV) are present along with the peak corresponding to Ag(0). We surmise that the emergence of this peak can be attributed to the bonding of Ag with S from WS_2 nanosheets. Many reports are available, showcasing the inevitability of the formation of oxide layers over Ag NPs under ambient conditions (Agnihotri et al., 2015; Ambroziak et al., 2019). Since the energy separation of Ag-S and Ag-O are not prominent, we could not separate these two peaks. The formation of Ag-O was confirmed by the emergence of a second peak in the lower energy range of the deconvoluted spectrum of oxygen, corresponding to the O-Ag bond apart from peak corresponding to the O-S bond (Figure 7.8 b).

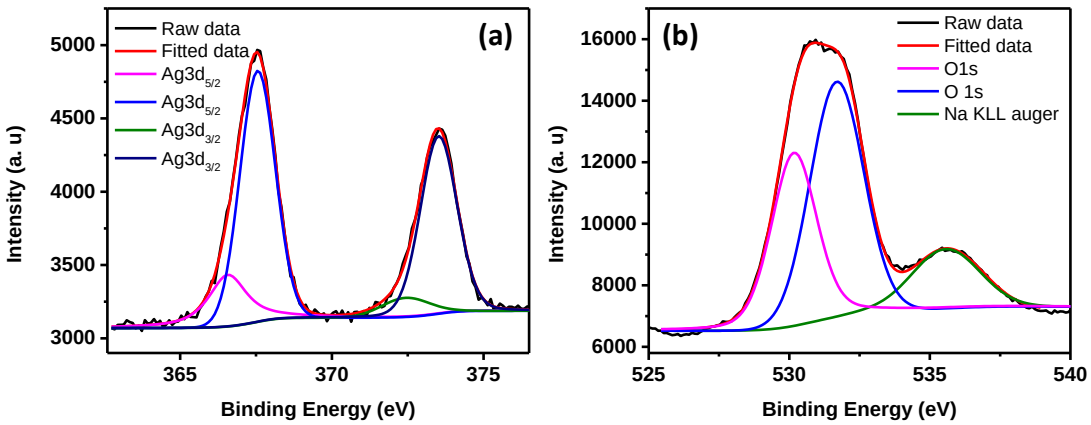

Figure 7.8: (a) High-resolution XPS peaks of Ag 3d (b) and O 1s (c) of WS_2 NSs-Ag NPs nanocomposite.

The significance of these WS_2 NSs-Ag NPs composite is that the PL of WS_2 nanosheets are quenched upon the formation of the composite. The general mechanisms of fluorescence quenching are electron transfer and energy transfer. Spectral overlap of donor emission and acceptor absorption are one of the prerequisites for excited-state quenching mechanisms; Förster resonance energy transfer (FRET). As can be seen in Figure 7.9, there is a remarkable spectral overlap of absorption of the nanocomposite with the emission of WS_2 nanosheets. Since the Ag NPs are dispersed on the surface of nanosheets, the proximity of donor and acceptor species, the second criterion to realize FRET is satisfied. Therefore, we ascribe the PL quenching to the FRET mechanism because of the presence of Ag NPs with a surface plasmon (SPR) absorption at ~400 nm.

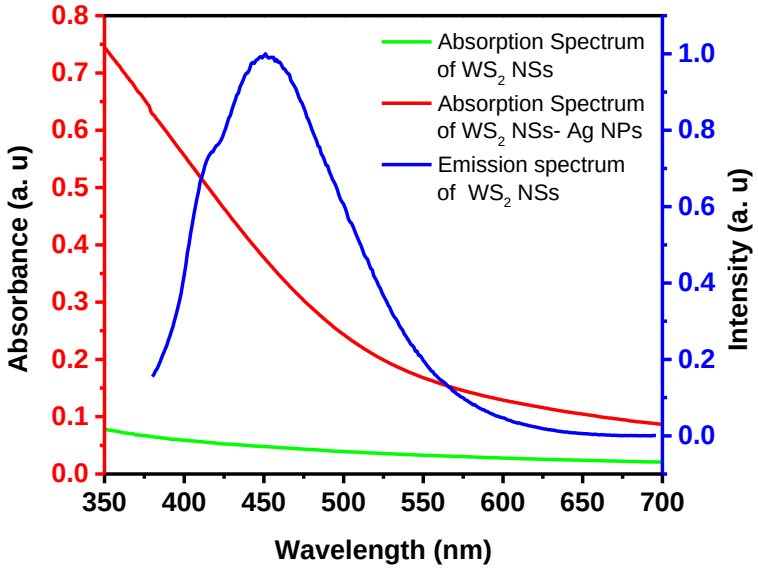

Figure 7.9: Spectral overlap of the absorption spectrum of the WS_2 NSs-Ag NPs composite (red trace) (by the addition of 3.5 mL $AgNO_3$) and the emission spectrum of WS_2 NSs (blue trace). The absorption spectrum of WS_2 NSs alone (green) is given for the comparison.

7.3.3 The nanocomposite as a turn-on sensor for basic amino acids

The quenched fluorescence of WS_2 NSs could be recovered by annihilating the nanosheet-nanoparticles dyad, which opens the possibility of creating a turn-on sensor. We have seen that the quenching is happening in the presence of Ag NPs. By disrupting these Ag NPs can shut the energy transfer pathways and the PL of WS_2 NSs can be recovered. The stability of any colloid is reasoned to the presence of charges on its surface and in the present case, it can be inferred by zeta potential measurements (Figure 7.10). Any moiety with counter charges can destroy this colloidal system and hence lead to aggregation of Ag NPs. Such aggregation of Ag NPs leads to the disappearance of SPR peaks, which is responsible for FRET. The biocompatibility and notable aqueous solubility of Ag NPs and WS_2 NSs prompted us to choose biologically relevant molecules as analytes. Interestingly, the quenched PL was found to regain upon the addition of the basic amino acids at a pH value lower than their isoelectric

point. We now formulated the WS_2 NSs-Ag NPs composite materials as a turn-on a sensor for the detection of the three basic amino acids; His, Lys and Arg.

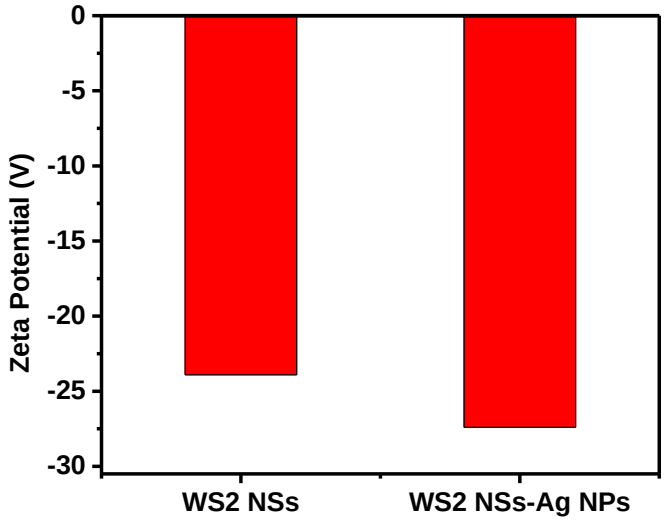

Figure 7.10: Zeta potential values of WS_2 Ns and WS_2 NSs-Ag NPs composite. The charge on the surface of nanocomposite is also negative, which endorse that the Ag NPs are of negatively charged.

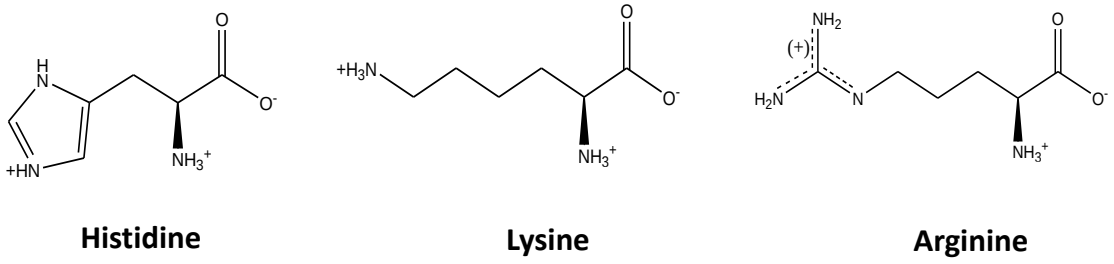

Structure of protonated basic amino acids: Histidine (His), Lysine (Lys) and Arginine (Arg).

Amino acids (AAs), though zwitterionic, tend to be positively charged at a pH below their isoelectric points (p^I) (Tsuru et al., 1994). The charges on the surface of AAs can be varied accordingly by changing the pH. The p^I of His, Lys and Arg are 7.59, 9.74 and 10.76, respectively. Hence at a pH of 7, all the three AAs will be positively charged and at pH 9, Lys and Arg will be positively charged, whereas, at pH

10, only Arg will be positively charged. The PL response of the composite towards three AAs at three different pH values are given in Figure 7.11.

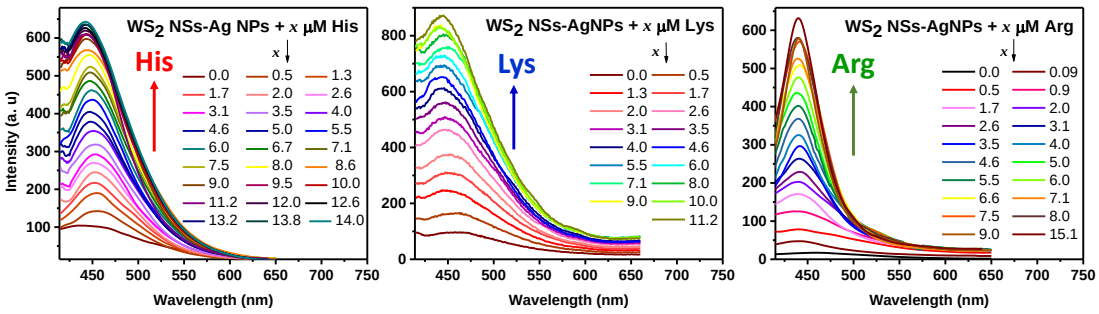

Figure 7.11: Response of His, Lys and Arg towards fluorescence emission of WS_2 NSs-Ag NPs composite. The concentration of amino acids in micromolar is given in the figure legend. The excitation wavelength was 360 nm. The pH of the solution was 7.

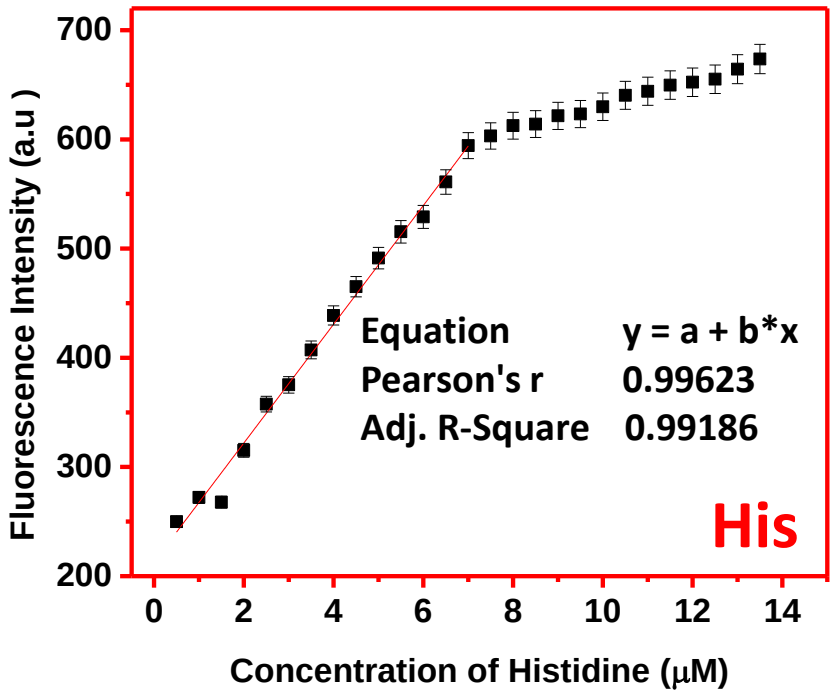

Figure 7.12: The calibration plots of the sensor solution (at pH 7) for His showing a linear range from 0.5- 7 µM.

It was noted that the PL response towards these three AAs (His, Lys and Arg) was distinct at a pH value less than its isoelectric point. We conducted the experiments in three different pH values; at pH 7, 9 and 10. As evident from Figure 7.13, at pH 7, all three AAs could turn-on the PL, whereas the recovery effect is negligible for other AAs and potential interfering biomolecules. Note that tyrosine and tryptophan show weak inherent emission at,407 and 372 nm, respectively at an excitation of 360 nm; therefore, we did not include them in the selectivity study. Thus, the composite is selective towards the detection of all the basic AAs at pH 7. The existence of protonated AAs structure at different pH gives a room for distinction within these basic AAs. For example, by changing the pH 7 to pH 9 or 10, the PL response of the nanocomposite, by the addition of AAs have collected. At pH 9 and 10, the His cannot turn-on the PL, whereas both Lys and Arg could turn-on the emission of nanocomposites. And at pH 10, Lys also fails to recover the PL of the composite; only Arg could turn-on the emission. Thus, screening of basic AAs can be accomplished by the WS_2 NSs-Ag NPs nanocomposite sensor solution, merely by altering the pH of the sensor solution. The fluorescence response of the sensor solution towards His and Arg at pH 9 and 10, respectively, is given in (Figure 7.14). In summary, the dynamic range of His (at pH) is 0.5–7.0 µM, Lys (at pH 9) is 0.5–12.0 µM and Arg (at pH) is 0.5–5.5 µM. This is summarized in the table given below. The photographs of WS_2 NSs, WS_2 NSs-Ag NPs nanocomposite, and nanocomposite solution containing His, Lys and Arg under visible and UV light have given in Figure 7.15. The photograph show the possibility of a visual screening.

	pH	**Dynamic range**
His	7.0	0.5–7.0 µM
Lys	9.0	0.5–12.0 µM
Arg	10.0	0.5–5.5 µM

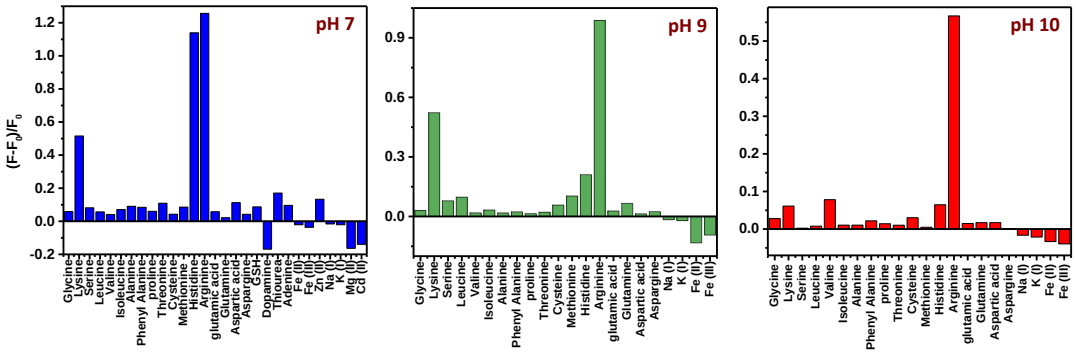

Figure 7.13: pH-dependent selectivity: Effect of different amino acids, other biomolecules, and metal ions on the fluorescence intensity of WS_2 NSs-Ag NPs composite at three different pH.

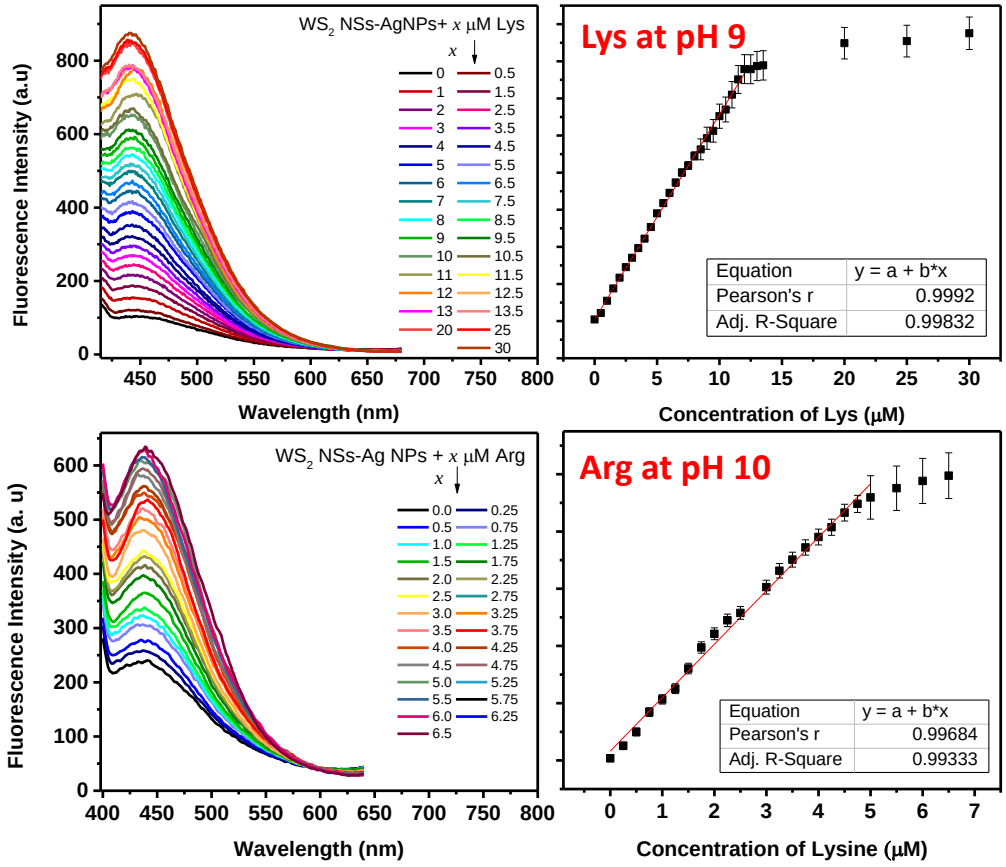

Figure 7.14: Response of Lys at pH 9, and Arg at pH 10. The calibration plots corresponding to Lys and Arg at these pH values are also given.

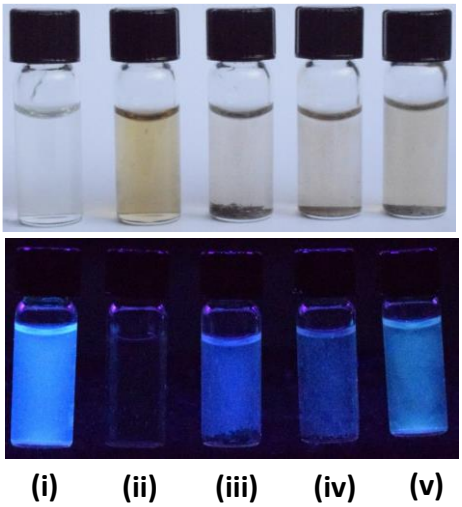

Figure 7.15: Photographs of WS_2 NS (i), WS_2 NSs-Ag NPs composite (ii), and nanocomposite solution containing Lys (iii), His (iv) and Arg (v) under visible (upper pane) and UV light (lower pane). The pH of the solution was 7.

7.3.4 Mechanism of formation of Ag NPs and fluorescence turn-on sensing

$AgNO_3$ is known to be prone to reduction even with mild reducing agents. We tried to unearth the mechanism of reducing action by WS_2 NSs. We hypothesize that the dangling S atoms of the nanosheets are taking part in the reaction, eventually leading to their removal from the sheets. We have done a careful evaluation of the results obtained from XPS spectroscopy to check the validity of this hypothesis.

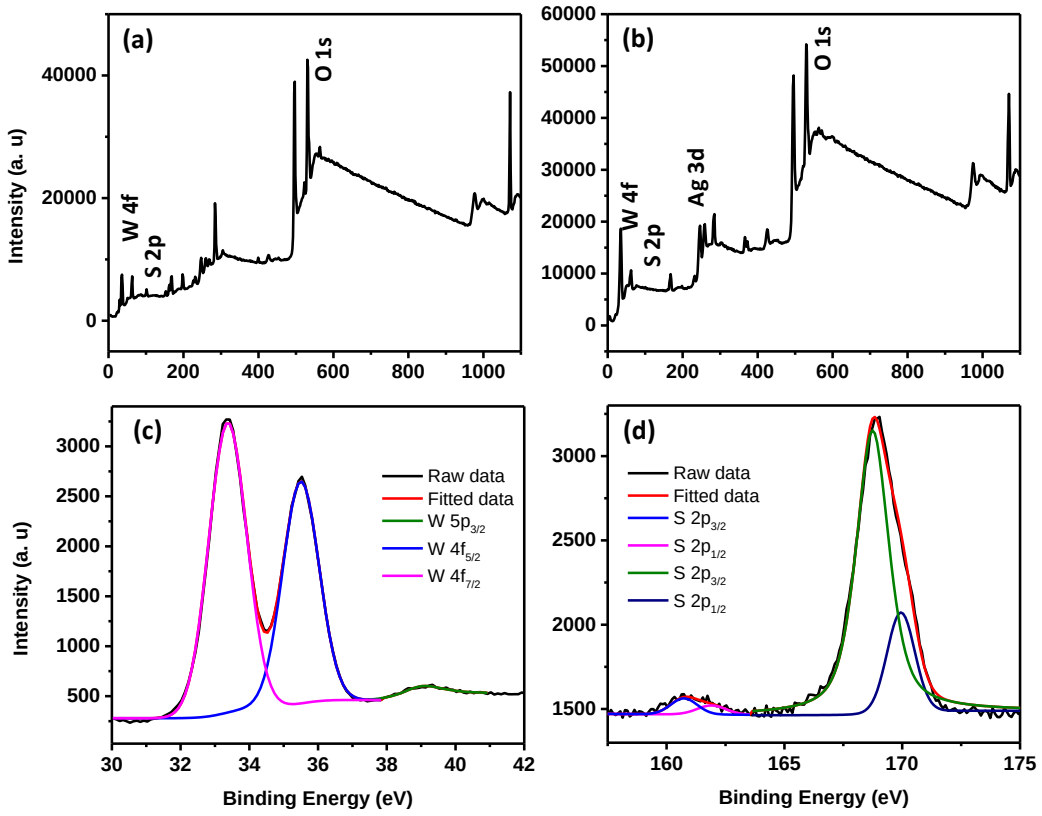

Figure 7.16: Survey scan XPS spectra of WS_2 NSs (a) and WS_2 NSs-Ag NPs nanocomposite (b). High-resolution XPS spectra of W (c), and S (d) region of WS_2 NSs-Ag NPs nanocomposite.

The survey scan XPS spectra of WS_2 NSs and WS_2-AgNPs composites show peaks corresponding to W, S, O, along with the peak of Ag in the case of WS_2 NSs-Ag NPs (Figure 7.16 a and b). The deconvoluted spectra of W of WS_2 NSs-Ag NPs composite show peaks corresponding to W $4f_{7/2}$, $4f_{5/2}$ and W $5p_{3/2}$ at slightly lower binding energy values (33.23, 35.33 and 39.13 eV, respectively) comparable to WS_2 nanosheets, due to the weaker W-S bond (Figure 7.16 c). These were having the binding values of 33.3, 35.5 and 39.3 for the case of WS_2 NSs (see Figure 7.3 and the discussion). High-resolution XPS peak corresponding to S illustrates the chemical reaction possibilities at the nanosheet surface. Although in both cases, viz. NSs alone and the 0D-2D composite, the peaks split to corresponding to S bonded to W and O, though the intensity of S bonded to W was decreased in the of 0D-2D nanocomposites (Figure 7.16 d). Besides, the atomic ratio of W to S in nanocomposite is 1: 1.12, a value

lower than the WS_2 nanosheets (Table 7.1). We deduce that the S on the nanosheets has taken part in the redox reaction (getting oxidized) during the reduction of Ag^{+1} to Ag^0, leading to the formation of Ag NPs.

Table 7.1: Elemental ratio from XPS studies

Parameter	W 4f	S 2p	O 1s	Ag 3d	N 1s	W: S Ratio
WS_2 NSs	4.2 %	13.6 %	82.2 %	-		1:3.2
WS_2-AgNPs	6.1 %	6.8 %	53.5 %	0.6 %	~ 0.1 %	1:1.12

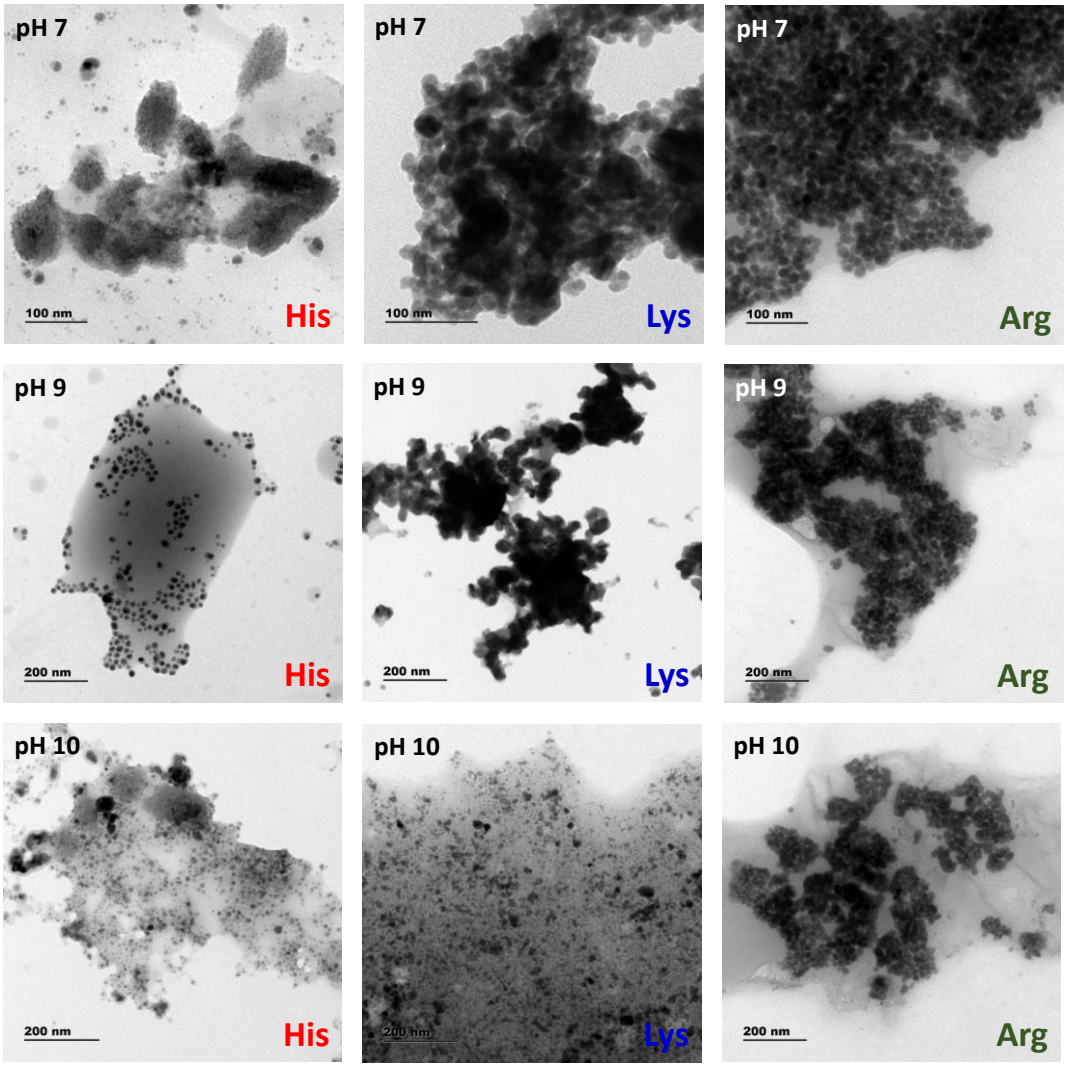

Figure 7.17: TEM images of WS_2 NSs-Ag NPs nanocomposite upon interaction with His, Lys and Arg at pH 7 (upper panel), at pH 9 (middle panel) and at pH 10 (bottom panel).

The crucial part of the turn-on sensing mechanism, on the other hand, was mainly determined by the protonated form of the basic AAs below their p^I. In the presence of AAs, the negative charges on the surface of Ag NPs are getting nullified, leading to the aggregation of Ag NPs and hence reduction of SPR peak intensity. This decrease in SPR absorption conduce for the shutting off the FRET pathway and the PL is getting recovered subsequently. The TEM micrographs, UV-visible absorption studies and lifetime analysis corroborate with these assumptions. As shown by TEM images given in Figure 7.17, Lys, His and Arg induces the aggregation of Ag NPs at pH 7. At pH 9, the intact Ag NPs are visible in the nanocomposite samples after the addition of His. At pH 10, the presence of His or Lys does not lead to aggregation. This observation further authenticates the involvement of aggregation for the PL recovery. The absence of SPR peaks in absorption spectra (Figure 7.18) in UV-visible spectra also validates the argument.

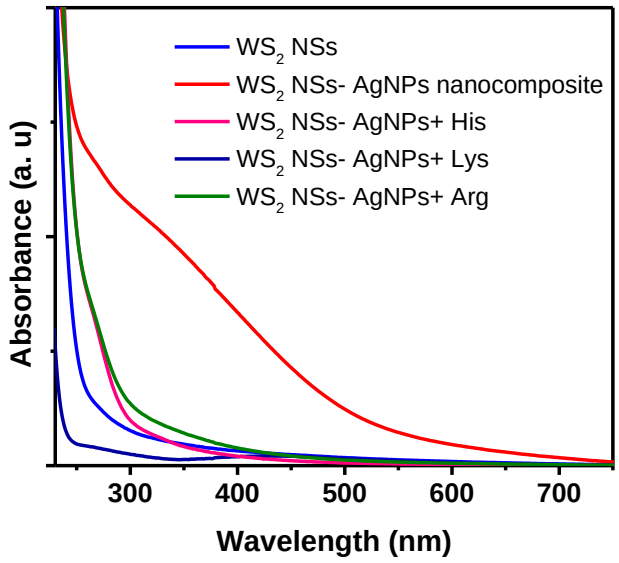

Figure 7.18: UV-visible absorption spectra of WS_2 NSs, WS_2 NSs-Ag NPs nanocomposite, WS_2 NSs-Ag NPs nanocomposite with Lys, His and Arg.

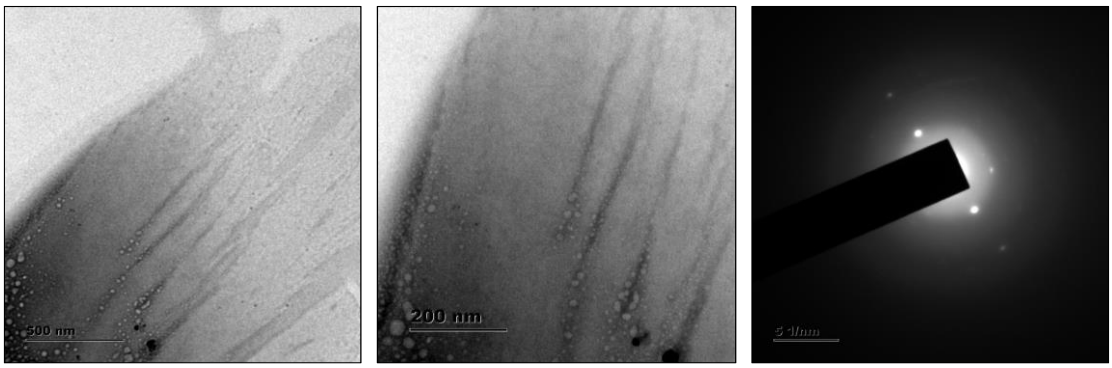

Figure 7.19: TEM image of the colorless supernatant solution after sedimentation of Ag NPs by the addition of excess amount (20 µM) of Arg at pH 7.

Another vital observation of the interaction of amino acids with the nanocomposite is the precipitation of Ag NPs upon the addition of excess amino acids (concentration above the dynamic range). The yellow color of the solution was disappeared with precipitation. The TEM analysis of this colorless supernatant solution shows that Ag NPs have been completely precipitated along with some WS_2 NSs and the solution contains only the remaining WS_2 NSs (Figure 7.19). The crystallinity and the neat morphology of the sheet were lost after the Ag NPs precipitation. We surmise that the locations with inscribed markings (in Figure 7.19) are the spots where the Ag NPs formed. This observation is supporting the argued mechanism of the formation of Ag NPs. The Ag NPs are formed onto the surface of WS_2 NSs by the reduction and may be stabilized by the groups containing S and O. When Ag NPs detach from the sheets by aggregation followed by precipitation, and the remaining sheets contain several etched areas due to the removal of adsorbed Ag NPs. The etched regions are primarily the defects due to S or its functional group vacancies. High-resolution XPS of S region shows very feeble peaks, which is proof of the removal of S from the sensor material by precipitation of Ag NPs. The oxygen region of the XPS spectrum, nonetheless, shows a peak at 531.9 eV, as in the case of WS_2 NS, which invariably shows S-O bond. Another peak around 530.3 eV might have emerged from the bonding of O with C from Histidine. Further, the high-resolution XPS analysis of W indicates that there is no significant peak shift from nanocomposite values (33.22, 35.32, and 39.02 eV), implying that the oxidation state of W was not affected (Figure 7.20).

Absence of peaks corresponding to W-O and (VI) oxidation of W display that the dangling bonds created by the removal of S was not satisfied by oxygen-containing groups. Notably, a full recovery of PL was not attained even after the addition of amino acids much above the dynamic range. This is attributed to the formation of new dangling bonds created at the sulphur vacancies upon the removal of Ag NPs along with the precipitation of portion of the WS_2 nanosheets with Ag NPs. (Figure 7.21).

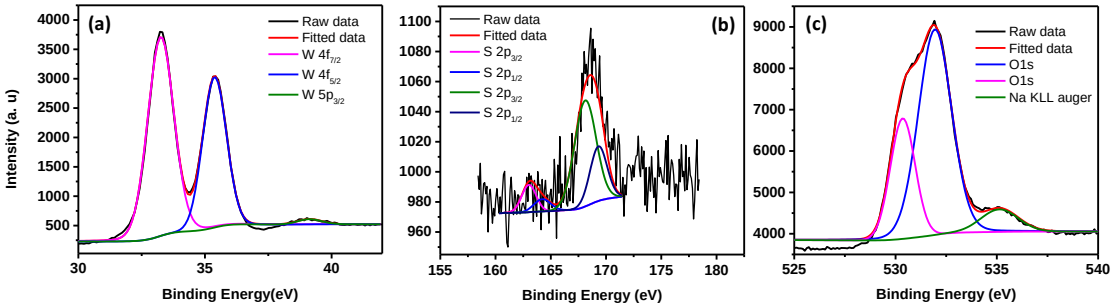

Figure 7.20: High resolution XPS peaks of (a) W, (b) S and (c) O of clear solution obtained after the full aggregation Ag NPs upon treated with excess Arg (0.8 mL of 0.1 mM, pH 7).

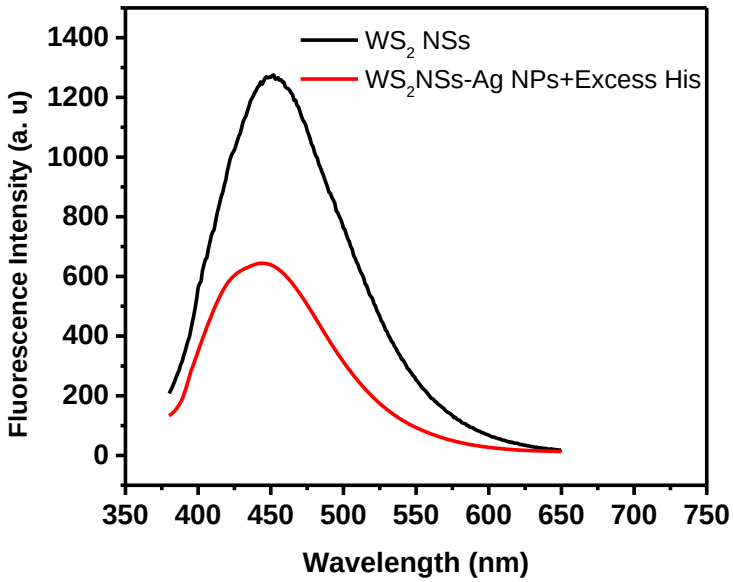

Figure 7.21: PL spectra of WS_2 NSs (black spectrum) and the solution obtained after the aggregation of Ag NPs upon addition of excess His (0.5 mL of 0.1 mM, pH 7).

The lifetime spectral analysis depicts the complexity of the interactions between AAs and the nanocomposite (**Figure 7.22**). The removal of FRET upon the addition of the amino acids is substantiated by the recovery of lifetime values (see **Table 7.2**). The emergence of a new non-radiative pathway for the solutions with His, Lys and Arg is attributed to the defect created in the sheets due to Ag NPs formation.

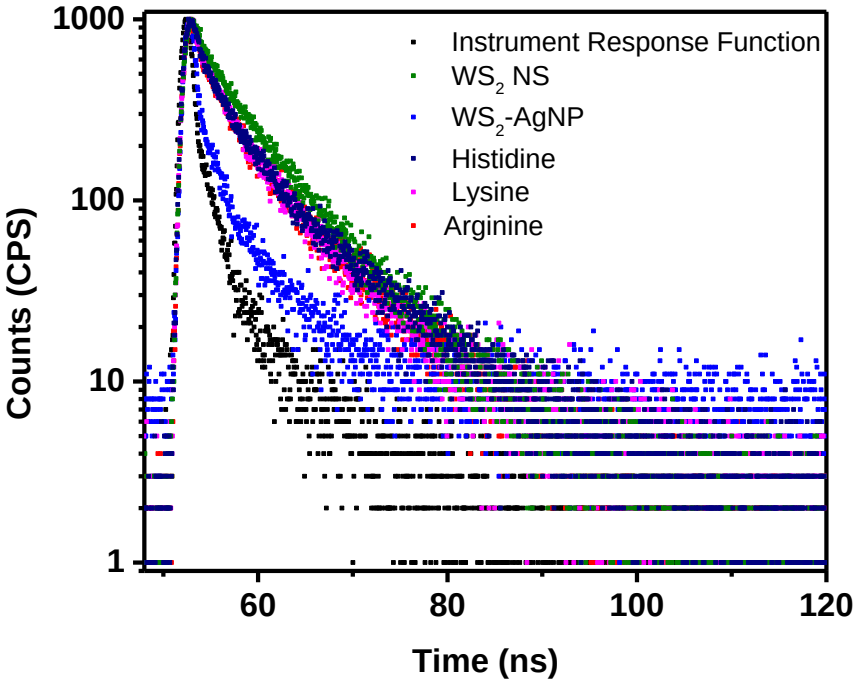

Figure 7.22: Lifetime spectra of WS_2 NSs, WS_2 NSs-Ag NPs nanocomposite, WS_2 NSs-Ag NPs nanocomposite with His, Lys and Arg (the pH was 7). A 3 mL of 0.2 mM Ag NO_3 solution was added to 2.5 mL WS_2 solution. The volume and concentrations of amino acids were 0.5 mL of 0.1 mM His, and Lys, 0.8 mL of 0.1 mM Arg, respectively.

Table 7.2: Table showing the lifetime of WS_2 NSs, WS_2 NSs-Ag NPs nanocomposite, WS_2 NSs-Ag NPs nanocomposite with Lys, His and Arg (the pH was 7). A 3 mL of 0.2 mM Ag NO_3 solution was added to 2.5 mL WS_2 solution. The volume and concentrations of amino acids were 0.5 mL of 0.1 mM His, and Lys, 0.8 mL of 0.1 mM Arg, respectively.

System	τ_1 (ns)	α_1	τ_2 (ns)	α_2	τ_3	α_3	$<\tau>$ (ns)	χ^2
WS_2	9.1	54.44	2.8	45.56			7.8	0.98

WS_2+$AgNO_3$	6.2	19.62	0.13	80.38			5.7	1.2
WS_2+$AgNO_3$+Lys	8.1	30.27	2.8	40.32	0.5	29.40	6.2	0.9
WS_2+$AgNO_3$+His	8.9	31.74	3.9	45.79	0.7	22.46	6.7	0.8
WS_2+$AgNO_3$+Arg	8.6	34.90	2.8	35.69	0.5	29.41	6.9	0.9

7.4 Conclusion

In this chapter, we demonstrated the potential of a luminescent 2D layered material, exfoliated WS_2 nanosheet as a sensor for biologically relevant molecules. The stable luminescent WS_2 nanosheets were synthesized using the facile hydrothermal synthetic route. Interestingly, Ag NPs were formed on the surface of sheets instantaneously by the addition of the $AgNO_3$ solution, which showcases the reducing capability of WS_2 nanosheets. The formation of Ag NPs leads to the reduction of PL from WS_2 NSs via FRET. We investigated the effect of positively charged basic nanoparticles on the PL of WS_2 nanosheet-Ag NPs composite and fabricated a turn-on sensor for three basic amino acids viz. His, Lys and Arg. The easy, straightforward synthetic method followed for the formation of stable and highly fluorescent WS_2 nanosheets without the use of any hazardous solvents, the in-situ formation of stable Ag NPs without the addition of any extra stabilizing agent, devising a simple aggregation strategy to shut the FRET pathway, thereby ensuing a turn-on detection and screening of all the basic amino acids are the highlights of the present sensor system.

CHAPTER 8

CONCLUSION AND FUTURE PERSPECTIVE

8.1 Conclusions

Atomically thin two-dimensional (2D) nanomaterials such as graphene, transition metal dichalcogenides (TMDs), transition metal oxides, boron nitride, etc. have garnered ample attention due to their unique properties such as geometrical structure, large specific surface area, electronic properties, the feasibility of dispersion in aqueous solutions, etc. They have widespread potential utility in the areas of optical, electrical, catalytic and biological applications. Although various synthetic routes and technological possibilities of these materials have been extensively explored over a decade or two, there are a few issues that need further attention. The quantum yield of these materials is generally meager (~0.3 % for single-layer MoS_2) compared to carbon-based or semiconductor-based QDs. Generation of thick layers (instead of mono or bilayers) upon simple techniques like liquid-phase exfoliation and phase change to metallic 1T phase upon using Li based intercalants for exfoliation are other issues to be looked upon. The choice and cost of precursors and monetary viability of the synthetic route need special attention. Our work aims to address a few of the issues mentioned above. Herein, we demonstrate a simple, low-cost and green preparative strategy towards highly stable and fluorescent MoS_2/WS_2 nanomaterials such as nanosheets, quantum dots, a hybrid of nanosheets-quantum dots, by hydrothermal treatment of bulk MoS_2/WS_2 crystal in the aqueous solution of NaOH. We have demonstrated the chemical sensing applications of selected materials for the detection of various analytes of having biological as well as industrial relevance.

Chapter 1 deals with the introduction to 2D layered materials with a detailed literature review. It gives an overview of the present status of various synthetic routes, general properties and various applications of 2D layered materials in general with particular emphasis on MoS_2 and WS_2 based nanomaterials. The basics of fluorescence,

mechanisms of fluorescence quenching and general approaches to various fluorescence sensing with a few interesting examples were highlighted in this Chapter.

A facile and green route for the synthesis of MoS_2 based nanomaterials such as nanosheets (NSs) and a hybrid system consist of quantum dots and nanosheets (abbreviated as QDNS) has been demonstrated in Chapter 2. The synthesis was accomplished by the high-temperature hydrothermal reaction of MoS_2 powder in various concentrations of NaOH. All the nanomaterials were found to be highly photoluminescent (QY up to 4%). The origin of PL from hybrid materials, MoS_2 QDNS were also unraveled by various spectroscopic investigations.

Fluorescence sensors for biologically active molecules are catching attention due to their excellent performance and simplicity. Chapter 3 comprised of fluorescent detection of dopamine (DA), a neurotransmitter in our body. MoS_2 QDNS in the alkaline medium was employed as the fluorescent probe. In the presence of DA, the PL intensity of MoS_2 QDNS was quenched linearly with the increasing concentration of the former. The quenching mechanisms operate via Förster resonance energy transfer (FRET), and the inner filter effect (IFE). The QDNS sensor demonstrates high selectivity towards DA, especially in the presence of ascorbic acid and uric acid, which are the most potential interference for DA in biological systems. The sensitivity of the system was as low as 0.9 nM and depicted two linear ranges from 2.5 nM to 5.0 μM and from 5.0 μM to 10.4 μM. The sensor demonstrated a remarkable ability in the analysis of real blood samples and excellent for visual detection.

In Chapter 4, the mechanism of variation in the fluorescence emission of MoS_2 nanohybrid (nanosheet-quantum dots) material with a change in pH is unraveled. Upon changing the pH of the solution from basic to acidic, the PL emission from these materials is found to be diminished remarkably, which can be recovered by the addition of an oxidizing agent, H_2O_2. We envisage that removal of dangling S atoms from the surface of MoS_2 QDNS upon the addition of acid could be a plausible mechanism for the initial PL quenching. This S, in turn, can create new compounds with the Na ions present in the solution, which aid additionally for the PL quenching via inner filter effect (IFE) and Förster resonance energy transfer (FRET). In the presence of H_2O_2,

these new compounds were getting oxidized, which is manifested as the recovery of PL emission. We made use of this strategy for the indirect detection of glucose by incorporating glucose oxidize, an enzyme with acidified MoS_2 QDNS. The sensor shows a linear range of 2- 90 µM, with a lower detection limit of 0.6 µM.

Synthesis of various water-soluble WS_2 nanomaterials such as WS_2 quantum dots, WS_2 quantum dots dispersed over nanosheets and the WS_2 nanosheets were detailed in Chapter 5. The synthesis was accomplished by hydrothermal reaction of bulk WS_2 powder in the presence of different concentration ratios of NaOH. The same strategy used in Chapter 2 for the synthesis of MoS_2 nanomaterials was utilized here. The WS_2 nanomaterials have demonstrated with high temporal as well as photostability and satisfactory photoluminescence. Various microscopic and photophysical characterization has been carried out to understand the materials.

In Chapter 6, we have shown a PL based sensing application of WS_2 QDs for the selective and sensitive detection of trinitrophenol (TNP), a dangerous explosive in the family of nitroaromatics (NAs). The addition of TNP into a solution of luminescent WS_2 QDs was manifested as quenching of fluorescence from WS_2 QDs in a linear fashion. We obtained two linear ranges from 0.5 to 63 µM and 63 to 94.5 µM indicating the possibility for multiple mechanisms involved during the interaction. Careful examination of absorption and emission features of quencher (TNP) and fluorophore, respectively and the zeta potential values, we surmise that Förster resonance energy transfer and electron transfer along with inner filter effect are the primary mechanisms which cause quenching. Since all the NAs are electron deficient, they can facilitate the quenching of PL emission by electron transfer. Howbeit, the other mechanisms of quenching give it room for the selectivity, particularly towards TNP over other NAs.

Chapter 7 describes the chemical sensor applications of WS_2 nanosheets synthesized by the hydrothermal reaction of a 1:1 mixture of WS_2 bulk and NaOH. Upon addition of $AgNO_3$ into a colloidal solution of WS_2 nanosheets, the PL emission from the latter is found to be decreased along with the formation of Ag NPs on the surface of nanosheets. The quenching of PL emission is attributed to the formation of Ag NPs. In the presence of basic amino acids, lysine, histidine and arginine, a pH below

their isoelectric points, the PL emission from the sheet are recovered. This is attributed to the aggregation of negatively charged Ag NPs by positively charged basic amino acids. Detailed microscopic, as well as spectroscopic studies such as TEM analysis, steady-state as well as time, resolved fluorescence spectra, Raman spectra, XPS analysis has been carried to unveil the mechanism of quenching and turn-on of PL.

8.2 Future Perspectives

The fact of growing interest in 2D layered materials, which has the potential to be applicable in various vistas, is apparent from the number of scientific articles published over a decade. The hydrothermal method that we have proposed for the generation of nanomaterials of MoS_2 and WS_2 with different dimensions and morphology can be extended for less explored layered materials, such as transition metal oxides, nitrides, phosphorenes, silicenes, etc. The tuning of optical and electronic properties of these nanomaterials can be achieved by functionalization using suitable ligands.

Calculations of HOMO-LUMO levels of various sheets, quantum dots, or hybrid dot-sheet materials can throw further light into their electrochemical behavior. The applicability of these materials as the fluorescence-based chemical sensor can be propelled by increasing their quantum yield, preferably by doping with various metal ions. Various studies have unraveled the role of edge S on MoS_2 nanosheets as HER catalyst. Hybrid materials such as MoS_2 QDNS or WS_2 QDNS, with the potential of both nanosheets and quantum dots, can be a preferable candidate for further pursuing such studies. It is interesting to study the chemi-resistive application of pristine nanosheets obtained. The utility of WS_2 nanosheets for protein sensing can also be explored, along with the tailoring of these nanosheets with organic molecules or nanoclusters for multiplexed detection. These materials have the propensity to be modified according to the needs. Carefully designed materials have the prospective to become next-generation bioimaging agents and optoelectronic devices.

REFERENCE

1. Aparna, R. S., Devi, J. A., Sachidanandan, P., & George, S. (2018). Polyethylene imine capped copper nanoclusters-fluorescent and colorimetric onsite sensor for the trace level detection of TNT. *Sensors and Actuators B: Chemical*, 254, 811-819.

2. Abo, M., Urano, Y., Hanaoka, K., Terai, T., Komatsu, T., & Nagano, T. (2011). Development of a highly sensitive fluorescence probe for hydrogen peroxide. *Journal of the American Chemical Society*, 133(27), 10629-10637.

3. Afanasiev, P., Xia, G. F., Berhault, G., Jouguet, B., & Lacroix, M. (1999). Surfactant-assisted synthesis of highly dispersed molybdenum sulfide. *Chemistry of materials*, 11(11), 3216-3219.

4. Agnihotri, S., Bajaj, G., Mukherji, S., & Mukherji, S. (2015). Arginine assisted immobilization of silver nanoparticles on ZnO nanorods: An enhanced and reusable antibacterial substrate without human cell cytotoxicity. *Nanoscale*, 7, 7415-7429. doi: 10.1039/c4nr06913g

5. Alem, N., Erni, R., Kisielowski, C., Rossell, M. D., Gannett, W., & Zettl, A. J. P. R. B. (2009). Atomically thin hexagonal boron nitride probed by ultrahigh-resolution transmission electron microscopy. *Physical review B*, 80(15), 155425.

6. Alexiev, V., Prins, R., & Weber, T. (2000). Ab initio study of MoS_2 and Li adsorbed on the (101 [combining macron] 0) face of MoS_2. *Physical Chemistry Chemical Physics*, 2(8), 1815-1827.

7. Alonso-Cristobal, P., Vilela, P., El-Sagheer, A., Lopez-Cabarcos, E., Brown, T., Muskens, O.L., Rubio-Retama, J. and Kanaras, A.G. (2015). Highly sensitive DNA sensor based on upconversion nanoparticles and graphene oxide. *ACS applied materials & interfaces*, 7(23), 12422-12429.

8. Ambroziak, R., Holdynski, M., Płociński, T., Pisarek, M., & Kudelski, A. (2019). Cubic Silver Nanoparticles Fixed on TiO_2 Nanotubes as Simple and Efficient Substrates for Surface Enhanced Raman Scattering. *Materials*, 12, 3373. doi: 10.3390/ma12203373

9. An, T., Lee, N., Cho, H. J., Kim, S., Shin, D. S., & Lee, S. M. (2017). Ultra-selective detection of Fe^{2+} ion by redox mechanism based on fluorescent polymerized dopamine derivatives. *RSC Advances*, 7(49), 30582-30587.

10. Ankireddy, S. R., & Kim, J. (2015). Dopamine-functionalized InP/ZnS quantum dots as fluorescence probes for the detection of adenosine in microfluidic chip. *International journal of nanomedicine*, 10(Spec Iss), 121.

11. Appel, J. H., Li, D. O., Podlevsky, J. D., Debnath, A., Green, A. A., Wang, Q. H., & Chae, J. (2016). Low cytotoxicity and genotoxicity of two-dimensional MoS_2 and WS_2. *ACS Biomaterials Science & Engineering*, 2(3), 361-367.

12. Artero, V., Chavarot-Kerlidou, M., & Fontecave, M. (2011). Splitting water with cobalt. *Angewandte Chemie International Edition*, 50(32), 7238-7266.

13. Bae, S., Kim, H., Lee, Y., Xu, X., Park, J.S., Zheng, Y., Balakrishnan, J., Lei, T., Kim, H.R., Song, Y.I. and Kim, Y.J. (2010). Roll-to-roll production of 30-inch graphene films for transparent electrodes. *Nature nanotechnology*, 5(8), 574.

14. Ban, R., Abdel-Halim, E. S., Zhang, J., & Zhu, J. J. (2015). β-Cyclodextrin functionalised gold nanoclusters as luminescence probes for the ultrasensitive detection of dopamine. *Analyst*, 140(4), 1046-1053.

15. Barua, S., Dutta, H. S., Gogoi, S., Devi, R., & Khan, R. (2017). Nanostructured MoS2-based advanced biosensors: a review. *ACS Applied Nano Materials*, 1(1), 2-25.

16. Bayat, A., & Saievar-Iranizad, E. (2017). Synthesis of blue photoluminescent WS_2 quantum dots via ultrasonic cavitation. *Journal of Luminescence*, 185, 236-240. doi: https://doi.org/10.1016/j.jlumin.2017.01.024

17. Benameur, M. M., Radisavljevic, B., Héron, J. S., Sahoo, S., Berger, H., & Kis, A. (2011). Visibility of dichalcogenide nanolayers. *Nanotechnology*, 22(12), 125706.

18. Benavente, E., Santa Ana, M. A., Mendizábal, F., & González, G. (2002). Intercalation chemistry of molybdenum disulfide. *Coordination chemistry reviews*, 224(1-2), 87-109.

19. Bertolazzi, S., Brivio, J., & Kis, A. (2011). Stretching and breaking of ultrathin MoS2. *ACS nano*, 5(12), 9703-9709.

20. Bisaglia, M., Mammi, S., & Bubacco, L. (2007). Kinetic and structural analysis of the early oxidation products of dopamine analysis of the interactions with α-synuclein. *Journal of Biological Chemistry*, 282(21), 15597-15605.

21. Bissessur, R., Kanatzidis, M. G., Schindler, J. L., & Kannewurf, C. R. (1993). Encapsulation of polymers into MoS_2 and metal to insulator transition in metastable MoS_2. *Journal of the Chemical Society, Chemical Communications*, (20), 1582-1585.

22. Böker, T., Severin, R., Müller, A., Janowitz, C., Manzke, R., Voß, D., Krüger, P., Mazur, A. and Pollmann, J. (2001). Band structure of MoS_2, $MoSe_2$, and α−$MoTe_2$: Angle-resolved photoelectron spectroscopy and ab initio calculations. *Physical Review B*, 64(23), 235305.

23. Cabán-Acevedo, M., Stone, M.L., Schmidt, J.R., Thomas, J.G., Ding, Q., Chang, H.C., Tsai, M.L., He, J.H. and Jin, S. (2015). Efficient hydrogen evolution catalysis using ternary pyrite-type cobalt phosphosulphide. *Nature materials*, 14(12), 1245-1251.

24. Cai, Z., Li, F., Wu, P., Ji, L., Zhang, H., Cai, C., & Gervasio, D. F. (2015). Synthesis of nitrogen-doped graphene quantum dots at low temperature for electrochemical sensing trinitrotoluene. *Analytical chemistry*, 87(23), 11803-11811.

25. Caigas, S. P., Santiago, S. R. M., Lin, T. N., Lin, C. A. J., Yuan, C. T., Shen, J. L., & Lin, T. Y. (2018). Origins of excitation-wavelength-dependent photoluminescence in WS_2 quantum dots. *Applied Physics Letters*, 112(9), 092106.

26. Cao, S., Liu, T., Hussain, S., Zeng, W., Peng, X., & Pan, F. (2014). Hydrothermal synthesis of variety low dimensional WS_2 nanostructures. *Materials Letters*, 129, 205-208.

27. Castellanos-Gomez, A., Barkelid, M., Goossens, A. M., Calado, V. E., van der Zant, H. S., & Steele, G. A. (2012). Laser-thinning of MoS_2: on demand generation of a single-layer semiconductor. *Nano letters*, 12(6), 3187-3192.

28. Chabot, V., Higgins, D., Yu, A., Xiao, X., Chen, Z., & Zhang, J. (2014). A review of graphene and graphene oxide sponge: material synthesis and applications to energy and the environment. *Energy & Environmental Science*, 7(5), 1564-1596.

29. Chang, H., Wang, X., Shiu, K.K., Zhu, Y., Wang, J., Li, Q., Chen, B. and Jiang, H. (2013). Layer-by-layer assembly of graphene, Au and poly (toluidine blue O) films sensor for evaluation of oxidative stress of tumor cells elicited by hydrogen peroxide. *Biosensors and Bioelectronics*, 41, 789-794.

30. Chatterjee, A., Banerjee, M., Khandare, D.G., Gawas, R.U., Mascarenhas, S.C., Ganguly, A., Gupta, R. and Joshi, H. (2017). Aggregation-induced emission-based chemodosimeter approach for selective sensing and imaging of Hg (II) and methylmercury species. *Analytical chemistry*, 89(23), 12698-12704.

31. Chen, Bin, Shuiqin Chai, Jiahui Liu, Chuanjun Liu, Yanjie Li, Jiahui He, Zeping Yu, Tong Yang, Changhao Feng, and Chengzhi Huang. (2019). 2, 4, 6-Trinitrophenol detection by a new portable sensing gadget using carbon dots as a fluorescent probe. *Analytical and bioanalytical chemistry*, 411(11), 2291-2300.

32. Chen, D., Liu, M., Yin, L., Li, T., Yang, Z., Li, X., Fan, B., Wang, H., Zhang, R., Li, Z. and Xu, H. (2011b). Single-crystalline MoO_3 nanoplates: topochemical synthesis and enhanced ethanol-sensing performance. *Journal of Materials Chemistry*, 21(25), 9332-9342.

33. Chen, F., Xia, J., Ferry, D. K., & Tao, N. (2009). Dielectric screening enhanced performance in graphene FET. *Nano letters*, 9(7), 2571-2574.

34. Chen, J. L., Yan, X. P., Meng, K., & Wang, S. F. (2011c). Graphene oxide based photoinduced charge transfer label-free near-infrared fluorescent biosensor for dopamine. *Analytical chemistry*, 83(22), 8787-8793.

35. Chen, Q., Espey, M.G., Krishna, M.C., Mitchell, J.B., Corpe, C.P., Buettner, G.R., Shacter, E. and Levine, M. (2005). Pharmacologic ascorbic acid concentrations selectively kill cancer cells: action as a pro-drug to deliver hydrogen peroxide to tissues. *Proceedings of the National Academy of Sciences*, 102(38), 13604-13609.

36. Chen, S. C., Lin, C. Y., Cheng, T. L., & Tseng, W. L. (2017b). 6-mercaptopurine-induced fluorescence quenching of monolayer MoS_2 nanodots: applications to glutathione sensing, cellular imaging, and glutathione-stimulated drug delivery. *Advanced Functional Materials*, 27(41), 1702452.

37. Chen, W.F., Sasaki, K., Ma, C., Frenkel, A.I., Marinkovic, N., Muckerman, J.T., Zhu, Y. and Adzic, R.R. (2012a). Hydrogen-evolution catalysts based on non-noble metal nickel–molybdenum nitride nanosheets. *Angewandte Chemie International Edition*, 51(25), 6131-6135.

38. Chen, Y.C., Lu, A.Y., Lu, P., Yang, X., Jiang, C.M., Mariano, M., Kaehr, B., Lin, O., Taylor, A., Sharp, I.D. and Li, L.J. (2017a). Structurally deformed MoS_2 for electrochemically stable, thermally resistant, and highly efficient hydrogen evolution reaction. *Advanced Materials*, 29(44), 1703863.

39. Chen, Z., Cummins, D., Reinecke, B. N., Clark, E., Sunkara, M. K., & Jaramillo, T. F. (2011a). Core–shell MoO_3–MoS_2 nanowires for hydrogen evolution: a functional design for electrocatalytic materials. *Nano letters*, 11(10), 4168-4175.

40. Cheng, Y., Peng, J., Xu, B., Yang, H., Luo, Z., Xu, H., . . . Weng, J. (2016). Passive Q-switching Of A Diode-pumped Pr:liyf_4 Visible Laser Using WS_2 As Saturable Absorber. *IEEE Photonics Journal*, 8, 1-1. doi: 10.1109/jphot.2016.2550804

41. Chhowalla, M., Shin, H. S., Eda, G., Li, L. J., Loh, K. P., & Zhang, H. (2013). The chemistry of two-dimensional layered transition metal dichalcogenide nanosheets. *Nature chemistry*, 5(4), 263.

42. Chhowalla, M., Voiry, D., Yang, J., Shin, H. S., & Loh, K. P. (2015). Phase-engineered transition-metal dichalcogenides for energy and electronics. *Mrs Bulletin*, 40(7), 585-591.

43. Coleman, J.N., Lotya, M., O'Neill, A., Bergin, S.D., King, P.J., Khan, U., Young, K., Gaucher, A., De, S., Smith, R.J. and Shvets, I.V. (2011). Two-dimensional nanosheets produced by liquid exfoliation of layered materials. *Science*, 331(6017), 568-571.

44. Cong, C., Shang, J., Wu, X., Cao, B., Peimyoo, N., Qiu, C., . . . Yu, T. (2014). Synthesis and optical properties of large-area single-crystalline 2D semiconductor WS_2 monolayer from chemical vapor deposition. *Advanced Optical Materials*, 2(2), 131-136.

45. Conley, H. J., Wang, B., Ziegler, J. I., Haglund Jr, R. F., Pantelides, S. T., & Bolotin, K. I. (2013). Bandgap engineering of strained monolayer and bilayer MoS_2. *Nano letters*, 13(8), 3626-3630.

46. Cunningham, G., Lotya, M., Cucinotta, C. S., Sanvito, S., Bergin, S. D., Menzel, R., Shaffer, M & Coleman, J. N. (2012). Solvent exfoliation of transition metal dichalcogenides: dispersibility of exfoliated nanosheets varies only weakly between compounds. *ACS nano*, 6(4), 3468-3480.

47. da Silva, J. L., Beluomini, M. A., Sedenho, G. C., & Stradiotto, N. R. (2017). Determination of amino acids in sugarcane vinasse by ion chromatographic using nickel nanoparticles on reduced graphene oxide modified electrode. *Microchemical Journal*, 134, 374-382.

48. Dagnino-Subiabre, A., Cassels, B. K., Baez, S., Johansson, A. S., Mannervik, B., & Segura-Aguilar, J. (2000). Glutathione transferase M2-2 catalyzes conjugation of dopamine and dopa o-quinones. *Biochemical and biophysical research communications*, 274(1), 32-36.

49. Das, R.K., Wang, Y., Vasilyeva, S.V., Donoghue, E., Pucher, I., Kamenov, G., Cheng, H.P. and Rinzler, A.G. (2014). Extraordinary hydrogen evolution and oxidation reaction activity from carbon nanotubes and graphitic carbons. *ACS Nano*, 8(8), 8447-8456.

50. Dean, C.R., Young, A.F., Meric, I., Lee, C., Wang, L., Sorgenfrei, S., Watanabe, K., Taniguchi, T., Kim, P., Shepard, K.L. and Hone, J. (2010). Boron nitride substrates for high-quality graphene electronics. *Nature nanotechnology*, 5(10), 722.

51. Deng, X., & Wu, D (2014). Highly sensitive photoluminescence energy transfer detection for 2, 4, 6-trinitrophenol using photoluminescent carbon nanodots. *RSC Advances*, 4(79), 42066-42070.

52. Dennis, A. M., Rhee, W. J., Sotto, D., Dublin, S. N., & Bao, G. (2012). Quantum Dot–Fluorescent Protein FRET Probes for Sensing Intracellular pH. *ACS Nano*, 6(4), 2917-2924. doi: 10.1021/nn2038077

53. Dinda, D., Gupta, A., Shaw, B. K., Sadhu, S., & Saha, S. K. (2014). Highly selective detection of trinitrophenol by luminescent functionalized reduced graphene oxide through FRET mechanism. *ACS applied materials & interfaces*, 6(13), 10722-10728.

54. Dines, M. B. (1975). Lithium intercalation via n-butyllithium of the layered transition metal dichalcogenides. *Materials Research Bulletin*, 10(4), 287-291.

55. Dong, H., Tang, S., Hao, Y., Yu, H., Dai, W., Zhao, G., ... & Ju, H. (2016). Fluorescent MoS_2 quantum dots: ultrasonic preparation, up-conversion and down-conversion bioimaging, and photodynamic therapy. *ACS applied materials & interfaces*, 8(5), 3107-3114.

56. Dong, M., Wang, Y. W., Zhang, A. J., & Peng, Y. (2013). Colorimetric and Fluorescent Chemosensors for the Detection of 2, 4, 6-Trinitrophenol and Investigation of their Co-Crystal Structures. *Chemistry–An Asian Journal*, 8(6), 1321-1330.

57. Doolen, R., Laitinen, R., Parsapour, F., & Kelley, D. F. (1998). Trap state dynamics in MoS_2 nanoclusters. *The Journal of Physical Chemistry B*, 102(20), 3906-3911.

58. Doroshow, J. H. (1986). Role of hydrogen peroxide and hydroxyl radical formation in the killing of Ehrlich tumor cells by anticancer quinones. *Proceedings of the National Academy of Sciences*, 83(12), 4514-4518.

59. Du, P., & Eisenberg, R. (2012). Catalysts made of earth-abundant elements (Co, Ni, Fe) for water splitting: recent progress and future challenges. *Energy & Environmental Science*, 5(3), 6012-6021.

60. Duan, J., Chen, S., Jaroniec, M., & Qiao, S. Z. (2015). Porous C3N4 nanolayers@ N-graphene films as catalyst electrodes for highly efficient hydrogen evolution. *ACS nano*, 9(1), 931-940.

61. Eda, G., Fujita, T., Yamaguchi, H., Voiry, D., Chen, M., & Chhowalla, M. (2012). Coherent atomic and electronic heterostructures of single-layer MoS_2. *ACS Nano*, 6(8), 7311-7317.

62. Eda, G., Yamaguchi, H., Voiry, D., Fujita, T., Chen, M., & Chhowalla, M. (2011). Photoluminescence from chemically exfoliated MoS_2. *Nano letters*, 11(12), 5111-5116.

63. Ergen, O., Gibb, A., Vazquez-Mena, O., Regan, W. R., & Zettl, A. (2015). Metal insulator semiconductor solar cell devices based on a Cu_2O substrate utilizing h-BN as an insulating and passivating layer. *Applied Physics Letters*, 106(10), 103904.

64. Faber, M. S., & Jin, S. (2014). Earth-abundant inorganic electrocatalysts and their nanostructures for energy conversion applications. *Energy & Environmental Science*, 7(11), 3519-3542.

65. Feng, C., Ma, J., Li, H., Zeng, R., Guo, Z., & Liu, H. (2009). Synthesis of molybdenum disulfide (MoS_2) for lithium ion battery applications. *Materials Research Bulletin*, 44(9), 1811-1815.

66. Frey, G. L., Reynolds, K. J., Friend, R. H., Cohen, H., & Feldman, Y. (2003). Solution-processed anodes from layer-structure materials for high-efficiency

polymer light-emitting diodes. *Journal of the American Chemical Society*, 125(19), 5998-6007.

67. Gan, Z., Gui, Q., Shan, Y., Pan, P., Zhang, N., & Zhang, L. (2016). Photoluminescence of MoS_2 quantum dots quenched by hydrogen peroxide: A fluorescent sensor for hydrogen peroxide. *Journal of Applied Physics*, 120(10), 104503.

68. Ganiga, M., & Cyriac, J. (2016). Understanding the Photoluminescence Mechanism of Nitrogen-Doped Carbon Dots by Selective Interaction with Copper Ions. *ChemPhysChem*, 17(15), 2315-2321.

69. Ganiga, M., Mani, N. P., & Cyriac, J. (2018). Synthesis of Organophilic Carbon Dots, Selective Screening of Trinitrophenol and a Comprehensive Understanding of Luminescence Quenching Mechanism. *ChemistrySelect*, 3(17), 4663-4668.

70. Ge, J., Ou, E. C., Yu, R. Q., & Chu, X. (2014). A novel aptameric nanobiosensor based on the self-assembled DNA–MoS_2 nanosheet architecture for biomolecule detection. *Journal of Materials Chemistry B*, 2(6), 625-628.

71. Geldert, A., Zhang, X., Zhang, H., & Lim, C. T. (2016). Highly sensitive and selective aptamer-based fluorescence detection of a malarial biomarker using single-layer MoS_2 nanosheets. *ACS Sensors*, 1(11), 1315-1321.

72. Germain, M. E., & Knapp, M. J. (2008). Turn-on fluorescence detection of H_2O_2 and TATP. *Inorganic chemistry*, 47(21), 9748-9750.

73. Gill, R., Bahshi, L., Freeman, R., & Willner, I. (2008). Optical detection of glucose and acetylcholine esterase inhibitors by H_2O_2-sensitive CdSe/ZnS quantum dots. *Angewandte Chemie International Edition*, 47(9), 1676-1679.

74. Gopalakrishnan, D., Damien, D., & Shaijumon, M. M. (2014). MoS_2 quantum dot-interspersed exfoliated MoS_2 nanosheets. *ACS nano*, 8(5), 5297-5303.

75. Gordon, R. A., Yang, D., Crozier, E. D., Jiang, D. T., & Frindt, R. F. (2002). Structures of exfoliated single layers of WS_2, MoS_2, and $MoSe_2$ in aqueous suspension. *Physical Review B*, 65(12), 125407.

76. Gu, W., Pei, X., Cheng, Y., Zhang, C., Zhang, J., Yan, Y., Ding, C. and Xian, Y. (2017a). Black phosphorus quantum dots as the ratiometric fluorescence probe for trace mercury ion detection based on inner filter effect. *ACS sensors*, 2(4), 576-582.

77. Gu, W., Yan, Y., Pei, X., Zhang, C., Ding, C., & Xian, Y. (2017b). Fluorescent black phosphorus quantum dots as label-free sensing probes for evaluation of acetylcholinesterase activity. *Sensors and Actuators B: Chemical*, 250, 601-607.

78. Gu, W., Yan, Y., Zhang, C., Ding, C., & Xian, Y. (2016). One-Step Synthesis of Water-Soluble MoS_2 Quantum Dots via a Hydrothermal Method as a

Fluorescent Probe for Hyaluronidase Detection. *ACS Applied Materials & Interfaces*, 8(18), 11272-11279. doi: 10.1021/acsami.6b01166

79. Guo, C., Wang, Y., Zhao, Y., & Xu, C. (2013). Non-enzymatic glucose sensor based on three dimensional nickel oxide for enhanced sensitivity. *Analytical Methods*, 5(7), 1644-1647.

80. Ha, H. D., Han, D. J., Choi, J. S., Park, M., & Seo, T. S. (2014). Dual role of blue luminescent MoS_2 quantum dots in fluorescence resonance energy transfer phenomenon. *Small*, 10(19), 3858-3862.

81. Haldar, D., Dinda, D., & Saha, S. K. (2016). High selectivity in water soluble MoS_2 quantum dots for sensing nitro explosives. *Journal of Materials Chemistry C*, 4(26), 6321-6326.

82. Han, G.-Q., Liu, Y.-R., Hu, W.-H., Dong, B., Li, X., Chai, Y.-M., Liu, C.-G. (2015). WS_2 nanosheets based on liquid exfoliation as effective electrocatalysts for hydrogen evolution reaction. *Materials Chemistry and Physics*, 167, 271-277.

83. Hasanzadeh, M., Karimzadeh, A., Shadjou, N., Mokhtarzadeh, A., Bageri, L., Sadeghi, S., & Mahboob, S. (2016). Graphene quantum dots decorated with magnetic nanoparticles: Synthesis, electrodeposition, characterization and application as an electrochemical sensor towards determination of some amino acids at physiological pH. *Materials Science and Engineering*: C, 68, 814-830.

84. Hazarika, S. J., & Mohanta, D. (2019). Excitation dependent light emission and enhanced photocatalytic response of WS_2/C-dot hybrid nanoscale systems. *Journal of Luminescence*, 206, 530-539.

85. Heising, J., & Kanatzidis, M. G. (1999). Exfoliated and restacked MoS_2 and WS_2: Ionic or neutral species? Encapsulation and ordering of hard electropositive cations. *Journal of the American Chemical Society*, 121(50), 11720-11732.

86. Hernandez, Y., Nicolosi, V., Lotya, M., Blighe, F.M., Sun, Z., De, S., McGovern, I.T., Holland, B., Byrne, M., Gun'Ko, Y.K. and Boland, J.J. (2008). High-yield production of graphene by liquid-phase exfoliation of graphite. *Nature nanotechnology*, 3(9), 563.

87. Hinnemann, B., Moses, P.G., Bonde, J., Jørgensen, K.P., Nielsen, J.H., Horch, S., Chorkendorff, I. and Nørskov, J.K. (2005). Biomimetic hydrogen evolution: MoS_2 nanoparticles as catalyst for hydrogen evolution. *Journal of the American Chemical Society*, 127(15), 5308-5309.

88. Ho, M. Y., D'Souza, N., & Migliorato, P. (2012). Electrochemical aptamer-based sandwich assays for the detection of explosives. *Analytical chemistry*, 84(10), 4245-4247.

89. Hoffmann, M. R. (1977). Kinetics and mechanism of oxidation of hydrogen sulfide by hydrogen peroxide in acidic solution. *Environmental Science & Technology*, 11(1), 61-66.

90. Hu, L., Ren, Y., Yang, H., & Xu, Q. (2014). Fabrication of 3D hierarchical MoS_2/polyaniline and MoS_2/C architectures for lithium-ion battery applications. *ACS applied materials & interfaces*, 6(16), 14644-14652.

91. Huang, Guochuang, Tao Chen, Weixiang Chen, Zhen Wang, Kun Chang, Lin Ma, Feihe Huang, Dongyun Chen, and Jim Yang Lee. (2013). Graphene-Like MoS_2/Graphene Composites: Cationic Surfactant-Assisted Hydrothermal Synthesis and Electrochemical Reversible Storage of Lithium. *Small*, 9(21), 3693-3703.

92. Huang, J (a)., Ye, L., Gao, X., Li, H., Xu, J., & Li, Z. (2015). Molybdenum disulfide-based amplified fluorescence DNA detection using hybridization chain reactions. *Journal of Materials Chemistry B*, 3(11), 2395-2401.

93. Huang, J., Wei, Z., Liao, J., Ni, W., Wang, C., & Ma, J. (2019). Molybdenum and tungsten chalcogenides for lithium/sodium-ion batteries: Beyond MoS_2. *Journal of energy chemistry*, 33, 100-124.

94. Huang, Y (b)., Shi, Y., Yang, H. Y., & Ai, Y. (2015). A novel single-layered MoS_2 nanosheet based microfluidic biosensor for ultrasensitive detection of DNA. *Nanoscale*, 7(6), 2245-2249.

95. Ivanova, B., & Kolev, T. (2011). Linearly polarized IR spectroscopy: theory and applications for structural analysis. *CRC Press*.

96. Jackson, R. K., Shi, Y., Yao, X., & Burdette, S. C. (2010). FerriNaphth: A fluorescent chemodosimeter for redox active metal ions. *Dalton Transactions*, 39(17), 4155-4161.

97. Jaramillo, T. F., Jørgensen, K. P., Bonde, J., Nielsen, J. H., Horch, S., & Chorkendorff, I. (2007). Identification of active edge sites for electrochemical H_2 evolution from MoS_2 nanocatalysts. *Science*, 317(5834), 100-102.

98. Jariwala, D., Sangwan, V. K., Lauhon, L. J., Marks, T. J., & Hersam, M. C. (2014). Emerging device applications for semiconducting two-dimensional transition metal dichalcogenides. *ACS nano*, 8(2), 1102-1120.

99. Jiang, N., Li, G., Che, W., Zhu, D., Su, Z., & Bryce, M. R. (2018). Polyurethane derivatives for highly sensitive and selective fluorescence detection of 2, 4, 6-trinitrophenol (TNP). *Journal of Materials Chemistry C*, 6(42), 11287-11291.

100. Jie, Y., Wang, N., Cao, X., Xu, Y., Li, T., Zhang, X., & Wang, Z. L. (2015). Self-powered triboelectric nanosensor with poly (tetrafluoroethylene) nanoparticle arrays for dopamine detection. *ACS nano*, 9(8), 8376-8383.

101. Joensen, P., Frindt, R. F., & Morrison, S. R. (1986). Single-layer MoS_2. *Materials research bulletin*, 21(4), 457-461.

102. Johari, P., & Shenoy, V. B. (2012). Tuning the electronic properties of semiconducting transition metal dichalcogenides by applying mechanical strains. *ACS nano*, 6(6), 5449-5456.

103. Junqueira, J. R., de Araujo, W. R., Salles, M. O., & Paixão, T. R. (2013). Flow injection analysis of picric acid explosive using a copper electrode as electrochemical detector. *Talanta*, 104, 162-168.

104. Kalantar-zadeh, K., Vijayaraghavan, A., Ham, M. H., Zheng, H., Breedon, M., & Strano, M. S. (2010). Synthesis of atomically thin WO_3 sheets from hydrated tungsten trioxide. *Chemistry of Materials*, 22(19), 5660-5666.

105. Kamat, P. V. (2008). Quantum dot solar cells. Semiconductor nanocrystals as light harvesters. *The Journal of Physical Chemistry C*, 112(48), 18737-18753.

106. Kamyshny, A., Ekeltchik, I., Gun, J., & Lev, O. (2006). Method for the determination of inorganic polysulfide distribution in aquatic systems. *Analytical chemistry*, 78(8), 2631-2639.

107. Kang, W., Wang, Y., & Xu, J. (2017). Recent progress in layered metal dichalcogenide nanostructures as electrodes for high-performance sodium-ion batteries. *Journal of Materials Chemistry A*, 5(17), 7667-7690.

108. Kee, C. W. (2015). Assignment of O–O and Mo= O stretching frequencies of molybdenum/tungsten complexes revisited. *Journal of Chemistry*, 2015.

109. Kim, T. H., Kim, Y. H., Park, S. Y., Kim, S. Y., & Jang, H. W. (2017). Two-dimensional transition metal disulfides for chemoresistive gas sensing: perspective and challenges. *Chemosensors*, 5(2), 15.

110. Kiriya, D., Hijikata, Y., Pirillo, J., Kitaura, R., Murai, A., Ashida, A., Yoshimura, T. and Fujimura, N. (2018). Systematic study of photoluminescence enhancement in monolayer molybdenum disulfide by acid treatment. *Langmuir*, 34(35), 10243-10249.

111. Kirmayer, S., Aharon, E., Dovgolevsky, E., Kalina, M., & Frey, G. L. (2007). Self-assembled lamellar MoS_2, SnS_2 and SiO_2 semiconducting polymer nanocomposites. *Philosophical Transactions of the Royal Society A: Mathematical, Physical and Engineering Sciences*, 365(1855), 1489-1508.

112. Kolanu, B. R., Boddula, V., Vadakedath, S., & Kandi, V. (2017). Amino acid (leucine) chromatography: a study of branched-chain aminoaciduria in type 2 diabetes. *Cureus*, 9(3).

113. Krishnamoorthy, K., Veerasubramani, G. K., Radhakrishnan, S., & Kim, S. J. (2014). Supercapacitive properties of hydrothermally synthesized sphere like MoS_2 nanostructures. *Materials Research Bulletin*, 50, 499-502.

114. Krishnan, U., Kaur, M., Singh, K., Kumar, M., & Kumar, A. (2019). A synoptic review of MoS_2: Synthesis to applications. *Superlattices and Microstructures*.

115. Kuc, A., Zibouche, N., & Heine, T. (2011). Influence of quantum confinement on the electronic structure of the transition metal sulfide T S $_2$. *Physical Review B*, 83(24), 245213.

116. Kwak, K., Kumar, S. S., & Lee, D. (2012). Selective determination of dopamine using quantum-sized gold nanoparticles protected with charge selective ligands. *Nanoscale*, 4(14), 4240-4246.

117. Lakowicz, J. R. (Ed.). (2013). Principles of fluorescence spectroscopy. *Springer Science & Business Media.*

118. Late, D.J., Huang, Y.K., Liu, B., Acharya, J., Shirodkar, S.N., Luo, J., Yan, A., Charles, D., Waghmare, U.V., Dravid, V.P. and Rao, C.N.R. (2013). Sensing behavior of atomically thin-layered MoS_2 transistors. *ACS nano*, 7(6), 4879-4891.

119. Lee , Y.H., Zhang, X.Q., Zhang, W., Chang, M.T., Lin, C.T., Chang, K.D., Yu, Y.C., Wang, J.T.W., Chang, C.S., Li, L.J. and Lin, T.W. (2012a). Synthesis of large-area MoS_2 atomic layers with chemical vapor deposition. *Advanced materials*, 24(17), 2320-2325.

120. Lee, C., Yan, H., Brus, L. E., Heinz, T. F., Hone, J., & Ryu, S. (2010a). Anomalous lattice vibrations of single-and few-layer MoS_2. *ACS nano*, 4(5), 2695-2700.

121. Lee, H.S., Min, S.W., Chang, Y.G., Park, M.K., Nam, T., Kim, H., Kim, J.H., Ryu, S. and Im, S (2012b). MoS_2 nanosheet phototransistors with thickness-modulated optical energy gap. *Nano letters*, 12(7), 3695-3700.

122. Lee, I., Kim, J. N., Kang, W. T., Shin, Y. S., Lee, B. H., & Yu, W. J. (2019). Schottky Barrier Variable Graphene/Multilayer–MoS_2 Heterojunction Transistor Used to Overcome Short Channel Effects. *ACS Applied Materials & Interfaces.*

123. Lee, K., Kim, H. Y., Lotya, M., Coleman, J. N., Kim, G. T., & Duesberg, G. S. (2011). Electrical characteristics of molybdenum disulfide flakes produced by liquid exfoliation. *Advanced materials*, 23(36), 4178-4182.

124. Lee, K.-S., & El-Sayed, M. A. (2006). Gold and Silver Nanoparticles in Sensing and Imaging: Sensitivity of Plasmon Response to Size, Shape, and Metal Composition. *The Journal of Physical Chemistry B*, 110(39), 19220-19225. doi: 10.1021/jp062536y

125. Lee, M. H., Van Giap, T., Kim, S. H., Lee, Y. H., Kang, C., & Kim, J. S. (2010b). A novel strategy to selectively detect Fe (III) in aqueous media driven by

hydrolysis of a rhodamine 6G Schiff base. *Chemical Communications*, 46(9), 1407-1409.

126. Lee, Y.H., Zhang, X.Q., Zhang, W., Chang, M.T., Lin, C.T., Chang, K.D., Yu, Y.C., Wang, J.T.W., Chang, C.S., Li, L.J. and Lin, T.W. (2012c). Synthesis of large-area MoS_2 atomic layers with chemical vapor deposition. *Advanced materials*, 24(17), 2320-2325.

127. Leong, S. X., Mayorga-Martinez, C. C., Chia, X., Luxa, J., Sofer, Z., & Pumera, M. (2017). 2H → 1T Phase Change in Direct Synthesis of WS_2 Nanosheets via Solution-Based Electrochemical Exfoliation and Their Catalytic Properties. *ACS Applied Materials & Interfaces*, 9(31), 26350-26356. doi: 10.1021/acsami.7b06898

128. Li, B. L., Zou, H. L., Lu, L., Yang, Y., Lei, J. L., Luo, H. Q., & Li, N. B. (2015). Size-dependent optical absorption of layered MoS_2 and dna oligonucleotides induced dispersion behavior for label-free detection of single-nucleotide polymorphism. *Advanced Functional Materials*, 25(23), 3541-3550.

129. Li, H., Lu, G., Yin, Z., He, Q., Li, H., Zhang, Q., & Zhang, H. (2012b). Optical identification of single-and few-layer MoS_2 sheets. *Small*, 8(5), 682-686.

130. Li, H., Yin, Z., He, Q., Li, H., Huang, X., Lu, G., Fam, D.W.H., Tok, A.I.Y., Zhang, Q. and Zhang, H. (2012c). Fabrication of single-and multilayer MoS_2 film-based field-effect transistors for sensing NO at room temperature. *Small*, 8(1), 63-67.

131. Li, H., Zhang, Q., Yap, C. C. R., Tay, B. K., Edwin, T. H. T., Olivier, A., & Baillargeat, D. (2012a). From bulk to monolayer MoS_2: evolution of Raman scattering. *Advanced Functional Materials*, 22(7), 1385-1390.

132. Li, Jing, and Jiangtao Li. (2018). A luminescent porous metal–organic framework with Lewis basic pyridyl sites as a fluorescent chemosensor for TNP detection. *Inorganic Chemistry Communications* 89: 51-54.

133. Li, L., Qin, Z., Ries, L., Hong, S., Michel, T., Yang, J., Salameh, C., Bechelany, M., Miele, P., Kaplan, D. and Chhowalla, M. (2019a). Role of sulfur vacancies and undercoordinated Mo regions in MoS_2 nanosheets toward the evolution of hydrogen. *ACS nano*, 13(6), 6824-6834.

134. Li, W. J., Shi, E. W., Ko, J. M., Chen, Z. Z., Ogino, H., & Fukuda, T. (2003). Hydrothermal synthesis of MoS_2 nanowires. *Journal of Crystal Growth*, 250(3-4), 418-422.

135. Li, X., Cai, W., An, J., Kim, S., Nah, J., Yang, D., Piner, R., Velamakanni, A., Jung, I., Tutuc, E. and Banerjee, S.K. (2009a). Large-area synthesis of high-quality and uniform graphene films on copper foils. *Science*, 324(5932), 1312-1314.

136. Li, X., Liu, J., Gong, X., Qing, T., Zhang, P., & Feng, B. (2019b). Synthesis of fluorescent tungsten disulfide by nitrogen atom doping and its application for mercury (ii) detection. *Journal of Materials Chemistry C*, 7(14), 4096-4101.

137. Li, X., Zhou, Y., Zheng, Z., Yue, X., Dai, Z., Liu, S., & Tang, Z. (2009b). Glucose biosensor based on nanocomposite films of CdTe quantum dots and glucose oxidase. *Langmuir*, 25(11), 6580-6586.

138. Li, Y., Liu, M., Xiang, C., Xie, Q., & Yao, S. (2006). Electrochemical quartz crystal microbalance study on growth and property of the polymer deposit at gold electrodes during oxidation of dopamine in aqueous solutions. *Thin Solid Films*, 497(1-2), 270-278.

139. Li, Z., Chen, J., Dhall, R., & Cronin, S. B. (2016). Highly efficient, high speed vertical photodiodes based on few-layer MoS_2. *2D Materials*, 4(1), 015004.

140. Lim, N. C., Pavlova, S. V., & Brückner, C. (2009). Squaramide hydroxamate-based chemidosimeter responding to iron (III) with a fluorescence intensity increase. *Inorganic chemistry*, 48(3), 1173-1182.

141. Lin, L., Rong, M., Lu, S., Song, X., Zhong, Y., Yan, J., Y., Wang & Chen, X. (2015). A facile synthesis of highly luminescent nitrogen-doped graphene quantum dots for the detection of 2, 4, 6-trinitrophenol in aqueous solution. *Nanoscale*, 7(5), 1872-1878.

142. Lin, L., Xu, Y., Zhang, S., Ross, I. M., Ong, A. C., & Allwood, D. A. (2013). Fabrication of luminescent monolayered tungsten dichalcogenides quantum dots with giant spin-valley coupling. *ACS nano*, 7(9), 8214-8223.

143. Lin, M.-W., Kravchenko, I. I., Fowlkes, J., Li, X., Puretzky, A. A., Rouleau, C. M., Geohegan, D.B., Xiao, K. (2016). Thickness-dependent charge transport in few-layer MoS_2 field-effect transistors. *Nanotechnology*, 27(16), 165203.

144. Lin, T. W., Dhenadhayalan, N., Lee, H. L., Lin, Y. T., Lin, K. C., & Chang, A. H. H. (2019). Fluorescence turn-on chemosensors based on surface-functionalized MoS_2 quantum dots. *Sensors and Actuators B: Chemical*, 281, 659-669.

145. Lin, W., Yuan, L., Feng, J., & Cao, X. (2008). A Fluorescence-Enhanced Chemodosimeter for Fe^{3+} Based on Hydrolysis of Bis (coumarinyl) Schiff Base. *European Journal of Organic Chemistry*, 2008(16), 2689-2692.

146. Lin, Y. C., Zhang, W., Huang, J. K., Liu, K. K., Lee, Y. H., Liang, C. T., Chu, C.W. & Li, L. J. (2012). Wafer-scale MoS_2 thin layers prepared by MoO_3 sulfurization. *Nanoscale*, 4(20), 6637-6641.

147. Lin, Y. H., & Tseng, W. L. (2009). Highly sensitive and selective detection of silver ions and silver nanoparticles in aqueous solution using an oligonucleotide-based fluorogenic probe. *Chemical communications*, (43), 6619-6621.

148. Lin, Y., Chen, C., Wang, C., Pu, F., Ren, J., & Qu, X. (2011). Silver nanoprobe for sensitive and selective colorimetric detection of dopamine via robust Ag–catechol interaction. *Chemical Communications*, 47(4), 1181-1183.

149. Lisdat, F., Wollenberger, U., Makower, A., Hörtnagl, H., Pfeiffer, D., & Scheller, F. W. (1997). Catecholamine detection using enzymatic amplification. *Biosensors and Bioelectronics*, 12(12), 1199-1211.

150. Liu, G., Rumyantsev, S. L., Jiang, C., Shur, M. S., & Balandin, A. A. (2015). Selective Gas Sensing With h -BN Capped MoS_2 Heterostructure Thin-Film Transistors. *IEEE Electron Device Letters*, 36(11), 1202-1204.

151. Liu, G., Rumyantsev, S., Shur, M. S., & Balandin, A. A. (2013). Origin of 1/f noise in graphene multilayers: Surface vs. volume. *Applied Physics Letters*, 102(9), 093111.

152. Liu, H., & Chi, D. (2015). Dispersive growth and laser-induced rippling of large-area singlelayer MoS_2 nanosheets by CVD on c-plane sapphire substrate. *Scientific Reports*, 5, 11756.

153. Liu, H., Shao, J., Shi, L., Ke, W., Zheng, F., & Zhao, Y. (2020). Electroactive NPs and D-amino acids oxidase engineered electrochemical chiral sensor for D-alanine detection. *Sensors and Actuators B: Chemical*, 304, 127333.

154. Liu, K.K., Zhang, W., Lee, Y.H., Lin, Y.C., Chang, M.T., Su, C.Y., Chang, C.S., Li, H., Shi, Y., Zhang, H. and Lai, C.S. (2012). Growth of large-area and highly crystalline MoS_2 thin layers on insulating substrates. *Nano Letters*, 12(3), 1538-1544.

155. Liu, N., Kim, P., Kim, J. H., Ye, J. H., Kim, S., & Lee, C. J. (2014a). Large-area atomically thin MoS_2 nanosheets prepared using electrochemical exfoliation. *ACS nano*, 8(7), 6902-6910.

156. Liu, S., Shi, F., Chen, L., & Su, X. (2013). Bovine serum albumin coated $CuInS_2$ quantum dots as a near-infrared fluorescence probe for 2, 4, 6-trinitrophenol detection. *Talanta*, 116, 870-875.

157. Liu, T., Li, N., Dong, J. X., Zhang, Y., Fan, Y. Z., Lin, S. M., . . . Li, N. B. (2017). A colorimetric and fluorometric dual-signal sensor for arginine detection by inhibiting the growth of gold nanoparticles/carbon quantum dots composite. *Biosensors and Bioelectronics*, 87, 772-778.

158. Liu, Y., Ghosh, R., Wu, D., Ismach, A., Ruoff, R., & Lai, K. (2014b). Mesoscale imperfections in MoS_2 atomic layers grown by a vapor transport technique. *Nano Letters*, 14(8), 4682-4686.

159. Loan, P. T. K., Zhang, W., Lin, C. T., Wei, K. H., Li, L. J., & Chen, C. H. (2014). Graphene/MoS_2 heterostructures for ultrasensitive detection of DNA hybridisation. *Advanced Materials*, 26(28), 4838-4844.

160. Loh, T. A., Chua, D. H., & Wee, A. T. (2015). One-step synthesis of few-layer WS_2 by pulsed laser deposition. *Scientific Reports*, 5, 18116.

161. López T, Bata-Garcia JL, Esquivel D, Ortiz-Islas E, Gonzalez R, Ascencio J, Quintana P, Oskam G, Alvarez-Cervera FJ, Heredia-Lopez FJ, Gongora-Alfaro JL. (2011). Treatment of Parkinson's disease: nanostructured sol–gel silica–dopamine reservoirs for controlled drug release in the central nervous system. *International Journal of Nanomedicine*, 6, 19.

162. Lu, G.Z., Wu, M.J., Lin, T.N., Chang, C.Y., Lin, W.L., Chen, Y.T., Hou, C.F., Cheng, H.J., Lin, T.Y., Shen, J.L. and Chen, Y.F. (2019). Electrically Pumped White-Light-Emitting Diodes Based on Histidine-Doped MoS_2 Quantum Dots. *Small*, 1901908.

163. Lu, X., Wang, W., Dong, Q., Bao, X., Lin, X., Zhang, W., Zhao, W. (2015). A multi-functional probe to discriminate Lys, Arg, His, Cys, Hcy and GSH from common amino acids. *Chemical Communications*, 51(8), 1498-1501.

164. Luo, F., Yin, J., Gao, F., & Wang, L. (2009). A non-enzyme hydrogen peroxide sensor based on core/shell silica nanoparticles using synchronous fluorescence spectroscopy. *Microchimica Acta*, 165(1-2), 23.

165. Ma, Y., Li, H., Peng, S., & Wang, L. (2012). Highly selective and sensitive fluorescent paper sensor for nitroaromatic explosive detection. *Analytical chemistry*, 84(19), 8415-8421.

166. Ma, Y., Yang, C., Li, N., & Yang, X. (2005). A sensitive method for the detection of catecholamine based on fluorescence quenching of CdSe nanocrystals. *Talanta*, 67(5), 979-983.

167. Maeda, H., Fukuyasu, Y., Yoshida, S., Fukuda, M., Saeki, K., Matsuno, H., Yamauchi, Y., Yoshida, K., Hirata, K. and Miyamoto, K. (2004). Fluorescent probes for hydrogen peroxide based on a non-oxidative mechanism. *Angewandte Chemie International Edition*, 43(18), 2389-2391.

168. Mak, K. F., Lee, C., Hone, J., Shan, J., & Heinz, T. F. (2010). Atomically thin MoS_2: a new direct-gap semiconductor. *Physical Review Letters*, 105(13), 136805.

169. Mani, N. P., Ganiga, M., & Cyriac, J. (2018). MoS_2 nanohybrid as a fluorescence sensor for highly selective detection of dopamine. *Analyst*, 143(7), 1691-1698.

170. Mann, J., Ma, Q., Odenthal, P.M., Isarraraz, M., Le, D., Preciado, E., Barroso, D., Yamaguchi, K., von Son Palacio, G., Nguyen, A. and Tran, T. (2014). 2-Dimensional transition metal dichalcogenides with tunable direct band gaps: $MoS_{2\,(1-x)}\,Se_{2x}$ monolayers. *Advanced Materials*, 26(9), 1399-1404.

171. Mao, K., Wu, Z., Chen, Y., Zhou, X., Shen, A., & Hu, J. (2015). A novel biosensor based on single-layer MoS_2 nanosheets for detection of Ag^+. *Talanta*, 132, 658-663.

172. Mao, X., Xu, Y., Xue, Q., Wang, W., & Gao, D. (2013). Ferromagnetism in exfoliated tungsten disulfide nanosheets. *Nanoscale research letters*, 8(1), 430.

173. Matte, H. R., Plowman, B., Datta, R., & Rao, C. N. R. (2011). Graphene analogues of layered metal selenides. *Dalton Transactions*, 40(40), 10322-10325.

174. McCranor, B.J., Szmacinski, H., Zeng, H.H., Stoddard, A.K., Hurst, T., Fierke, C.A., Lakowicz, J.R. and Thompson, R.B. (2014). Fluorescence lifetime imaging of physiological free Cu (II) levels in live cells with a Cu (II)-selective carbonic anhydrase-based biosensor. *Metallomics*, 6(5), 1034-1042.

175. Meyer, E. A., Castellano, R. K., & Diederich, F. (2003). Interactions with aromatic rings in chemical and biological recognition. *Angewandte Chemie International Edition*, 42(11), 1210-1250.

176. Minami, T., Esipenko, N. A., Zhang, B., Isaacs, L., & Anzenbacher, P. (2014). "Turn-on" fluorescent sensor array for basic amino acids in water. [10.1039/C3CC47416J]. *Chemical Communications*, 50(1), 61-63. doi: 10.1039/c3cc47416j

177. Mishra, A. K., Lakshmi, K. V., & Huang, L. (2015). Eco-friendly synthesis of metal dichalcogenides nanosheets and their environmental remediation potential driven by visible light. *Scientific Reports*, 5(1), 15718. doi: 10.1038/srep15718

178. Molina-Sanchez, A., & Wirtz, L. (2011). Phonons in single-layer and few-layer MoS_2 and WS_2. *Physical Review B*, 84(15), 155413.

179. Moquin, A., Hutter, E., Choi, A. O., Khatchadourian, A., Castonguay, A., Winnik, F. M., & Maysinger, D. (2013). Caspase-1 Activity in Microglia Stimulated by Pro-Inflammagen Nanocrystals. *ACS Nano*, 7(11), 9585-9598. doi: 10.1021/nn404473g

180. Mouri, S., Miyauchi, Y., & Matsuda, K. (2013). Tunable photoluminescence of monolayer MoS_2 via chemical doping. *Nano Letters*, 13(12), 5944-5948.

181. Mu, Q., Xu, H., Li, Y., Ma, S., & Zhong, X. (2014). Adenosine capped QDs based fluorescent sensor for detection of dopamine with high selectivity and sensitivity. *Analyst*, 139(1), 93-98.

182. Mukherjee, S., Maiti, R., Katiyar, A. K., Das, S., & Ray, S. K. (2016). Novel colloidal MoS_2 quantum dot heterojunctions on silicon platforms for multifunctional optoelectronic devices. *Scientific Reports*, 6, 29016.

183. Naddo, T., Che, Y., Zhang, W., Balakrishnan, K., Yang, X., Yen, M., Zhao, J., Moore, J.S. and Zang, L., (2007). Detection of explosives with a fluorescent nanofibril film. *Journal of the American Chemical Society*, 129(22), 6978-6979.

184. Nag, A., Raidongia, K., Hembram, K. P., Datta, R., Waghmare, U. V., & Rao, C. N. R. (2010). Graphene analogues of BN: novel synthesis and properties. *ACS nano*, 4(3), 1539-1544.

185. Naqvi, S. T. R., Rasheed, T., Ashiq, M. N., ul Haq, M. N., Majeed, S., Fatima, B., Nawaz, R., Hussain, D. & Shafi, S. (2020). Fabrication of Iron Modified Screen Printed Carbon Electrode for Sensing of Amino Acids. *Polyhedron*, 114426.

186. Nguyen, E. P., Carey, B. J., & Ou, J. Z. (2015). J. vanEmbden, ED Gaspera, AF Chrimes, MJS Spencer, S. Zhuiykov, K. Kalantar-zadeh, T. Daeneke. *Adv. Mater*, 27, 6225-6229.

187. Nguyen, T. P., Sohn, W., Oh, J. H., Jang, H. W., & Kim, S. Y. (2016). Size-dependent properties of two-dimensional MoS_2 and WS_2. *The Journal of Physical Chemistry C*, 120(18), 10078-10085.

188. Njagi, J., Chernov, M. M., Leiter, J. C., & Andreescu, S. (2010). Amperometric detection of dopamine in vivo with an enzyme based carbon fiber microbiosensor. *Analytical chemistry*, 82(3), 989-996.

189. Norskov, J. K., & Christensen, C. H. (2006). Toward efficient hydrogen production at surfaces. *Science*, 312(5778), 1322-1323.

190. Nourbakhsh, A., Zubair, A., Sajjad, R.N., Tavakkoli KG, A., Chen, W., Fang, S., Ling, X., Kong, J., Dresselhaus, M.S., Kaxiras, E. and Berggren, K.K. (2016). MoS_2 field-effect transistor with sub-10 nm channel length. *Nano Letters*, 16(12), 7798-7806.

191. Novoselov, K. S., Fal, V. I., Colombo, L., Gellert, P. R., Schwab, M. G., & Kim, K. (2012). A roadmap for graphene. *Nature*, 490(7419), 192-200.

192. Novoselov, K. S., Jiang, D., Schedin, F., Booth, T. J., Khotkevich, V. V., Morozov, S. V., & Geim, A. K. (2005). Two-dimensional atomic crystals. *Proceedings of the National Academy of Sciences*, 102(30), 10451-10453.

193. Novoselov, K.S., Geim, A.K., Morozov, S.V., Jiang, D., Zhang, Y., Dubonos, S.V., Grigorieva, I.V. and Firsov, A.A. (2004). Electric field effect in atomically thin carbon films. *Science*, 306(5696), 666-669.

194. O'Neill, A., Khan, U., & Coleman, J. N. (2012). Preparation of high concentration dispersions of exfoliated MoS_2 with increased flake size. *Chemistry of Materials*, 24(12), 2414-2421.

195. Ono, A., Cao, S., Togashi, H., Tashiro, M., Fujimoto, T., Machinami, T., Oda, S., Miyake, Y., Okamoto, I. and Tanaka, Y. (2008). Specific interactions

between silver (I) ions and cytosine–cytosine pairs in DNA duplexes. *Chemical communications*, (39), 4825-4827.

196. Osada, M., & Sasaki, T. (2012). Two-dimensional dielectric nanosheets: novel nanoelectronics from nanocrystal building blocks. *Advanced Materials*, 24(2), 210-228.

197. Ou, J. Z., Chrimes, A. F., Wang, Y., Tang, S. Y., Strano, M. S., & Kalantar-zadeh, K. (2014). Ion-driven photoluminescence modulation of quasi-two-dimensional MoS_2 nanoflakes for applications in biological systems. *Nano letters*, 14(2), 857-863.

198. Pagliari, F., Mandoli, C., Forte, G., Magnani, E., Pagliari, S., Nardone, G., Licoccia, S., Minieri, M., Di Nardo, P. and Traversa, E. (2012). Cerium oxide nanoparticles protect cardiac progenitor cells from oxidative stress. *ACS nano*, 6(5), 3767-3775.

199. Palanisamy, S., Zhang, X., & He, T. (2015). Fast, sensitive and selective colorimetric gold bioassay for dopamine detection. *Journal of Materials Chemistry B*, 3(29), 6019-6025.

200. Pallikkarathodi Mani, N., Ganiga, M., & Cyriac, J. (2017). Synthesis of MoS_2 quantum dots uniformly dispersed on low dimensional MoS_2 nanosheets and unravelling its multiple emissive states. *ChemistrySelect*, 2(21), 5942-5949.

201. Park, J., Kim, M. S., Cha, E., Kim, J., & Choi, W. (2017). Synthesis of uniform single layer WS_2 for tunable photoluminescence. *Scientific reports*, 7(1), 16121.

202. Parsons, R. (1958). The rate of electrolytic hydrogen evolution and the heat of adsorption of hydrogen. *Transactions of the Faraday Society*, 54, 1053-1063.

203. Patel, G., & Menon, S. (2009). Recognition of lysine, arginine and histidine by novel p-sulfonatocalix [4] arene thiol functionalized gold nanoparticles in aqueous solution. *Chemical Communications* (24), 3563-3565.

204. Peng, Y., Meng, Z., Zhong, C., Lu, J., Yu, W., Jia, Y., & Qian, Y. (2001b). Hydrothermal synthesis and characterization of single-molecular-layer MoS_2 and $MoSe_2$. *Chemistry Letters*, 30(8), 772-773.

205. Peng, Y., Meng, Z., Zhong, C., Lu, J., Yu, W., Yang, Z., & Qian, Y. (2001a). Hydrothermal synthesis of MoS_2 and its pressure-related crystallization. *Journal of Solid State Chemistry*, 159(1), 170-173.

206. Peng, Y., Zhang, A. J., Dong, M., & Wang, Y. W. (2011). A colorimetric and fluorescent chemosensor for the detection of an explosive—2, 4, 6-trinitrophenol (TNP). *Chemical Communications*, 47(15), 4505-4507.

207. Pickup, J. C., Hussain, F., Evans, N. D., Rolinski, O. J., & Birch, D. J. (2005). Fluorescence-based glucose sensors. *Biosensors and bioelectronics*, 20(12), 2555-2565.

208. Pletcher, D. (1984). Electrocatalysis: present and future. *Journal of applied electrochemistry*, 14(4), 403-415.

209. Popczun, E. J., McKone, J. R., Read, C. G., Biacchi, A. J., Wiltrout, A. M., Lewis, N. S., & Schaak, R. E. (2013). Nanostructured nickel phosphide as an electrocatalyst for the hydrogen evolution reaction. *Journal of the American Chemical Society*, 135(25), 9267-9270.

210. Popczun, E. J., Read, C. G., Roske, C. W., Lewis, N. S., & Schaak, R. E. (2014). Highly active electrocatalysis of the hydrogen evolution reaction by cobalt phosphide nanoparticles. *Angewandte Chemie International Edition*, 53(21), 5427-5430.

211. Pumera, M., & Loo, A. H. (2014). Layered transition-metal dichalcogenides (MoS_2 and WS_2) for sensing and biosensing. *TrAC Trends in Analytical Chemistry*, 61, 49-53.

212. Pumera, M., Sofer, Z., & Ambrosi, A. (2014). Layered transition metal dichalcogenides for electrochemical energy generation and storage. *Journal of Materials Chemistry A*, 2(24), 8981-8987.

213. Qiao, W., Yan, S., Song, X., Zhang, X., He, X., Zhong, W., & Du, Y. (2015). Luminescent monolayer MoS_2 quantum dots produced by multi-exfoliation based on lithium intercalation. *Applied Surface Science*, 359, 130-136.

214. Radisavljevic, B., & Kis, A. (2013). Mobility engineering and a metal–insulator transition in monolayer MoS_2. *Nature materials*, 12(9), 815-820.

215. Radisavljevic, B., Radenovic, A., Brivio, J., Giacometti, V., & Kis, A. (2011b). Single-layer MoS_2 transistors. *Nature nanotechnology*, 6(3), 147.

216. Radisavljevic, B., Whitwick, M. B., & Kis, A. (2011a). Integrated circuits and logic operations based on single-layer MoS_2. *ACS nano*, 5(12), 9934-9938.

217. Radisavljevic, B., Whitwick, M. B., & Kis, A. (2012). Small-signal amplifier based on single-layer MoS_2. *Applied Physics Letters*, 101(4), 043103.

218. Ramakrishna Matte, H. S. S., Gomathi, A., Manna, A. K., Late, D. J., Datta, R., Pati, S. K., & Rao, C. N. R. (2010). MoS_2 and WS_2 analogues of graphene. *Angewandte Chemie International Edition*, 49(24), 4059-4062.

219. Ramasubramaniam, A. (2012). Large excitonic effects in monolayers of molybdenum and tungsten dichalcogenides. *Physical Review B*, 86(11), 115409.

220. Rao, C. N. R., Ramakrishna Matte, H. S. S., & Maitra, U. (2013). Graphene analogues of inorganic layered materials. *Angewandte Chemie International Edition*, 52(50), 13162-13185.

221. Reale, F., Sharda, K., & Mattevi, C. (2016). From bulk crystals to atomically thin layers of group VI-transition metal dichalcogenides vapour phase synthesis. *Applied Materials Today*, 3, 11-22.

222. Ren, X., Pang, L., Zhang, Y., Ren, X., Fan, H., & Liu, S. F. (2015). One-step hydrothermal synthesis of monolayer MoS_2 quantum dots for highly efficient electrocatalytic hydrogen evolution. *Journal of Materials Chemistry A*, 3(20), 10693-10697.

223. Roberts, J. G., Hamilton, K. L., & Sombers, L. A. (2011). Comparison of electrode materials for the detection of rapid hydrogen peroxide fluctuations using background-subtracted fast scan cyclic voltammetry. *Analyst*, 136(17), 3550-3556.

224. Rong, Mingcong, Liping Lin, Xinhong Song, Tingting Zhao, Yunxin Zhong, Jiawei Yan, Yiru Wang, and Xi Chen. (2014). A label-free fluorescence sensing approach for selective and sensitive detection of 2, 4, 6-trinitrophenol (TNP) in aqueous solution using graphitic carbon nitride nanosheets. *Analytical chemistry* 87(2): 1288-1296.

225. Sahoo, S. K., Sharma, D., Bera, R. K., Crisponi, G., & Callan, J. F. (2012). Iron (III) selective molecular and supramolecular fluorescent probes. *Chemical Society Reviews*, 41(21), 7195-7227.

226. Salmeron, M., Somorjai, G. A., & Chianelli, R. R. (1983). A LEED-AES study of the structure of sulfur monolayers on the Mo (100) crystal face. *Surface Science*, 127(3), 526-540.

227. Samadi, M., Sarikhani, N., Zirak, M., Zhang, H., Zhang, H. L., & Moshfegh, A. Z. (2018). Group 6 transition metal dichalcogenide nanomaterials: synthesis, applications and future perspectives. *Nanoscale Horizons*, 3(2), 90-204.

228. Sanford, A. L., Morton, S. W., Whitehouse, K. L., Oara, H. M., Lugo-Morales, L. Z., Roberts, J. G., & Sombers, L. A. (2010). Voltammetric detection of hydrogen peroxide at carbon fiber microelectrodes. *Analytical chemistry*, 82(12), 5205-5210.

229. Sathe, B. R., Zou, X., & Asefa, T. (2014). Metal-free B-doped graphene with efficient electrocatalytic activity for hydrogen evolution reaction. *Catalysis Science & Technology*, 4(7), 2023-2030.

230. Segura-Aguilar J, Baez S, Widersten M, Welch C J and Mannervik B (1997) Human Class Mu Glutathione Transferases, in Particular Isoenzyme M2-2, Catalyze Detoxication of the Dopamine Metabolite Aminochrome. *J Biol Chem* 272:5727-5731.

231. Segura-Aguilar, J., Paris, I., Muñoz, P., Ferrari, E., Zecca, L., & Zucca, F. A. (2014). Protective and toxic roles of dopamine in Parkinson's disease. *Journal of neurochemistry*, 129(6), 898-915.

232. Shanmugaraj, K., & John, S. A. (2019). Water-soluble MoS_2 quantum dots as effective fluorescence probe for the determination of bilirubin in human fluids. *Spectrochimica Acta Part A: Molecular and Biomolecular Spectroscopy*, 215, 290-296.

233. Shao, Y., Wang, J., Wu, H., Liu, J., Aksay, I. A., & Lin, Y. (2010). Graphene based electrochemical sensors and biosensors: a review. Electroanalysis: An *International Journal Devoted to Fundamental and Practical Aspects of Electroanalysis*, 22(10), 1027-1036.

234. Sharma, S. S., & Dietz, K.-J. (2006). The significance of amino acids and amino acid-derived molecules in plant responses and adaptation to heavy metal stress. *Journal of experimental botany*, 57(4), 711-726.

235. Sharma, S., Bhagat, S., Singh, J., Singh, R. C., & Sharma, S. (2017). Excitation-dependent photoluminescence from WS_2 nanostructures synthesized via top-down approach. *Journal of Materials Science*, 52(19), 11326-11336.

236. Shi, J., Ji, Q., Liu, Z., & Zhang, Y. (2016). Recent advances in controlling syntheses and energy related applications of MX_2 and MX_2/graphene heterostructures. *Advanced Energy Materials*, 6(17), 1600459.

237. Shi, J., Lyu, J., Tian, F., & Yang, M. (2017b). A fluorescence turn-on biosensor based on graphene quantum dots (GQDs) and molybdenum disulfide (MoS_2) nanosheets for epithelial cell adhesion molecule (EpCAM) detection. *Biosensors and Bioelectronics*, 93, 182-188.

238. Shi, Y., Zhou, W., Lu, A.Y., Fang, W., Lee, Y.H., Hsu, A.L., Kim, S.M., Kim, K.K., Yang, H.Y., Li, L.J. and Idrobo, J.C. (2012). van der Waals epitaxy of MoS_2 layers using graphene as growth templates. *Nano letters*, 12(6), 2784-2791.

239. Shi, Y., Zhou, Y., Yang, D.R., Xu, W.X., Wang, C., Wang, F.B., Xu, J.J., Xia, X.H. and Chen, H.Y. (2017a). Energy level engineering of MoS_2 by transition-metal doping for accelerating hydrogen evolution reaction. *Journal of the American Chemical Society*, 139(43), 15479-15485.

240. Shin, G.H., Lee, G.B., An, E.S., Park, C., Jin, H.J., Lee, K.J., Oh, D., Kim, J.S., Choi, Y.K. and Choi, S.Y. (2020). High-Performance Field-Effect Transistor and Logic Gates based on GaS-MoS_2 van der Waals Heterostructure. *ACS Applied Materials & Interfaces.*

241. Shu, X., Chen, Y., Yuan, H., Gao, S., & Xiao, D. (2007). H_2O_2 sensor based on the room-temperature phosphorescence of nano TiO_2/SiO_2 composite. *Analytical chemistry*, 79(10), 3695-3702.

242. Sinha, A., Tan, B., Huang, Y., Zhao, H., Dang, X., Chen, J., & Jain, R. (2018). MoS_2 nanostructures for electrochemical sensing of multidisciplinary targets: A review. *TrAC Trends in Analytical Chemistry*, 102, 75-90.

243. Smith, R.J., King, P.J., Lotya, M., Wirtz, C., Khan, U., De, S., O'Neill, A., Duesberg, G.S., Grunlan, J.C., Moriarty, G. and Chen, J. (2011). Large-scale exfoliation of inorganic layered compounds in aqueous surfactant solutions. *Advanced materials*, 23(34), 3944-3948.

244. Song, D., Wang, Y., Lu, X., Gao, Y., Li, Y., & Gao, F. (2018). Ag nanoparticles-decorated nitrogen-fluorine co-doped monolayer MoS_2 nanosheet for highly sensitive electrochemical sensing of organophosphorus pesticides. *Sensors and Actuators B: Chemical*, 267, 5-13.

245. Song, I., Park, C., & Choi, H. C. (2015). Synthesis and properties of molybdenum disulphide: from bulk to atomic layers. *RSC Advances*, 5(10), 7495-7514.

246. Song, Y., Qu, K., Zhao, C., Ren, J., & Qu, X. (2010). Graphene oxide: intrinsic peroxidase catalytic activity and its application to glucose detection. *Advanced Materials*, 22(19), 2206-2210.

247. Splendiani, A., Sun, L., Zhang, Y., Li, T., Kim, J., Chim, C.Y., Galli, G. and Wang, F. (2010). Emerging photoluminescence in monolayer MoS_2. *Nano letters*, 10(4), 1271-1275. doi: 10.1021/nl903868w

248. Štengl, V., & Henych, J. (2013). Strongly luminescent monolayered MoS_2 prepared by effective ultrasound exfoliation. *Nanoscale*, 5(8), 3387-3394.

249. Sui, Y., & Appenzeller, J. (2009). Screening and interlayer coupling in multilayer graphene field-effect transistors. *Nano letters*, 9(8), 2973-2977.

250. Sun, X., Brückner, C., Nieh, M. P., & Lei, Y. (2014). A fluorescent polymer film with self-assembled three-dimensionally ordered nanopores: preparation, characterization and its application for explosives detection. *Journal of Materials Chemistry A*, 2(35), 14613-14621.

251. Sun, Y. F., Sun, J. H., Wang, J., Pi, Z. X., Wang, L. C., Yang, M., & Huang, X. J. (2019). Sensitive and anti-interference stripping voltammetry analysis of Pb (II) in water using flower-like MoS_2/rGO composite with ultra-thin nanosheets. *Analytica chimica acta*, 1063, 64-74.

252. Sun, Y., Zhang, L., & Li, H. (2012). Chiral colorimetric recognition of amino acids based on silver nanoparticle clusters. [10.1039/C2NJ40098G]. *New Journal of Chemistry*, 36(7), 1442-1444. doi: 10.1039/c2nj40098g

253. Suprun, E. V., Karpova, E. V., Radko, S. P., & Karyakin, A. A. (2020). Advanced electrochemical detection of amino acids and proteins through flow injection analysis and catalytic oxidation on Prussian Blue. *Electrochimica Acta*, 331, 135289.

254. Swaminathan, H (b)., & Balasubramanian, K. (2018). Förster resonance energy transfer between MoS_2 quantum dots and polyaniline for turn-on bovine serum albumin sensing. *Sensors and Actuators B: Chemical*, 264, 337-343.

255. Swaminathan, H., Ramar, V., & Balasubramanian, K. (2017). Excited-State Electron and Energy Transfer Dynamics between 2D MoS_2 and GO/RGO for Turn ON BSA/HSA Sensing. *The Journal of Physical Chemistry C*, 121(23), 12585-12592.

256. Sylvia, J. M., Janni, J. A., Klein, J. D., & Spencer, K. M. (2000). Surface-enhanced Raman detection of 2, 4-dinitrotoluene impurity vapor as a marker to locate landmines. *Analytical chemistry*, 72(23), 5834-5840.

257. Tan, X., Liu, X., Zeng, W., Zhao, G., Zhang, Z., Huang, T., & Yang, L. (2019). Control assembly of Au nanoparticles on macrocyclic host molecule cationic pillar [5] arene functionalized MoS_2 surface for enhanced sensing activity towards p-dinitrobenzene. *Analytica chimica acta*, 1078, 60-69.

258. Tang, G., Tang, H., Li, C., Li, W., & Ji, X. (2011). Surfactant-assisted hydrothermal synthesis and characterization of WS_2 nanorods. *Materials Letters*, 65(23-24), 3457-3460.

259. Tang, H., Niu, W., Liao, F., Zhang, H., Xu, H., Deng, J., Chen, J., Qiu, Z., Wan, J., Pu, Y. and Bao, W. (2019). Realizing Wafer-Scale and Low-Voltage Operation MoS_2 Transistors via Electrolyte Gating. *Advanced Electronic Materials*, 1900838.

260. Tang, Q., & Jiang, D. E. (2016). Mechanism of hydrogen evolution reaction on 1T-MoS_2 from first principles. *ACS Catalysis*, 6(8), 4953-4961.

261. Tantama, M., Hung, Y. P., & Yellen, G. (2011). Imaging Intracellular pH in Live Cells with a Genetically Encoded Red Fluorescent Protein Sensor. *Journal of the American Chemical Society*, 133(26), 10034-10037. doi: 10.1021/ja202902d

262. Teng, Y., Zhao, H., Zhang, Z., Li, Z., Xia, Q., Zhang, Y., Zhao, L., Du, X., Du, Z., Lv, P. and Świerczek, K. (2016). MoS_2 nanosheets vertically grown on graphene sheets for lithium-ion battery anodes. *ACS nano*, 10(9), 8526-8535.

263. Therese, H. A., Li, J., Kolb, U., & Tremel, W. (2005). Facile large scale synthesis of WS_2 nanotubes from WO_3 nanorods prepared by a hydrothermal route. *Solid State Sciences*, 7(1), 67-72.

264. Tonkikh, A. A., E. N. Voloshina, P. Werner, H. Blumtritt, B. Senkovskiy, G. Güntherodt, S. S. P. Parkin, and Yu S. Dedkov. (2016). Structural and electronic properties of epitaxial multilayer h-BN on Ni (111) for spintronics applications. *Scientific reports*, 6, 23547.

265. Tsai, M.L., Su, S.H., Chang, J.K., Tsai, D.S., Chen, C.H., Wu, C.I., Li, L.J., Chen, L.J. and He, J.H. (2014). Monolayer MoS_2 heterojunction solar cells. *ACS nano*, 8(8), 8317-8322.

266. Tse, D. C., McCreery, R. L., & Adams, R. N. (1976). Potential oxidative pathways of brain catecholamines. *Journal of medicinal chemistry*, 19(1), 37-40.

267. Tsuru, T., Shutou, T., Nakao, S.-I., & Kimura, S. (1994). Peptide and Amino Acid Separation by Nanofiltration Membranes. *Separation Science and Technology - SEPAR SCI TECHNOL*, 29, 971-984. doi: 10.1080/01496399408005611

268. Van Der Zande, A.M., Huang, P.Y., Chenet, D.A., Berkelbach, T.C., You, Y., Lee, G.H., Heinz, T.F., Reichman, D.R., Muller, D.A. and Hone, J.C. (2013). Grains and grain boundaries in highly crystalline monolayer molybdenum disulphide. *Nature materials*, 12(6), 554.

269. Vasileva, P., Donkova, B., Karadjova, I., & Dushkin, C. (2011). Synthesis of starch-stabilized silver nanoparticles and their application as a surface plasmon resonance-based sensor of hydrogen peroxide. *Colloids and Surfaces A: Physicochemical and Engineering Aspects*, 382(1-3), 203-210.

270. Wan, C., Regmi, Y. N., & Leonard, B. M. (2014). Multiple phases of molybdenum carbide as electrocatalysts for the hydrogen evolution reaction. *Angewandte Chemie International Edition*, 53(25), 6407-6410.

271. Wang Y, Ou JZ, Balendhran S, Chrimes AF, Mortazavi M, Yao DD, Field MR, Latham K, Bansal V, Friend JR, Zhuiykov S. (2013a). Electrochemical control of photoluminescence in two-dimensional MoS_2 nanoflakes. *ACS nano*, 7(11), 10083-10093.

272. Wang, D., Pan, Z., Wu, Z., Wang, Z., & Liu, Z. (2014a). Hydrothermal synthesis of MoS_2 nanoflowers as highly efficient hydrogen evolution reaction catalysts. *Journal of Power Sources*, 264, 229-234.

273. Wang, F., Liu, X., Lu, C. H., & Willner, I. (2013). Cysteine-mediated aggregation of Au nanoparticles: the development of a H_2O_2 sensor and oxidase-based biosensors. *ACS nano*, 7(8), 7278-7286.

274. Wang, J., Yan, M., Zhao, K., Liao, X., Wang, P., Pan, X., Yang, W. and Mai, L. (2017a). Field effect enhanced hydrogen evolution reaction of MoS_2 nanosheets. *Advanced Materials*, 29(7), 1604464.

275. Wang, L., Abraham, A., Lutz, D. M., Quilty, C. D., Takeuchi, E. S., Takeuchi, K. J., & Marschilok, A. C. (2019). Toward Environmentally Friendly Lithium Sulfur Batteries: Probing the Role of Electrode Design in MoS_2-Containing Li–S Batteries with a Green Electrolyte. *ACS Sustainable Chemistry & Engineering*, 7(5), 5209-5222.

276. Wang, Q. H., Kalantar-Zadeh, K., Kis, A., Coleman, J. N., & Strano, M. S. (2012). Electronics and optoelectronics of two-dimensional transition metal dichalcogenides. *Nature nanotechnology*, 7(11), 699.

277. Wang, T., Zhu, R., Zhuo, J., Zhu, Z., Shao, Y., & Li, M. (2014b). Direct detection of DNA below ppb level based on thionin-functionalized layered MoS_2 electrochemical sensors. *Analytical chemistry*, 86(24), 12064-12069.

278. Wang, X., Feng, H., Wu, Y., & Jiao, L. (2013). Controlled synthesis of highly crystalline MoS_2 flakes by chemical vapor deposition. *Journal of the American Chemical Society*, 135(14), 5304-5307.

279. Wang, X., Nan, F., Zhao, J., Yang, T., Ge, T., & Jiao, K. (2015a). A label-free ultrasensitive electrochemical DNA sensor based on thin-layer MoS_2 nanosheets with high electrochemical activity. *Biosensors and Bioelectronics*, 64, 386-391.

280. Wang, X., Wu, Q., Jiang, K., Wang, C., & Zhang, C. (2017b). One-step synthesis of water-soluble and highly fluorescent MoS_2 quantum dots for detection of hydrogen peroxide and glucose. *Sensors and Actuators B: Chemical*, 252, 183-190.

281. Wang, Y., & Ni, Y. (2014). Molybdenum disulfide quantum dots as a photoluminescence sensing platform for 2, 4, 6-trinitrophenol detection. *Analytical chemistry*, 86(15), 7463-7470.

282. Wang, Y., Ou, J.Z., Balendhran, S., Chrimes, A.F., Mortazavi, M., Yao, D.D., Field, M.R., Latham, K., Bansal, V., Friend, J.R. and Zhuiykov, S. (2013). NV Medhekar, MS Strano and K. Kalantar-zadeh. *ACS Nano*, 7, 10083.

283. Wen, F., Dong, Y., Feng, L., Wang, S., Zhang, S., & Zhang, X. (2011). Horseradish peroxidase functionalized fluorescent gold nanoclusters for hydrogen peroxide sensing. *Analytical chemistry*, 83(4), 1193-1196.

284. Wen, Y., Xing, F., He, S., Song, S., Wang, L., Long, Y., Li, D. and Fan, C. (2010). A graphene-based fluorescent nanoprobe for silver (I) ions detection by using graphene oxide and a silver-specific oligonucleotide. *Chemical communications*, 46(15), 2596-2598.

285. Wieting, T. J., & Verble, J. L. (1971). Infrared and Raman Studies of Long-Wavelength Optical Phonons in Hexagonal Mo S_2. *Physical Review B*, 3(12), 4286.

286. Wilson, J. M. (1975). LEED and AES study of the interaction of H_2S and Mo (100). *Surface Science*, 53(1), 330-340.

287. Wu, P., Cai, Z., Gao, Y., Zhang, H., & Cai, C. (2011). Enhancing the electrochemical reduction of hydrogen peroxide based on nitrogen-doped graphene for measurement of its releasing process from living cells. *Chemical Communications*, 47(40), 11327-11329.

288. Wu, Q., Wang, X., Jiang, Y., Sun, W., Wang, C., Yang, M., & Zhang, C. (2018). MoS_2-QD-Based Dual-Model Photoluminescence Sensing Platform for Effective Determination of Al3+ and Fe3+ Simultaneously in Various Environment. *ChemistrySelect*, 3(8), 2326-2331.

289. Wu, S., Du, Y., & Sun, S. (2017). Transition metal dichalcogenide based nanomaterials for rechargeable batteries. *Chemical Engineering Journal*, 307, 189-207.

290. Wypych, F., & Schöllhorn, R. (1992). 1T-MoS_2, a new metallic modification of molybdenum disulfide. *Journal of the Chemical Society, Chemical Communications*, (19), 1386-1388.

291. Xiang, X., Shi, J., Huang, F., Zheng, M., Deng, Q., & Xu, J. (2015). MoS_2 nanosheet-based fluorescent biosensor for protein detection via terminal protection of small-molecule-linked DNA and exonuclease III-aided DNA recycling amplification. *Biosensors and Bioelectronics*, 74, 227-232.

292. Xiao, J., Choi, D., Cosimbescu, L., Koech, P., Liu, J., & Lemmon, J. P. (2010). Exfoliated MoS_2 nanocomposite as an anode material for lithium ion batteries. *Chemistry of Materials*, 22(16), 4522-4524.

293. Xiao, S. J., Zhao, X. J., Hu, P. P., Chu, Z. J., Huang, C. Z., & Zhang, L. (2016). Highly photoluminescent molybdenum oxide quantum dots: one-pot synthesis and application in 2, 4, 6-trinitrotoluene determination. *ACS applied materials & interfaces*, 8(12), 8184-8191.

294. Xie, W. Y., Huang, W. T., Li, N. B., & Luo, H. Q. (2012). Design of a dual-output fluorescent DNA logic gate and detection of silver ions and cysteine based on graphene oxide. *Chemical Communications*, 48(1), 82-84.

295. Xiong, D., Chen, M., & Li, H. (2008). Synthesis of para-sulfonatocalix [4] arene-modified silver nanoparticles as colorimetric histidine probes. *Chemical Communications*(7), 880-882.

296. Xu, M., Han, J. M., Zhang, Y., Yang, X., & Zang, L. (2013). A selective fluorescence turn-on sensor for trace vapor detection of hydrogen peroxide. *Chemical Communications*, 49(100), 11779-11781.

297. Xu, S., Feng, X., Gao, T., Liu, G., Mao, Y., Lin, J., Yu, X. and Luo, X. (2017a). Aptamer induced multicoloured Au NCs-MoS_2 "switch on" fluorescence resonance energy transfer biosensor for dual color simultaneous detection of multiple tumor markers by single wavelength excitation. *Analytica chimica acta*, 983, 173-180.

298. Xu, S., Li, D., & Wu, P. (2015). One-pot, facile, and versatile synthesis of monolayer MoS_2/WS_2 quantum dots as bioimaging probes and efficient electrocatalysts for hydrogen evolution reaction. *Advanced Functional Materials*, 25(7), 1127-1136.

299. Xu, Y. L., Niu, X. Y., Chen, H. L., Zhao, S. G., & Chen, X. G. (2017b). Switch-on fluorescence sensor for ascorbic acid detection based on MoS_2 quantum dots-MnO_2 nanosheets system and its application in fruit samples. *Chinese Chemical Letters*, 28(2), 338-344.

300. Xu, Y., Liu, Z., Zhang, X., Wang, Y., Tian, J., Huang, Y., Ma, Y., Zhang, X. and Chen, Y. (2009). A graphene hybrid material covalently functionalized with porphyrin: synthesis and optical limiting property. *Advanced Materials*, 21(12), 1275-1279.

301. Yan, H., Song, P., Zhang, S., Zhang, J., Yang, Z., & Wang, Q. (2016a). A low temperature gas sensor based on Au-loaded MoS_2 hierarchical nanostructures for detecting ammonia. *Ceramics International*, 42(7), 9327-9331.

302. Yan, Y., Zhang, C., Gu, W., Ding, C., Li, X., & Xian, Y. (2016b). Facile synthesis of water-soluble WS_2 quantum dots for turn-on fluorescent measurement of lipoic acid. *The Journal of Physical Chemistry C*, 120(22), 12170-12177.

303. Yang, T., Chen, M., Kong, Q., Luo, X., & Jiao, K. (2017). Toward DNA electrochemical sensing by free-standing ZnO nanosheets grown on 2D thin-layered MoS_2. *Biosensors and Bioelectronics*, 89, 538-544.

304. Yang, Z., Feng, J., Qiao, J., Yan, Y., Yu, Q., & Sun, K. (2012). Copper oxide nanoleaves decorated multi-walled carbon nanotube as platform for glucose sensing. *Analytical Methods*, 4(7), 1924-1926.

305. Ye, G., Gong, Y., Lin, J., Li, B., He, Y., Pantelides, S.T., Zhou, W., Vajtai, R. and Ajayan, P.M. (2016). Defects engineered monolayer MoS_2 for improved hydrogen evolution reaction. *Nano letters*, 16(2), 1097-1103.

306. Ye, Junwei, Limei Zhao, Raji Feyisa Bogale, Yuan Gao, Xiaoxiao Wang, Xiaomin Qian, Song Guo, Jianzhang Zhao, and Guiling Ning. (2015). Highly Selective Detection of 2, 4, 6-Trinitrophenol and Cu^{2+} Ions Based on a Fluorescent Cadmium–Pamoate Metal–Organic Framework. *Chemistry–A European Journal*, 21(5), 2029-2037.

307. Yildirim, A., & Bayindir, M. (2014). Turn-on fluorescent dopamine sensing based on in situ formation of visible light emitting polydopamine nanoparticles. *Analytical chemistry*, 86(11), 5508-5512.

308. Yin, W., Bai, X., Zhang, X., Zhang, J., Gao, X., & Yu, W. W. (2019). Multicolor Light-Emitting Diodes with MoS_2 Quantum Dots. *Particle & Particle Systems Characterization*, 36(2), 1800362.

309. Yoshida, H., Nakano, Y., Koiso, K., NOHTA, H., ISHIDA, J., & YAMAGUCHI, M. (2001). Liquid chromatographic determination of ornithine and lysine based on intramolecular excimer-forming fluorescence derivatization. *Analytical sciences*, 17(1), 107-112.

310. You, Y., Ye, Y., Wei, M., Sun, W., Tang, Q., Zhang, J., ... & Xu, J. (2019). Three-dimensional MoS_2/rGO foams as efficient sulfur hosts for high-performance lithium-sulfur batteries. *Chemical Engineering Journal*, 355, 671-678.

311. Yu, X. Y., Feng, Y., Jeon, Y., Guan, B., Lou, X. W., & Paik, U. (2016). Formation of Ni–Co–MoS_2 nanoboxes with enhanced electrocatalytic activity for hydrogen evolution. *Advanced Materials*, 28(40), 9006-9011.

312. Yu, X., Hu, L., Zhang, F., Wang, M., Xia, Z., & Wei, W. (2018). MoS_2 quantum dots modified with a labeled molecular beacon as a ratiometric fluorescent gene probe for FRET based detection and imaging of microRNA. *Microchimica Acta*, 185(4), 239.

313. Yu, Y., Li, C., Liu, Y., Su, L., Zhang, Y., & Cao, L. (2013). Controlled Scalable Synthesis of Uniform, High-Quality Monolayer and Few-layer MoS_2 Films. [Article]. *Scientific Reports*, 3, 1866. doi: 10.1038/srep01866

314. Yuan, J., Cen, Y., Kong, X. J., Wu, S., Liu, C. L., Yu, R. Q., & Chu, X. (2015). MnO_2-nanosheet-modified upconversion nanosystem for sensitive turn-on fluorescence detection of H_2O_2 and glucose in blood. *ACS applied materials & interfaces*, 7(19), 10548-10555.

315. Yuan, L., & Huang, L. (2015). Exciton dynamics and annihilation in WS_2 2D semiconductors. [10.1039/C5NR00383K]. *Nanoscale*, 7(16), 7402-7408. doi: 10.1039/c5nr00383k

316. Yuan, W., & Shi, G. (2013). Graphene-based gas sensors. *Journal of Materials Chemistry A*, 1(35), 10078-10091.

317. Zafar, K. S., Siegel, D., & Ross, D. (2006). A potential role for cyclized quinones derived from dopamine, DOPA, and 3, 4-dihydroxyphenylacetic acid in proteasomal inhibition. *Molecular pharmacology*, 70(3), 1079-1086.

318. Zeng, H., Liu, G.B., Dai, J., Yan, Y., Zhu, B., He, R., Xie, L., Xu, S., Chen, X., Yao, W. and Cui, X. (2013). Optical signature of symmetry variations and spin-valley coupling in atomically thin tungsten dichalcogenides. *Scientific reports*, 3, 1608.

319. Zeng, Z., Yin, Z., Huang, X., Li, H., He, Q., Lu, G., Boey, F. and Zhang, H. (2011). Single-Layer Semiconducting Nanosheets: High-yield preparation and device fabrication. *Angewandte Chemie International Edition*, 50(47), 11093-11097.

320. Zhai, Y.J., Li, J.H., Chu, X.Y., Xu, M.Z., Jin, F.J., Li, X., Fang, X., Wei, Z.P. and Wang, X.H. (2016). MoS_2 microflowers based electrochemical sensing platform for non-enzymatic glucose detection. *Journal of Alloys and Compounds*, 672, 600-608.

321. Zhan, Y., Liu, Z., Najmaei, S., Ajayan, P. M., & Lou, J. (2012). Large-area vapor-phase growth and characterization of MoS_2 atomic layers on a SiO2 substrate. *Small*, 8(7), 966-971.

322. Zhan, Y., Yan, J., Wu, M., Guo, L., Lin, Z., Qiu, B., Chen, G. and Wong, K.Y. (2017). Boron nitride nanosheets as a platform for fluorescence sensing. *Talanta*, 174, 365-371.

323. Zhan, Y., Yang, J., Guo, L., Luo, F., Qiu, B., Hong, G., & Lin, Z. (2019). Targets regulated formation of boron nitride quantum dots–Gold nanoparticles nanocomposites for ultrasensitive detection of acetylcholinesterase activity and its inhibitors. *Sensors and Actuators B: Chemical*, 279, 61-68.

324. Zhang, F., Wang, M., Zhang, L., & Su, X. (2019). Ratiometric fluorescence system for pH sensing and urea detection based on MoS_2 quantum dots and 2, 3-diaminophenazine. *Analytica chimica acta*, 1077, 200-207.

325. Zhang, H. (2015). Ultrathin two-dimensional nanomaterials. *ACS nano*, 9(10), 9451-9469.

326. Zhang, J., Wu, J., Guo, H., Chen, W., Yuan, J., Martinez, U., Gupta, G., Mohite, A., Ajayan, P.M. and Lou, J. (2017). Unveiling active sites for the hydrogen evolution reaction on monolayer MoS_2. *Advanced Materials*, 29(42), 1701955.

327. Zhang, K., Fu, L., Zhang, W., Pan, H., Sun, Y., Ge, C. Tang, N. (2018b). Ultrasmall and Monolayered Tungsten Dichalcogenide Quantum Dots with Giant Spin–Valley Coupling and Purple Luminescence. *ACS omega*, 3(9), 12188-12194.

328. Zhang, Kaiyu, Lin Fu, Weili Zhang, Hongzhe Pan, Yuanyuan Sun, Chuannan Ge, Youwei Du, and Nujiang Tang. (2018a). Ultrasmall and Monolayered Tungsten Dichalcogenide Quantum Dots with Giant Spin–Valley Coupling and Purple Luminescence. *ACS Omega*, 3(9), 12188-12194.

329. Zhang, S., Jia, X., & Wang, E. (2016). Facile synthesis of optical pH-sensitive molybdenum disulfide quantum dots. *Nanoscale*, 8(33), 15152-15157.

330. Zhang, X., Chen, X., Kai, S., Wang, H. Y., Yang, J., Wu, F. G., & Chen, Z. (2015b). Highly sensitive and selective detection of dopamine using one-pot synthesized highly photoluminescent silicon nanoparticles. *Analytical chemistry*, 87(6), 3360-3365.

331. Zhang, X., Lei, W., Ye, X., Wang, C., Lin, B., Tang, H., & Li, C. (2015c). A facile synthesis and characterization of graphene-like WS_2 nanosheets. *Materials Letters*, 159, 399-402.

332. Zhang, Y., Bai, X., Wang, X., Shiu, K. K., Zhu, Y., & Jiang, H. (2014). Highly sensitive graphene–Pt nanocomposites amperometric biosensor and its

application in living cell H_2O_2 detection. *Analytical chemistry*, 86(19), 9459-9465.

333. Zhang, Y., Zheng, B., Zhu, C., Zhang, X., Tan, C., Li, H., ... & Wang, L. (2015a). Single-layer transition metal dichalcogenide nanosheet-based nanosensors for rapid, sensitive, and multiplexed detection of DNA. *Advanced Materials*, 27(5), 935-939.

334. Zhao, D., Song, H., Hao, L., Liu, X., Zhang, L., & Lv, Y. (2013a). Luminescent ZnO quantum dots for sensitive and selective detection of dopamine. *Talanta*, 107, 133-139.

335. Zhao, G. (2019). Design, fabrication and characterization of integrated electronic devices based on wafer-scale 2D materials.

336. Zhao, W., Ghorannevis, Z., Chu, L., Toh, M., Kloc, C., Tan, P.-H., & Eda, G. (2013b). Evolution of Electronic Structure in Atomically Thin Sheets of WS_2 and WSe_2. *ACS nano*, 7(1), 791-797. doi: 10.1021/nn305275h

337. Zhao, W., Ribeiro, R. M., & Eda, G. (2015). Electronic structure and optical signatures of semiconducting transition metal dichalcogenide nanosheets. *Accounts of chemical research*, 48(1), 91-99.

338. Zhao, X., He, D., Wang, Y., & Fu, C. (2018). Facile fabrication of tungsten disulfide quantum dots (WS_2 QDs) as effective probes for fluorescence detection of dopamine (DA). *Materials Chemistry and Physics*, 207, 130-134.

339. Zheng, Y., Jiao, Y., Zhu, Y., Li, L. H., Han, Y., Chen, Y., ... & Qiao, S. Z. (2014). Hydrogen evolution by a metal-free electrocatalyst. *Nature communications*, 5(1), 1-8.

340. Zhi, C., Bando, Y., Tang, C., Kuwahara, H., & Golberg, D. (2009). Large-scale fabrication of boron nitride nanosheets and their utilization in polymeric composites with improved thermal and mechanical properties. *Advanced Materials*, 21(28), 2889-2893.

341. Zhong, Y., Xue, F., Wei, P., Li, R., Cao, C., & Yi, T. (2018). Water-soluble MoS_2 quantum dots for facile and sensitive fluorescence sensing of alkaline phosphatase activity in serum and live cells based on the inner filter effect. *Nanoscale*, 10(45), 21298-21306.

342. Zhou, Y., & Yoon, J. (2012). Recent progress in fluorescent and colorimetric chemosensors for detection of amino acids. *Chemical Society Reviews*, 41(1), 52-67.

343. Zhou, Y., Qu, Z. B., Zeng, Y., Zhou, T., & Shi, G. (2014). A novel composite of graphene quantum dots and molecularly imprinted polymer for fluorescent detection of paranitrophenol. *Biosensors and Bioelectronics*, 52, 317-323.

344. Zhu, B., Chen, X., & Cui, X. (2015). Exciton Binding Energy of Monolayer WS_2. *Scientific reports*, 5(1), 9218. doi: 10.1038/srep09218

345. Zhu, C., Zeng, Z., Li, H., Li, F., Fan, C., & Zhang, H. (2013). Single-layer MoS_2-based nanoprobes for homogeneous detection of biomolecules. *Journal of the American Chemical Society*, 135(16), 5998-6001.

346. Zhu, H., Zhang, H., & Xia, Y. (2018). Planar is better: monodisperse three-layered MoS_2 quantum dots as fluorescent reporters for 2, 4, 6-trinitrotoluene sensing in environmental water and luggage cases. *Analytical chemistry*, 90(6), 3942-3949.

347. Zhu, L., Zhang, Y., Xu, P., Wen, W., Li, X., & Xu, J. (2016). PtW/MoS_2 hybrid nanocomposite for electrochemical sensing of H_2O_2 released from living cells. *Biosensors and Bioelectronics*, 80, 601-606.

348. Zhuo, J., Wang, T., Zhang, G., Liu, L., Gan, L., & Li, M. (2013). Salts of $C_{60}(OH)_8$ electrodeposited onto a glassy carbon electrode: surprising catalytic performance in the hydrogen evolution reaction. *Angewandte Chemie International Edition*, 52(41), 10867-10870.

349. Zou, W. S., Sheng, D., Ge, X., Qiao, J. Q., & Lian, H. Z. (2011). Room-temperature phosphorescence chemosensor and rayleigh scattering chemodosimeter dual-recognition probe for 2, 4, 6-trinitrotoluene based on manganese-doped ZnS quantum dots. *Analytical chemistry*, 83(1), 30-37.

350. Zou, X., & Zhang, Y. (2015). Noble metal-free hydrogen evolution catalysts for water splitting. *Chemical Society Reviews*, 44(15), 5148-5180.

LIST OF PUBLICATIONS

Based on the Thesis

1. Pallikkarathodi Mani, N., Ganiga, M., & Cyriac, J. (2017). Synthesis of MoS_2 quantum dots uniformly dispersed on low dimensional MoS_2 nanosheets and unravelling its multiple emissive states. *ChemistrySelect*, *2*(21), 5942-5949.
2. Mani, N. P., Ganiga, M., & Cyriac, J. (2018). MoS_2 nanohybrid as a fluorescence sensor for highly selective detection of dopamine. *Analyst*, *143*(7), 1691-1698.
3. Mani, N. P., & Cyriac, J. (2019). pH- sensitive response of a highly photoluminescent MoS_2 nanohybrid material and its application in the non-enzymatic detection of H_2O_2. *Analytical and bioanalytical chemistry*, *411*(21), 5481-5488.
4. Mani, N. P., Tomy, A. M., & Cyriac, J. (2019). Chemical sensor platforms based on fluorescence resonance energy transfer (FRET) and 2D materials. *TrAC Trends in Analytical Chemistry*, 115797.
5. Mani, N. P., & Cyriac, J. (2020). Hydrothermal synthesis of WS_2 quantum dots and their application as a fluorescence sensor for the selective detection of 2,4,6-trinitrophenol. *New Journal of Chemistry* , DOI: 10.1039/C9NJ06159B)
6. Mani, N. P., Balachandran, N., & Cyriac, J. One pot hydrothermal synthesis of various WS_2 nanomaterials from common precursors by optimizing reaction conditions (*Material Letters; submitted)*
7. Mani, N. P., & Cyriac, J; Facile approach for the synthesis of MoS_2 nanosheets and a hybrid of quantum dots and nanosheets from common precursors by optimizing reaction conditions (*Bulletin of Materials Science;* submitted)
8. Mani, N. P., Sunil, K. S., Tomy, A. M., & Cyriac, J; Reducing action of WS2 nanosheets for the in-situ synthesis of silver nanoparticle and rapid detection of basic amino acids using luminescence switching of WS2- AgNP (0D-2D) nanocomposite (*Submitted*)

Other Publications

1. Ganiga, M., Mani, N. P., & Cyriac, J. (2018). Synthesis of Organophilic Carbon Dots, Selective Screening of Trinitrophenol and a Comprehensive Understanding of Luminescence Quenching Mechanism. *ChemistrySelect*, *3*(17), 4663-4668.

CONFERENCES/WORKSHOPS ATTENDED

Oral Presentations

1. International Conference on Functional Materials- ICFM 2020- IIT Kharagpur, West Bengal; **January 2020** "Reducing action of WS_2 nanosheets for the in-situ synthesis of silver nanoparticle and detection of basic amino acids using WS_2-Ag NP nanocomposite."
2. Indian Analytical Science Congress 2019- Thiruvananthapuram, Kerala; **September 2019** "Acidified molybdenum disulphide nanohybrid material as a chemical sensor for quantification of glucose in blood samples **(Best oral presentation)**
3. International Conference on Chemistry and Physics of Materials- ICCPM- St. Thomas College, Thrissur, Kerala; **December 2018** "One-pot hydrothermal synthesis of molybdenum based nanohybrid material" **(Best oral presentation)**
4. International Conference on Recent Trends in Material Science & Technology- ICMST, Thiruvananthapuram, Kerala; **October 2018** "One-pot hydrothermal synthesis of molybdenum based nanohybrid material and its application as H_2O_2 sensor."
5. IIM- Thiruvananthapuram Chapter Research Scholars Symposium on Materials Science and Engineering, Kerala; **April 2018** "Synthesis, characterization and chemical sensor applications of molybdenum based nanoparticles."

Poster Presentations

1. International Winter School 2018, "Frontiers in Materials Science"; Jawaharlal Nehru Centre for Advanced Scientific Research, Bangalore, Karnataka; **December 2018** "A label-free fluorescence sensing approach for selective and sensitive detection of picric acid using WS_2 nanodots synthesized by one-pot hydrothermal reaction."

2. International Conference on Nanomaterials and Their Applications- ICNA Mysore, Karnataka; **March, 2018** "Facile hydrothermal synthesis of MoS_2

nanohybrid material and its application as a fluorescent sensor for the detection of dopamine" **(Best poster award)**

3. Bengulure INDIA NANO 2017, Bangalore, Karnataka; **December 2017** "Fluorescent MoS_2 nanohybrid material as a sensor for selective and sensitive detection of dopamine."

4. 21st CRSI National Symposium in Chemistry (NSC-21) Indian Institute of Chemical Technology (IICT), Hyderabad, Telangana; **July 2017** "Luminescent MoS_2 quantum dots dispersed over nanosheets- elucidation of its photoluminescence origin."

5. International Conference of Young Researchers on Advanced Materials (IUMRS- ICYRAM)- Bangalore, Karnataka; **December 2016** "One-pot synthesis of highly luminescent MoS_2 quantum dots interspersed in nanosheets" **(Best poster award)**

Workshop

1. Two-day training program on High-Resolution Transmission Electron Microscopy, Scanning Electron Microscopy and Scanning Probe Microscopy, PSG Institute of Advanced Studies, Coimbatore, **September 2018** (Workshop)